Diagnosing the Role of Planetary Wave Propagation for the Coupling of the Middle Atmosphere to the Troposphere

Zur Erlangung des akademischen Grades eines
DOKTORS DER NATURWISSENSCHAFTEN
der Fakultät für Physik des
Karlsruher Instituts für Technologie (KIT), Germany

genehmigte

PhD Dissertation

von

MSc. Khalil Karami (Universität Teheran)
aus Zanjan, Islamische Republik Iran

Tag der mündlichen Prüfung:	4. November 2016
Referent:	Prof. Dr. Peter Braesicke
Korreferent:	Prof. Dr. Johannes Orphal
Betreuer der Doktorarbeit :	Dr. Miriam Sinnhuber

Publications:

The work discussed in Chapter 3 and Chapter 5 of this thesis have respectively appeared in the following publications:

Karami K., Braesicke P., Sinnhuber M., and Versick S. (2016). On the climatological probability of the vertical propagation of stationary planetary waves. *Atmos. Chem. Phys.* 16, doi:10.5194/acp-16-8447-2016.

Karami K., Braesicke P., Kunze M., Langematz U., Sinnhuber M., and Versick S. (2015). Modelled thermal and dynamical responses of the middle atmosphere to EPP-induced ozone changes. *Atmos. Chem. Phys. Discuss.* 15, doi: 10.5194/acpd-15-33283-2015.

The work in Chapter 6 of this thesis is in preparation for a publication:

Karami, K., Braesicke, P., Falk, S., Sinnhuber, B-M., Sinnhuber, M., Versick, S.: Upper tropospheric synoptic-scale Rossby waves propagation characteristics and baroclinicity as influenced by the persistent stratospheric wind regimes.

Abstract

Over the last two decades, dynamical coupling from the middle atmosphere to the troposphere has been shown to be important for tropospheric variability on a range of timescales, and as a consequence the middle atmosphere is now included in many atmospheric models from global climate models to seasonal forecasting systems. Most of previous research attempted to show either an empirical or a qualitative relationship between the middle atmosphere and troposphere. This thesis provides a dynamical framework for understanding the underlying mechanisms and processes for the downward coupling of the middle atmosphere and troposphere.

Two major research questions are addressed in this thesis. The first question is whether the confined ozone changes in the middle atmosphere due to geomagnetic and solar activity can trigger large-scale dynamical anomalies in the middle atmosphere. The second major research question of this thesis is how changes in the middle atmosphere can influence the weather (storm-tracks in particular) in the troposphere. Since storm-tracks play a major role in the transport of moisture, momentum and heat in the mid-latitudes, exploring the relationship between changes in the middle atmosphere due to geomagnetic and solar activity and associated changes in the storm-tracks has an important implication for the seasonal weather prediction in the troposphere.

In this thesis I introduce a new diagnostic tool to understand the influence of the background atmospheric state on planetary wave propagation. I first discuss some of the problematic features of the time mean of the Rossby wave vertical wavenumber squared in climatologies. In order to improve these unsatisfactory results, I objectively generate a modified set of Probability Density Functions (mPDFs) and demonstrate their superior performance compared to the climatological mean of vertical wavenumber. I show that without any reduction in the information, $Pr_{Ro}(y, z)$, (probability of favorable Rossby wave propagation) estimates the likeliness for stationary Rossby waves to propagate from one region to another at any time, altitude and latitude in a climatological sense. I suggest that $Pr_{Ro}(y, z)$ has the capacity to be used in assessing planetary wave propagation condition in climate models as well as reanalysis datasets.

A chemistry-climate model (EMAC) is used to investigate the impact of changed ozone concentration due to the Energetic Particle Precipitation (EPP) as well as 11-year solar cycle on temperature and wind fields. The results of our simulations show that ozone perturbation is a starting point for a chain of processes resulting in temperature and circulation changes over a wide range of latitudes and altitudes.

Consistent Eliassen-Palm (EP) flux and divergence changes are diagnosed to demonstrate the importance of the large-scale vertical propagation of Rossby waves in full understanding of the different temperature and zonal wind responses (due to ozone-perturbed simulations) in the Northern and Southern hemispheres.

I perform a series of perturbation experiments with EMAC model and analyze ERA-Interim reanalysis data, to explore the role of persistent stratospheric flow on the Rossby Wave Packets (RWPs) during winter in the Northern hemisphere. I also investigate the role of the near-pole persistent Stratospheric Wind Regimes (SWRs) on the tropopause height variations and its potential influence on the upper-tropospheric baroclinicity. I find that the stratospheric persistent wind regimes can alter the stability (of both stratosphere and troposphere), and hence the baroclinicity of the troposphere. I also investigate the role of the spatially long synoptic waves (wavenumbers 4-7) and smaller synoptic waves (wavenumbers 7-11) on the meridional shift of the eddy activities in the upper troposphere in response to variations in the strength of the stratospheric wind. The results obtained from my work show an enhancement of significant Rossby Wave Packets (RWPs) over east coast of USA and Atlantic region which extends to the Eurasian region, indicating a poleward shift of the storm-tracks during strong stratospheric vortex regime.

To conclude, I have shown that solar and geomagnetic variability can affect the middle atmosphere dynamics over a wide range of latitudes and altitudes, in particular, by affecting the persistent stratospheric flow during polar winter. In the second part of the thesis I have shown that this persistent stratospheric flow in turn has an impact on tropospheric baroclinity and storm tracks, thus effectively affecting weather regimes during Northern hemisphere winter.

Zusammenfassung

Während der letzten zwei Jahrzehnte hat sich gezeigt, dass die Troposphäre und die mittlere Atmosphäre (Stratosphäre, Mesosphäre und untere Thermosphäre) über dynamische Prozesse miteinander verbunden sind. Diese Vorgänge führen auf verschiedenen Zeitskalen auch zu Variationen in der Troposphäre. Deshalb findet die mittlere Atmosphäre nun auch in einer Reihe von Modellen Berücksichtigung, von der Klimamodellierung bis hin zur saisonalen Wettervorhersage. In bisherigen Studien lag der Fokus zumeist auf empirischen oder qualitativen Untersuchungen hinsichtlich der Wechselwirkungen zwischen der Troposphäre und der mittleren Atmosphäre. Dahingegen liegt der Schwerpunkt dieser Arbeit auf der Untersuchung kausaler Zusammenhänge, um das Verständnis der zu Grunde liegenden Antriebs- und Kopplungsmechanismen von der mittleren Atmosphäre hinunter in die Troposphäre zu verbessern.

Dafür wird diese Arbeit in zwei inhaltliche Schwerpunkte unterteilt. Zunächst wird im 1. Teil untersucht, ob geomagnetisch und solar induzierte Ozonänderungen in der mittleren Atmosphäre auch Veränderungen in der Dynamik der mittleren Atmosphäre auslösen können. Anschließend erfolgt im 2. Teil eine Analyse der Auswirkungen dieser dynamischen Veränderungen auf das troposphärische Wettergeschehen, wobei der Fokus auf den Zugbahnen von Sturmtiefs liegt. Die Sturmtiefs spielen wiederum eine wichtige Rolle beim Transport von Feuchtigkeit, Impuls and Wärme in mittleren Breiten. Somit kommt der Untersuchung der Zusammenhänge zwischen geomagnetisch und solar induzierten Veränderungen in der mittleren Atmosphäre und deren mögliche Auswirkungen auf die Zugbahnen der Sturmtiefs vor allem in Hinblick auf die langfristige Wettervorhersage eine hohe Bedeutung zu.

In dieser Arbeit stelle ich eine neue Methode zur Analyse des Einflusses der Hintergrundatmosphäre auf die Ausbreitung planetarer Wellen vor. Auf der Basis von klimatologischen Daten diskutiere ich dafür zunächst einige bestehende, wesentliche Probleme hinsichtlich des zeitlich gemittelten Quadrates der vertikalen Wellenzahl der Rossy-Wellen. Zur Verbesserung der sich daraus ergebenden Defizite wurde von mir eine wertungsfreie Anpassung der bereits vorhandenen Wahrscheinlichkeitsdichte-Funktionen (engl. modified Probability Density Function, mPDFs) entwickelt. Anschließend zeige ich die Vorteile der neuen Funktionen im Vergleich zu den Werten der vertikalen Wellenzahl aus Klimatologien. Insbesondere lässt sich mit Hilfe der Größe PrRo(y,z) (=Wahrscheinlichkeit der bevorzugten Ausbreitungsrichtung der Rossby-Welle) die Ausbreitungsrichtung stationärer Rossby-Wellen in Abhängigkeit von Zeit, Höhe und geografischer Breite auf klimatologischen Zeitskalen ohne Infor-

mationsverlust abschätzen. Der neu entwickelte Parameter PrRo(y,z) kann daher auch für die Analyse der Ausbreitungsbedingungen planetarer Wellen in Klimamodellen und in Reanalysedaten verwendet werden.

Mit Hilfe des Chemie-Klimamodells (EMAC) wurde der Einfluss von Ozonvariationen auf Grund von präzipitierenden Teilchen (engl. Energetic Particle Precipitation, EPP) und des 11-jährigen solaren Zyklus' auf Temperatur- und Windfelder untersucht. Die Ergebnisse meiner Simulationen zeigen, dass Ozonveränderungen eine Reihe von Folgeprozessen initialisieren, welche letztlich zu Temperatur- und Zirkulationsänderungen auf großen horizontalen und vertikalen Skalen führen. In Übereinstimmung mit diesen Ergebnissen treten auch Divergenzänderungen im Eliassen-Palm (EP) Fluss auf, welcher das kausale Bindeglied zwischen der vertikalen Ausbreitung der Rossy-Wellen und globalen Änderungen in Temperatur und zonalem Wind ist.

Im weiteren Verlauf untersuche ich den Einfluss der Stärke des stratosphärischen Hintergrundwindes auf Rossby-Wellenpakete (RWP) im polaren Winter auf der Nordhemisphäre. Hierfär verwende ich zum einen ERA-Interim Reanalysedaten und führe zum anderen eine Reihe von Sensitivitätsstudien mit EMAC durch. Die Ergebnisse zeigen, dass die unterschiedlichen stratosphärischen Windfelder (=Stratosphärische Windregime, SWR) eine Einfluss auf die Tropopausenhöhe haben und dadurch auch Veränderungen in der Baroklinität der oberen Troposphäre verursachen. Weiterhin kommt es auf Grund der SWR zur Anpassung der atmosphärischen Stabilität in der Tropos- und Strtosphŕe, was letztlich ebenfalls zu einer Modifikation der vertikalen Scherung des zonalen Windes in der Troposphäre führt. Die SWRs bewirken außerdem eine unterschiedliche Ausprägung von langen (Zonale Wellenzahl 4-7) und kurzen synoptischen Wellen (Wellenzahl 7-11), wodurch es zu einer meridionalen Verschiebung von dynamischen Prozessen in der oberen Troposphäre kommt.

Symbols

a= Radius of the Earth ($6.37 \times 10^6\ m$)
$\overline{X}$=small-scale gravity waves not resolved by model
F_ϕ= meridional component of EP flux
F_p= vertical component of EP flux
$\nabla \cdot \vec{F}$= divergence of EP flux
$\overline{u}_t$=Variability in the speed of the stratospheric circumpolar westerly flow
c= zonal phase speed for Rossby waves ($\frac{m}{s}$)
c_p= Specific heat capacity of dry air at constant pressure ($1005\frac{J}{Kkg}$)
f= Coriolis parameter ($2\Omega \sin\phi$)
$F(\lambda)$= zonal component of the friction force in the momentum equation
$F(\phi)$= meridional component of the friction force in the momentum equation
g=acceleration due to the gravity of the Earth ($9.8\frac{m}{s^2}$)
H= density scale height at the Earth's atmosphere ($7km$)
k= zonal wavenumber (dimensionless)
l= meridional wavenumber (dimensionless)
$n^2(\lambda, \phi)$= refractive index squared as a function of longitude and latitude
N= Brunt-Väisälä (buoyancy frequency)
p=Pressure (hPa)
p_s=Pressure at the surface (hPa)
Q= diabatic heating
q= potential vorticity
$q(\phi)$= meridional gradient of the potential vorticity ($\frac{1}{s\ rad}$)
R= Gas constant ($287\frac{J}{KgK}$)
t= time
u= zonal wind
v= meridional wind
T =Temperature
v^*= Transformed Eulerian Mean (TEM) meridional wind
ω^*= Transformed Eulerian Mean (TEM) vertical wind
x= longitude (m)
y= latitude (m)
z= height as vertical coordinate ($z \equiv -H\ln(\frac{p}{p_s})$)
θ= potential temperature
$\kappa = \frac{R_d}{c_p}$=ratio of the specific gas constant to the specific heat of the dry air at constant pressure $\kappa = 0.286$
λ=longitude in degree

ϕ=latitude in degree

ρ_0=one-dimensional (z only) density profile of the atmospheric basic state

ρ=atmospheric density

$\sigma = \frac{p}{p_s}$=ration of the pressure to the surface pressure

Φ= geopotential height

ψ=stream function

Ω= angular velocity of the Earth ($\Omega = 7.2 \times 10^{-5} \frac{1}{s}$)

Contents

1 Introduction

1.1 The Mean State of the Atmospheric Structure and Circulation

The Earth's atmosphere has been divided to the several layers on the basis of temperature stratification. Troposphere (the atmospheric layer between surface and about 10-16 km height) consist of about 85% of the atmospheric mass and almost all atmospheric moisture. Therefore the primary reason for the changes in the day-to-day weather variabilities is the changes in the state of the troposphere. The term middle atmosphere (which contains two layers of the atmosphere e.g. stratosphere and mesosphere) is the atmospheric region above the tropopause (about 10-16 km depending on latitude and season) to about 100 km. Figure. 1.1 shows the wintertime climatology of the zonal mean temperature profile at $30^{\circ}N$. Troposphere is a layer of atmosphere that the temperature drops with increasing altitude. In the stratosphere the temperature rises with increasing altitude due to the absorption of the Sun's shortwave radiation by ozone. The tropopause is a relatively narrow layer of the atmosphere between these two layers. Above about 50 km is an atmospheric layer which is called mesosphere. The mesosphere is the coldest atmospheric layer. Temperature in the mesosphere drops with increasing altitude mainly due to the reduced solar heating of ozone Holton (2004).

Figure. 1.2 shows the climatology of the zonal mean temperature cross section from the surface up to 1 hPa (almost 50 km) during different seasons. DJF refers to the December-January-February condition, MAM referes to the March-April-May period, JJA referes to the June-July-August condition and finally SON refers to the September-October-November condition. The thermal structure of the troposphere (below about 250 hPa in the mid-latitudes) is determined by a balance between atmospheric infrared radiative cooling, vertical transport of the heat and energy by sensible and latent heat releases away from the surface, and larger-scale heat distribution by atmospheric eddies. The net effects of these processes result in the mean temperature structure in which the temperature drops from the maximum near the surface to lower values in the troposphere. Furthermore the temperaure has its maximum in the equator and decreases toward the higher latitudes. However,

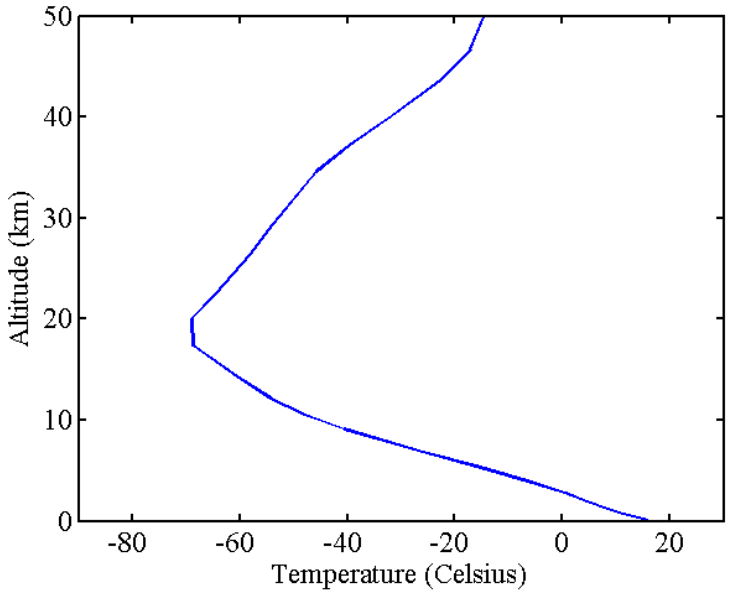

Figure 1.1: Climatology of the zonal mean temperature profile during January at $30°N$ based on ERA-Interim dataset (1979-2014).

the rate of temperature reduction from the equator to the pole is larger during winter season compared to the other seasons. Temperature drops with increasing altitude (also know as atmospheric lapse rate) about $6°C.km^{-1}$ in the midlatitude of the troposphere. In the stratosphere the radiative cooling is in equilibrium with radiative heating due to the absorption of the solar shortwave radiation by ozone and therefore temperature rises with rising altitude in the stratosphere and reaches its maximum in the stratopause heights (about 1 hPa) (Holton (2004)).

The stratospheric temperature structure is significantly different from that in the troposphere. While the maximum temperature in the troposphere is near the equator, in the lower stratosphere the minimum temperature is observed in the equatorial regions and the maxima take places in the summer pole. In the upper part of the stratosphere (between 1-30 hPa) the temperature structure is mainly determined by the local absorption of the solar radiation and therefore the temperature increases almost uniformly from the winter pole to the summer pole.

Seasonal climatology of the zonal mean zonal wind cross sections are provided in Fig. 1.3. Tropospheric jets in both hemispheres are westerly winds located in the midlatitudes and the winter-time jet is stronger than its summer-time counterpart due to the larger equator-to-pole temperature gradients in the winter season compared to the summer season. While the zonal mean zonal wind varies in different seasons

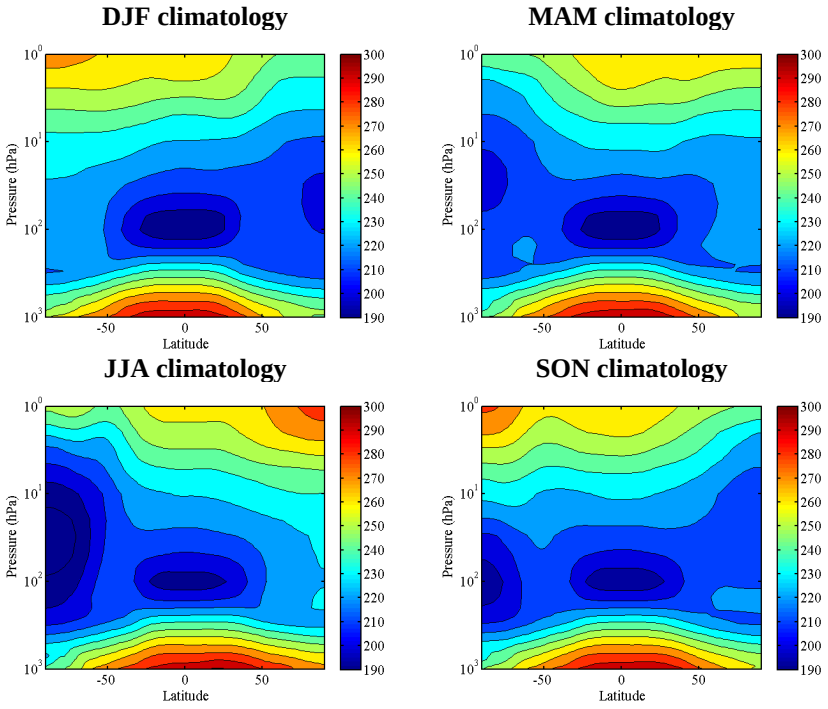

Figure 1.2: Climatology (based on ERA-Interim dataset) of the zonal mean temperature cross sections during different seasons.

in the troposphere, the climatological mean structure of the zonal mean zonal wind is always positive (westerly winds) in the mid-latitudes. However the stratospheric jet shows quite different behaviour compared to the tropospheric jets. A strong easterly jet in the summer hemisphere and a westerly jet in the winter hemisphere is observed in ERA-Interim data. The near pole westerlies in the Southern hemisphere during winter is much stronger than the northern hemisphere counterpart. These strong westerlies are called the polar night jet which provide a strong waveguide for large-scale wave propagation from the troposphere to the stratosphere. The polar vortex variability and its influence on the tropospheric circulation is the subject of the next sections of the thesis.

Atmospheric waves are an important element of the atmospheric circulation. They distribute heat, momentum and moisture across the Earth. A major deviation from the radiative equilibrium state of the atmospheric fields are related to the wave contribution. These eddy-driven departures from the radiative equilibrium induce a significant departure from the radiatively determined state, particularly in the winter-time stratosphere. Atmospheric waves which are observed in many meteo-

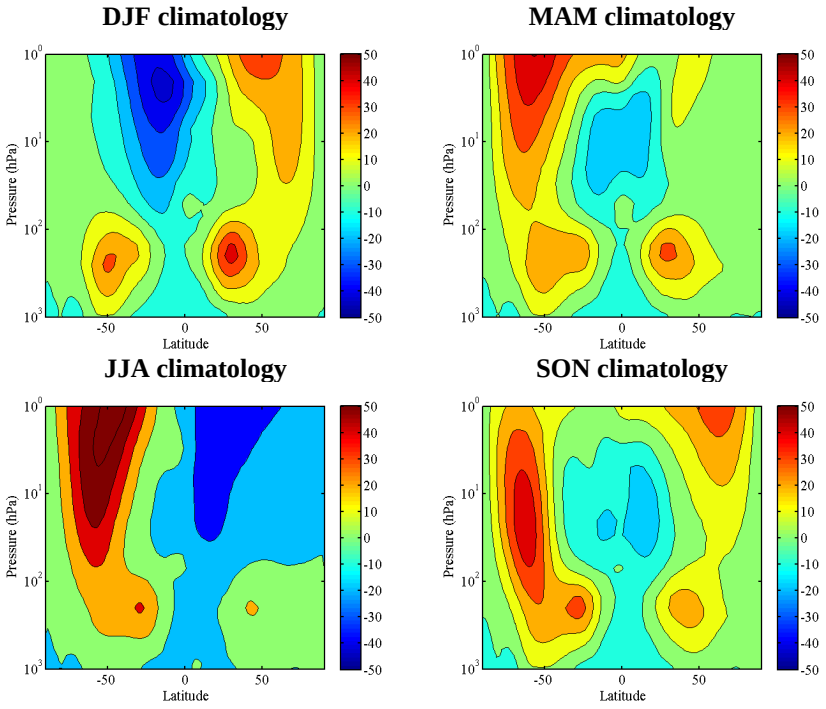

Figure 1.3: Climatology (based on ERA-Interim dataset) of the zonal mean zonal wind cross sections during different seasons.

rological variables propagate in both space and time. Figure. 1.4 and Fig. 1.5 show the zonal mean of the stationary eddy heat ($\overline{V'T'}$) and momentum fluxes ($\overline{V'U'}$) cross section in different months. Here the overbar denotes the zonal mean and prime denotes departures from the zonal mean. T, V and U are temperature, meridional and zonal wind respectively. Note that in the southern hemisphere the poleward fluxes are negative as a result of our arbitrary defining north as the positive direction. The differences in the eddy heat fluxes between January and July climatologies show that in the Northern hemisphere the poleward heat fluxes are much more stronger than in the Southern hemisphere. That is the primary reason for the warmer polar stratosphere in the northern hemisphere compared to that in the southern hemisphere during wintertime. Atmospheric Rossby waves carry both momentum and heat fluxes from the lower atmosphere to the stratosphere and cause a significant change in the zonal wind and temperature between Southern and Northern hemispheres particularly in the polar vortex region of the middle atmosphere (northward of $60°N$ in the northern hemisphere and southward of $60°S$ in the Southern hemisphere.

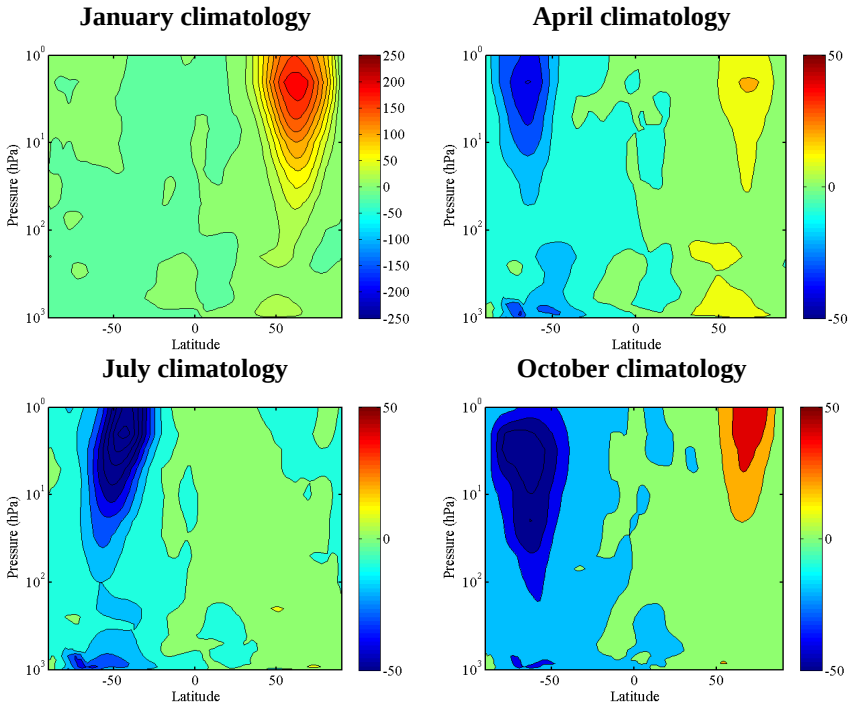

Figure 1.4: Climatology of the stationary eddy heat fluxes cross sections in different months based on ERA-Interim dataset. The units for heat fluxes are in mKs^{-1}.

1.2 Stratospheric Polar Vortex, Quasi-Biennial Oscillation and Sudden Stratospheric Warmings

Since most of the small scale waves are filtered out at the lower part of the stratosphere by the zonal mean zonal winds only large scale Rossby waves may propagate to the upper stratosphere (Charney and Drazin (1961)). In addition, the water vapour concentration in the middle atmosphere is lower than that in the troposphere. Because of these reasons understanding the stratospheric dynamics and variabilities should be much simpler than that in the troposphere. Stratospheric processes occur in much slower pace than the tropospheric processes (except for a phenomenon known as the Sudden Stratospheric Warmings (SSWs) which are relatively fast-occuring phenomenon in the middle atmosphere). Atmospheric waves play a crucial role in the stratospheric dynamics. For instance two important strato-

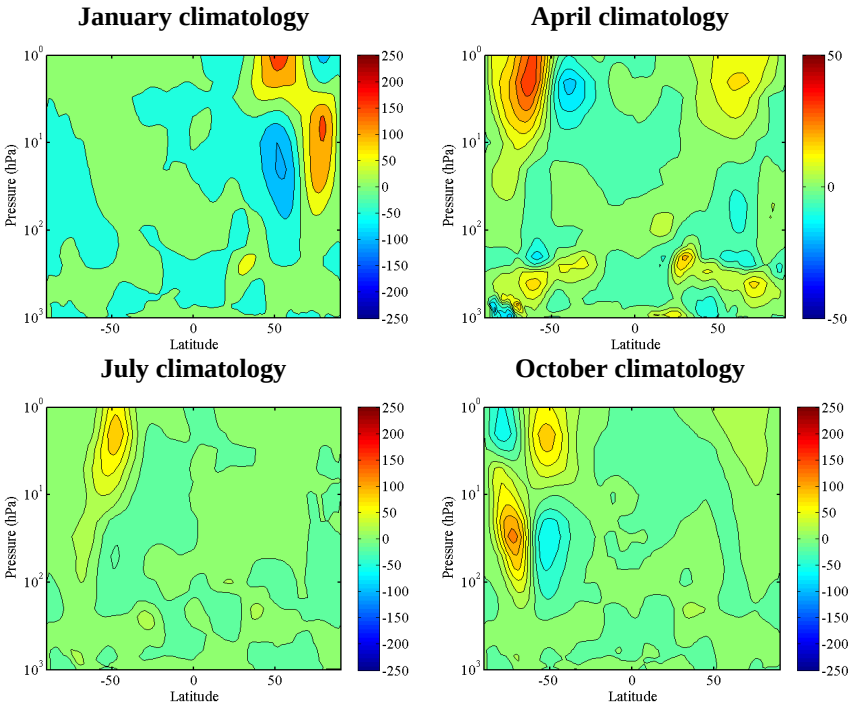

Figure 1.5: Climatology of the stationary momentum fluxes cross sections in different months based on ERA-Interim dataset. The units for the momentum fluxes are in $m^2 s^{-2}$.

spheric variations of the zonal wind known as the Quasi-Biennial Oscillation (QBO) and SSWs are directly connected to the gravity and planetary waves respectively.

The QBO is the variation of the equatorial zonal mean zonal wind regimes (both easterly and westerly winds) with periods of about 24-30 months. The zonal mean zonal wind regimes first appear above 30 km and move downward at $1km.month^{-1}$ rate. The amplitude of the zonal mean zonal wind reduces with reducing height and vanishes near the tropopause (Holton (2004)). The QBO is best depicted by the time-height cross section of the equatiorial zonal winds (Fig. 1.6).

During polar night time (from November to March in the northern hemisphere and May-October in the Southern hemisphere) the polar regions receive no energy from the sun. At the same time lower latitudes receive considerable amount of sunlight, resulting in a strong meridional temperature gradient between the equator and the pole. The strong temperature gradients creates a very strong wind current known as the polar night jet. Figure. 1.7 shows the climatology of the temperature at 50 hPa as a function of month in the northern hemisphere. Figure. 1.8 shows the same vari-

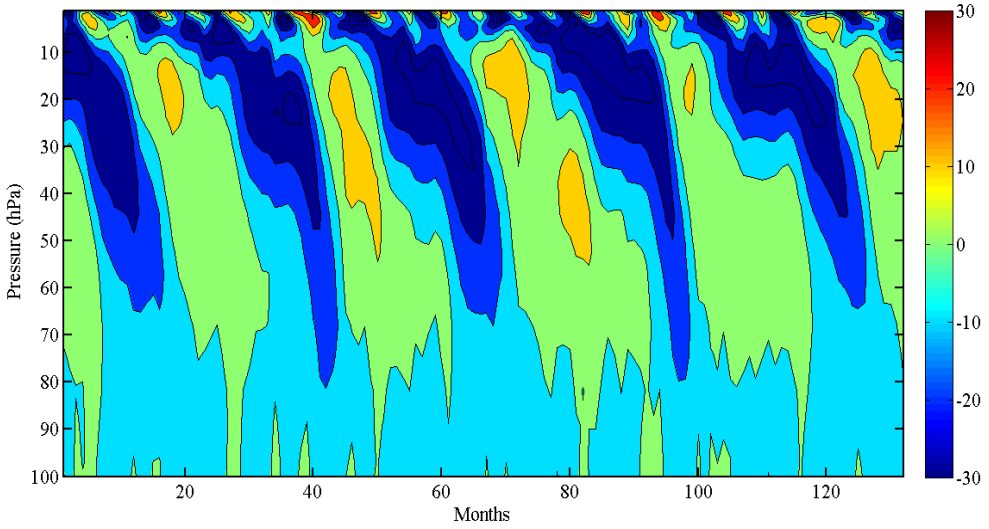

Figure 1.6: Equatorial ($-6°S$- $6°N$) zonal mean zonal wind regimes (based on ERA-Interim dataset) show a periodic oscillation of about 24-30 months, known as Quasi-Biennial Oscillation (QBO). The horizontal axis is the number of months following January 1979.

able in the Southern hemisphere. The strong polar night jets create a strong barrier between ozone-riched regions in the mid-latitudes and inside of the polar vortex. Every year in early winter-time of both hemispheres the polar vortex form and weaken in the late spring. Zonal winds are weak and easterly during summer-time in the stratosphere in both hemispheres. The stratospheric polar vortex in the Southern hemisphere is more symmetric and cold than its counterpart in the Northern hemisphere. This differences are mainly due to the more frequent planetary-scale waves that propagates upward from the troposphere to the stratosphere in the Northern hemisphere compared to the Southern hemisphere.

A Sudden Stratospheric Warming (SSW) refers to the fast (less than a week) deceleration of the zonal wind in the stratosphere during wintertime. The wintertime wind of the stratospheric vortex is westerly but once a SSW occurs the jet stream weakens and even reverses to easterly winds. The wind reversal is usually accompanied by a temperature rise of about (10-50 K) at the polar regions of the middle atmosphere. SSW occurance is one of the best examples of the two-way coupling of the stratosphere-troposphere systems. The frequency of this phenomenon is about 6 events per decade (according to reanalysis datasets) Charlton and Polvani (2007). Due to less quasi-stationary large-scale wave propagation in the Southern hemi-

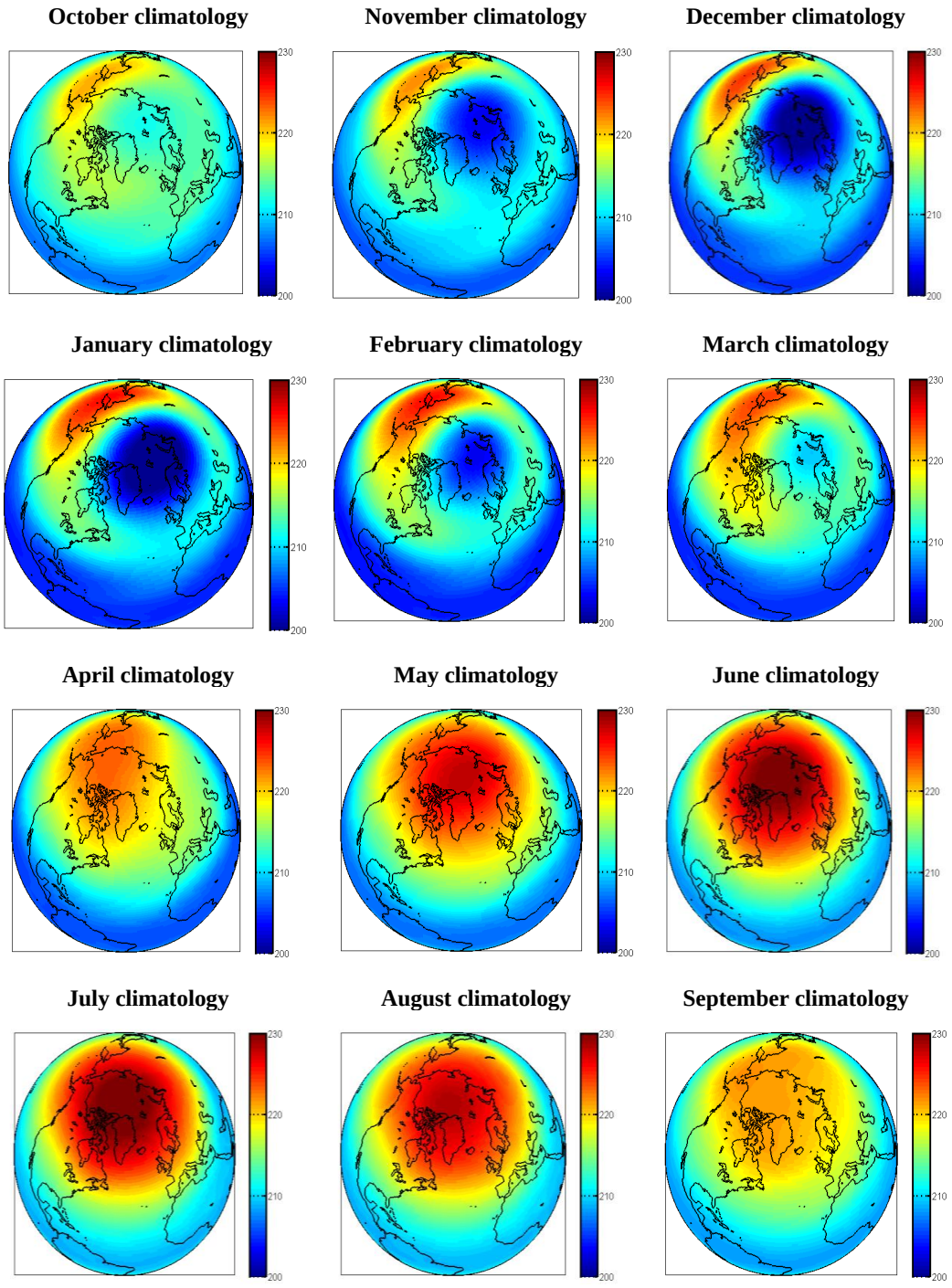

Figure 1.7: Time evolution of the Northern hemisphere polar vortex. The figure shows the long-term climatology of temperature (based on ERA-Interim dataset from 1979-2014) at 50 hPa as a function of time of the year.

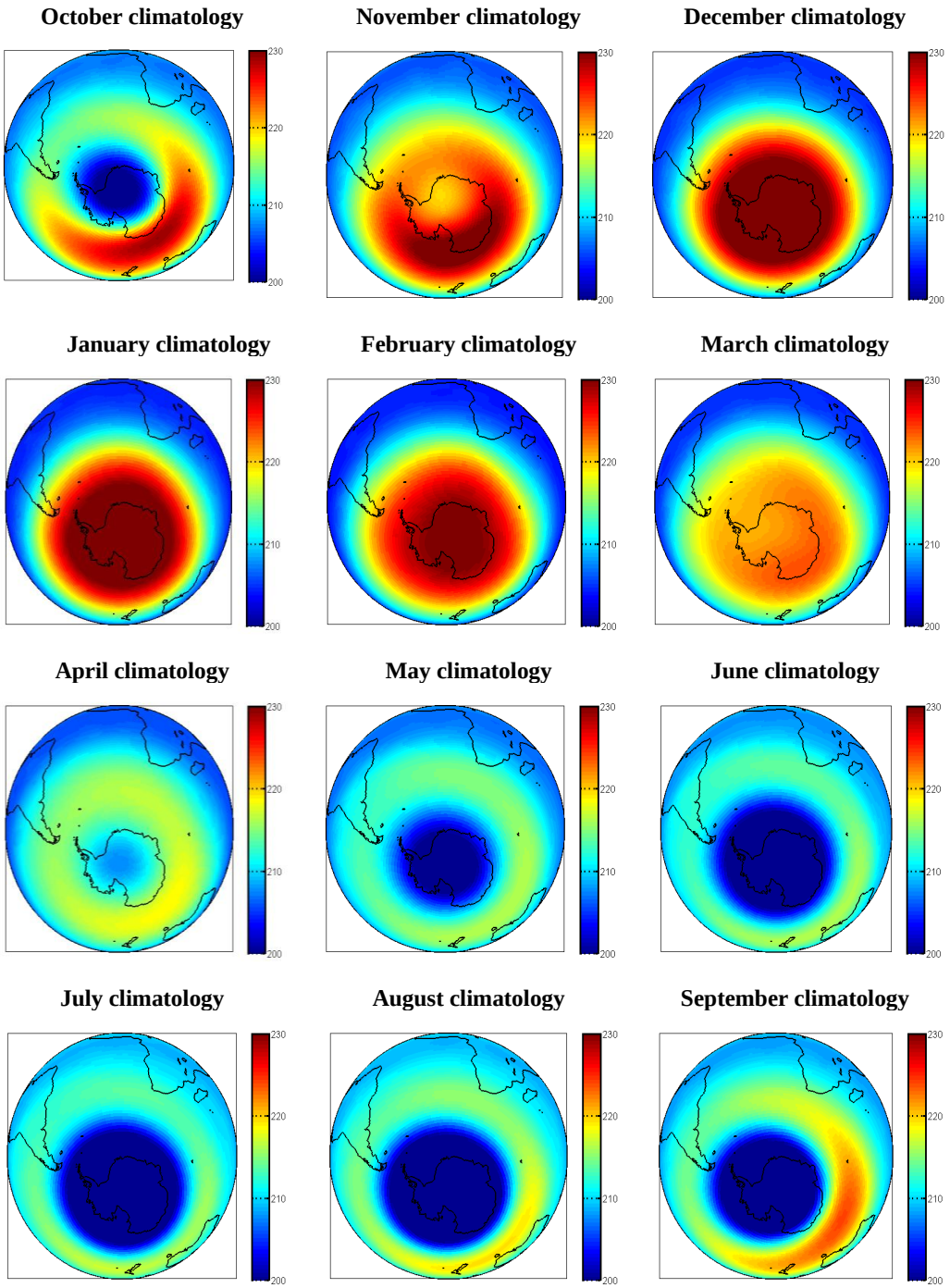

Figure 1.8: Time evolution of the southern hemisphere polar vortex. The figure shows the long-term climatology of temperature (based on ERA-Interim dataset from 1979-2014) at 50 hPa as a function of time of the year.

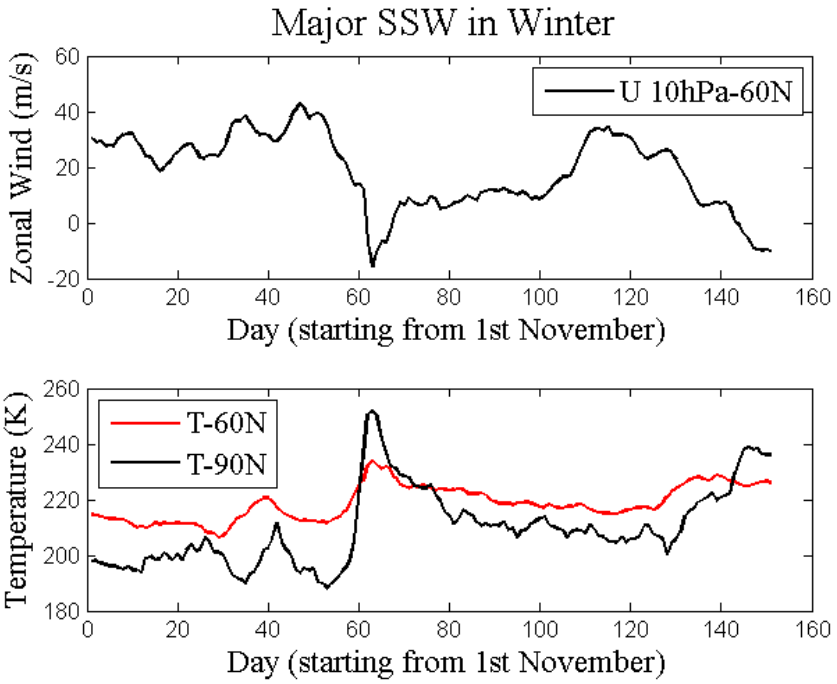

Figure 1.9: Top: Zonal mean zonal wind at 60°N- 10 hPa during winter 1984-1985. 1 January 1985 a major SSW occurs and the zonal mean zonal wind reverses and becomes easterly. Bottom: Zonal mean temperature at 60°N- 10 hPa (red line) and 90°N- 10 hPa (black line) druing winter 1984-1985 (based on ERA-Interim dataset.

sphere compared to the Northern hemisphere, SSWs occur very rarely in the Southern hemisphere (VanLoon and Jenne (1972)). Enhanced wave activity leaking from the troposphere to the stratosphere and non-linear interaction of the planetary waves and mean flow of the stratosphere are two important mechanisms for SSW occurrence in the Northern hemisphere (Palmer (1981)). The first date on which the daily mean zonal mean zonal wind at 60°N and 10 hPa falls below zero (reversing from westerlies to easterly wind) is defined as date of SSW occurrence. At the same time the zonal mean temperature gradient from 60°N and north pole requires to reverse at the central date of SSW occurrence. Once a warming is identified, a long-lasting fluctuation (about several weeks) of zonal wind has been observed. Therefore no day within 20 days following the SSW onset can be defined as an SSW (McInturff (1978), Charlton and Polvani (2007)). Figure. 1.9 shows the time evolution of the zonal mean zonal wind at 60°N-10 hPa during winter 1984-1985 starting from November first 1984. A major SSW occurs at 1 January 1985 and zonal wind changes its sign to easterly winds. At the oncet date of the SSW, temperature at 90°N and 10 hPa

is warmer than at $60°N$ and 10 hPa.

1.3 Stratosphere-Troposphere Dynamical Coupling

The stratosphere, contains about 15% of the atmospheric mass. Unlike the troposphere (the atmospheric layer between surface and about 10-16 km height) the stratosphere with its significant stability and dryness (due to the lack of significant amounts of water vapour compared to the tropospheric water vapour concentration) as well as its strong winds cannot maintain the dynamics of the day-to-day tropospheric weather variabilities. The wind speed of the wintertime stratospheric polar vortex can reach of up to 90 $m.s^{-1}$ and 50 $m.s^{-1}$ in the Southern and Northern Hemispheres respectively (Kidston et al. (2015)).

Early efforts on the stratosphere-troposphere dynamical coupling considered the stratosphere as a merely passive receiver of the tropospheric energy and wave activity. In other words the stratosphere was considered as a "slave" to a tropospheric "master" (Charlton et al. (2005)). The implicit assumption was that the changes in the stratospheric flow have no effects on the troposphere. This description of the coupling mechanism is best captured by the study of Matsuno (1970) who successfully described the occurrence of sudden stratospheric warmings with a "fixed input of planetary waves" at the lower boundary near the tropopause.

The seminal paper by Baldwin and Dunkerton (2001) for the first time showed an apparent "downward propagation of anomalous circulation signal" from the stratosphere to the surface in the Northern Hemisphere wintertime (See Fig. 1.10). They found that the surface pressure anomalies associated with the changes in the stratospheric flow resembles the annular mode. The annular modes are large scale patterns of climate variabilities that owe their existence to the internal atmospheric dynamics. The annular modes are associated with large anomalies of precipitation and surface temperature variabilities in both Northern and Southern hemispheres. A relatively long time scale of the downward propagating signal from the stratosphere to the surface (10-60 days) has been attracting an increasing interest due to the finding that stratospheric changes can be a potential source of improved tropospheric seasonal forecasting. This potential source of skill for seasonal forecasting is currently almost untapped (Smith et al. (2012), Smith et al. (2014)).

Until recently most weather forecasting centres have been ignoring the influence of the stratosphere in improving weather predictions since their models did not include adequate stratospheric processes and dynamics. Recently, weather centres such as the European Center for Medium-Range Weather Forecasts (ECMWF) moved their operational model lid from the tropopause to the stratopause and hence emphasized

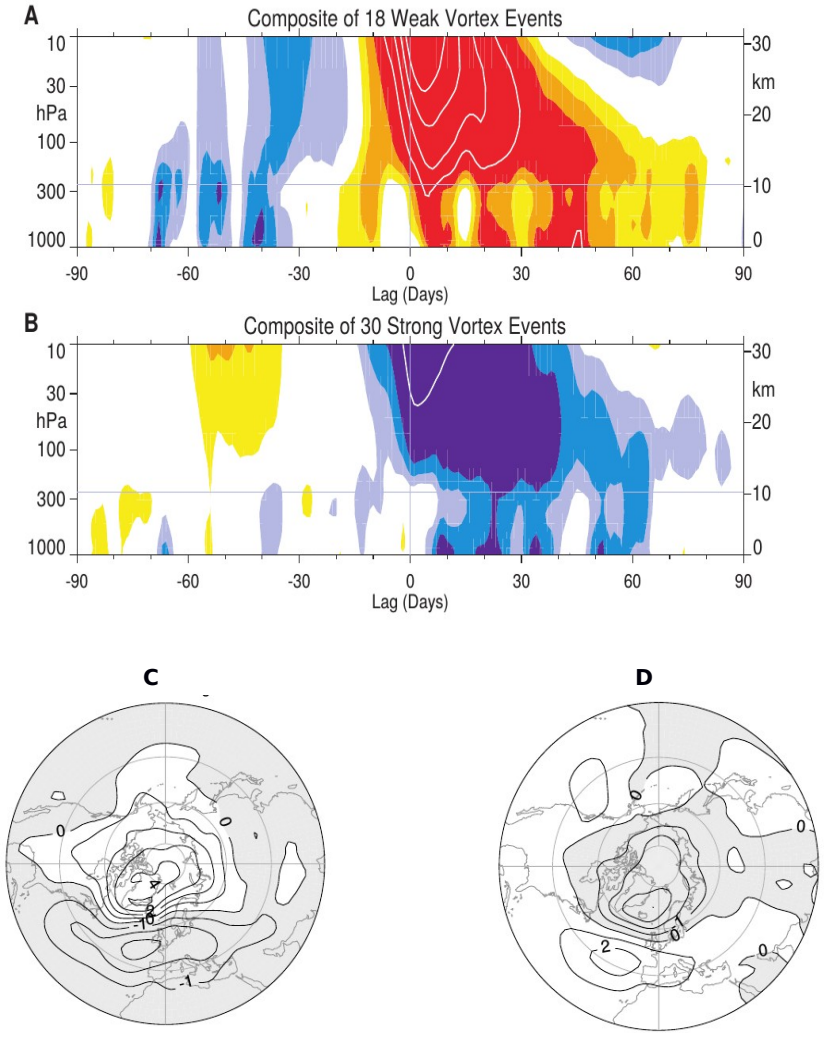

Figure 1.10: (A): Time-altitude cross section of the northern annular mode values during weak vortex events. Weak vortex events are defined by the dates on which the annular mode values at 10 hPa drops below -3.0. (B): The same as (A) for strong vortex events. Strong vortex events are defined by the dates on which the annular mode values at 10 hPa is more than 1.0 threshold. The indices of annular modes are non-dimensional values. (C): The average sea-level pressure anomalies (hPa) during weak vortex regimes. (D): The same as (C) for strong vortex regimes. (schematic view is taken from Baldwin and Dunkerton (2001)).

the stratospheric processes and dynamics. In fact over the last two decades or so, the stratosphere-troposphere dynamical coupling has been shown to be important for tropospheric variability on a range of timescales. For example Ineson and Scaife (2009) showed that the stratospheric processes are crucial in capturing the teleconnections between El Nino-Southern Oscillation (ENSO) and the Northern Annular Oscillation (NAO). In addition one must take into account the stratospheric role for understanding the NAO response to changes in the solar radiation (Ineson et al. (2011)). As a consequence of these findings, the stratosphere is now included in many atmospheric models from global climate models to seasonal forecasting systems (Tripathi et al. (2015), Scaife et al. (2005)).

1.4 Mechanisms Proposed for the Stratosphere-Troposphere Coupling

In general two categories of mechanisms are proposed for the stratosphere-troposphere coupling, direct and indirect (Simpson (2009)). The direct mechanisms refers to changes in the lower most regions of the stratosphere where the changes are very close to the troposphere. The indirect mechanisms refers to the changes in the middle and upper troposphere that affects large or small scale wave propagation from the troposphere to the stratosphere. Changes in the large-scale wave propagation via interaction with mean-flow can affect the tropospheric weather and circulation. Table 1.1 shows the mechanisms proposed for the stratosphere-troposphere coupling.

1.4.1 The direct coupling mechanisms

The stratospheric mass redistribution theory suggested by Baldwin and Dunkerton (1999) explains the influence of an anomalous zonal force in the stratosphere that induces a meridional circulation in the stratosphere. It is suggested that the tropospheric branch of the above-mentioned circulation might not compensate the stratospheric branch (mainly due to the surface friction). As consequence the mass (or alternatively surface pressure) in the polar cap region will respond to any changes in the stratospheric meridional circulation. Due to the changes in the surface pressure gradient the zonal wind near the surface (in particular around the southern boundary of the polar cap region) will be changed accordingly (Sigmond et al. (2003)).

The downward control principle suggested by Haynes et al. (1991) links changes in the circulation below any given height in the atmosphere to the zonal force per

Table 1.1: The proposed mechanisms involved in the stratosphere- Troposphere coupling. These mechanisms are proposed by (Simpson, 2009).

Indirect Mechanisms	Direct Mechanisms
1 Stratospheric mass redistribution especially at polar cap regions	**1 Changes in the propagation conditions of Rossby waves**
2 Induced meridional circulation by the downward control principle	**2 Wave mean-flow interactions**
3 Changes in the tropopause height due to the variations in the stratospheric potential vorticity	**3 Changes in the tropospheric baroclinic eddies**
4 Direct radiative impact on the stratospheric temperature and circulation	

unit mass (for instance due to the wave breaking and eddy dissipation processes) above the given height. The downward control principle is valid in the steady state (no acceleration or deceleration of the flow). The downward control mechanism is mainly valid in the middle atmosphere because the atmospheric mass is concentrated mainly in the troposphere compared to the middle and upper atmosphgere.

The third dynamical mechanism that explains the dynamical coupling between stratosphere and troposphere is the potential vorticity inversion. A form of the quasi-geostrophic potential vorticity (PV) that can be used to explain the non-local responses of the atmosphere to the local changes in the atmosphere is defined as:

$$q = \frac{1}{f_0}\nabla^2\Phi + f + \frac{\partial}{\partial p}\frac{f_0}{\sigma}\frac{\partial \Phi}{\partial p} \tag{1.1}$$

where q is the potential vorticity, Φ is the geopotential height, f is the coriolis parameter, p is the pressure and $\sigma = \frac{p}{p_s}$ where p_s is the surface pressure. According to this definition the PV is the sum of relative vorticity, planetary vorticity (coriolis force) and the stretching vorticity. Following the geostrophic motion the net tendency in the PV is zero ($\frac{D_g q}{Dt} = 0$) (Holton (2004)). Since the quasi-geostrophic potential vorticity can be changed through frictional and diabatic processes therefore any changes in the PV can result in changes in the geopotential height and therefore induce changes in the zonal wind and temperature. The quasi-geostrophic form of the PV equation shows that the PV is linked to the geopotential height

by the second order differential operator. Therefore any anomaly in the PV can induce changes in the geopotential height that are non-local and might be stretched horizontally and vertically. The quasi-geostrophic form of the PV is a fundamental quantity in the atmospheric dynamics because it explains how local changes of PV (through adiabatic and frictioanl processes) is connected to the non-local changes in the zonal wind and temperature. The Ertel form of the PV is also a helpful dynamical quantitiy that can be used as diagnostic tool to explain the connection between stratospheric processes and it tropospheric counterpart. This quantity will be explained in the next section.
The last direct mechanism in which one can explain the stratosphere-troposphere dynamical coupling is the direct alteration of the middle atmosphere through radiative forcing. The previous mechanisms that drive changes in the troposphere in response to changes in the stratosphere were purely dynamical mechanisms. Nevertheless the study of (Grise et al. (2009)) shows that the role of radiative processes in the stratosphere-troposphere coupling cannot be ruled out. Direct radiative forcing can alter both temperature and ozone fields in the middle atmosphere. Trough geostrophic and hydrostatic adjustments the tropospheric circulation responses to the changes in the middle atmosphere (Grise et al. (2009)).

1.4.2 The Indirect Coupling Mechanisms

The first indirect mechanism for the coupling between the stratsphere and the troposphere involves changes in the large-scale Rossby wave propagation or smaller-scale synoptic eddies. According to (Charney and Drazin (1961)) only large-scale Rossby waves (wavenumbers 1-3) can propagate upward and penetrate from the troposphere to the stratosphere. During winter-time of both hemispheres when the zonal mean zonal wind is westerly in the stratosphere Rossby waves have chance to propagate upward to the stratosphere. However the probability of the upward planetary-scale wave propagation depends on several other factors as well. These factor can be understood through the well-known Charney-Drazin criterion:

$$0 < u_0 - c < u_c = \frac{\beta}{(k^2 + l^2) + \frac{f_0}{4H^2N^2}} \tag{1.2}$$

where u_0 is the background stratospheric mean flow (zonal mean zonal wind), u_c is the Rossby wave critical velocity, $\beta = \frac{\partial f}{\partial y}$ where f is the coriolis parameter, k and l are zonal and meridional wavenumbers, c is the Rossby waves phase speed, H is the atmospheric scale height and finally N is the buoyancy frequency. It is clear that during summer time of both hemispheres when the stratospheric background flow (u_0) is easterly Rossby waves cannot propagate upward. The same is true after the

occurrence of sudden stratospheric warmings when during Northern hemisphere wintertime the stratospheric background flow change its sign from dominantly westerly flow to an easterly flow. Since the zonal mean zonal wind in the Southern hemisphere (u_0) is much stronger than its Northern hemisphere counterpart, the Charney-Drazin criterion is not fulfilled in the Southern hemisphere wintertime condition and hence waves cannot penetrate to the stratosphere in the Southern hemisphere (Charney and Drazin (1961)). This criterion explains the seasonal cycle of stratospheric planetary waves. According to the study of (Plumb (1989)) in the Southern hemisphere wintertime the Rossby waves amplitude is minimum. On the other hand Rossby waves-mean flow interaction in the Northern hemisphere wintertime prevents the zonal stratospheric flow to becomes so strong.
Since only large-scale Rossby waves (wavenumbers 1-3) can penetrate to the stratosphere from the troposphere, therefore changes in the stratospheric flow and subsequent changes in the propagation conditions of vertically propagating waves provide a pathway for the downward transmission of the stratospheric changes to the troposphere. The observational evidences for this mechanism is provided by the study of (Perlwitz and Harnik (2003), Perlwitz and Harnik (2003)). These studies show that through the downward planetary wave reflection by the stratospheric flow, the changes in the stratosphere can affect the tropospheric circulation.
The second indirect mechanism for the coupling between the stratosphere and troposphere is the alteration of wave-mean flow processes in response to changes in the stratosphere (Boville (1984)). If the Charney-Drazin criterion is fulfilled the large-scale Rossby waves can propagate upward and deposit their easterly momentum to the mean stratospheric flow. This mechanism leads to changes in the mean stratospheric flow which can subsequently alter the propagation condition of Rossby waves which result in downward propagation of the zonal wind anomalies. It is also important to mention that the wave-mean flow interaction and planetary wave propagation can only explain the stratosphere-troposphere coupling in the wintertime in the Northern hemisphere. Since the planetary waves are produced by the flow over the large-scale mountains as well as land-sea temperature contrasts, therefore the planetary waves are more stronger in the Northern hemisphere than in the Southern hemisphere. It is the reason why these mechanisms (planetary wave propagation and wave-mean flow interaction) cannot explain the stratosphere-troposphere coupling in other seasons or coupling that is observed in the Southern hemisphere (Holton (2004), Simpson (2009)).
To explain the observed stratosphere-troposphere coupling in seasons other than wintertime northern hemisphere or the coupling in the Southern hemisphere another mechanism is required. One such mechanism is the change in the baroclinic systems in the troposphere in response to the changes in the stratosphere flow. Tropospheric baroclinic eddies are mainly developed in the mid-latitudes due to the

strong meridional temperature gradient (or alternatively vertical wind shear) and therefore are present in both Northern and Southern hemispheres. These eddies are responsible for transferring heat and momentum from the lower latitudes to the higher latitudes (Holton (2004). Since eddies owe their existence to the meridional temperature gradients between the tropics and the poles, the eddy development is stronger in the cold seasons in both hemispheres. This mechanism links the phase speed of eddies (Chen and Held (1992)), eddy length scales (Riviere (2011)), direction of propagation of synoptic eddies (Simpson et al. (2009)) and the types of synoptic wave-breaking (Kunz et al. (2009)) to the anomalies of the stratospheric wind.

1.5 Solar and Geomagnetic Variability and its Influence on Climate

The Sun is the primary source of energy for the Earth's climate system. Different regions of the Sun from its atmosphere, photosphere and convection zone vary on a range of time scales, from minutes to hundreds of years. For example Fröhlich and Lean (2004) show an enhancement of the Total Solar Irradiance (TSI) during a solar flare that reach to 0.003 %. The TSI is the integral of irradiance (the power arriving to the Earth per unit area, per unit wavelength) over all wavelengths. However, from the climate perspective the longer time scales of solar variability are more important than the shorter time scales (Ogurtsov et al. (2002)). Figure. 1.11 demonstrates the 11-year solar variability in several quantities which either directly or indirectly are related to the radiation output from the Sun. Sunspots are relatively colder spots on the Sun's surface (between 4200 K at the center of the sunspot to 5700 K at the edge) compared to the quiet chromosphere (about 6050 K). When a sunspot forms it can last between several days and a few weeks. Around the sunspots the magnetic fields are thousands of times stronger than its counterpart at the Earth.

The available solar power to the Earth's climate (at the top of the atmosphere) is about 239 Wm^2 with variations of about 0.17 Wm^2 during the 11-year solar cycle. The variation in the TSI during the 11-year solar cycle (0.07 %) is almost negligible compared to the available TSI Gray et al. (2010). However spectral variability of the irradiance (Fig. 1.12) shows that the shorter wavelengths (less than 200 nm) can vary significantly between the periods of 11-year solar cycles (more than 50 % between 120-150 nm and about 100 % near 100 nm) . The UV variations can reach up to 6 % near 200 nm (where oxygen dissociation and ozone production occur). The UV variations of up to 4 % is also observed between 240-320 nm where stratospheric ozone can significantly absorb the UV radiation in this band. The 11-year variations in the solar irradiance in the UV band can induce variations in the production or

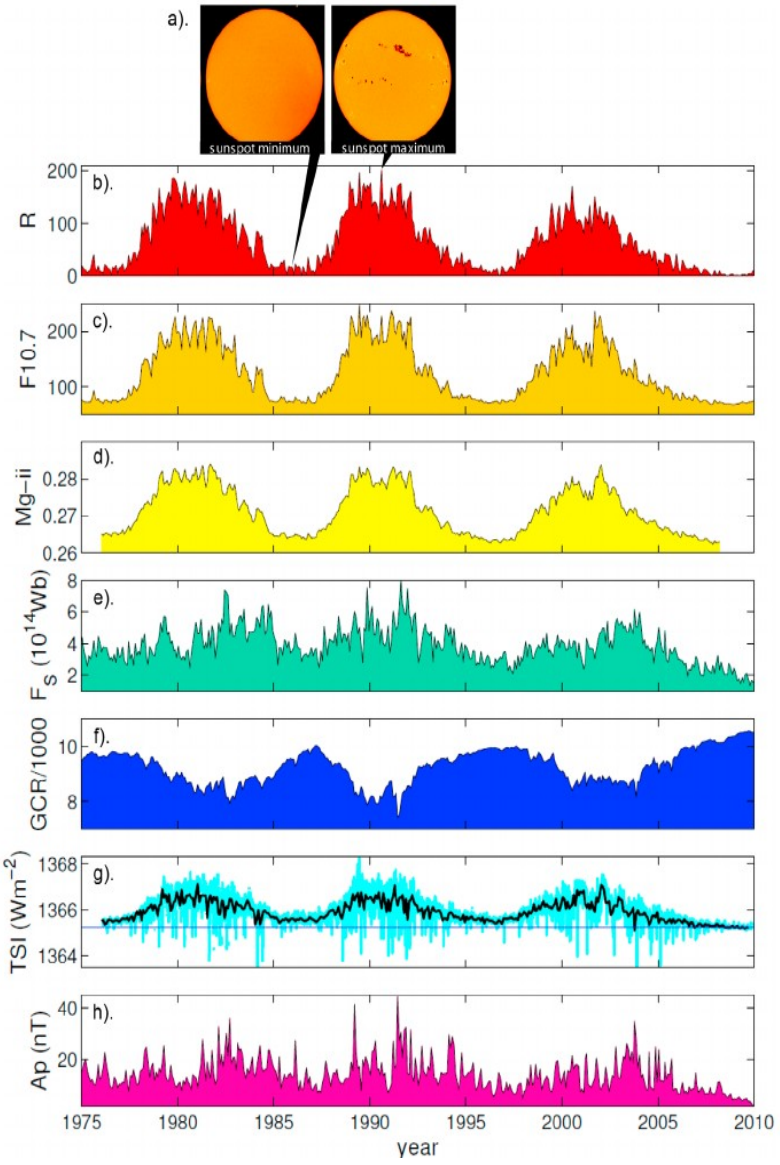

Figure 1.11: (a): Two imagaes of the Sun during the minimum sunspot and maximum sunspot. (b); The sunspot number R that shows the mean of sunspot numbers derived from the global network of solar observations; (c) The 10.7 solar radio flux measured at Ottawa, Canada; (d): The Mg ii line which is a measure of Mg II ion emission from the Sun's chromosphere and is highly correlated with the UV irradiance (150-400 nm); (e): The open solar flux derived from the observed radial component of interplanetary field near the Earth. (f): The Galactic Cosmic Rays (GCR) counts per minute recorded at McMurdo, Antarctica; (g): TSI observation; (h) geomagnetic Ap index. (schematic view is taken from Gray et al. (2010)).

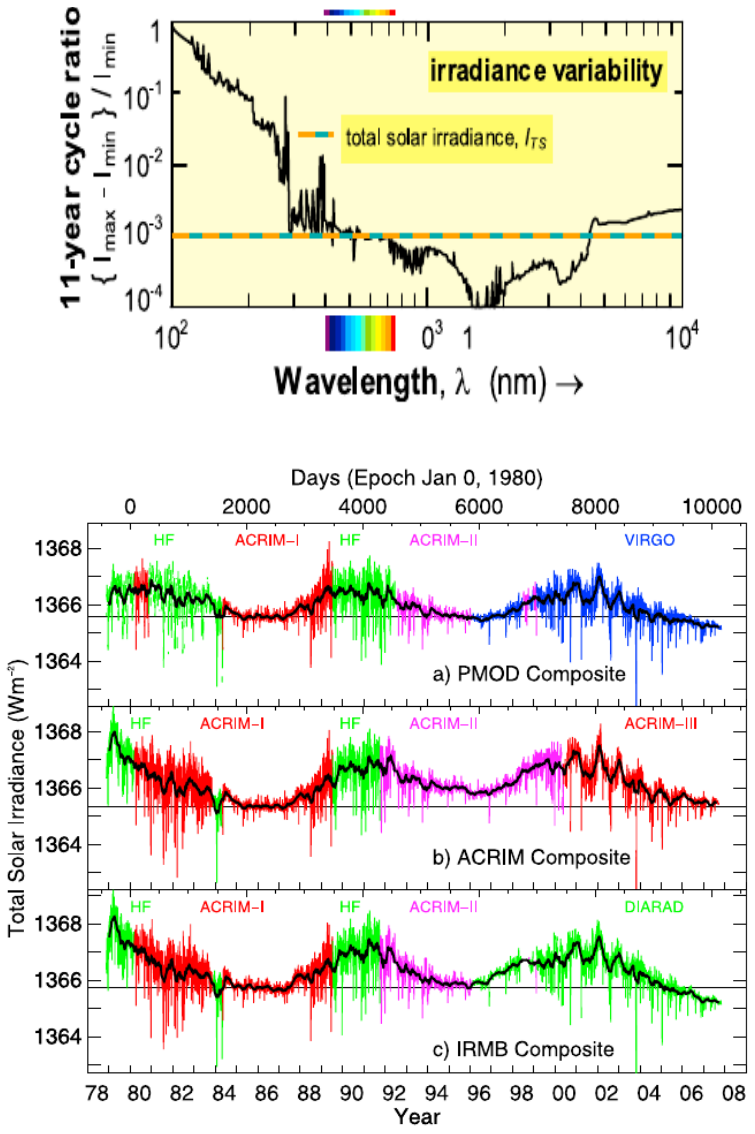

Figure 1.12: (a): Top: Irradiance variability as a function of wavelength during 11-year solar cycles. The horizontal dashed line is the variation of the TSI during 11-year solar cycles. Bottom: Instrumental (PMOD (a), ACRIM, (b), IRMB (c)) measure of TSI variability for the period of 1978-2007. Daily values are shown in colored and 81 day running means are shown in black lines. (schematic view is taken from Gray et al. (2010)).

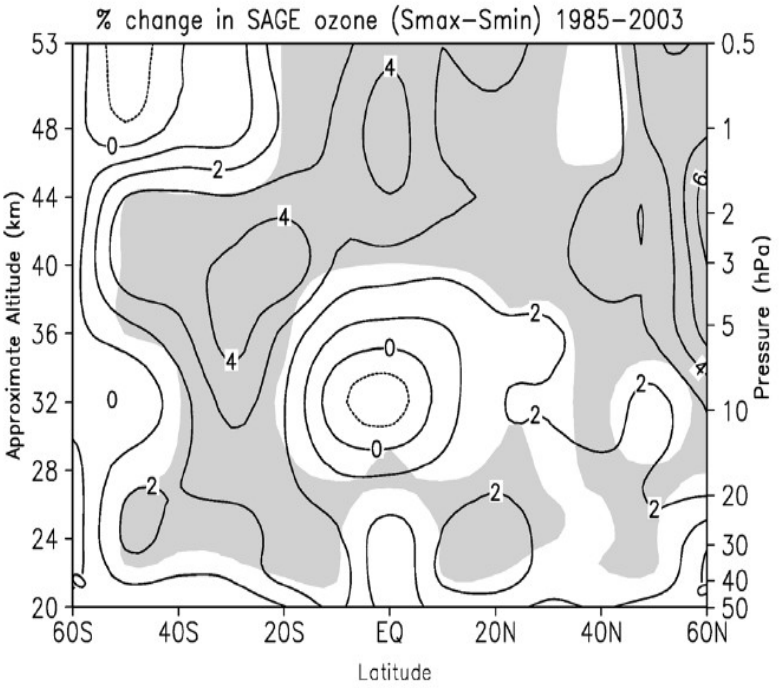

Figure 1.13: (a): A multiple regression analysis of SAGE satellite data of annual average of the ozone differences (%) during 11-year solar cycle (solar maximum minus solar minimum) as a function of latitude and height for the period of 1985-2003 . In this analysis several years following Mt. Pinatubo volcanic eruption are discarded. Shaded areas are statistically significant at the 95 % confidence level. (schematic view is taken from Soukharev and Hood (2006)).

destruction of stratospheric ozone.
?) show the annual mean of the 11-year solar cycle induced ozone variation as a function of height and latitude obtained from a multiple regression analysis of SAGE satellite data for 1958-2003 period. They found a statistically significant change of ozone (up to 4 %) near the tropical stratospause where the direct UV radiation can affect the ozone production rate. It is also suggested that the changes in the lower stratosphere are not a response of the changes in the UV variation and are induced by changes in the dynamical condition that may cause changes in the ozone transport from a region to another (Fig. 1.13).

Though it suggests that the apparantly small variations in the TSI cannot derive large changes in the Earth's climate, however observational evidences show a correlation between solar variability and climate parameters (Labitzke (1987), Labitzke and van Loon (1995)). Two mechanisms are suggested to link the small variation in the TSI to the observed changes in the climate parameters. The first mechanism involves the direct absorption of the TSI by the Earth's atmosphere and oceans.

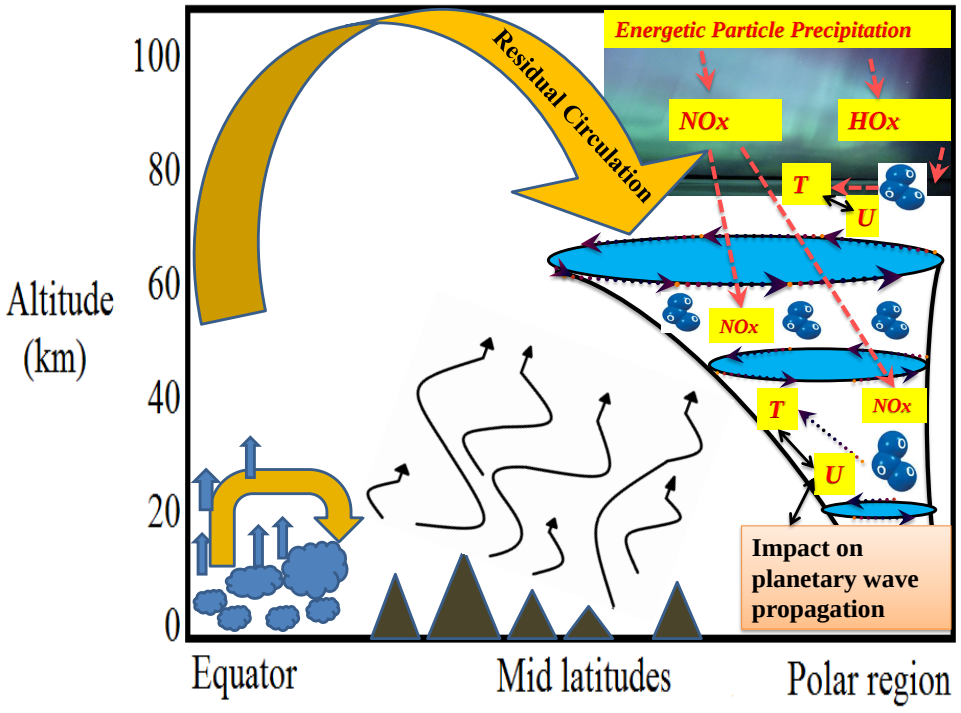

Figure 1.14: (a): In the wintertime polar region, nitric oxide enriched air by energetic particle precipitation can be transported from the mesosphere and lower thermosphere down to the stratosphere due to downward branch of residual circulation, where it can destroy ozone. The depleted ozone has the potential to modify temperature, wind shear and planetary wave propagation and breaking (schematic view is taken from Karami et al. (2015)).

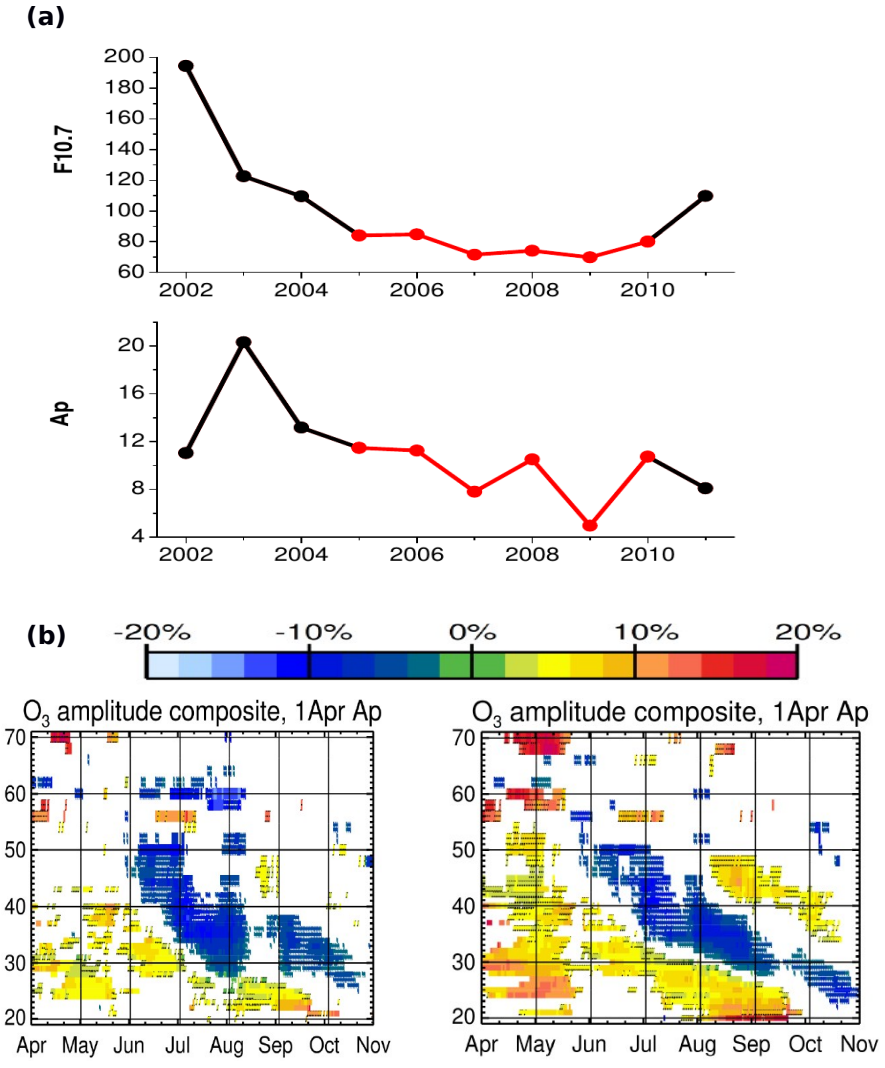

Figure 1.15: (a): Time series from 2002 to 2011 of the 26-day averages centred around 1 April fo the F10.7 cm solar radio flux and Ap index (a measure of geomagnetic forcing and precipitation of energetic particles into the atmosphere. The period of low solar activity from 2005 to 2010 is marked in red. (b-left): Ozone amplitude inside Antarctic polar vortex between years of high geomagnetic activity and low geomagnetic activity centred around 1 April derived from MIPAS, SMR, SABER observations from 2002-2011. (b-right): same as (b-left) but only for Ap index from 2005-2010 (schematic view is taken from Fytterer et al. (2015)).

Tropospheric water vapor and stratospheric ozone are by far the most important radiatively active components of the Earth's atmosphere and they absorb the solar radiation in different wavelengths. Ozone mainly absorbs the Ultra Violet (UV) radiation in the region 240-320 nm and water vapor absorption occurs mainly in the infrared region. Due to the large oceanic heat capacity, it is suggested that the direct absorption of the TSI by oceans is also significant (Gray et al. (2010)).
The second mechanism includes the precipitation of charged particles including protons, electrons and heavier ions. At polar regions, the Energetic Particle Precipitation (EPP) can influence the middle atmosphere (mesosphere and stratosphere) through ionization, dissociation and excitation of atmospheric constituents. At polar regions, EPP has the potential to penetrate deep into the mesosphere and on rare occasions into the stratosphere via the prevailing downward air motions (see Fig. 1.14). As a result the chemical composition of the middle and upper atmsopehre alter significantly (Sinnhuber et al. (2012), Jackman et al. (2007)). Most important are changes to the budget of atmospheric nitric oxides and to atmospheric reactive hydrogen oxides which both contribute to ozone loss in the stratosphere and mesosphere. While hydrogen oxides are short-lived species, however odd nitrogen (produced by energetic particles and in the absence of solar radiation) has a lifetime of days to weeks in the mesosphere and months or longer in the stratosphere. So, if dynamical conditions permit, the odd nitrogen produced by energetic particles can be transported downward and catalytically destroy ozone in the mesosphere and stratosphere (Funke et al. (2014), Randall et al. (2009)) (see Fig. 1.15). The study of (**?**)) show that during years with high geomagnetic activities ozone depletion can be up to 10-15 % insdie the Antarctic stratospheric vortex compared to years with low geomagnetic activities. This negative signal (depleted ozone) first appears in early winter in mesospheric heights and moves downward with time and in early spring (October) reachs to lower stratospheric heights.

1.6 Observational and modelling basis for the influence of the energetic particle precipitation and solar activity on atmospheric composition and dynamics

In addition to the dynamical coupling between atmospheric layers, a photochemical coupling also exists between the upper atmosphere (thermosphere) and middle atmosphere (mesosphere-stratosphere) (Solomon et al. (1982)). The shortwave radiation emitted from the sun and auroral ionization in the thermosphere are able to produce large amounts of NO_y that might be transported downward during polar

winter. The study of (Solomon et al. (1982)) by using a global two-dimensional model confirms the downward transport of the NO_y from the lower thermosphere-upper mesosphere to the stratosphere during polar winter. By using the Limb Infrared Monitor of the Stratosphere (LIMS) (Russell et al. (1984)) investigated the nighttime high-latitude NO_2 in the Northern hemisphere winter 1979. They reported that the zonally-symmetric mesospheric NO_2 is coupled to the transport from above and they zonally-asymmetric component is related to the upward propagation of planetary waves from below during the polar night. Table 1.2 shows a summary of the observational evidences of the NO_y enhancements related to the auroral or geomagnetic activities.

HO_x and NO_x can destroy ozone above $\sim$ 45 km and below $\sim$ 45 km respectively (Lary (1997)). The observational studies confirm the ozone loss due to Energetic Particle Precipitation (EPP) and geomagnetic activity (Andersson et al. (2014), Fytterer et al. (2015b)). It is also important to mention that due to the significant interannual variations of the ozone in the middle atmosphere, it is very difficult to attribute all the changes of the ozone concentration to merely changes in the EPP and geomagnetic activity (Seppala et al. (2007b), Randall et al. (2005)).

Recently Fytterer et al. (2015a) reported a ozone loss inside of the Antarctic polar vortex during polar night due to the high geomagnetic activity from three sets of satellite observations (MIPAS, SMR, SABER). The period of this study was 2002-2010 which is a period with a relatively low-moderate solar and geomagnetic activity (especially between 2004-2010 (Fig. 1.16)). The negative anomaly of the ozone concentrations move downward with time from the upper stratosphere in June to nearly lower stratosphere in October. Within the downwelling tongue the amplitude of the ozone loss between years with high minus years with low geomagnetic activity was about 8-10 %. Unfortunately the differences of the ozone loss between years with high geomagnetic activity and years with low-moderate geomagnetic activity is not available at the moment. However it is reasonable to assume that the amplitude of the negative ozone loss during years with high geomagnetic activity should be higher than those reported in the study of (Fytterer et al. (2015a)).

From the climate modeling perspective, numerous studies deal with the understanding of the impact of EPP-NOy on ozone in the stratosphere and lower mesosphere (Rozanov et al. (2005), Baumgaertner et al. (2009), Reddmann et al. (2010), Semeniuk et al. (2011)). Different approaches are used to implement the EPP in climate models. For instance in the study of (Reddmann et al. (2010)) and (Baumgaertner et al. (2009)) the EPP-NO_y is prescribed in the upper boundary based on MIPAS and HALOE observations respectively. The daily NO_x or NO_y production rate scaled by observed electron fluxes are used in the study of (Rozanov et al. (2005), Semeniuk et al. (2011)). Although different approaches are used for investigating

Table 1.2: The observational evidences of the NOy enhancements related to the auroral or geomagnetic activity.

Study	Observations and measurements
1. Russel et al. (1984)	**1. LIMS**
2. Siskind et al. (1996)	**2. HALOE**
3. Siskind et al. (2000)	**3. HALOE**
4. Natarajan et al. (2004)	**4. HALOE**
5. Randall et al. (2005)	**5. HALOE**
6. Randall et al. (2007)	**6. HALOE**
7. Randall et al. (1998)	**7. POAMII+III**
8. Randall et al. (2005)	**8. POAMII+III**
9. Randall et al. (2007)	**9. POAMII+III**
10. Randall et al. (2006)	**10. ACE-FTS**
11. Randall et al. (2007)	**11. ACE-FTS**
12. Randall et al. (2009)	**12. ACE-FTS**
13. Salmi et al. (2011)	**13. ACE-FTS**
14. Bailey et al. (2014)	**14. SOFIE**
15. Perot (2014)	**15. SMR**
16. LopezPuertas et al. (2006)	**16. MIPAS**
17. Funke et al. (2014)	**17. MIPAS**
18. Sinnhuber et al. (2014)	**18. MIPAS**
19. Seppala et al. (2007a)	**19. GOMOS**
20. Seppala et al. (2007b)	**20. GOMOS**
21. Hauchecorne et al. (2007)	**21. GOMOS**

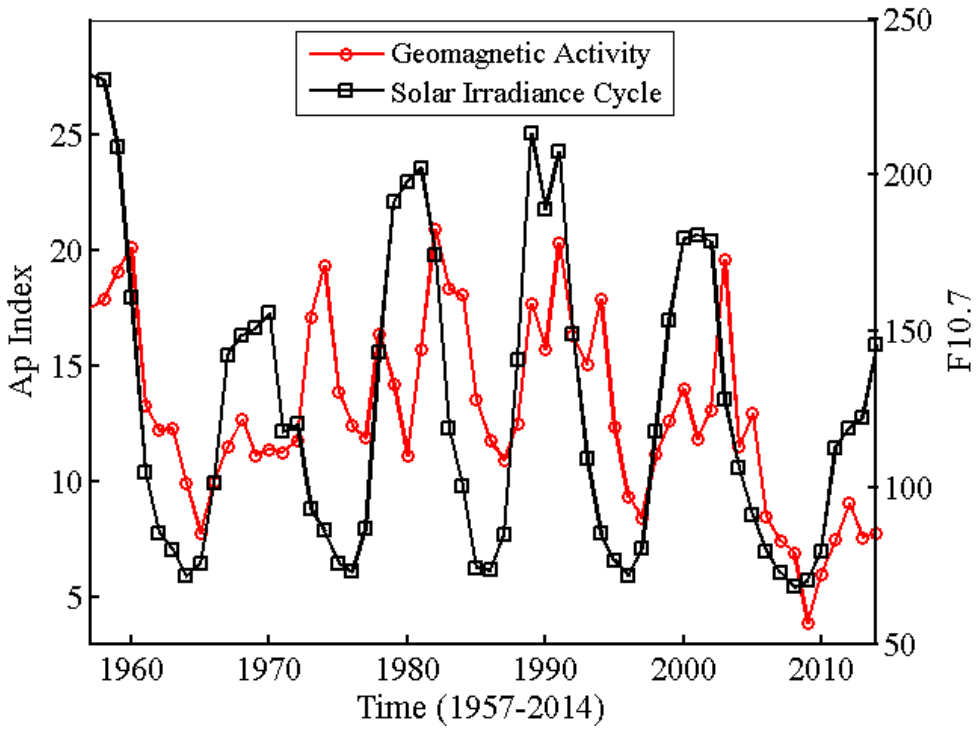

Figure 1.16: $F_{10.7}$ solar radio flux that shows the solar irradiance cycles (black line) and geomagnetic activity (A_p index) (red line) for 1957-2014 period. The solar radio flux units are $[10^{-22} W.m^{-2}.Hz^{-1}]$ and the A_p index is dimensionless. The data is from the National Geophysical Data Center (NGDC, http://spidr.ngdc.noaa.gov/spidr).

the EPP-induced ozone variations in the middle atmosphere in these studies, all modeling studies confirm a downward movement of negative ozone anomaly from the upper stratosphere in early winter to the lower stratosphere in late winter which are consistent with the observational evidences of (Fytterer et al. (2015a)). It is also important to mention that the model responses to changes in the geomagnetic activity are different from each other mainly due to the different assumptions made for the implementation of the EPP forcing in the models and the differences in the derivation of the percentage changes.

The study of (Gray et al. (2010), Lean et al. (1997), Woods et al. (2002)) show that the variations in the UV radiation has a relatively large 11 year solar cycle compared to the negligible variation of the total incoming solar irradiance during 11 year solar cycle. The variation in the UV radiation during 11 year solar cycle can be as large as 50 % at 120 nm to smaller values (6 % near 200 nm to 4 % mear 240-320 nm). Larger variations in the UV (over 50 %) are less important for the middle atmosphere because they are mainly absorbed in the upper atmosphere (above 100

km). However UV variations near 200 nm and 240-320 nm are important due to oxygen dissociation-ozone production and absorption by stratospheric ozone respectively. Observational evidences provided by the satellite instruments show that the maximum of ozone changes in response to the 11 year solar cycle occurs near the tropical stratopause (Soukharev and Hood (2006), Austin et al. (2007), Remsberg (2008), Merkel et al. (2011), Hood and Soukharev (2012), Bronnimann et al. (2013), Dhomse et al. (2013), Gruzdev (2014), Hood et al. (2015)). The amplitude of the ozone variation from solar minimum condition to solar maximum condition in these studies are between 1 % and up to 6 %. The region of the maximum ozone changes (tropical stratopause) in response to variations in the solar UV is where the maximum ozone formation rates is expected.
Numerous modeling studies have been devoted to the understanding of the ozone depletion in the middle atmosphere and its impact on atmospheric temperature and circulation (Haigh (1994), Austin et al. (2007), Haigh et al. (2010), Yamashita et al. (2010), Swartz et al. (2012), Hood et al. (2015),Christiansen et al. (1997), Kiehl and Boville (1988), Braesicke and Pyle (2003), Langematz et al. (2003), Sinnhuber et al. (2012b)). Since ozone is an important radiatively active gas in the atmosphere, changes in the ozone concentration leads to changes in the atmospheric heating and cooling rates as well as subsequent changes in the atmospheric temperature. Due to the hydrostatic and geostrophic balances of the atmosphere a local change in the ozone concentration can affect much wider region of the atmosphere which is reported in the above-mentioned modeling studies.

1.7 Motivations, Goals and Methods of the Thesis

Direct observation evidences show that after weakening or strengthening of the stratospheric polar vortex (due to increases in the concentration of greenhouse gases, stratospheric ozone depletion and recovery, different phases of ENSO and Quasi-Biennial Oscillation (QBO), volcanic eruption and 11-year solar variability), tropospheric circulation can be affected significantly (Baldwin and Dunkerton (2001), Kidston et al. (2015) and references in it). Among the above-mentioned mechanisms that induce changes in the stratospheric temperature and flow, the EPP-induced ozone changes are missing in all low-top models (Andersson et al. (2014)). Low-top climate models refer to the climate models that the higher lid of the model is usually around 10 hPa. To our best knowledge no one sofar has investigated the influence of the EPP-induced ozone changes on thermal and dynamical conditions of the middle atmosphere in a low-top climate model. One of the goals of the current thesis is to implement the overal effect of the EPP-induced ozone changes in the low-top models

and investigate its role in climate variability.

In this thesis I use both reanalysis datasets (such as NCEP, ERA-40 and ERA-Interim) and a chemistry-climate model (ECHAM5-MESSy known as EMAC model) to investigate two broad research topics. The first research topic involves the thermal and dynamical impact of the solar and EPP-induced ozone changes in the middle atmosphere (10-90 km approximately). The second research topic is how tropospheric storm track and Rossby Wave Packets (RWPs) as well as baroclinicity (generation of new eddies) changes with regards to changes in the stratospheric flow above it.

In chapter 2, the description of the EMAC model and the performed model runs are given. Based upon the explanations given in the previous section, I have applied different scenarios and model setup to investigate the main research questions of the current thesis which will be explained in detail. This chapter deals with the theoretical aspects of the stratosphere-troposphere coupling.

In chapter 3, a vector quantity known as the Eliassen-Palm flux (EP flux) that is a useful tool for the description of small amplitude waves propagating in mean zonal shear flows will be discussed. I have developed an algorithm that can objectively measure the influences of the zonal flow on Rossby wave propagation. This diagnostic tool is called probability of the stationary planetary wave propagation and will be reviewed in detail in this chapter.

In chapter 4 the usefulness of the Hilbert transform technique in tracking Rossby wave packets in the upper part of the troposphere will be demonstrated and based upon this method the storm tracks (both in model and reanalysis) will be constructed. Afterwards I will show how changes in the stratospheric winds can affect the tropospheric wave packets and hence storm tracks. I also will distinguish the contribution of the large and small scale waves in shaping the response of the storm track to changes in the stratospheric flow.

Thermal (shortwaves and longwaves heating rates) and dynamical (temperature, wind, wave driving) responses of the middle atmosphere to solar and geomagnetic variability will be investigated in chapter 5. Changes in the frequency of Sudden Stratospheric Warmings (SSWs) and stratospheric final warming dates due to the ozone depletion scenarios will be discussed in this chapter. A comparison between climate effects of the solar-induced ozone changes and EPP-induced ozone changes will be presented in this chapter.

In chapter 6 I will define different zonal flow regimes in the stratosphere based upon the strength of the westerly winds in the lower part of the polar stratosphere. Changes in the propagation condition of stationary large-scale waves with regards to changes in the stratospheric flow will be discussed in this chapter. Tropospheric baroclinicity as influenced by the stratospheric wind regimes will be discussed in this

chapter. I will show how determining factors for the baroclinicity in the atmosphere (wind shear and stability of the atmosphere) might change in response to changes in the stratospheric flow. I also analyse the changes in the tropopause height according to different states of the stratospheric winds above it.

Finally, the conclusions of my work are presented in chapter 7.

2 Fundamental Equations, Model Description and the Performed Model Runs

2.1 Conservation of Potential Vorticity following the Quasi-Geostrophic Motion

Matsuno (1970) for the first time introduced the refractive index for studying the variations in the stationary planetary waves as a diagnostic tool for studying the influence of the background zonal flow on stationary planetary wave propagation. Karoly and Hoskins (1982) used the quasi-geostrophic refractive index of Rossby waves for studying the influence of the background zonal flow on the transient planetary wave propagation. Here I present the procedure for deriving the refractive index formulation. The primitive equations contains five coupled equations that determine the global atmospheric flow. By using $z \equiv -H \ln(\frac{p}{p_s})$ as vertical coordinate and a horizontal spherical coordinate (λ, ϕ) where λ and ϕ denote the longitude and latitude respectively, the primitive equation can be written as:

$$\frac{Du}{Dt} - (f + \frac{u \tan\phi}{a})v + \frac{\Phi_\lambda}{a\cos\phi} = F(\lambda) \tag{2.1}$$

$$\frac{Dv}{Dt} + (f + \frac{u \tan\phi}{a})u + \frac{\Phi_\phi}{a} = F(\phi) \tag{2.2}$$

$$\Phi_z = H^{-1} R\theta \exp(-\frac{\kappa z}{H}) \tag{2.3}$$

$$\frac{1}{a\cos\phi}\frac{\partial u}{\partial\lambda} + \frac{1}{a\cos\phi}\frac{\partial(v\cos\phi)}{\partial\phi} + \frac{1}{\rho_0}\frac{\partial(\rho_0\omega)}{\partial z} = 0 \tag{2.4}$$

$$\frac{D\theta}{Dt} = Q \tag{2.5}$$

where the quantities are the same as symbol list given in the thesis. Φ_λ and Φ_ϕ are longitudinal and latitudinal derivatives respectively. This form of the primitive equations can be found in (Andrews et al. (1987)). Equation 2.1 and 2.2 represent the momentum balance in the zonal and meridional directions respectively. Equation

2.3 expresses the hydrostatic balance. Atmospheric mass conservation (continuity) and thermodynamic equations are represented in equation 2.4 and 2.5 respectively. The operator $\frac{D}{Dt}$ is the Lagrangian derivative that links the Lagrangian and Eulerian frameworks which is defined by:

$$\frac{D}{Dt} \equiv \frac{\partial}{\partial t} + \frac{u}{a\cos\phi}\frac{\partial}{\partial \lambda} + \frac{v}{a}\frac{\partial}{\partial \phi} + \omega\frac{\partial}{\partial z} \tag{2.6}$$

The Lagrangian (material) derivative describes the rate of change of a quantity subjected to the time and space variations.
For large-scale extratropical motions the Coriolis force and the pressure gradient force are in approximate balance which is known as geostrophic balance. The geostrophic balance is simply a balance between the pressure field and horizontal velocity for large-scale extratropical systems (Holton (2004)). Based on geostrophic approximation it is possible to define a purely horizontal velocity field called the geostrophic wind which is given as follows:

$$v_g = \frac{1}{f}\frac{\partial \Phi}{\partial x} \qquad and \qquad u_g = -\frac{1}{f}\frac{\partial \Phi}{\partial y} \tag{2.7}$$

where Φ is the geopotential height and u_g and v_g are the zonal and meridional geostrophic velocities respectively. The ageostrophic velocity is the geostrophic departure from the original three-dimensional velocity which is given by $u_a = u - u_g$, $v_a = v - v_g$ and $\omega_a = \omega$. By using the Cartesian coordinates (x,y,z) on a β plane (*e.g.* $f = f_0 + \beta y$ where $\beta = \frac{\partial f}{\partial y}$) one can derive the primitive equation on β plane under the quasi-geostrophic approximation in the absence of friction as follows:

$$D_g u_g - f_0 v_a - \beta y v_g = 0 \tag{2.8}$$

$$D_g v_g + f_0 u_a + \beta y u_g = 0 \tag{2.9}$$

$$\frac{\partial u_a}{\partial x} + \frac{\partial v_a}{\partial y} + \frac{1}{\rho_0}(\rho_0 \omega_a)_z = 0 \tag{2.10}$$

$$\Phi_z = \frac{R\theta}{H}\exp(-\frac{\kappa z}{H}) \tag{2.11}$$

$$D_g \theta_d + \omega_a \frac{d\theta_0}{dz} = 0 \tag{2.12}$$

Equations 2.8 to 2.12 are the same as equations 2.1 to 2.5 for the quasi-geostrophic, β plane in the absense of friction using the cartesian coordinates (x,y,z). D_g is the advective derivative following geostrophic motion which is defined as $D_g = \frac{\partial}{\partial t} + u_g\frac{\partial}{\partial x} + v_g\frac{\partial}{\partial y}$. θ_d and ρ_d is a potential temperature and density departure from the three-dimensional potential temperature and density fields respectively that are defined as follows:

$$\theta_d(x,y,z) = \theta(x,y,z) - \theta_0(z) \qquad and \qquad \rho_d(x,y,z) = \rho(x,y,z) - \rho_0(z) \tag{2.13}$$

where $\theta_0(z)$ and $\rho_0(z)$ are the one-dimensional basic state potential temperature and density respectively.
In order to arrive to the vorticity equation from the primitive equations the following procedures are required (see e.g. Andrews et al. (1987)). Taking $\frac{\partial 2.9}{\partial x} - \frac{\partial 2.8}{\partial y}$ and using the mass conservation equation (2.10) one can arrive to the quasi-geostrophic vorticity equation as follows:

$$D_g\zeta_g + \beta v_g - \frac{f_0}{\rho_0}\frac{\partial(\rho_0\omega_a)}{\partial z} = 0 \tag{2.14}$$

where $\zeta_g = \frac{\partial v_g}{\partial x} - \frac{\partial u_g}{\partial y}$ is the quasi-geostrophic vorticity equation. Similar to the equation (2.13) one can define a basic state for the geopotential height as $\Phi_0(z) = \Phi(x, y, z) - \Phi_d(x, y, z)$ and based on that the geostrophic stream function is defined as follows:

$$\psi(x, y, z) = \frac{(\Phi(x, y, z) - \Phi_0(z))}{f_0} \tag{2.15}$$

By using the definition given for the geostrophic stream function one can define the geostrophic velocities as follows:

$$u_g = -\frac{\partial\psi}{\partial y} \qquad and \qquad v_g = \frac{\partial\psi}{\partial x} \tag{2.16}$$

Now I define the departure of potential temperature from the basic state by using the hydrostatic balance (equation 2.11) and stream function as follows:

$$\theta_d = \frac{H}{R}\exp(\frac{\kappa z}{H})f_0\psi_0 \tag{2.17}$$

In terms of stream function the vertical velocity can be written as:

$$\omega_a = -D_g(\frac{f_0\psi_z}{N^2}) \tag{2.18}$$

To arrive to this equation I have used the thermodynamic equation (equation 2.12). Here N^2 is the buoyancy frequency defined as follows:

$$N^2 = \frac{g}{\theta}\frac{d\theta_0}{dz} = H^{-1}R\exp(-\frac{\kappa z}{H})\frac{d\theta_0}{dz} \tag{2.19}$$

Since ω_a is very small, one can neglect it in the quasi-geostrophic vorticity equation (equation 2.14) and by considering $D_g f = \beta v_g$ a new form of the quasi-geostrophic vorticity equation can be derived as follows:

$$D_g q = 0 \qquad and \qquad q = f + \zeta_g + \frac{1}{\rho_0}\frac{\partial}{\partial z}(\frac{f_0^2\rho_0}{N^2}\frac{\partial\psi}{\partial z}) \tag{2.20}$$

where q is the potential vorticity. The three terms in the q equation are, the planetary vorticity, the geostrophic relative vorticity and the stretching vorticity. Equation 2.20 expresses an important conservation law in atmospheric dynamics: Following the geostrophic motion and in the absence of friction and diabatic heating the

potential vorticity is a conserved quantity. This equation simply expresses that as an air parcel displaces horizontally or vertically in the atmosphere all forms of its vorticity (planetary, relative and stretching) may change but the sum of the three (as potential vorticity) is conserved following the geostrophic motion.

2.2 Deriving the Quasi-Geostrophic Rossby Waves Refractive Index

Rossby wave propagation is supported in the baroclinic flows. A baroclinic flow is a flow in which density depends on both pressure and temperature ($\rho = \rho(p, T)$). A barotropic flow is a flow in which density depends only on pressure ($\rho = \rho(p)$). A barotropic flow has a serious limitation for supporting the large-scale motions; the large-scale wave propagation depends only on horizontal position, not on height. The absence of horizontal temperature gradients and vertical wind shear in the barotropic flow hinder the vertical wave propagation. Therefore the three-dimensional large-scale motions in the atmosphere is best described in the baroclinic flows (Holton (2004)). Now I consider a meridional perturbation ($v = v'$) to a purely zonal basic state ($u = u_0(y, z) \quad and \quad u' = 0 \quad and \quad v_0 = 0$):

$$u = u_0(y, z) \qquad and \qquad v = v'(y) \tag{2.21}$$

By substituting equation 2.21 to the equation 2.20 and making use of ($D_g = \frac{\partial}{\partial t} + u_g\frac{\partial}{\partial x} + v_g\frac{\partial}{\partial y}$) and considering the fact that $\frac{\partial f}{\partial t} = 0$, $\frac{\partial f}{\partial x} = 0$, $\frac{\partial f}{\partial y} = \beta$, $\zeta_g = \frac{\partial v}{\partial x} - \frac{\partial u}{\partial y} = -\frac{\partial u}{\partial y}$ because $\frac{\partial v}{\partial x} = 0$ and finally $u_g = -\frac{\partial \psi}{\partial y}$ I arrive to the perturbed PV equation as follows:

$$\frac{\partial q'}{\partial t} + u_0\frac{\partial q'}{\partial x} + v'\frac{\partial \overline{q}}{\partial y} = 0 \tag{2.22}$$

where

$$q' = \zeta'_g + \frac{1}{\rho_0}\frac{\partial}{\partial z}(\frac{f_0^2\rho_0}{N^2}\frac{\partial \psi'}{\partial z}) \tag{2.23}$$

$$\frac{\partial \overline{q}}{\partial y} = \beta - \frac{\partial^2 u_0}{\partial y^2} - \frac{1}{\rho_0}\frac{\partial}{\partial z}(\frac{f_0^2\rho_0}{N^2}\frac{\partial \overline{u_0}}{\partial z}) \tag{2.24}$$

and making use of equation 2.16 the perturbed PV equation (q') in term of stream function perturbation (ψ') can be defined as follows:

$$(\frac{\partial}{\partial t} + u_0\frac{\partial}{\partial x})\{[\frac{\partial^2}{\partial x^2} + \frac{\partial^2}{\partial y^2} + \frac{1}{\rho_0}\frac{1}{\partial z}(\frac{f_0^2\rho_0}{N^2}\frac{\partial}{\partial z})]\psi'\} + \frac{\partial \overline{q}}{\partial y}\frac{\partial \psi'}{\partial x} = 0 \tag{2.25}$$

Equation 2.25 links the changes in the zonal basic state (v') to the perturbation of the stream function (ψ') (Andrews et al. (1987), Simpson (2009)). Now I consider

a solution for the equation 2.25 by assuming that the amplitude of the perturbed stream function grows exponentially with height (e.g. in response to the exponential reduction in density with increasing height). A possible form of the solution for equation 2.25 is:

$$\psi'(x,y,z,t) = \exp(\frac{z}{2H})\Re(\Psi(y,z)\exp(i(k_m x - k_m ct))) \tag{2.26}$$

where k_m is the zonal wavenumber the phase speed in the zonal direction is denoted by c and $\Re(\Psi(y,z)$ is the real part of the stream function. Finally I arrive to the amplitude of the perturbed stream function $(\Psi(y,z))$ as follows:

$$\frac{\partial^2\Psi}{\partial y^2} + \frac{f_0^2}{N^2}\frac{\partial^2\Psi}{\partial z^2} + n^2\Psi = 0 \tag{2.27}$$

where

$$n^2 = \frac{\overline{q}_y}{\overline{u}-c} - \frac{k^2}{a^2\cos^2(\phi)} - \frac{f^2}{4N^2H^2} \tag{2.28}$$

$$\overline{q_\phi} = cos(\phi)[\frac{2\Omega}{a}cos(\phi) - \frac{1}{a^2}\frac{\partial}{\partial\phi}[\frac{\frac{\partial}{\partial\phi}(\overline{u}cos(\phi))}{cos(\phi)}] - \frac{f^2}{\rho_0}[\frac{\partial}{\partial z}\frac{(\rho_0\frac{\partial}{\partial z}\overline{u})}{N^2}]] \tag{2.29}$$

where $\overline{q_\phi}$ is the meridional gradient of the zonal mean potential vorticity which is a fundamental quantity in Planetary wave dynamics and the stability of the zonal mean flow Andrews et al. (1987). Equation 2.28 is a form of refractive index that depends only to the zonal wavenumber. Recently (Sun et al. (2014), Sun and Li (2012)) introduced a version of the refractive index of Rossby waves that depends on the two-dimensional wavenumbers (zonal and meridional wavenumbers) as follows:

$$n^2_{k,l}(y,z) = (\frac{N^2}{f^2\cos^2(\phi)})[\frac{\overline{q_\phi}}{\overline{u}} - (\frac{k}{a})^2 - (\frac{\pi l}{2a})^2 - (\frac{fcos(\phi)}{2NH})^2] \tag{2.30}$$

In chapter 3 of the thesis the climatology of the refractive index will be shown and discussed. Some problematic features of this index will be shown.

2.3 Link between Tropopause Height and Arctic Stratospheric Potential Vorticity

Ambaum and Hoskins (2002) established a theoritical basis for the relationship between the strength of the stratospheric vortex and surface pressure based on ECMWF reanalysis dataset. According to this theory, an increase in the North Atlantic Oscillation (NAO) index results in an increased equatorward refraction of the upward propagating Rossby waves. Since the polar region receives less wave forcings, in time period of a few days a stronger stratospheric vortex can be formed. The stronger polar vortex results in an elevated tropopause. The elevated Arctic

tropopause results in a deeper troposphere and the stretched tropospheric column is associated with a lower surface pressure near the North pole. The envisioned connections of the NAO-stratospheric vortex strength and tropopause height is depicted in Fig. 2.1.

Ambaum and Hoskins (2002) quantify the changes in the tropopause height associated with the strength of the stratospheric vortex (or alternatively a PV anomaly in the stratosphere). The PV can be defined as:

$$PV = \frac{f+\xi}{\sigma}, \quad with \qquad \sigma = -\frac{1}{g}\frac{\partial p}{\partial \theta} \tag{2.31}$$

where f is the Coriolis parameter, ξ relative vorticity, g gravitational accelaration, θ potential temperature and p is the pressure. Since the PV is a conserved quantity following fluid parcels, therefore any changes in the PV will be associated with changes in both σ and $(f+\xi)$. According to quasigeostrophic scaling, the Burger number equals to the relative magnitude of the stratification and vorticity ($Bu = (\frac{NH}{fL})^2$) where L and H are horizontal length scale and scale height and N is the buoyancy frequency. The logarithmic derivative of the PV equals to:

$$\frac{(\Delta PV)}{PV} \approx -(1+Bu)\frac{\Delta\sigma}{\sigma} \tag{2.32}$$

We now consider a PV anomaly between two isentropic surfaces (constant-potential temperature surfaces). θ_{top} is the isentropic surface above the PV anomaly and θ_{tpp} is the isentropic surface that touches the Arctic tropopause. In the stratosphere the following equations can be derived from the finite difference approximation:

$$\sigma \approx -\frac{1}{g}\frac{p_{top}-p_{tpp}}{\theta_{top}-\theta_{tpp}}, \qquad \Delta\sigma \approx -\frac{1}{g}\frac{\Delta p_{top}-\Delta p_{tpp}}{\theta_{top}-\theta_{tpp}} \tag{2.33}$$

In these equations it is assumed that θ_{top} and θ_{tpp} do not change in the stratosphere. If we neglect the pressure variation at the top of the domain compared to the pressure variation at the tropopause height one can reach to following equation:

$$\frac{(\Delta PV)}{PV} \approx -(1+Bu)\frac{\Delta p_{tpp}}{p_{tpp}} \tag{2.34}$$

This relationship suggests that the fractional changes in the tropopause height are opposite to the fractional changes in the PV field. For instance, the fractional changes in the PV field in the stratosphere for a positive unit change in NAO index is about 10%. Therefore for a Burger number of about 1, the fractional change in the tropopause height is about 5%. The hydrostatic balance suggest the following changes in the tropopause height associated with the variations in the tropopause level pressure:

$$\Delta h_{tpp} = -\frac{\Delta p_{tpp}}{p_{tpp}}\frac{RT_{tpp}}{g} \tag{2.35}$$

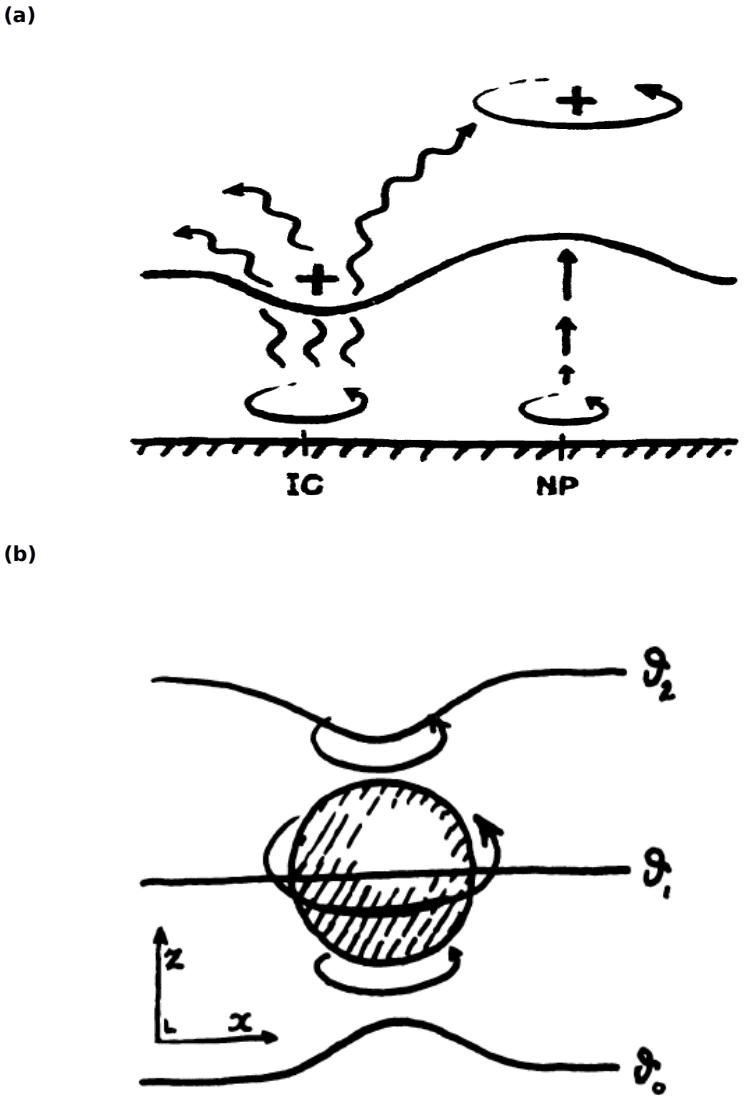

Figure 2.1: (a): Schematic of the relationship between the NAO, tropopause height and strength of the stratospheric vortex. A cyclonic circulation over Iceland (IC) is associated with an increase in the NAO index. The tropopause height (the thick line) lowers and more upward propagating Rossby waves (wavy lines) are refracted toward the equator. As result the stratospheric vortex enhances (associated with the positive Potential Vorticity (PV) anomaly). The tropopause height below the positive PV anomaly is elevated and which results in an enhanced cyclonic circulation near the north pole. (b) Schematic of the bending of the constant-potential temperature surfaces toward a positive PV anomaly. The arrows represent circulation associated with the positive PV anomaly. A schematic view is taken from (Ambaum and Hoskins (2002)).

For a typical tropopause temperature over the Arctic (210 K), the changes in the tropopause is about 300 m (Ambaum and Hoskins (2002)). A further example provided by Ambaum and Hoskins (2002) is the changes in the tropopause heights over the Arctic associated with the changes in the stratospheric PV. For 1 standard deviation of the PV at 500 K isentropic surface (surfaces with constant potential temperature), the changes in the PV field in the stratosphere is about 10 PVU (PV unit). The maximum PV in the climatological PV field is about 60 PVU at the 500 K isentropic surface. Therefore equation. 2.35 and equ. 2.34 suggest that if the fractional changes in the PV field is about $\frac{1}{6}$ in the stratosphere, the fractional changes in the tropopause heights is about $\frac{1}{12}$. The hydrostatic relation suggest a change in the tropopause heights of about 500 m associated with the related variation in the PV field in the stratosphere (Ambaum and Hoskins (2002)). In the current thesis I will examine the existance of this relationship in the EMAC model and I will expand the implication of this relationship for the stratosphere-troposphere coupling. I will show that if the tropopause heights undulate according to the different states of the stratospheric flow, then wind shear, stability and baroclinicity of the troposphere will change. I also will investigate how changes in the stratospheric wind may change the propagation condition of the Rossby Wave Packets (RWPs) in the upper troposphere.

2.4 The EMAC Model

The General Circulation Model (GCM) ECHAM5 is developed at the Max Planck Institute for Meteorology (MPI-MET) in Hamburg, Germany. The dynamical core of ECHAM5 is a spectral implementation of the primitive equations for the dry atmosphere which is originally based on the Numerical Weather Prediction (NWP) model of the European Centre for Medium-range Weather Forecasts (ECMWF) in the United Kingdom (Roeckner et al. (2003), Roeckner et al. (2004)). The model describes the dynamics, theromodynamics, chemistry and transport of the Earth's atmosphere. At the Max Planck Institute for Chemistry (MPI-C) in Mainz, the ECHAM5 model has been combined with the Modular Earth Submodel System (MESSy) (Joeckel et al. (2006)). In the EMAC model the research questions that deals with chemistry or extension of the ECHAM5 model can be addressed with MESSy. This can be done by coupling of the processes relevant for the dynamics.

Simulations with the EMAC model can be performed in different spatial and temporal resolutions. Since in the ECHAM5 dynamical core of EMAC, calculations are performed in spectral space, the resolution is defined by the triangular truncation

of the waves. Theoritically any truncation is possible, but in EMAC the horizantal resolution varies between T21-T256 (T for the triangular truncation). This corresponds to a grid box size of about $5.6° \times 5.6°$ and $0.36° \times 0.36°$ respectively. The hybrid pressure grid is used as vertical coordinate which employs terrain-following levels to the surface. For the upper troposphere and stratosphere constant pressure levels are used. The vertical resolutions in EMAC covers 19, 31 and 60 levels for the standard tropospheric simulations (up to 10 hPa). There is an additional option for the middle atmospheric simulations (MA-ECHAM5) whose vertical resolution can be 39 or 90 levels (from surface up to 0.01 hPa).

The time step length in the ECHAM5 model depends on the vertical and horizontal resolutions and must fullfill the Courant-Friedrich-Lewy (CFL) criterion. In solving partial differential equations the CFL criterion is a necessary condition for convergence of the numerical solutions. An important aspect of this criterion restricts the time step of the computational simulation to be smaller than a certain value, otherwise the results of the simulation will be incorrect (Roeckner et al. (2003), Roeckner et al. (2004)). The standard horizontal and vertical resolutions and a related time step of the ECHAM5 model for tropospheric simulations are given in Table 2.4).

The Modular Earth Submodel System (MESSy) includes different submodels

Table 2.1: The standard ECHAM5 model resolutions and time steps for the tropospheric (up to 10 hPa) simulations.

Resolution	Number of Boxes (Longitude-Latitude)	Approximated Box Width (degrees)	Approximated Box Width (km)	Time Step (s)
T21 L19	**64 x 32**	**5.6 x 5.6**	**621**	**2400**
T31 L31	**96 x 48**	**4.2 x 4.2**	**467**	**1800**
T42 L31	**128 x 64**	**2.8 x 2.8**	**311**	**1200**
T63 L31	**192 x 96**	**2.1 x 2.1**	**233**	**720**
T85 L31	**256 x 128**	**1.4 x 1.4**	**156**	**480**
T106 L31	**320 x 160**	**1.1 x 1.1**	**122**	**360**
T159 L31	**480 x 240**	**0.7 x 0.7**	**81**	**180**

(about 50 submodels in the current version of the MESSy2) with various purposes and capabilities. The basic idea of the MESSy concept is to provide new possibilities to study the complex feedback mechanisms in the Earth System Models (ESM) in a

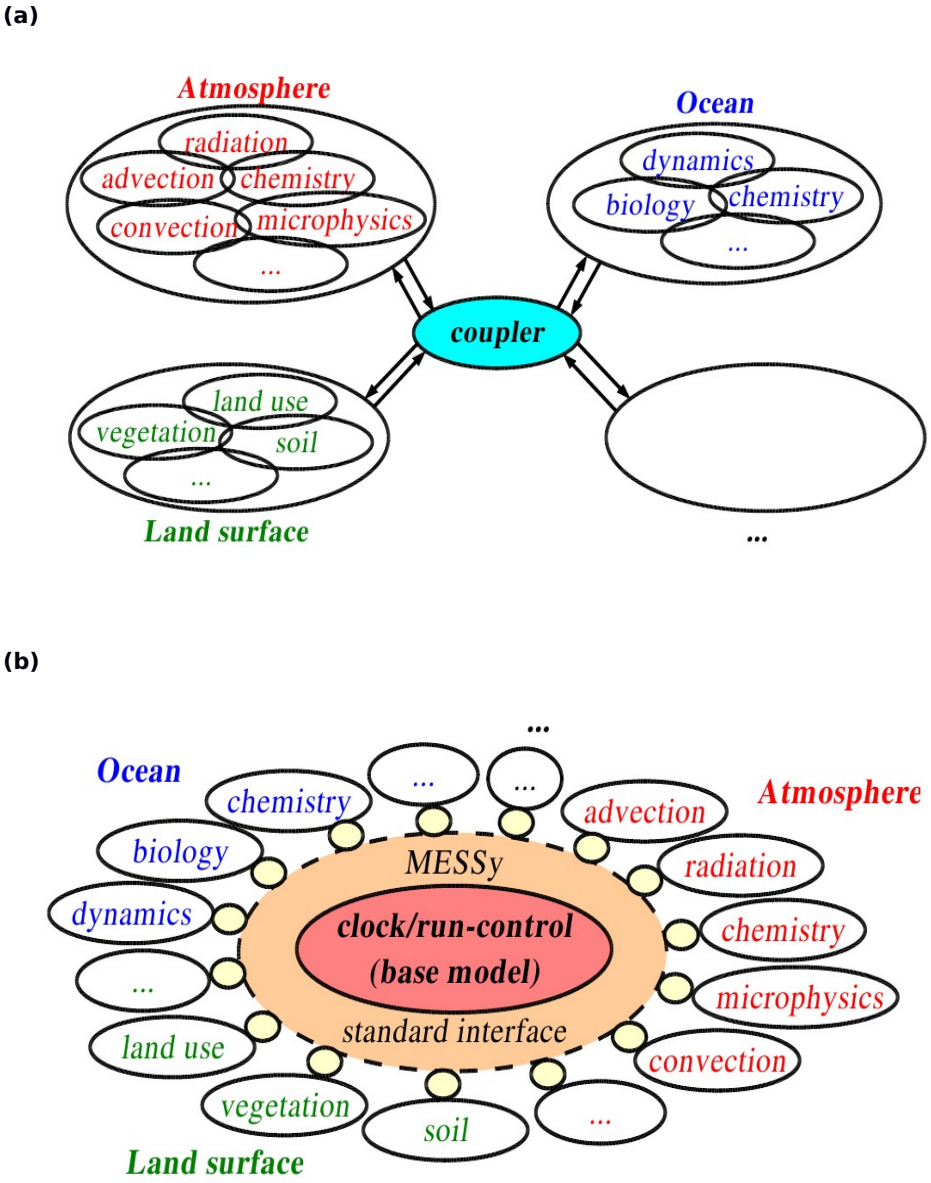

Figure 2.2: Two possible approaches for building an ESM. (a): Domain-oriented approach for building an ESM from existing domain specific models (atmosphere, ocean, land surface, ...). Data exchange can be controlled from each domain model and organized via a universal coupler. The domain models and the coupler are self-contained executables running simultaneously; communication is performed via the coupler. (b) MESSy approach (process-oriented approach) to establish an ESM. Each physical process is coded as a modular entity connected via a standard interface to a common base model. The base model can be for instance an atmosphere or ocean GCM. (A schematic figure is taken from Joeckel et al. (2005)).

transparent and user friendly approach. To study the complex interactions between chemical, physical, and biological processes, one need to couple the different domain (land, ocean, atmosphere, ...). MESSy provides a remarkable solution for this demand which provides: (a) a modular interface structure to connect submodels to a base model, (b) an extendable set of such submodels for miscellaneous processes, and (c) a coding standard. Therefore MESSy provides an exciting possibility to study the feedback mechanisms within the climate system (Joeckel et al. (2005), Joeckel et al. (2010)). Figure. 2.2 shows two possible approaches for bulding an ESM. More details of the MESSy approach to build an ESM can be found in (Joeckel et al. (2005), Joeckel et al. (2010)).

In the current thesis, 4 submodels are used to perform the simulations. These are the submodels CLOUD, CONVECT, GWAVE and FUBRAD. The CLOUD submodel contains the original cloud and cover routines from ECHAM5 in a modularised, MESSy - conform structure and calculates the cloud cover as well as cloud microphysics including precipitation. The CONVECT submodel calculates the process of convection. It consists of an interface to choose different convection schemes and the calculations themselves. The GWAVE submodule contains the original Hines non-orographic gravity wave routines from ECHAM5 in a modularised, MESSy - conform structure and calculates the momentum fluxes and wind drag. FUBRAD is a high-resolution short-wave heating rate parameterisation for solar variability studies. If switched on it replaces the RAD radiation at wavelengths most sensitive to solar variability (UV and visible) between the model top and 70 hPa. Elsewhere RAD is retained. More information about the MESSy submodels can be found in the MESSy website (http://www.messy-interface.org).

2.5 The Model set up I: Stratospheric influence on the Tropospheric Climate

2.5.1 Stratosphere-Troposphere coupling scenarios

In the current thesis, in order to study the influence of the strong and weak westerlies in the stratosphere on the tropospheric baroclinicity and RWPs propagation characteristics, I run five different simulations with the EMAC model (see Table 2.2). We use the ECHAM/MESSy Atmospheric Chemistry (EMAC) general circulation model (version 2.50) to perform the simulations. In the FRE-RUN simulation the applied model set up comprised the submodels RAD4ALL, CONVECT, GWAVE

Table 2.2: Summary of the three EMAC simulations. In the fully nudged simulations (FUL-NUDINTCHEM and FUL-NUD-NOCHEM) both stratosphere (STRA) and troposphere (TROP) are nudged toward the ECMWF data. In the only stratosphere nudged experiments (STR-NUD-INTCHEM and STR-NUD-NOCHEM) the atmospheric quantities are nudged toward the reanalysis data only above~116 hPa (level 65 in the L90 vertical resolution of the EMAC model). rmscon is a tuning parameter for the gravity wave parametrization and might be used to control .the vertically propagating gravity waves in the EMAC model

Interactive chemistry	**Gravity wave parametrization**	**Running mode**	**Analyzed time period**	**Resolution**	**Model Simulation**
Yes	rmscon=0.92	TROP and STRA are nudged	1979-2014	T42L90	FUL-NUD-INTCHEM
No	rmscon=0.92	TROP and STRA are nudged	1979-2014	T42L90	FUL-NUD-NOCHEM
Yes	rmscon=0.92	Above~116 hPa is nudged	1979-2014	T42L90	STR-NUD-INTCHEM
No	rmscon=0.92	above~116 hPa is nudged	1979-2014	T42L90	STR-NUD-NOCHEM
No	rmscon=1	time slice-free running	years 100	T42L90	FRE-RUN

and CLOUD. Moreover, the interactive chemistry is not used in this study. Instead constant mixing ratios are assumed for CO_2, CH_4, N_2O, $CFC-11$ and $CFC-12$, whereas a climatology (FUB-ozone) is used for O_3. I carried out a time slice model simulation over a period of 100 years (1988 year condition) with a free-running version of the model with constant boundary conditions (average incoming solar flux, sea ice distribution and sea surface temperature) during the whole year. However, these boundary conditions have a seasonal cycle. FUL-NUD-INTCHEM, FUL-NUD-NOCHEM, STR-NUD-INTCHEM and STR-NUD-NOCHEM simulations are nudged with ERA. The nudged atmospheric quantities include divergence, vorticity, temperature and surface pressure. The surface pressure is not nudged in the STR-NUD-INTCHEM and STR-NUD-NOCHEM simulations. In the STR-NUD-INTCHEM and STR-NUD-NOCHEM simulations, the nudged quantities are nudged only above 116 hPa, e.g., well above the tropopause in polar latitudes. For the STR-NUD-NOCHEM and STR-NUD-INTCHEM simulations, the Sea Surface Temperature (SST) and Sea Ice Cover (SIC) are from the climatology of the HadISST from 1995-2004.

The GWAVE submodule contains the original Hines non-orographic gravity wave routines from ECHAM5 in a modularised, MESSy-conform structure and the rmscon parameter calculates the momentum fluxes and wind drag. A correct value of

the rmscon for the free running setup of the model is crucial to obtain a realistic period of the Quasi-Biennial Oscillation (QBO) (Fig. 2.3).
The QBO is a quasiperiodic (with a period of 28-29 months) of the equatorial zonal wind between westerlies and easterlies in the tropical (between 5°S and 5°N) stratosphere. The wind regimes of the QBO usually develop at the middle stratosphere (about 10 hPa) and propagate downwards with time (about 1 km per month). The wind regimes of the QBO dissipate at the tropical tropopause. Holton and Tan (1980) and Holton and Tan (1982) established a relationship between the QBO and the strength of the wintertime polar vortex in the Northern hemisphere. When the QBO is in the westerly phase the vortex becomes stronger and colder and when the QBO is in the easterly phase the polar vortex becomes weaker and warmer. In addition during easterly phase of the QBO more frequent Sudden Stratospheric Warming (SSW) are found which give rise to the warmer temperatures and weaker zonal winds in the polar vortex regions. Therefore it is important to make a correct setup in the EMAC model to obtain a realistic QBO and hence a realistic westerly winds in the polar vortex regions.

2.6 The Model set up II: Solar and Geomagnetic Forcings on the Climate System

2.6.1 Geomagnetic and Solar induced changes in the ozone concentration scenario

In the current thesis, the monthly mean ozone climatology of Fortuin and Langematz (1994) is used (FUB-ozone). FUB-ozone has 34 vertical levels ranging from surface to mesospheric altitudes (1000-0.003 hPa). The annual climatology of the ozone volume mixing ratio (ppmv) is presented in Fig. 2.4.

In EMAC model, the climatology is read in as monthly mean data, but daily data are provided by interpolating from the 15^{th} of each months to the next. A multi-year model run (time slice experiment under 1982 year condition) with this climatology is carried out as a base scenario (called BASE in the following). This model run can also be understood as a reference scenario with moderate solar and without geomagnetic forcing.
Three additional model scenarios are carried out to exemplify scenarios with high geomagnetic forcing in the Southern and Northern hemisphere during wintertime and low solar UV forcing. In these model simulations the FUB-ozone climatology is changed either in the polar regions of both hemispheres (mimicing high geomagnetic forcing) or in the tropical stratopause (resembles the low solar UV condition). In

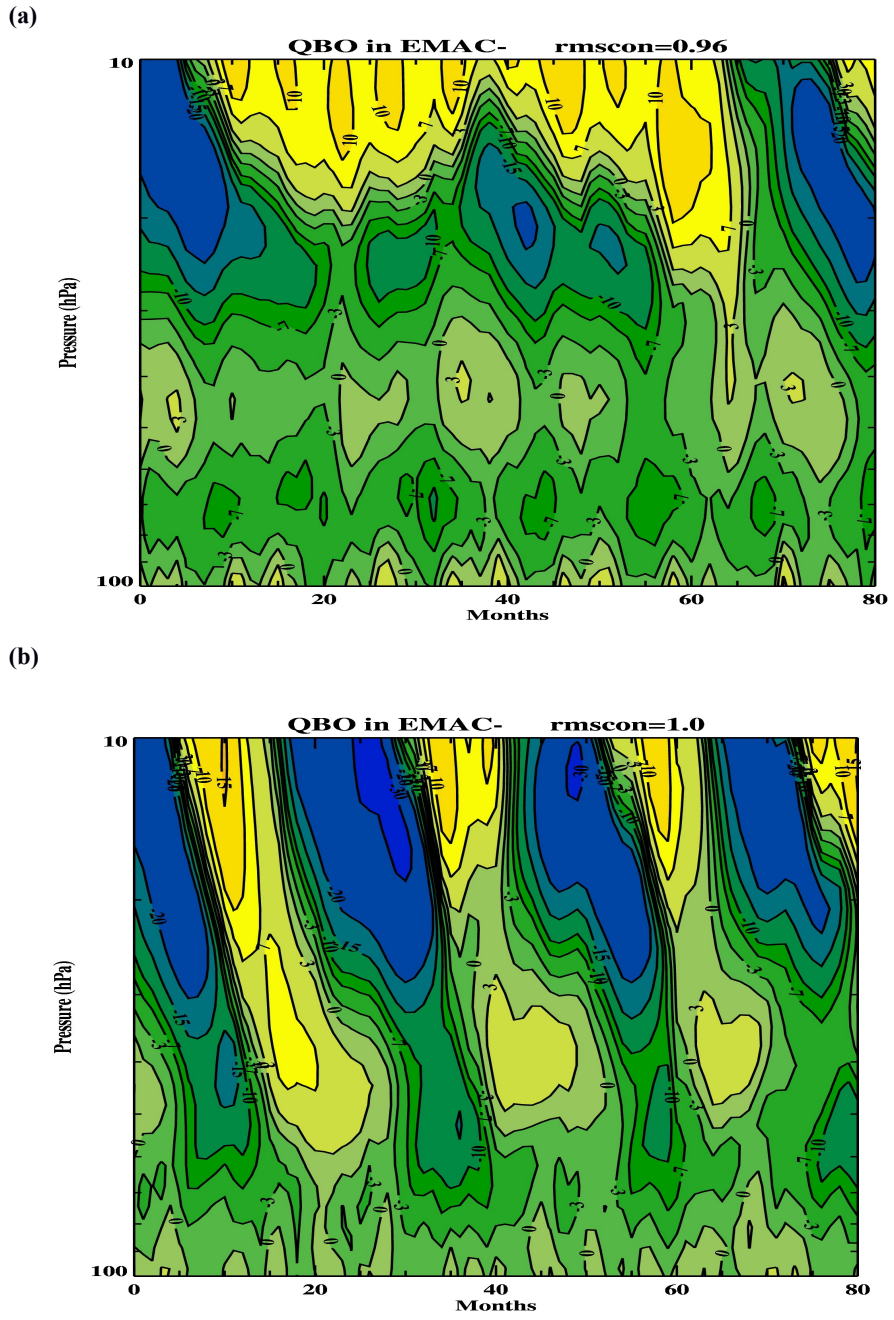

Figure 2.3: Zonal wind averaged between 5°S and 5°N in the EMAC model. (a):rmscon=0.96 give rise to an unrealistic QBO in the tropical stratosphere. (b): with rmscon=1.0 the EMAC model produces a realistic QBO. rmscon is a tuning parameter in the EMAC model to control the vertically propagating gravity waves.

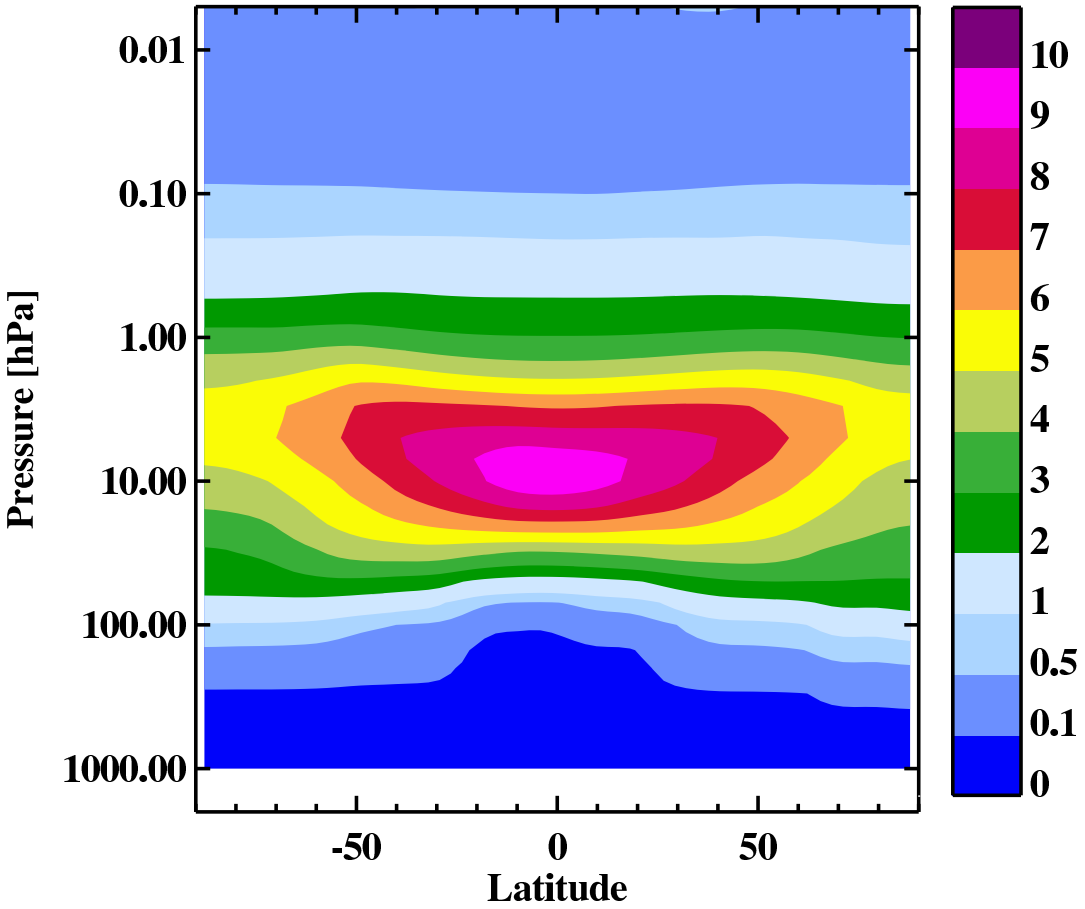

Figure 2.4: FUB-ozone annual climatology of ozone volume mixing ratio (ppmv).

the two "high geomagnetic forcing" scenarios, a negative ozone anomaly is imposed at high latitudes (poleward of 60Âř) propagating down from the mesosphere to the mid-stratosphere throughout polar winter in the respective winter hemisphere. The shape of the negative ozone anomaly is based on the observations of Fytterer et al. (2015a) and the model results of (Baumgaertner et al. (2009), Reddmann et al. (2010), Rozanov et al. (2012)) and is consistent with the area showing clear EPP-NOy signals in most winters as shown by Funke et al. (2014).

Figure 2.5 show the ozone depletion according to $(\Delta O_3 - NH)$ and $(\Delta O_3 - SH)$ scenarios. The amplitude of the ozone depletion anomaly is set to 30% in all affected months. This was chosen to be higher than the values provided by Fytterer et al. (2015a) and Rozanov et al. (2012) which exemplify an average EPP-NOy signal, but in range of the results of Baumgaertner et al. (2009) and Reddmann et al. (2010) who provide results for a known winter with very strong EPP-NOy forcing, Southern hemisphere winter 2003. To be consistent with the results obtained by Fytterer et al. (2015a) and the model results of Rozanov et al. (2005) and Semeniuk et al. (2011) a negative ozone anomaly was imposed already in the early winter mesosphere

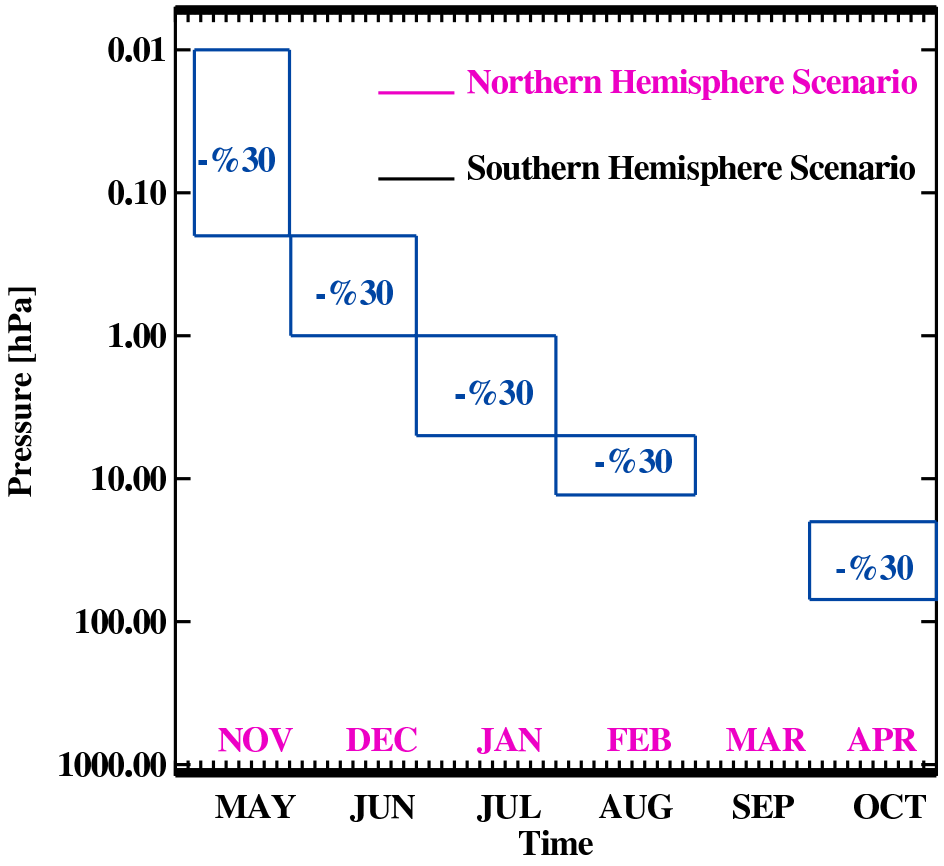

Figure 2.5: Ozone depletion according to $(\Delta O_3 - NH)$ and $(\Delta O_3 - SH)$ scenarios.

(May/June above 1 hPa), which might be formed by an interaction of NOx with the mesospheric HOx ozone-loss cycles as indicated by Verronen and Lehmann (2015). In this sense, our scenario exemplifies a winter with strong, but not extreme, particle forcing. Hereafter ozone change scenarios in the Northen and Southern hemispheres will be called $(\Delta O_3 - NH)$ and $(\Delta O_3 - SH)$, respectively.

Two additional model runs were carried out with a prescribed ozone change of -4% around the tropical stratopause (Fig. 2.6). Hereafter this scenario will be called $(\Delta O_3 - TS)$. This scenario is based on the SBUV and SAGE time-series as presented in Soukharev and Hood (2006). The magnitude of the ozone anomaly in the tropical stratopause is set to -4 % because these cover the longest time-series of vertically resolved observations so far, and are reasonably well in agreement with each other. A 4% change is at the upper edge but in range of these data. This was chosen to exemplify a strong forcing. The vertical extent of the ozone anomaly ia around 2-0.5 hPa (40-53 km) provided for SAGE and SBUV in Soukharev and Hood (2006) for the upper stratospheric enhancement.
In both the particle forcing and the UV solar forcing scenarios, I aimed at a simple scenario only including the direct impact on ozone: ozone loss directly related to

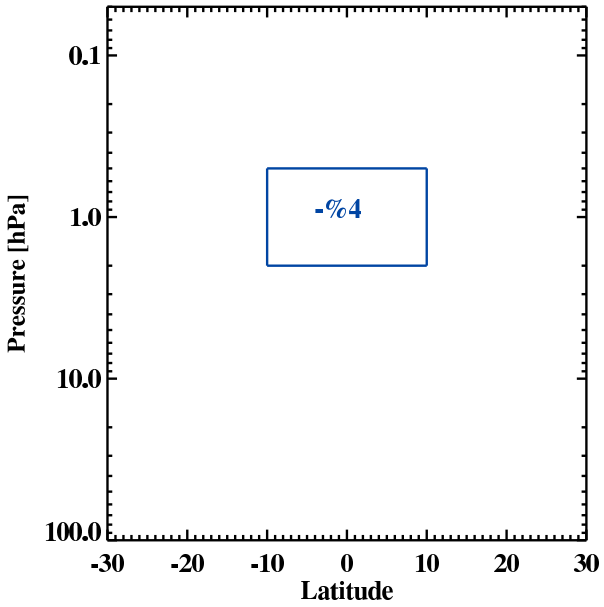

Figure 2.6: Ozone depletion according to ($\Delta O_3 - TS$) scenario.

downwelling NOy for the particle forcing, the region of strongest ozone formation for the UV forcing. Indirect effects as showing up in some observational records are not included. These are, e.g., the positive ozone anomalies below the negative anomalies observed by Fytterer et al. (2015a), which might be due either to self-healing, a dynamical, or a chemical feedback. For the solar spectral radiation, the lower stratospheric enhancement was not included, because it is assumed to be derived from a dynamical feedback Soukharev and Hood (2006).

In the current thesis the monthly mean ozone climatology is used to impose the ozone-depletion scenarios. The following procedures describes the required steps for interpolating the monthly mean data into the actual time of the integration in EMAC model. Figure 2.7 demonstrates how EPP-induced ozone depletion scenario described in Fig. 2.5 affects the ozone concentration in EMAC model. The ozone zonal mean and monthly mean climatology is linearly interpolated to the actual time of the integration and integrated from $P = 0$ to the surface $P = P_s$. For any given month, in the middle of month the ozone concentration is reduced by 30%. Forward and backward in time from the middle of month, for every day a reduction of about 1% from the central 30% ozone depletion is imposed in EMAC model. The time interpolated profile of ozone is interpolated to the model full levels and integrated again from $P = 0$ to $P = P_s$. Finally the ozone profile on the model levels is normalized such that the integrated amount on the model grid is identical to that on the grid of the climatology.

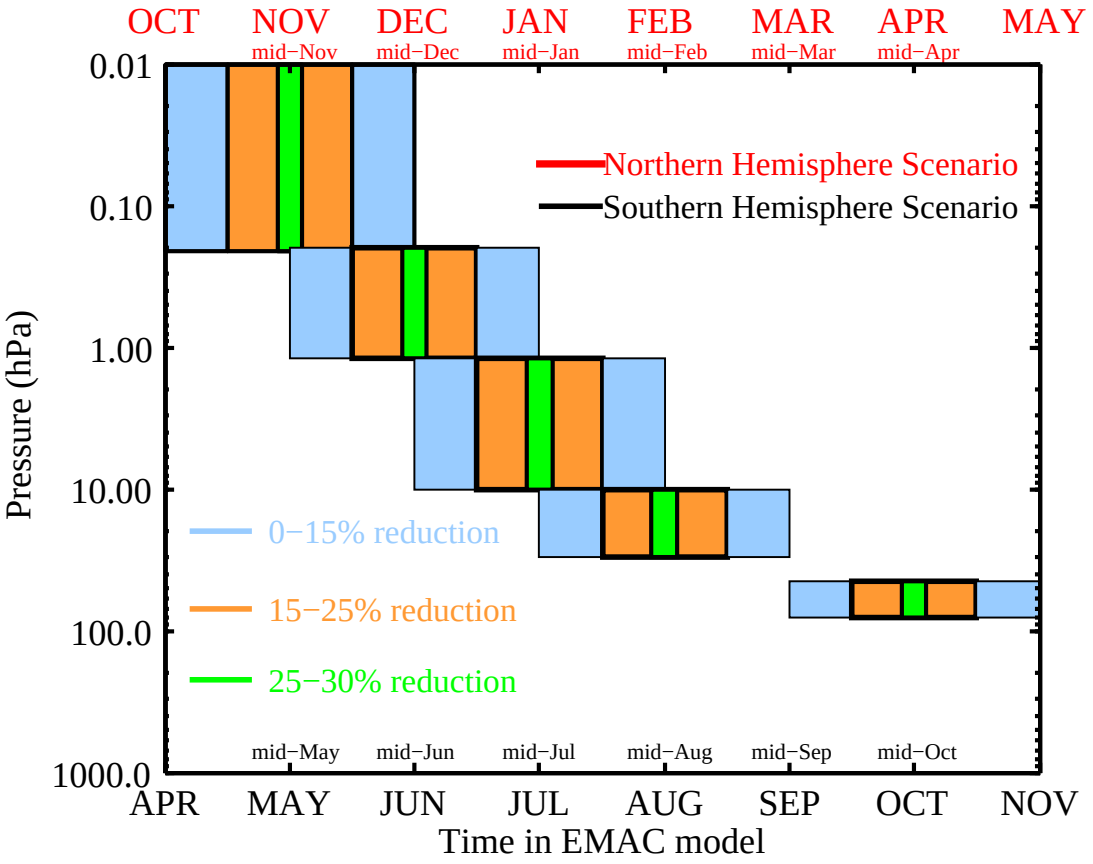

Figure 2.7: The actual changes in the ozone concentration in EMAC model based on the EPP-induced ozone depletion scenario described in Fig. 2.5. In the regions shaded by the green, orange and blue colors the ozone concentration is reduced by $25-30\%$, $15-25\%$ and $0-15\%$, respectively.

2.7 Reanalysis datasets

In the current thesis I used daily mean zonal wind and temperature from the National Center for Environmental Prediction-National Centre for Atmospheric Research (NCEP-NCAR) (Kalnay et al. (1996)) to calculate the refractive index of Rossby waves for 50 winters (1961-2010) of both Northern and Southern hemispheres. I also use sea level pressure, zonal and meridional wind and temperature data obtained from the European Centre for Medium-Range Weather Forecasts (ECMWF) to investigate the dynamical coupling between stratosphere and troposphere. The period of the ECMWF data are (1958-2013) and the data are obtained for every 12 hours. In both NCEP and ECMWF datasets 1.5° resolution are used.

3 Diagnostic Tools

3.1 Eliassen-Palm Fluxes and its Divergences

The "non-acceleration theorem" derived by Eliassen and Palm (1960) for gravity waves and by Charney and Drazin (1961) for planetary waves are the leading studies of wave-mean flow interactions. This theory simply states that in the absence of friction and heating, small amplitude (linear), stationary (time-independent) Rossby waves in a vertical shear flow is not able to alter the mean flow. Further theoretical investigation of (Dickinson (1969a), Dickinson (1969b)) revealed that for the forcing of the zonal atmospheric motions on large scale as implied by the non-acceleration theorem at least a critical line or a Newtonian cooling process must exist. Later, observational evidence confirmed that wave transience has a great role in violating the non-acceleration theorem. In fact, the transience of vertically propagating planetary waves originated from lower atmosphere has an effect on the mean zonal wind states. A vector quantity known as the EP flux provides a powerful tool for the description of small amplitude waves propagation in mean zonal shear flows. This diagnostic vectors are parallel to the direction of energy provided by quasi-geostrophic finite-amplitude waves. On the other hand its divergence represents wave-induced forcing of the mean flow in a transformed version of Eulerian-mean equations. In other words, the divergence of EP flux shows the zonal force per unit mass on the zonal mean flow by waves. In the transformed Eulerian mean formalism the non-acceleration theorem occurs when the divergence of EP flux is zero. The quasi-geostrophic EP flux ($\mathbf{F} = (F_\phi, F_p)$) in log pressure coordinate is defined by

$$\mathbf{F} = (F_\phi, F_p) = \begin{cases} F_p = \rho_0 a f cos(\phi) \frac{\overline{v'\theta'}}{\frac{\partial\overline{\theta}}{\partial p}}, \\ F_\phi = -\rho_0 a cos(\phi) \overline{u'v'}, \end{cases} \tag{3.1}$$

where, the primes denote departure from the zonal mean and the overbars denote zonal mean for any atmospheric variable. In Eq. 3.1, u, v are zonal and meridional velocities, θ is potential temperature,$f = f(\phi)$ is the Coriolis parameter, a is Earth's radius, ϕ is the latitude and finally ρ_0 is atmospheric density as a function of height. The vertical derivative of the zonal-mean potential temperature $\frac{\partial\overline{\theta}}{\partial p}$ measures the static stability of the atmosphere and is negative for a statically stable atmosphere.

The divergence of the EP flux vector is derived from the following equation:

$$\nabla .\ F = \frac{1}{acos(\phi)} \frac{\partial F_\phi cos(\phi)}{\partial \phi} + \frac{\partial F_p}{\partial p} \tag{3.2}$$

positive values of EP flux divergence imply acceleration of the zonal flow, while negative values (convergence of EP flux) result in zonal flow deceleration. It is worthwhile to mention that in the extratropics there is a competition between horizontal divergence of meridional eddy momentum flux ($\nabla .\ F_\phi$) and vertical divergence of the meridional eddy heat flux ($\nabla .\ F_p$) which largely cancel each other. Furthermore, the primary forcing in the deccelaration of the polar night jet of the Northern hemisphere in the winter time and spring time of the Southern hemisphere is the EP flux divergence. In other words, most of the departure from radiatively determined condition of the atmosphere can be explained by the divergence of EP flux Monier and Weare (2011). For more information about the transformed Eulerian mean formalism, the reader may refer to (Edmon et al. (1980), Dunkerton (1981)).
Figure 3.1 shows the wintertime climatology of the EP flux and its divergences. The positive values of the horizontal divergences of the EP flux act to accelerate the zonal wind and negative values of the vertical divergences act to decelerate the mean flow in the wintertime. The net effect of the opposite contributions of the horizontal and vertical divergences of the EP flux on the mean flow is the deceleration of the mean flow in the middle atmosphere around the Arctic polar vortex (Monier and Weare (2011)). In the Southern hemisphere wintertime, the magnitude of the wave forcing is relatively smaller than the Northern hemisphere which is mainly due to less land-sea contrasts and less topography in the Southern hemisphere compared to the Northern hemisphere Bracegirdle (2011).

3.2 Rossby waves refractive index

It is suggested that the impact of the background atmospheric state on planetary wave propagation can be diagnosed by using the refractive index of Rossby waves (Matsuno (1970), Simpson (2009)). According to linear wave theory planetary waves, away from the source regions, tend to propagate to the region of large positive refractive index squared. The existence of Rossby waves are prohibited where the refractive index squared is small or negative which can happen if the zonal mean zonal wind is easterly, or westerly exceeding the critical strength. Another important feature of refractive index is that EP flux convergence reaches to its maximum values where refractive index squared is very large Smith (1983).

Figure. 3.2 and Fig. 3.3 show the Time Mean Refractive Index Squared (TMRIS, in the plots weighted with the Earth radius squared) of 50 winters for the Northern

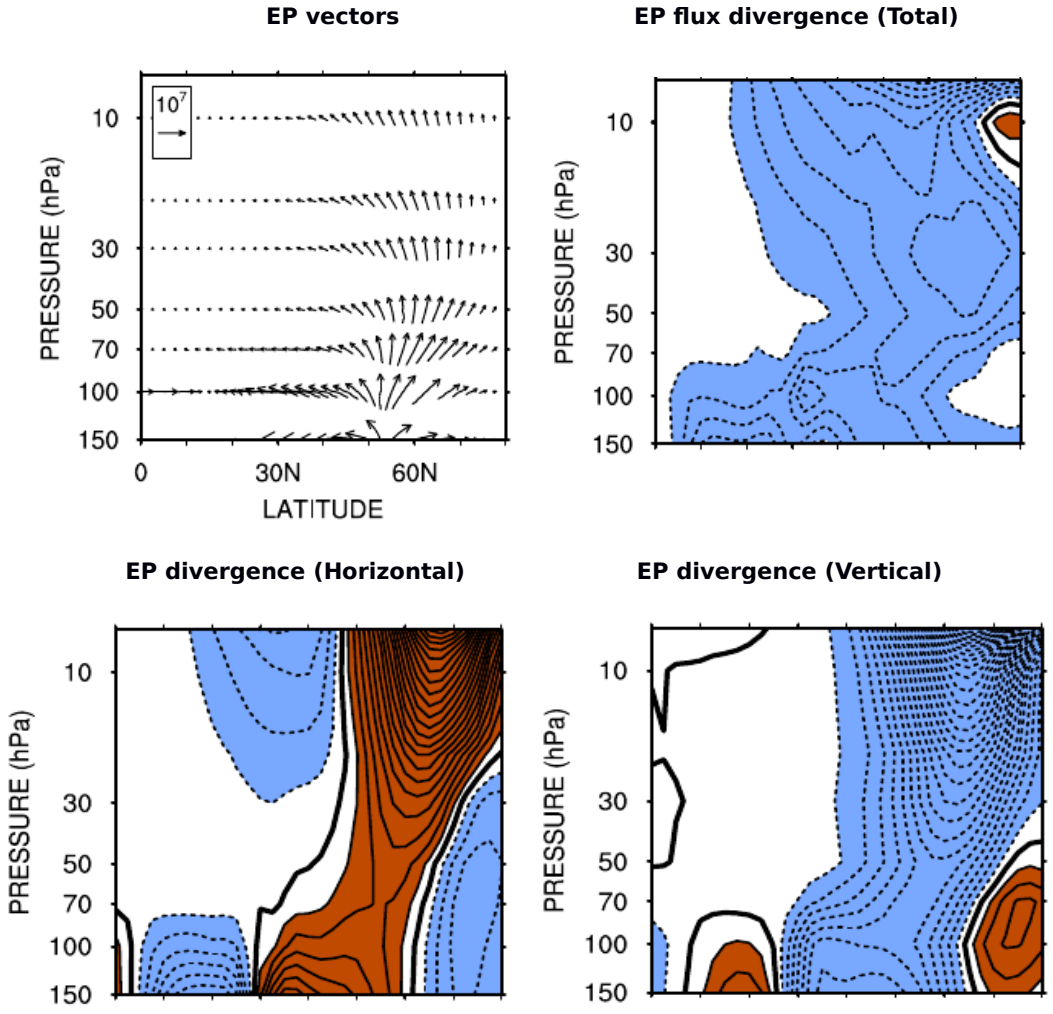

Figure 3.1: Latitude-height cross-sections of the EP vectors and its divergences in the Northern Hemisphere averaged over January-March 1980-2001 for the ERA-40 reanalysis. Dashed (solid) lines and blue (brown) shadings represent negative (positive) values while the bold solid line represent the zero-line. Countour interval is 0.5 $ms^{-1}day^{-1}$ for the EP flux divergences. The magnitude of the vertical divergences of the EP flux is larger than the horizontal EP flux. Therefore in the Northern hemisphere wintertime negative values of the divergence of the EP fluxes act to decelerate the mean flow in the stratosphere (the figure is taken from Monier and Weare (2011)).

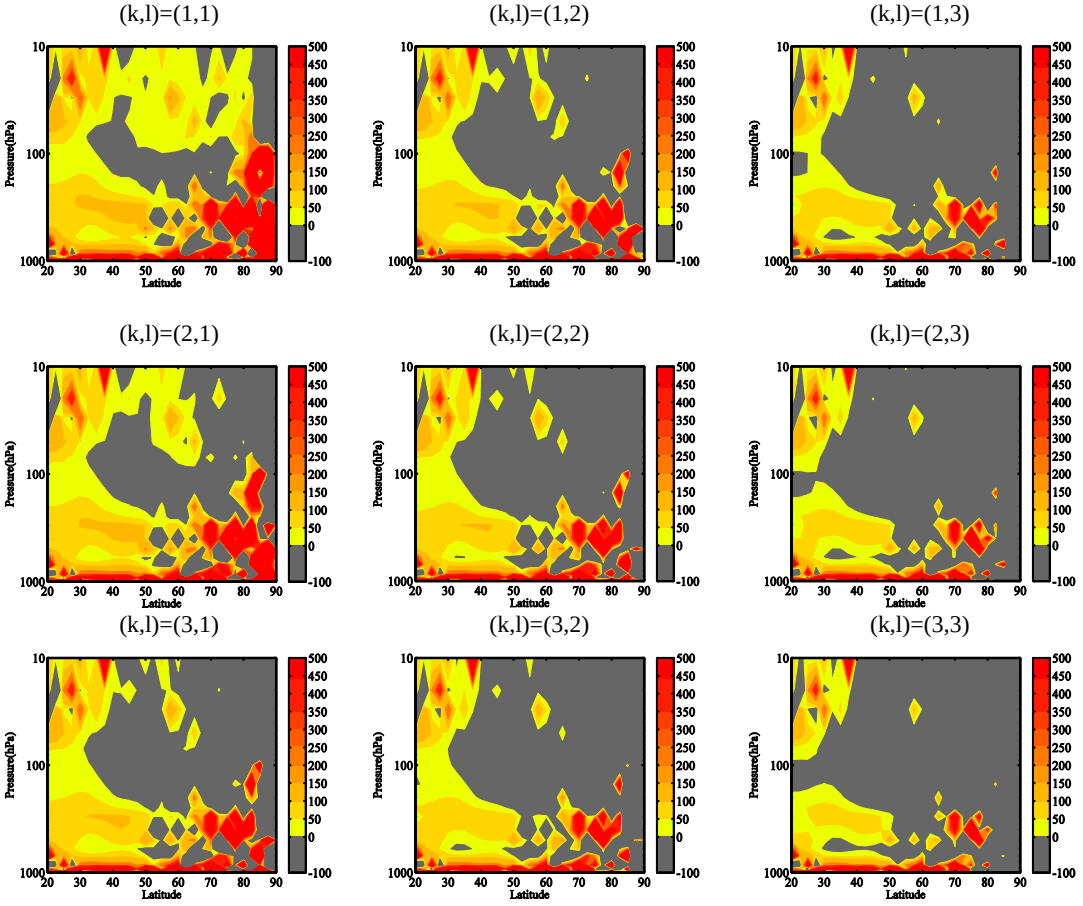

Figure 3.2: Climatology of refractive index squared $a^2 n^2_{k,l}(y,z)$ of 50 winters (1961-2010) in the Northern hemisphere. Regions with negative $a^2 n^2_{k,l}(y,z)$ are shaded with gray color. The higher the value of the refractive index it is easier waves to propagate to that regions. Planetary waves tend to be absorbed or reflected back from the regions of negative refractive index. The figure is taken from (Karami et al. (2016)).

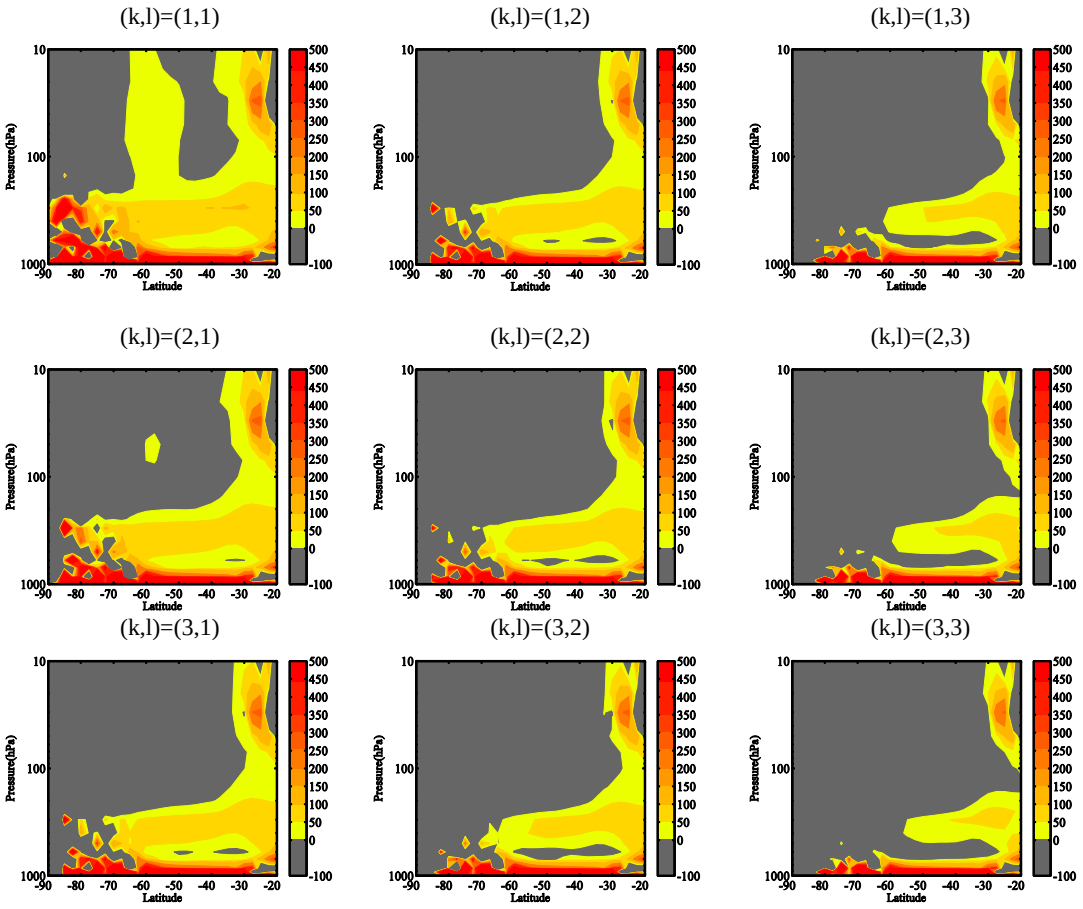

Figure 3.3: Climatology of refractive index squared $a^2 n^2_{k,l}(y,z)$ of 50 winters (1961-2010) in the Southern hemisphere. Regions with negative $a^2 n^2_{k,l}(y,z)$ are shaded with gray color. The higher the value of the refractive index it is easier waves to propagate to that regions. Planetary waves tend to be absorbed or reflected back from the regions of negative refractive index. The figure is taken from (Karami et al. (2016)).

and Southern hemispheres respectively. The NCEP-NCAR daily mean zonal wind and temperature from 1961-2010 are used to calculate the TMRIS. Here I focus on the cold months (December-January-February (DJF) for the Northern hemisphere and June-July-August (JJA) for the Southern hemisphere) because in the wintertime Rossby waves are more prounounced in the troposphere (Holton (2004), Andrews et al. (1987)). In both Northern amd Southern hemispheres the wave-scale dependency of the TMRIS can be seen. In these plots TMRIS for the the zonal wavenumber (k=1,2,3) and meridional wavenumbers (l=1,2,3) are calculated. It can be seen that for (k,l)=(1,1) very high values of the refractive index squared are found in high latitudes of the troposphere and the lower stratosphere. It can be seen that the strong stratospheric polar night jet of the Southern hemisphere in the winter (Fig. 3.3) block and reflect large scale waves.
One of the prounounced characteristics of the TMRIS is its noiseness. In large areas of the mid and high latitudes of the troposphere and stratosphere alternating positive and negative values of the refractive index squared leads to a noisy structure and makes the interpretation very difficult. The problem originates from the overlapping of positive and negative values in the time-series and results in a reduction of climatological information. Other researchers (e.g. Mukougawa and Hirooka (2004), Li et al. (2007)) have reported the problematic features of the time mean refractive index. In the next section I will review some of the important shortcomings of the refractive index and I will propose a method to overcome to this problematic features. It is assumed that any diagnostic tool attempting to provide a climatology of the stationary Rossby wave propagation conditions should be consistent with the criteria listed in Table 3.1. Though I have provided a limited number of references for the criteria given in Table 3.1 many more studies are in agreement with our assumptions provided in Table 3.1 (e.g. Li et al. (2007), Huang and Gambo (2002), Hu and Tung (2002)).

The first unsatisfactory results of the TMRIS is the large values of this quantity poleward of 75° N in the lower stratosphere. In this region it is expected that the strong jet blocks the wave penetration from the troposphere to the stratosphere (Fig. 3.4 (left)). The TMRIS also shows unsatisfactory results regarding the meridional wavenumber dependency on the wave propagation conditions. For instance, in Fig. 3.3 (middle row) the differences between the TMRIS for wave (2,1), (2,2) and (2,3) in the stratosphere (above 100 hPa) is negligible that implies there is negligible influence from the meridional wavenumbers on the vertical propagation of planetary waves from the tropopshere to the stratosphere. Criterion 4 in Table 3.1 is also not met between 20-40° N in the lower and middle stratosphere in the Northern hemisphere because a negative wind shear in the lower stratosphere at this region reduces the chances for the wave penetration from below.
The above-mentioned shortcomings of the time mean refractive index squared is a

Table 3.1: The table provides a concise summary of the known facts about the propagation of the stationary Rossby waves. We assume that any diagnostic tool that attempts to provide a long-term climatology for the stationary Rossby wave propagation should meet these criteria.

1	The most favorable regions for the Rossby wave propagation is the lower troposphere of the mid-latitude. Upper troposphere and occasionally lower stratosphere are also favorable regions for the wave propagation.	Matsuno (1970), Charney and Drazin (1961)
2	The larger the waves it is easier for waves to propagate vertically from the troposphere to the stratosphere. For large scale waves (horizontal and meridional wave numbers 1 to 3) it is easier for waves to penetrate to the stratosphere.	Matsuno (1970), Charney and Drazin (1961)
3	Rossby waves avoid penetrating through the jet maxima. Especially the polar night jet of the Southern hemisphere in the wintertime greatly block and reflect the large scale waves. These waves tend to propagate on the edges of the strong westerlies (jet stream).	Karoly and Hoskins (1982)
4	Positive wind shear enhances the upward propagation of the stationary Rossby waves.	Chen and Robinson (1992)

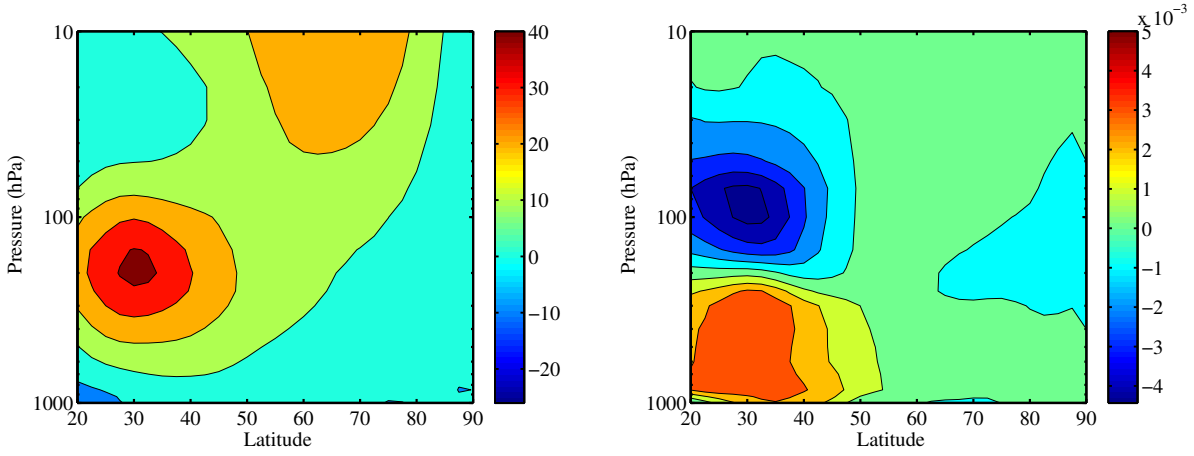

Figure 3.4: Climatology of the zonal mean zonal wind (left) and the vertical shear of zonal mean zonal wind (right) for the Northern hemisphere during DJF. The units are ms^{-1} for zonal mean zonal wind and $ms^{-1}km^{-1}$ for the vertical shear of zonal mean zonal wind respectively. The figure is taken from (Karami et al. (2016)).

motivation for further work to come up with an improved diagnostic tools to study the influence of the background flow on the wave propagation. Theoritically there are numerous ways to reduce the level of noise in the time mean of the refractive index. For instance a possible approach is the "trimmed-mean" of the refractive index squared. In this method one should remove a small percentage (for instance 10%) of the largest and smallest values before calculating the mean value. Li et al. (2007) proposed a method that reduces the level of noise in the time mean refractive index squared. They calculate the the frequency distribution of days with negative refractive index squared as a method that might be used to describe the upward planetary-scale wave propagation from the troposphere to the stratosphere. As an alternative interpretation, this method calculates the probability of positive refractive index squared. Since Rossby waves tend to propagate to the regions where the refractive index is either positive or large positive values, the higher the probability it is easier for waves to propagate to these regions.

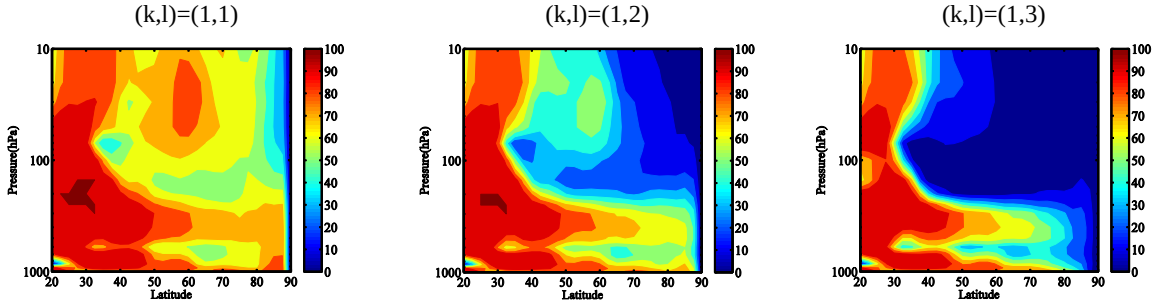

Figure 3.5: Probability of positive refractive index squared based on the method proposed by (Li et al. (2007)) for Northern hemisphere wintertime (DJF) for wave (1,1), (1,2) and (1,3). Rossby waves tend to avoid to propagate to the regions where the probability is low (less than 50%) and easily propagate to the regions where the probability is higher. The figure is taken from (Karami et al. (2016)).

Figure. 3.5 shows the probability of positive refractive index squared based on the method proposed by (Li et al. (2007)) for Northern hemisphere wintertime (DJF) for wave (1,1), (1,2) and (1,3). Rossby waves tend to avoid to propagate to the regions where the probability is low (less than 50%) and easily propagate to the regions where the probability is higher. It can be seen that the largest meridional wave (k,l)=(1,1) has higher probability to penetrate to the stratosphere. It is also evident that the wintertime polar night jet of the Northern hemisphere blocks the meridional wavenumber (l=3) to propagate to the stratosphere. This method suggest a waveguide in which waves can penetrate to the stratosphere from the troposphere. This waveguide can be found in the regions where probability is more than 70%. This is generally between 20-40 °N and this waveguide is wider for the meridional wavenumber (l=1). For l=3 the waveguide is narrower suggesting less probability

for this wave to propagate upward from the troposphere to the stratosphere.

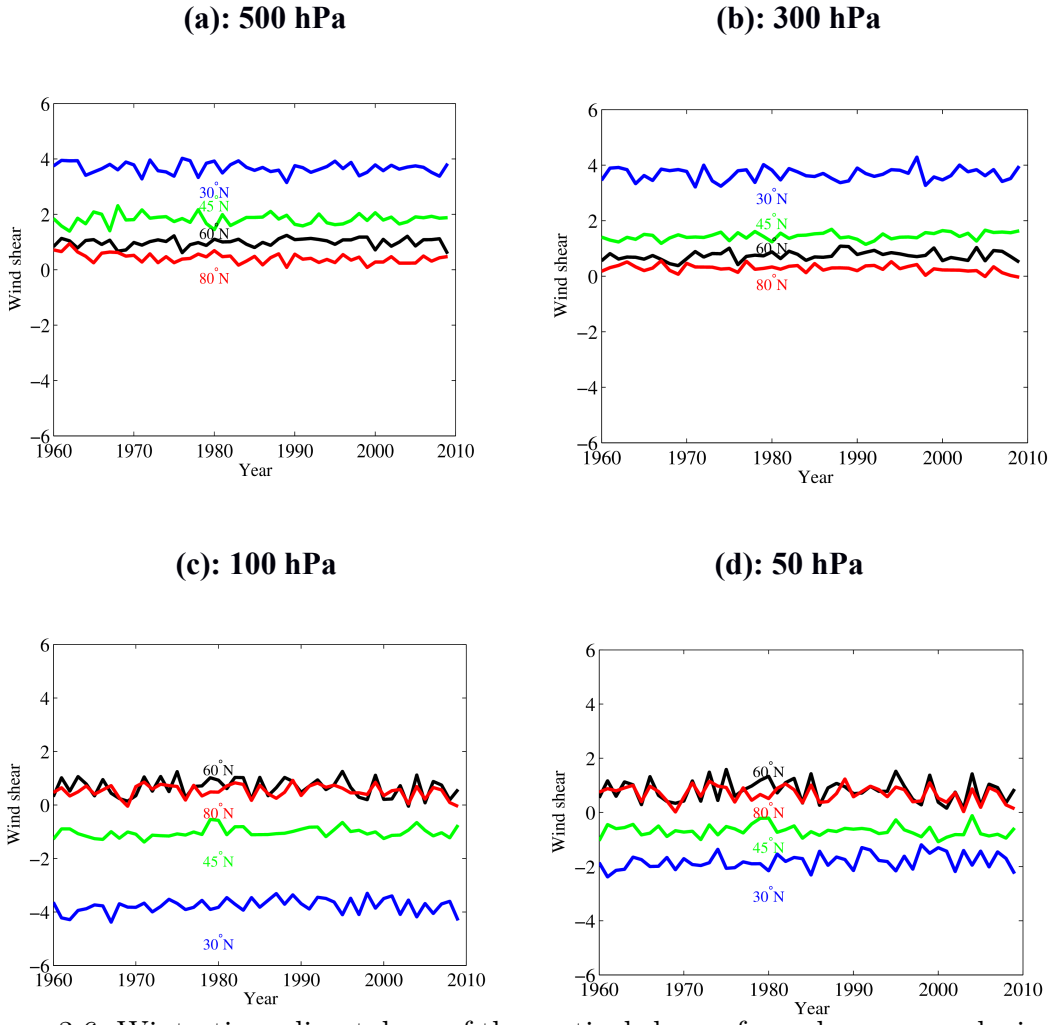

Figure 3.6: Wintertime climatology of the vertical shear of zonal mean zonal wind in $(ms^{-1}km^{-1})$ in the Northern hemisphere for four different latitudes. In the lower stratosphere (50-100 hPa) the vertical wind shear is negative over the extra-tropics (30-45 °N) and in the same latitude range in the troposphere (300-500 hPa) the vertical wind shear is positive (based on NCEP-NCAR dataset).

Though the probability of positive refractive index squared describes the required wave properties better than the time mean refractive index, it has itw own shortcomings. For instance it results in high values of probability between 20-40 °N in the lower and middle stratosphere. According to (Chen and Robinson (1992)) a strong positive vertical shear is likely to enhance the vertical propagation of waves. The probability for the upward wave propagation reduces where the vertical wind shear is negative. Figure. 3.6 provides a time-series for the year-to-year variations in the vertical wind shear at different latitude and altitude ranges. The vertical wind shear betwen 60-80 °N (denoted by black and red lines respectively) is always a small

positive value (less than 2 $ms^{-1}km^{-1}$) regardless of different altitudes. However in the lower stratosphere (50-100 hPa) the vertical wind shear is negative over the extra-tropics (30-45 °N) and in the same latitude range in the troposphere (300-500 hPa) the vertical wind shear is positive. This argument suggest that the results of Fig. 3.5 might be an over-optimistic result, because it is due to small positive values at extra-tropics of the lower stratosphere that exist throughout the winter season. In this respect the climatology of probability of positive refraction index squared does not meet the criterion 4 in Table 3.1.

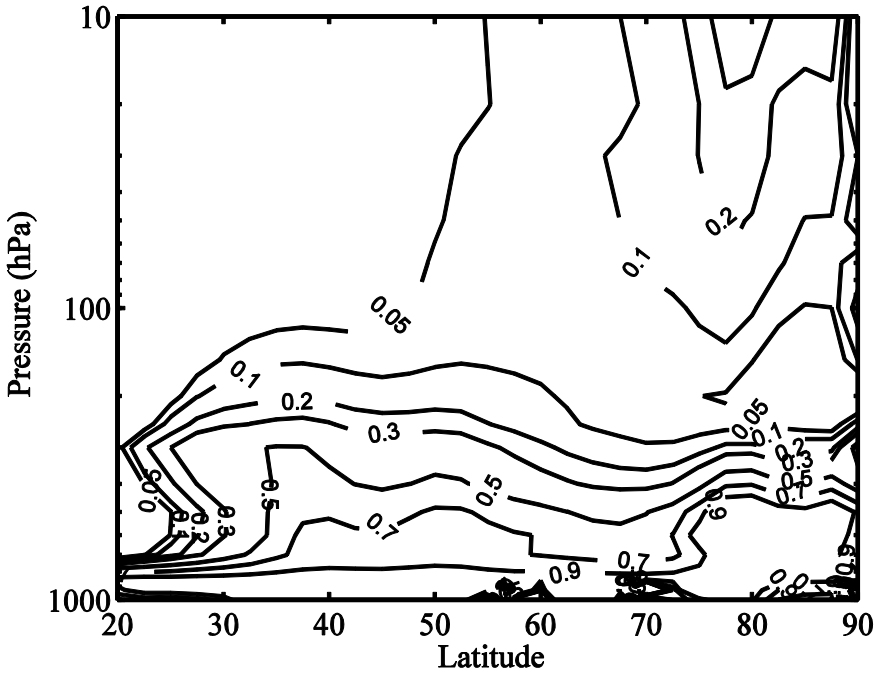

Figure 3.7: Climatology of the vertical component of EP flux normalized by vertical component of EP flux at 850 hPa for DJF at Northern hemisphere. Discontinuity of this quantity at the tropopause heights indicates the strong suppression of wave penetration from troposphere into the stratosphere at lower stratosphere. The upward penetration of Rossby waves is suppressed by the negative values of the vertical wind shear above tropopause heights. The figure is taken from (Karami et al. (2016)).

A further argument to show the importance of vertical shear of zonal mean zonal wind for the upward propagation of Rossby waves is the behavior of the vertical component of the Eliassen-Palm (EP) flux. Figure. 3.7 shows the vertical component of EP flux divided by vertical component of EP flux at 850 hPa for DJF at Northern hemisphere. It is clear from Fig. 3.7 that the magnitude of the EP flux is much less in the stratosphere compared to the troposphere. As suggested by (Hu and Tung (2002)) the upward penetration of Rossby waves is suppressed

by the negative values of the vertical wind shear above tropopause heights. I now argue that any diagnostic tool attempting to provide a climatology for the upward wave propagation should be consistent with this fact. However the probability of positive refractive index (Fig. 3.5) fails to meet this criterion because the values of the probability in the stratosphere is as large as values in the troposphere between 20-40 °N

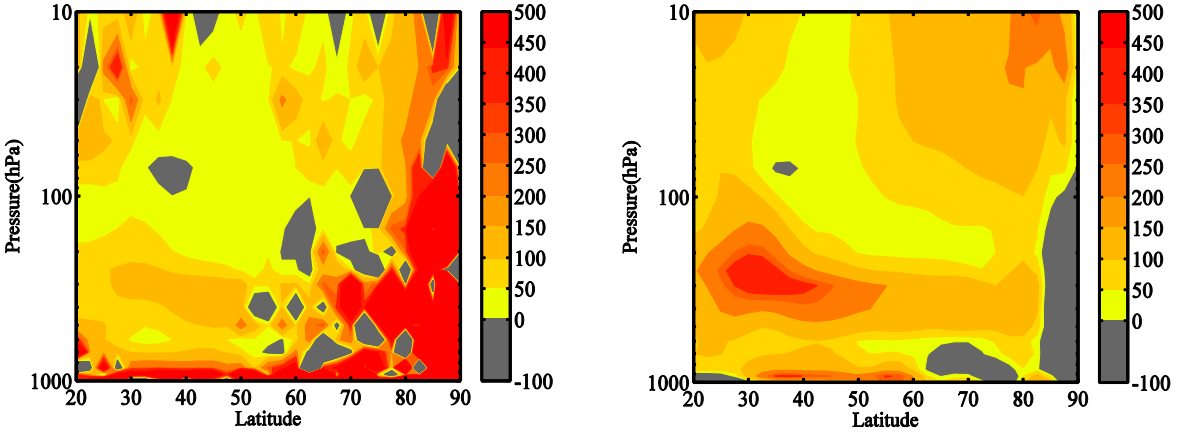

Figure 3.8: Wintertime climatology of the $a^2\frac{\overline{q_\phi}}{\overline{u}}$ (left) and $a^2\frac{\overline{q_\phi}}{10ms^{-1}}$ (right) in the Northern hemisphere. The small values of $\overline{u}$ rather than $\frac{\partial}{\partial z}\overline{u}$ at subpolar regions cause the maxima of $n^2_{k,l}(y,z)$ at these regions. The figure is taken from (Karami et al. (2016)).

Sensitivity of $n^2_{k,l}(y,z)$ to $\overline{u}$ can be studied by comparing the values of $a^2\frac{\overline{q_\phi}}{\overline{u}}$ and $a^2\frac{\overline{q_\phi}}{10ms^{-1}}$. The climatology of $a^2\frac{\overline{q_\phi}}{\overline{u}}$ and $a^2\frac{\overline{q_\phi}}{10ms^{-1}}$ for DJF in the Northern Hemisphere are presented in Fig. 3.8. A subpolar maxima of the $a^2\frac{\overline{q_\phi}}{\overline{u}}$ suggest that there is high probability for waves to penetrate through the polar night jet in the lower stratosphere. Too high values of the time mean refractive index square poleward of 75 °N in the lower stratosphere do not meet the criterion 3 in Table 3.1. It is expected that the strong polar night jet block and reflect the wave penetration from the troposphere to the stratosphere. By taking away the $\overline{u}$, the maxima are shifted to subtropics (25-40 °N). This infers that small values of $\overline{u}$ rather than $\frac{\partial}{\partial z}\overline{u}$ at subpolar regions cause the maxima of $n^2_{k,l}(y,z)$ at these regions.

3.3 Baroclinic Instability and Eady Parameter

Baroclinic instability refers to a mechanism for the formation of eddies in the mid and high latitudes. Baroclinic instability explains how eddies draw their energy from the mean flow (Holton (2004)). I start from the fact that there is a surplus of energy received by the Earth from the sun in the tropics and an energy deficit polewards

of about $40°N$. Now we show that there is a vertical shear of geostrophic wind in the presence of a horizontal temperature gradient. By using the geostrophic wind equation and the hydrostatic equilibrium:

$$v_g = \frac{1}{f}\frac{\partial \Phi}{\partial x} \qquad and \qquad u_g = -\frac{1}{f}\frac{\partial \Phi}{\partial y} \qquad and \qquad \frac{\partial \Phi}{\partial p} = -\frac{RT}{P} \tag{3.3}$$

and differentiating geostrophic wind equation with respect to pressure:

$$u_g = -\frac{1}{f}\frac{\partial}{\partial y}(-\frac{RT}{P}dp) \qquad and \qquad v_g = \frac{1}{f}\frac{\partial}{\partial x}(-\frac{RT}{P}dp) \tag{3.4}$$

and we obtain:

$$\frac{\partial u_g}{\partial \ln p} = \frac{R}{f}(\frac{\partial T}{\partial y}) \qquad and \qquad \frac{\partial v_g}{\partial \ln p} = -\frac{R}{f}(\frac{\partial T}{\partial x}) \tag{3.5}$$

Equation 4.3 refers to the the rate of change of the geostrophic wind with respect to $\ln p$ or the thermal wind equation. The thermal wind refers to the differences of geostrophic winds at two atmospheric levels. Figure 3.9 illustrates an example from the real atmosphere that shows a vertical shear of wind in the presence of a horizontal temperature gradient. From thermal wind balance, the vertical shear of the zonal wind is proportional to a meridional temperature gradient. In other words, the thermal wind equation suggests that for the higher horizontal temperature gradient, the rate of geostrophic wind changes are also higher. It is the main reason that the Northern hemisphere tropospheric jet is stronger during DJF than the Southern hemisphere counterpart. It also explains why the maximum of jet is not near the surface and is about 250 hPa in both hemispheres (Fig. 3.9). Figure 3.10 shows an example of barotropic flow in which there is no vertical wind shear. Similar to Fig. 3.9 a baroclinic flow is a flow in which wind speeds are almost linearly increasing with increasing height.

In their seminal paper on baroclinic instability (Pierrehumbert and Swanson (1995)) discuss how differentially heated rotating planets spontaneously generate transient eddies rather than settling into a local radiative equilibrium. In fact the energy for the generation of the eddies release from the potential energy is stored in the pole-equator temperature gradient of the Earth and similar planets. The process that leads to the growth of synoptic-scale disturbances is called dynamical instability. The small disturbances grow in the vicinity of the jets and draw their energy from the jets (mean flow). The process of growing disturbances that obtain their energy from the mean flow is called baroclinic instability. In the real atmosphere synoptic disturbances develop near to the maximum of the time-mean zonal wind (western Atlantic and western Pacific jets) and propagate eastward and follow the jet axes (Holton (2004)).

Eady growth rate is a popular measure of atmospheric baroclinicity. This parameters defines how fast the amplification of a wavy-like disturbances in the atmosphere

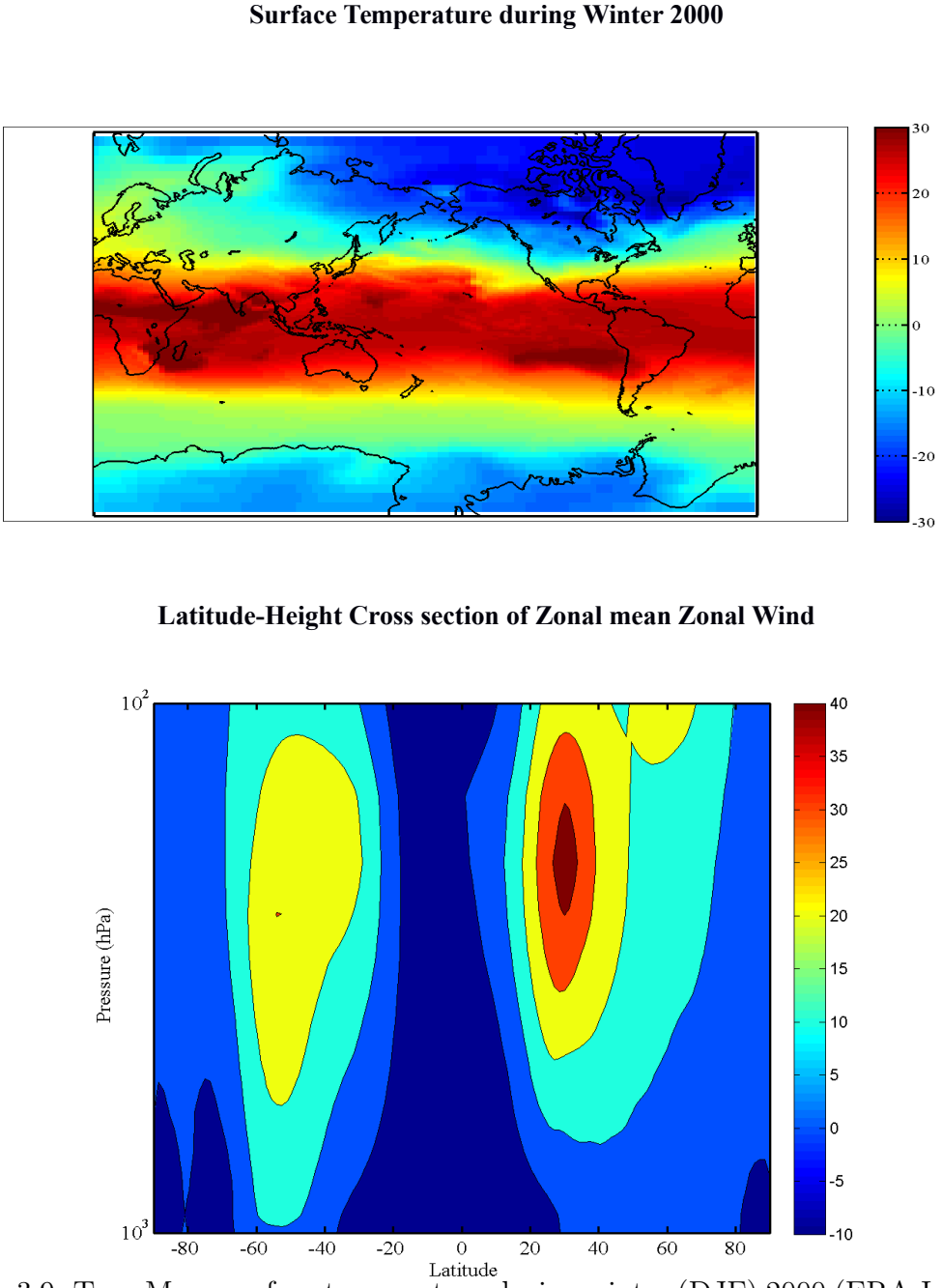

Figure 3.9: Top: Mean surface temperature during winter (DJF) 2000 (ERA-Interim dataset). During Northern hemisphere winter the temperature gradient between equator and north pole is larger than the equator and south pole. Bottom: Latitude-height cross section of zonal mean zonal wind during winter 2000. Since the temperature gradient between equator and pole is larger in the Northern hemisphere, therefore the Northern hemisphere jet is stronger during DJF than the jet in the Southern hemisphere. It is also clear from the thermal wind equation that why the maximum of the jet is near the 250 hPa and not at the surface. Era-Interim data are used for these figures.

is. The Eady model of baroclinic growth explains the baroclinic instability with constant stratification and no β-effect. Four basic assumptions are required for the Eady model. The first assumption is the uniformly stratified atmosphere. In other words it is assumed that the Brunt-Viäsälä frequency is constant throughout the atmosphere which is a reasonable assumption in the troposphere. The second approximation is the so-called f-place approximation where $\beta = 0$. Therefore the coriolis parameter is a constant quantity $f = f_0$. The third assumption is related to the upper and lower boundaries of the model. The Eady model assumes two rigid lids at the upper and lower boundaries without any vertical velocities near these lids. The last assumption is the constant vertical wind shear throughout the model ($\frac{\partial \overline{u}}{\partial z} = \Lambda$) where Λ is a constatnt value (Holton (2004), Seland (2009)). A schematic view of the basic setup of the Eady model of baroclinic growth is presented in Fig. 3.11.

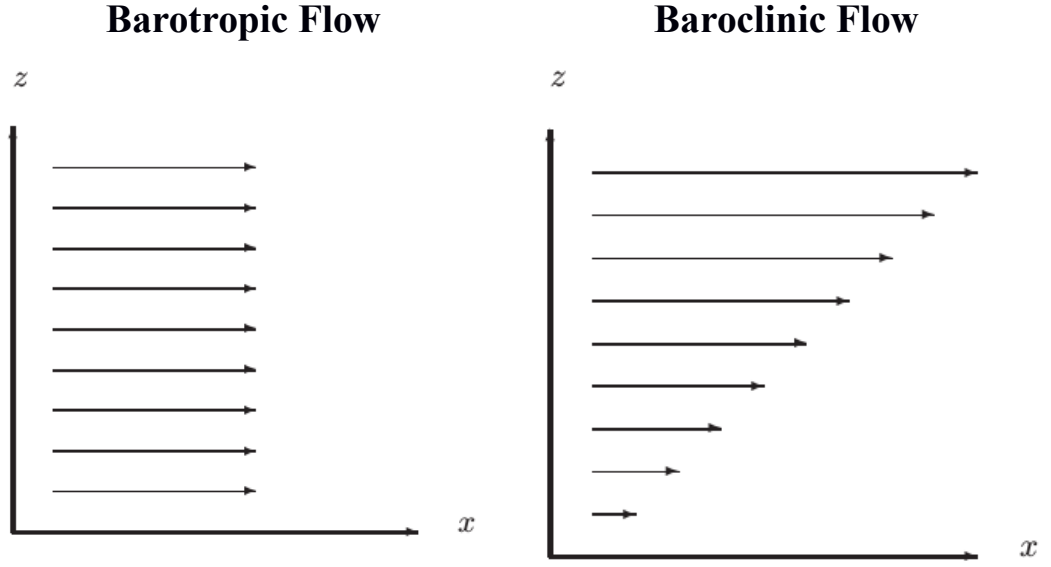

Figure 3.10: Left: an example of barotropic atmosphere in which there is no vertical wind shear. Right: an example of a baroclinic atmosphere where wind speeds are linearly increasing with increasing height.

The quasi-geostrophic potential vorticity equation governs the evolution of the flow in the Eady model:

$$\frac{D_g q}{Dt} = 0 \qquad and \qquad q = \nabla^2 \psi + \beta y + \frac{\partial}{\partial z}(\frac{f_0^2}{N^2}\frac{\partial \psi}{\partial z}) \tag{3.6}$$

where

$$\frac{D_g}{Dt} = \frac{\partial}{\partial t} + u_g \frac{\partial}{\partial x} + v_g \frac{\partial}{\partial y} \qquad and \qquad u_g = -\frac{\partial \psi}{\partial y} \qquad and \qquad v_g = \frac{\partial \psi}{\partial x} \tag{3.7}$$

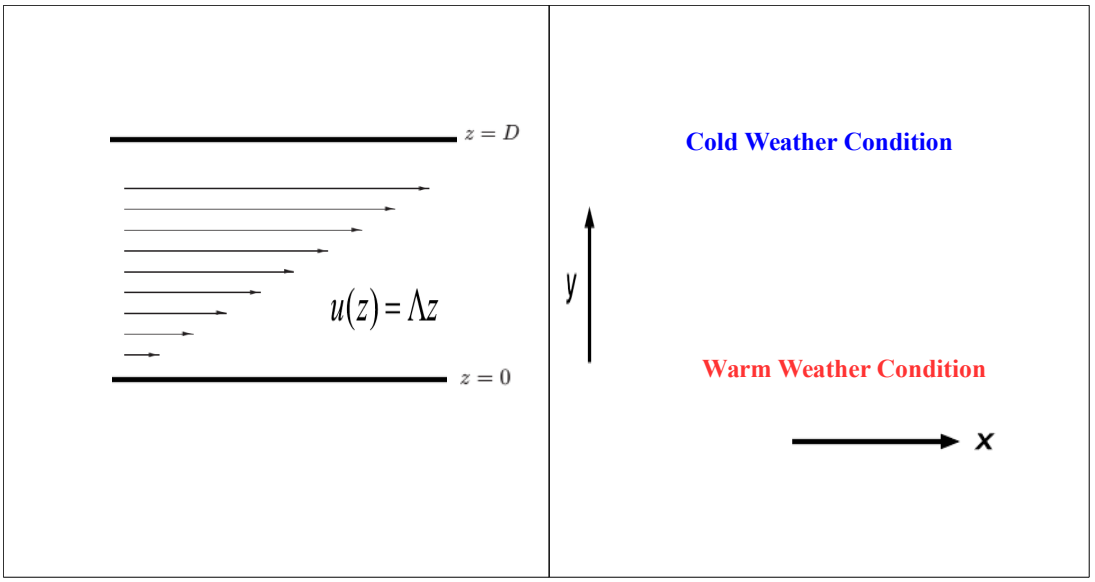

Figure 3.11: The basic setup of the Eady model of baroclinic growth. Left: The motion in the Eady model is between two rigid horizontal surfaces. The upper lid might be considered as tropopause where the static stability inhibits vertical motion. By thermal wind balance the vertical wind shear is associated with a horizontal temperature gradient at the surface (right).

The quasi-geostrophic relative vorticity (ζ_g) is defined as:

$$\zeta_g = \frac{\partial v_g}{\partial x} - \frac{\partial u_g}{\partial y} = \frac{\partial(\frac{\partial \psi}{\partial x})}{\partial x} - \frac{\partial(-\frac{\partial \psi}{\partial y})}{\partial y} = \frac{\partial^2 \psi}{\partial x^2} + \frac{\partial^2 \psi}{\partial y^2} = \nabla^2 \psi \tag{3.8}$$

Due to the advection terms, the quasi-geostrophic potential vorticity equation ($\frac{D_g q}{Dt} = 0$) is a non-linear equation. In order to simplify the solution of this equation we use linearization technique by using the perturbation method as described by (Holton (2004)). In the perturbation technique every quantity might be seperated to a mean basic state and a perturbation from the mean state:

$$u_g = \overline{u} + u' \qquad and \qquad v_g = \overline{v} + v' \qquad and \qquad \psi = \overline{\psi} + \psi' \tag{3.9}$$

where $\overline{u}$ and $\overline{v}$ are the mean zonal and meridional velocities and $\overline{\psi}$ is the mean streamfunction. u' and v' are deviations from the mean state and are assumed to be small compared to the basic state. Observational evidences in the mid-latitude region as well as in the Eady model show that $\overline{v} = 0$ and since $\overline{u} = \Lambda z$ and hence $\overline{u} = \overline{u}(z)$. Now we insert the equation (3.9) into equation (3.6). Since the perturbed fields are assumed to be small any producted of perturbed fields are neglected. The mean streamfunction ($\overline{\psi}$) is a two-dimensional field while its perturbation (ψ') is a function of all dimensions:

$$\frac{\partial \overline{\psi}}{\partial y} = -\overline{u} = \Lambda z \qquad and \qquad \overline{\psi} = \Lambda z y + const. \tag{3.10}$$

Therefore we can write the streamfunction as follows:

$$\psi(x,y,z,t) = \overline{\psi}(y,z) + \psi'(x,y,z,t) \tag{3.11}$$

$$\nabla^2\psi = \nabla^2\overline{\psi}(y,z) + \nabla^2\psi'(x,y,z,t) = \nabla^2\psi'(x,y,z,t) \tag{3.12}$$

because $\overline{\psi} = \Lambda zy + const$ and therefore $\nabla^2\overline{\psi}(y,z) = 0$. The linearized quasi-geostrophic potential vorticity is:

$$(\frac{\partial}{\partial t} + \overline{u}\frac{\partial}{\partial x})[\nabla^2\psi' + \frac{f_0^2}{N^2}\frac{\partial^2\psi'}{\partial^2 z}] = 0 \tag{3.13}$$

For the boundaries of the Eady model, the quasi-geostrophic temperature equation is applied as:

$$\frac{D_g}{Dt}\frac{\partial\psi}{\partial z}|_{z=0,D} + \frac{N^2\omega}{f_0}|_{z=0,D} = 0 \tag{3.14}$$

Since in the Eady model in both upper and lower rigid boundaries vertical velocity is assumed to be zero ($\omega = 0$), the quasi-geostrophic temperature equation is:

$$\frac{D_g}{Dt}\frac{\partial\psi}{\partial z}|_{z=0,D} = 0 \tag{3.15}$$

The linearized quasi-geostrophic temperature equation written for the v' in terms of streamfunction is:

$$(\frac{\partial}{\partial t} + \overline{u}\frac{\partial}{\partial x})\frac{\partial\psi'}{\partial z}|_{z=0,D} + v'\Lambda|_{z=0,D} = 0 \tag{3.16}$$

because $\frac{\partial}{\partial y}\frac{\partial}{\partial z}\overline{\psi} = \frac{\partial}{\partial y}\frac{\partial}{\partial z}\Lambda zy + const. = \frac{\partial}{\partial y}\Lambda y = \Lambda$. Now we consider a wave solution for this equation:

$$\psi = \hat{\psi}(z)\cos(ly)e^{kc_it}e^{ik(x-c_rt)} \tag{3.17}$$

where c is the complex phase speed ($c = ic_i + c_r$, c_i is the imaginary phase speed and c_r is the real phase speed). k and l are zonal and meridional wavenumbers and $\hat{\psi}(z)$ is the amplitude of the wave. It is important to mention that because the streamfunction (ψ) is proportional to $e^{-ik(c_r+ic_i)t}$ the solution of the quasi-geostrophic potential vorticity equation is unstable (grows with time) when the imaginary part of the phase speed is positive. Under this conditions waves start to exponentially grow in time and the solutions are unstable. By substituting equation (3.16) in the quasi-geostrophic potential vorticity equation we have:

$$(\overline{u} - c)[(-k^2 - l^2)\hat{\psi} + \frac{f_0^2}{N^2}\frac{\partial^2\hat{\psi}}{\partial z^2}] = 0 \tag{3.18}$$

The following conditions can satisfy the equation (3.18): 1) $\overline{u} = c$. Therefore the imaginary part of the phase speed is zero and there is no exponentially growing wave and hence the wave is stable.

2) $\frac{\partial^2\hat{\psi}}{\partial z^2} - \alpha^2\hat{\psi} = 0, \qquad where \quad \alpha^2 \equiv \frac{N^2(K^2+l^2)}{f_0^2}$. In order to have an imaginary phase speed for the solution of this equation the following criteria must be satisfied:

$$kc_i = \frac{k\Lambda}{\alpha}\sqrt{(\coth(\frac{\alpha D}{2}) - \frac{\alpha D}{2}))(\frac{\alpha D}{2} - \tanh(\frac{\alpha D}{2}))} \tag{3.19}$$

where kc_i is the Eady growth rate. The typical atmospheric values of $N = 0.01s^{-1}$, $f_0 = 10^{-4}s^{-1}$, $\Lambda = 0.005s^{-1}$, $D = 10km \ and \ L = 2000km$ results in the typical Eady growth rate as a function of zonal wavenumber (by assuming $l = 0$) which is shown in Fig. 3.12. The growth rate reaches to its maximum at $k_{peak} = 1.2 \times 10^{-6}$. The peak zonal wavenumber for the most unstable condition in the Eady model corresponds to a wavelength of $\lambda_{peak} = \frac{2\pi}{k_{peak}} \simeq 5020km$ which is very close to the length of the observed cyclones in midlatitudes. The growth rate reaches to zero immediatelly after the k_{peak} which suggests that for zonal wavenumbers larger than $k \simeq 1.7$ the growth rate is negligible and there is no amplifications in the amplitude of the waves. Equation (3.19) is a measure of baroclinic growth in the Eady model. This

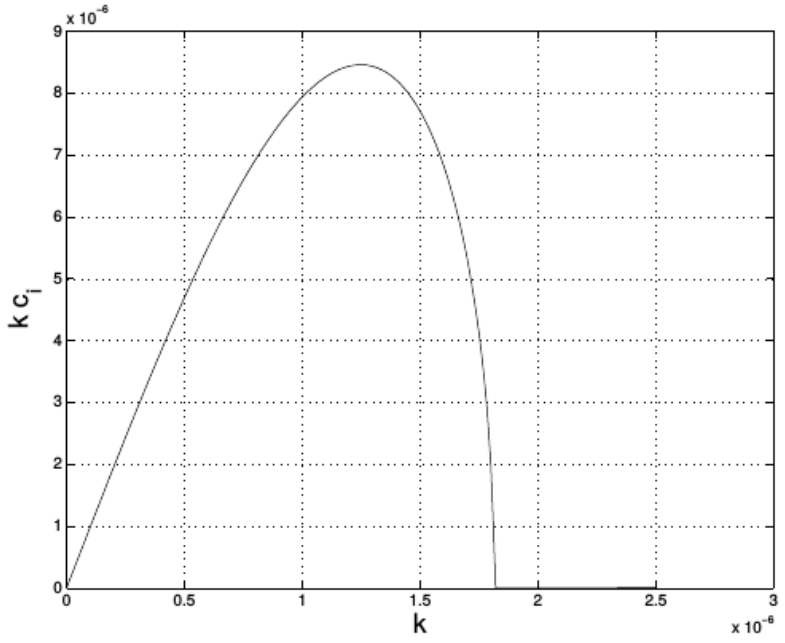

Figure 3.12: The Eady growth rate as a function of zonal wavenumber. The typical atmospheric values of $N = 0.01s^{-1}$, $f_0 = 10^{-4}s^{-1}$, $\Lambda = 0.005s^{-1}$, $D = 10km \ and \ L = 2000km$ are used for the calculation of the Eady growth rate. The figure is taken from Seland (2009).

equation calculates the growth rate of the most unstable wave. In this thesis we use the formula suggested by (Yin (2005)) to calculated the Eady growth rate:

$$\sigma = (kc_i)_{max} = \frac{k\Lambda}{\alpha} = 0.31\frac{g}{NT} \mid \frac{\partial T}{\partial y} \mid \qquad where \qquad N = \sqrt{g\frac{\partial\theta}{\partial z}} \tag{3.20}$$

The Eady growth rate is determined by two factors: meridional temperature gradient (or alternatively vertical wind shear by thermal wind equation) and Brunt-Väisälä frequency.
A 10-year (1980-1989) climatology of the Eady growth rate for different altitudes during January, April, August and October in the Northern hemisphere are shown in Fig. 3.13, Fig. 3.14, Fig. 3.15 and Fig. 3.16 respectively. Here we try to show the seasonal variability of the Eady growth rate (only a month as a representative for each season). In all months the maximum of the Eady growth rate occurs in the west Atlantic and west Pacific regions. The maximum of the Eady growth rate in the Atlantic region shows a northward tilt during January and October. The Pacific maxima starts from Asia and reaches its maximum in the middle of Pacific ocean. Since the Eady growth rate depends on the meridional temperature gradient between equator and pole, therefore the maximum of the Eady growth rate occurs in January for all altitudes. The Pacific maximum of the Eady growth rate is more zonally symmetric than its Atlantic counterpart. In addition the Pacific Eady growth rate is stronger than the Atlantic counterpart for all months and all altitudes. In all months the minimum of the Eady growth rate occurs at 250 hPa. The main reason for this is that the Brunt-Väisälä frequency reaches its minimum in the tropopause region (stratosphere is more stable than troposphere in general).

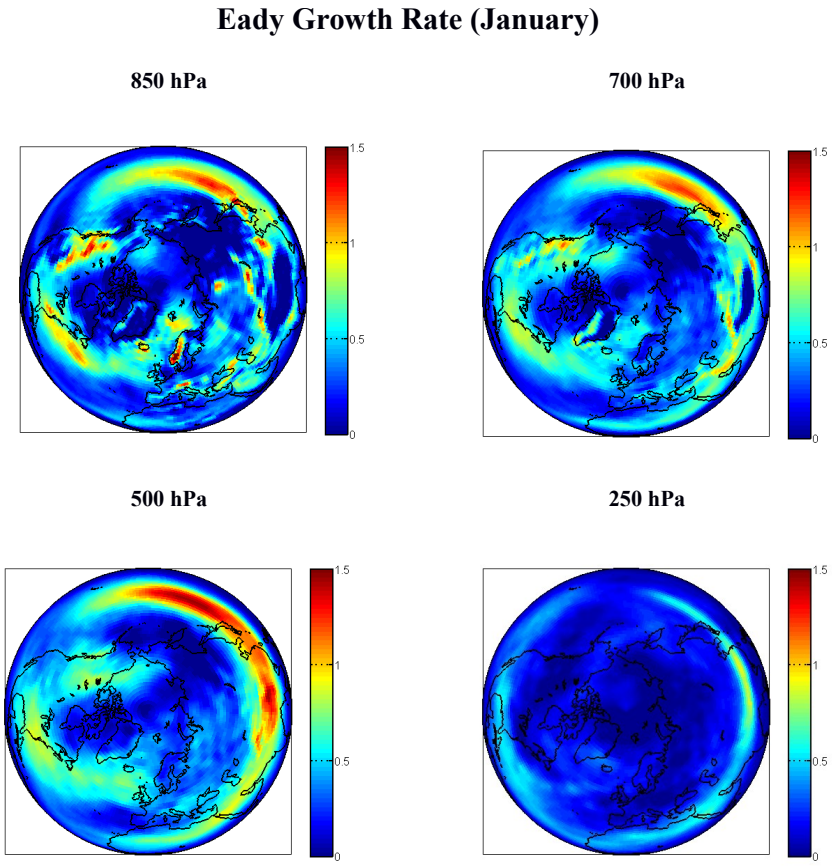

Figure 3.13: A 10-year (1980-1989) climatology of the Eady growth rate during January for different altitudes in the Northern hemisphere. The values of the Eady growth rate are between 0-1.5 day^{-1}.

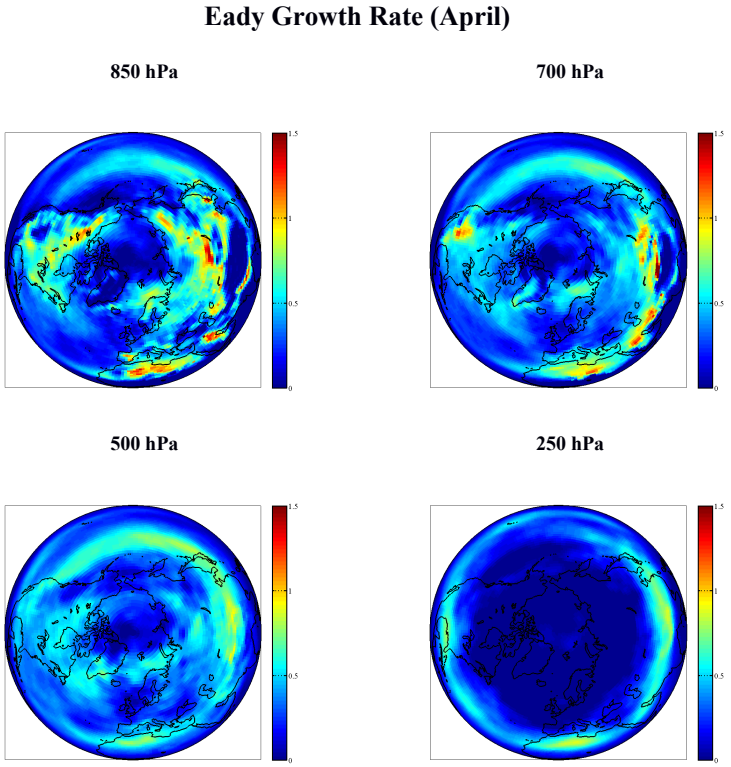

Figure 3.14: A 10-year (1980-1989) climatology of the Eady growth rate during April for different altitudes in the Northern hemisphere. The values of the Eady growth rate are between 0-1.5 day^{-1}.

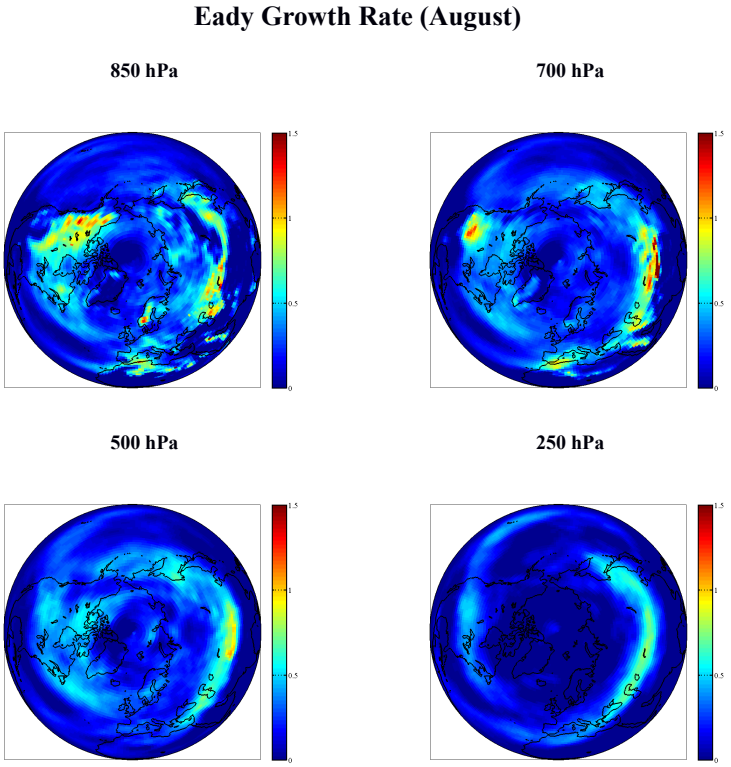

Figure 3.15: Same as Fig. 4.7 for August.

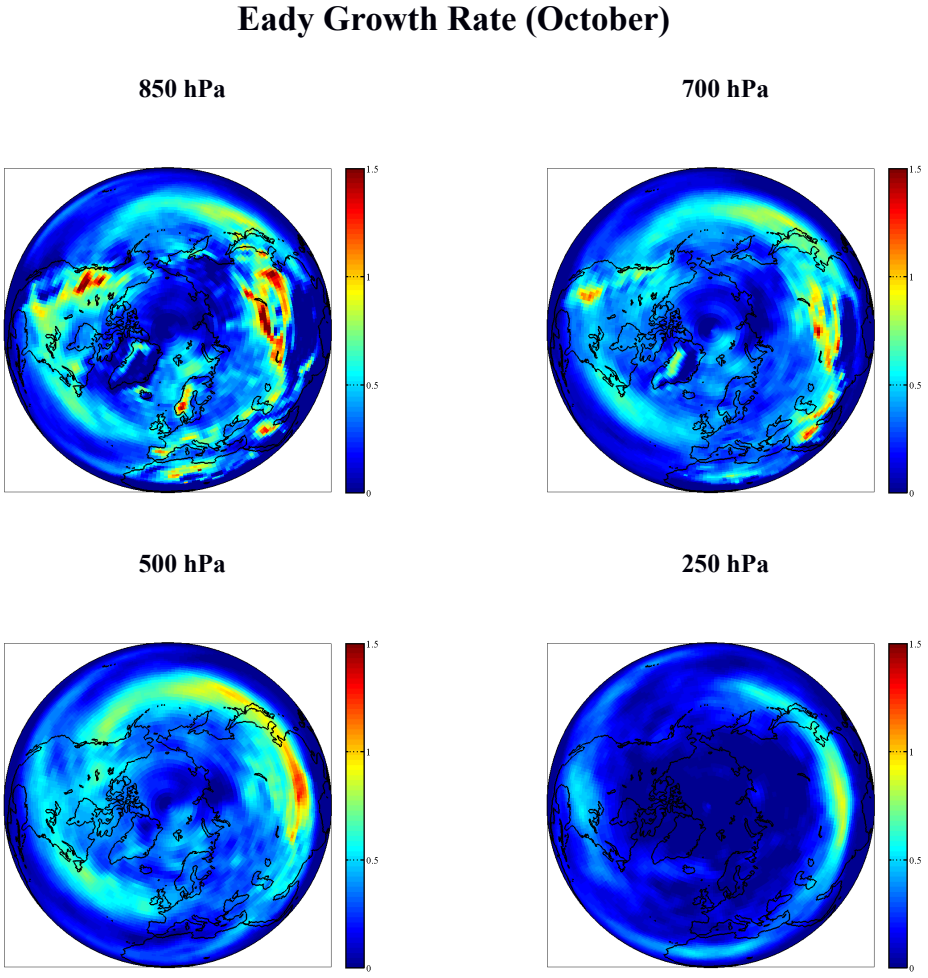

Figure 3.16: A 10-year (1980-1989) climatology of the Eady growth rate during October for different altitudes in the Northern hemisphere. The values of the Eady growth rate are between 0-1.5 day^{-1}.

4 Applications of the Diagnostic Tools to Reanalysis Data

4.1 Probability of Favorable Propagation Condition for Rossby waves

The time mean of refractive index squared is calculated based on the time average of the daily mean zonal wind and temperature. As discussed earlier (Chapter 3) this approach produces a noisy structure which makes the interpretation of the results difficult. One possibility to reduce the noise level is to calculate the refractive index of the time-mean zonal mean fields instead. The differences between these approaches for the time mean refractive index are shown in Fig. 4.1. The refractive index squared of the time mean fields is much less noisier than the time mean of the instantaneous refractive index squared. The main problem with the refractive index squared of the time mean fields is that Rossby waves obviously propagate in the instantaneous fields rather than time mean fields. Alternatively one can use other statistical methods like truncated means or trimmed means to reduce the noisiness. Another alternative to reduce the level of noise that I discussed earlier is besed on a simple calculation of the probability of positive refractive index squared (proposed by Li et al. (2007)). All of this methods has a common shortcomings. All of them are based on a purely statistical technique to reduce the level of noise in the time mean of the refractive index squared.

The vagueness in the interpretation of $n^2_{k,l}(y,z)$ is a long standing issue in the studies of the vertical wave propagation from the troposphere to the stratosphere. Smith (1983) found that planetary-scale waves tend to propagate to the regions where the refractive index is positive and large and avoids the regions where the refractive index is negative and large. Obviously large positive and negative values of the refractive index are arbitrary. Later Randel (1988) warned that while using the refractive index one should not overemphasize the details, since the refractive index is a qualitative tool rather than quantitave.

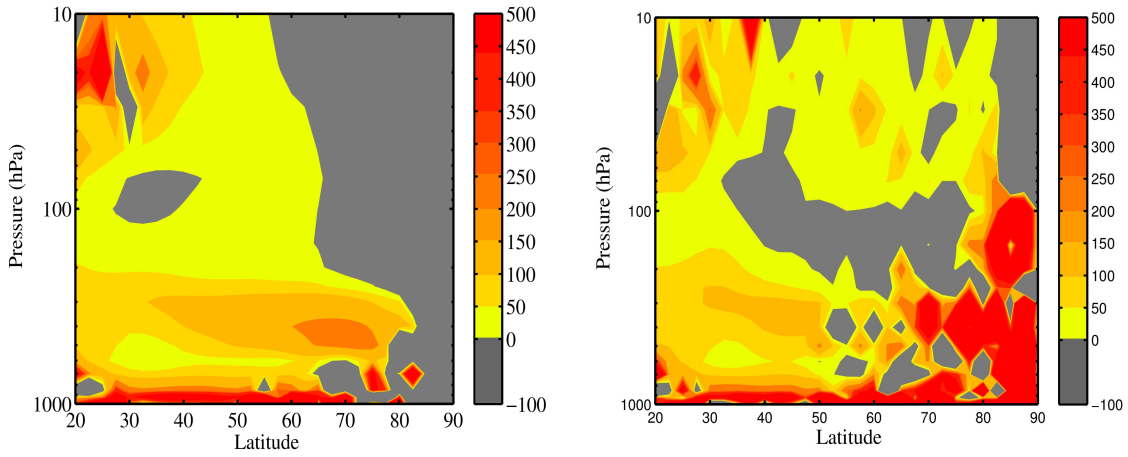

Figure 4.1: The time averaged zonal mean fields are used to calculate the refractive index squared (left, only for (k,l)=(1,1)). The time mean of the rafractive index squared calculated from the instantaneous fields is shown on the right. The refractive index squared of the time mean fields is much less noisier than the time mean of the instantaneous refractive index squared. The main problem with the refractive index squared of the time mean fields is that Rossby waves obviously propagate in the instantaneous fields rather than time mean fields. The figure is taken from (Karami et al. (2016)).

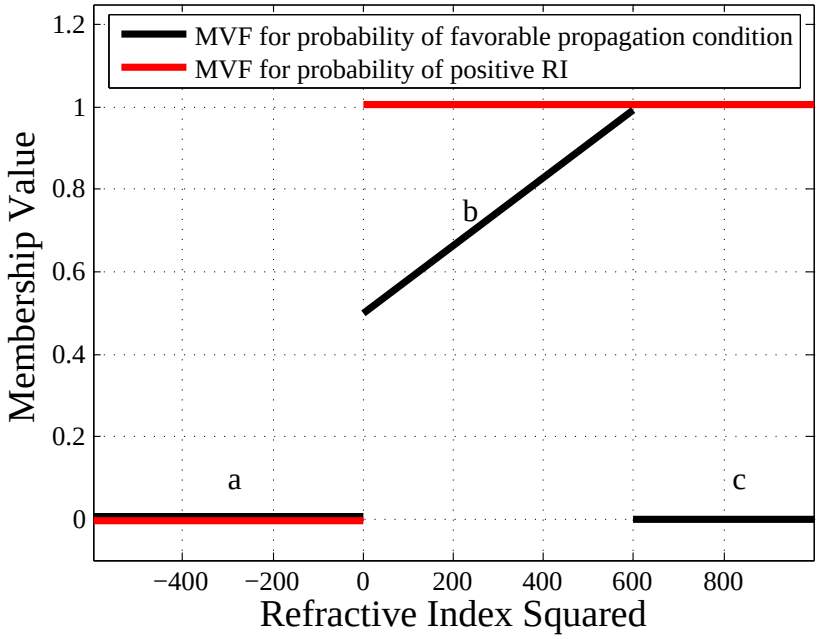

Figure 4.2: MVF used in the calculation of favorable propagation condition of Rossby waves (black curve). Red lines show MVF for calculating probability of positive refractive index which are used by (Li et al. (2007)). In their study the effect of the critical layer (part c) is not considered. The figure is taken from (Karami et al. (2016)).

The fuzzy sets and logic is an excellent mathematical method to deal with the modleing of the imprecise information and vagueness. This mathematical approach is appropriate for answering questions with imprecise information (such as very large or very small refractive index). The fuzzy logic deals with reasoning that is approximate rather than fixed and precise. In classical logic everything is either true or false. However, in fuzzy logic truth is a matter of degree (Zadeh (1965), Novak et al. (1999)). The basic approach is to assign a value between zero and one for every value of the refractive index squared. The value between zero and one is called membership value. The basic approach is to assign a value between zero and one to describe the area between the upper and lower limit of the refractive index square. The upper and lower limits are referring to the maximum and minimum values of any variable that fuzzy logics tries to set a membership value for them. Here I introduce a Membership Value Function (MVF) which is based on fuzzy logic to objectively generate a probabilistic climatology for the favorable conditions of the Rossby waves propagation. Later I will demonstrate a superior performance of this diagnostic tool compared to the climatological mean of the refractive indices.
A basic assumption in my approach is that I assume that not all individual (instantanous) $n^2_{k,l}(y,z,t)$ contribute equally to the final (time-mean) $n^2_{k,l}(y,z)$. In other words, some $n^2_{k,l}(y,z)$ contribute more than others in the final results. Based on this approach, I distinguish between large and small values of the refractive indices and I let very large positive values influence the final result more than small positive values. Therefore I introduce a classes or a set whose boundary is not sharp. I introduce $\mu_{Ro}(y,z,t)$ as the Rossby wave MVF which provides a modified probability of positive refractive index and estimate the probability of favorable propagation condition of Rossby wave ($Pr_{Ro}(y,z)$) which is a function of latitude and height. The advantage of my proposed method is that it maps well and in a physical way on the list of criteria formulated in Table 3.1. A further advantage of my method over the traditional analysis of the time mean of the refractive index is that I estimate the likliness for planetary waves to propagate from one region to another at any time and space without any reduction in the information due to the cancelletation of negative and positive values of the refractive index squared.
The probability of favorable propagation condition of Rossby waves $Pr_{Ro}(y,z)$ can be written as:

$$Pr_{Ro}(y,z) = \frac{\sum_{t=1}^{n} \mu_{Ro}(y,z,t)}{\sum_{t=1}^{n} t} \times 100 \tag{4.1}$$

where $\mu_{Ro}(y,z,t)$ as modified set of Probability Density Functions (mPDFs) is defined as:

$$\mu_{Ro} = \begin{cases} 0 \qquad if \qquad n^2_{k,l} \leq 0, \\ (8.3 \times 10^{-4} \times n^2_{k,l}(y,z)) + 0.5 \qquad if \qquad 0 < n^2_{k,l} < 600, \\ 0 \qquad if \qquad n^2_{k,l} \geq 600 \end{cases} \tag{4.2}$$

Here 8.3×10^{-4} is the slope of line b in the Fig. 4.2. The variable t is the time step and in the current study the daily mean values of the temperature and zonal wind are used in the calculations. In the study of (Li et al. (2007)) PDFs (red lines in the Fig. 4.2) are defined as:

$$\mu_{Ro} = \begin{cases} 0 \qquad if \qquad n^2_{k,l} < 0, \\ 1 \qquad if \qquad n^2_{k,l} > 0, \end{cases} \tag{4.3}$$

In Fig. 4.2 the black curve shows the MVF used in the calculation of favorable propagation condition of Rossby waves. Part (a) of the function shown be black line in the Fig. 4.2 describes a large rate of attenuation for the negative $n^2_{k,l}(y,z,t)$ and hence propagation of Rossby waves are prohibited in this region. Since the refractive index is based on linear wave theory and my method is based on this assumption, we assume a linear relationship between the magnitude of the $n^2_{k,l}(y,z,t)$ and the probability of the favorable wave prpagation for positive values of the $n^2_{k,l}(y,z)$. In this region (part b) the shape of function suggest that the higher the values of the $n^2_{k,l}(y,z,t)$ the chances for wave propagation increases linearly. The region where the zonal mean zonal wind approaches zero ($\overline{u} < 0.5\ m.s^{-1}$) is defined as critical line in this study. According to the linear wave theory Rossby waves start to break or are absorbed in the vicinity of the critical lines (part c). Therefore this region is also not favorable for Rossby wave propagation. The time mean of the refractive index squared for ($\overline{u} < 0.5\ m.s^{-1}$) condition is 600. Based on this analysis I assume that any refractive index squared larger than 600 at any time and space refers to the critical line where wave breaking occurs and waves are absorbed. This condition often happens in the upper troposphere/lower stratosphere where westerlies become weak in the winter season near the Arctic.

In the study of (Li et al. (2007)) all the positive value of the $n^2_{k,l}(y,z,t)$ are equally important for the final $n^2_{k,l}(y,z)$ as if small and very large positive values of the $n^2_{k,l}(y,z,t)$ are equally favorable places for wave propagation. Therefore in the study of (Li et al. (2007)) the effect of the critical line on the Rossby wave propagation is neglected. As discussed earlier very high values of the $n^2_{k,l}(y,z,t)$ are not necessarily favorable conditions for the Rossby wave propagation. As I will show, this function gives us an improved picture of planetary wave propagation condition (based

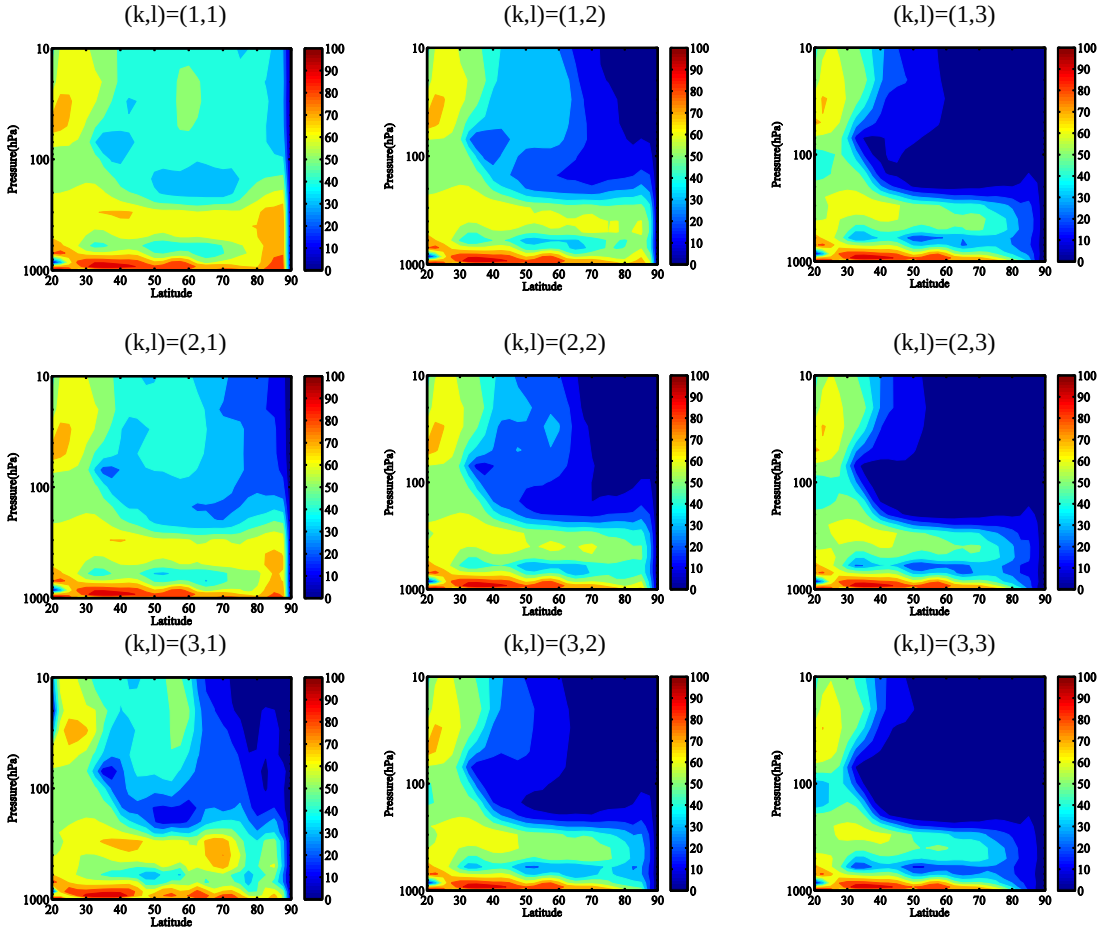

Figure 4.3: Climatology of the probability of favorable propagation condition for Rossby waves derived from 50 winters (1961-2010) in the Northern hemisphere. The higher the values, it is easier for planetary waves to propagate to that regions. In contrast, planetary waves tend to propagate away from regions of low values of this quantity. The figure is taken from (Karami et al. (2016)).

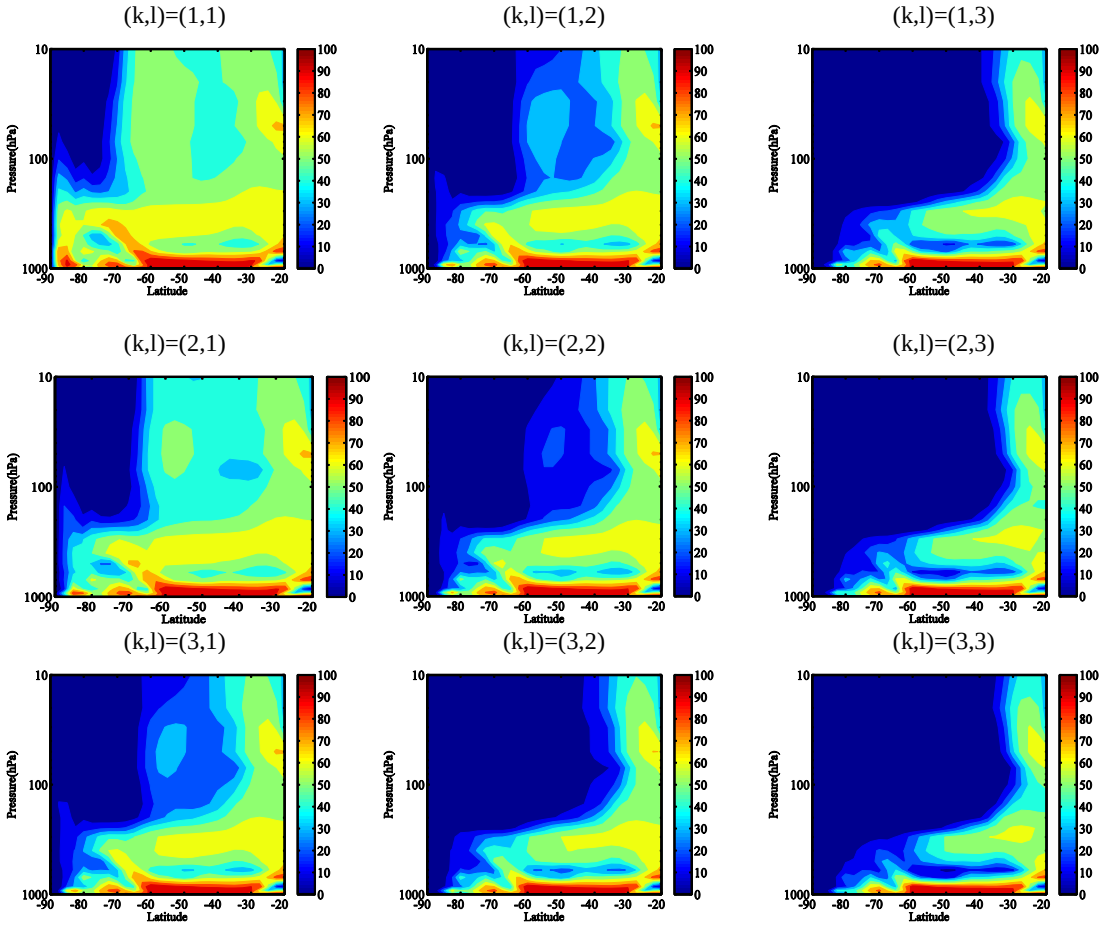

Figure 4.4: Climatology of the probability of favorable propagation condition for Rossby waves derived from 50 winters (1961-2010) in the Southern hemisphere. The higher the values, it is easier for planetary waves to propagate to that regions. In contrast, planetary waves tend to propagate away from regions of low values of this quantity. The figure is taken from (Karami et al. (2016)).

on criteria listed in Table 3.1). Higher values of $Pr_{Ro}(y, z)$ provide a window of opportunity for planetary waves to propagate at any latitude and height. Likewise, smaller values of this quantity demonstrate the places where Rossby waves propagate away from these regions.

The climatology of the probability of favorable propagation condition for Rossby waves for different zonal wavenumbers (k=1, 2, 3) and meridional wavenumbers (l=1, 2, 3) for the Northern hemisphere winter season are presented in Fig. 4.3. It is evident from Fig. 4.3 that the most common characteristics of favorable condition for wave propagation for all wavenumbers is that the most favorable propagation condition is in the lower troposphere of the mid-latitude region. It is also important to mention that this features are independent of determining factors for Rossby wave generation and explain how the waves, when generated, would propagate given the structure of the mean flow. Our analysis show that the region of highly favorable Rossby wave propagation condition and the source region for wave generation (due to land-sea contrasts, sea surface temperature anomalies and topography) are coincident. It is also evident that longer waves have more chance to penetrate to the stratosphere from the troposphere compared to the smaller waves. Similar to Fig. 4.3 the climatology of the probability of the favorable condition for Rossby wave propagation for the Southern hemisphere is presented in Fig. 4.4. Similar to the Northern hemisphere, all large scale waves have a rather large chance to propagate in the troposphere in winter. It is also evident in both Fig. 4.3 and Fig. 4.4 that the larger the waves, the probability of favorable condition for them to propagate upward are larger.

By using ray tracing technique (which is a technique for calculating the path that waves will travel or propagate through a medium with varying features such as different absorption characteristics and different reflection fatures) Karoly and Hoskins (1982) showed that Rossby waves tend to refract toward larger refractive index squared. In other words it is easier for Rossby waves to propagate to the regions with positive refractive index and avoids regions with negative refractive index. Another important results obtained from the study of (Karoly and Hoskins (1982)) is that Rossby waves have a tendency to propagate along great circles and most of the upward propagation of Rossby waves will be refracted toward the equator (even if the refractive index squared were positive at all height in their study). Our results confirm the results of (Karoly and Hoskins (1982)) because I found a a channel or waveguide of large probability of favorable propagation condition for Rossby waves. The strong westerlies act as a waveguide of Rossby waves and direct them vertically through the tropopause and allow them to penetrate to higher altitudes from their source region (troposphere). This waveguide or channel for the upward propagating waves are south of 40 °N in the wintertime of the Northern hemisphere and are indicated by regions where $Pr_{Ro}(y, z) > 50$. This waveguide is narrower for larger

wavenumbers and is wider for smaller wavenumbers.
Another important results of (Karoly and Hoskins (1982)) is that Rossby waves tend to propagate on the edges of strong westerlies and avoid penetrating through the polar night jet. Our results also confirm this fact because north of 60°N and above 200 hPa, the probability of favorable condition for Rossby waves show relatively smaller values, comparing to similar altitude ranges between 30°N and 50°N. The maxima south of 40°N at 100 hPa in the mPDF shows that the region is favorable for wave propagation. The vertical component of EP fluxes (Fig. 3.7) that have small magnitudes in these regions confirm these results.

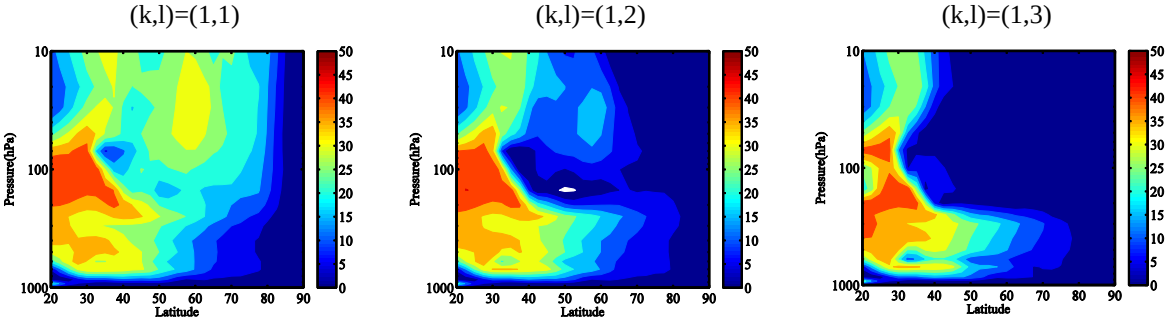

Figure 4.5: The differences between the probability of positive refractive index squared (Fig. 3.5) and the probability of favorable propagation condition of stationary Rossby waves (Fig. 4.3) in the Northern hemisphere for k=1, l=1,2,3. The figure is taken from (Karami et al. (2016)).

The differences between probability of positive refractive index (Fig. 3.5) and the probability of favorable propagation condition of stationary Rossby waves (Fig. 4.3) in the Northern hemisphere for zonal wavenumber=1 and different meridional wavenumbers is presented in Fig. 4.5. It can be seen that the maximum of the differences are found between 20-40°N of the middle and upper troposphere which can reach to 50%. Small positive values of the refractive index squared which is consistent throughout the winter season leads to this unsatisfactory result.
Now I concentrate on the differences of $Pr_{Ro}(y, z)$ between Northern and Southern hemispheres. A theoritical explanation of the vertical propagation of Rossby waves from the troposphere to the stratosphere by (Charney and Drazin (1961)) predicts that the strong polar night jet of the Southern hemsiphere during winter blocks most of the upward wave propagation. Our analysis are consistent with the theoritical explanation of (Charney and Drazin (1961)) because in the high latitudes of the stratosphere, for zonal wavenumber=1 there is a good chance for wave propagation

in the Northern hemisphere ($Pr_{Ro}(y,z) > 40\%$). In the Southern hemisphere the probability for the upward wave propagation is smaller compared to the Northern hemisphere. As discussed in Chapter 1 the zonal mean zonal wind should be weaker than a critical strength for upward propagation of Rossby waves. The strong polar night jet of the Southern hemisphere is too strong to support the upward wave propagation.
In the time mean of the refractive index squared, it is difficult to study the role of meridional wavenumbers on the wave propagation. For instance, in the Southern hemisphere, the difference between the time mean of $n^2_{k,l}(y,z)$ for wave (2,1), (2,2) and (2,3) in the stratosphere (above 100 hPa) is not large which is one of the unsatisfactory results of time mean of $n^2_{k,l}(y,z)$. However the results obtained from the analysis of the $Pr_{Ro}(y,z)$ are promising because one can easily understand the differences of $Pr_{Ro}(y,z)$ for different meridional wavenumbers with an identical zonal wavenumber. For instance, at the same latitude range of the Southern hemisphere,$Pr_{Ro}(y,z)$ values are as high as 45% for wave (2,1) in mid-latitudes of stratosphere, while the $Pr_{Ro}(y,z)$ values reach to less than 5% for wave (2,3).

4.2 Rossby Wave Packets

A Rossby Wave Packet (RWP) is defined as a region of high-amplitude meandering flow in the upper troposphere that in the mid-latitudes travel in coherent wave train structures or wave packets (Chang (2005)). In analogy to the electromagnetic wave propagation, gradients of the potential vorticity act as a waveguide to reduce meridional dispersion of the RWPs and make the long longitudinal propagation possible. RWPs follow the storm tracks and hence any changes in their location or intensity reflect changes in the storm tracks (Blackmon et al. (1984), Maritus et al. (2010), Chang (2005)). Large-scale regime changes, extreme weather events and more importantly model errors and uncertainties have been linked to the RWPs (Hakim (2005), Li and Lau (2012), Maritus et al. (2008)). Since much of the wave mean-flow interactions occur within RWPs (Chang (2005)), therefore both poleward-breaking and equator-ward breaking waves are associated with the significant RWPs (Maritus et al. (2007)).
The equation governing the evolution of the Eddy Kinetic Energy (EKE) as presented by (Chang (2001)) contains five terms:

$$\frac{\partial K}{\partial t} = -\nabla.(vK + v_a\phi') - \omega'\alpha' - [v.(v_3.\nabla_3)\overline{v} - v'.(\overline{v'_3.\nabla_3)v'}] - [\frac{\partial}{\partial p}\omega K + \frac{\partial}{\partial p}\omega'\phi'] + Res.$$
$$Term\ A \quad , \quad Term\ B \quad , \quad Term\ C \quad , \quad Term\ D \quad , \quad Term\ E \tag{4.4}$$

where K is the eddy kinetic energy. In this equation the eddy is defined as deviation from the time mean flow. The local advection of EKE and divergence of eddy geopotential height ϕ' by the ageostrophic wind (v_a) are represented in Term A. Conversion of eddy available potential energy to eddy kinetic energy through baroclinic growth (cyclogenesis) is represented in Term B. This term is usually called boroclinic conversion term. Barotropic conversion of mean kinetic energy and eddy EKE through eddy momentum flux is presented in Term C. The local advection of EKE and divergence of eddy geopotential height (ϕ') by the ageostrophic wind (ω_a) are represented in Term D. Therefore Term A and Term D are similar except Term D and Term A refers to the transfer of kinetic energy vertically and horizontally respectively. Therefore, equation (4.4) explains the sources and sinks of EKE. The results obtained by (Chang (2001)) show that Term B is an important factor for the formation of RWPs due to the development of RWPs after an intense baroclinic eddy. Friction (Term E) (in the absense of baroclinic growth) acts to weaken the EKE and may result in dissipating of the RWP. Term D (vertical energy flux) usually play a minor role in the time evolution of EKE (Chang (2001)).
At the end of storm-tracks (east coasts of Pacific and Atlantic oceans) the baroclinic growth (Term B) becomes negative and the waveguide weakens resulting in dissipating RWPs. Term B is large in regions that are favorable for cyclogenesis. Therefore RWPs tend to develop near the western Pacific and Atlantic oceans and dissipate near their eastern boundaries. Some RWPs may travel from one storm-track to another, though the regions between two storm-tracks might not be favorable for propagation of RWPs. A strong waveguide is required for the downstream development of RWPs from one strom-track to another.

Now we concentrate on the identification of the Rossby wave packets. The interest for extracting wave packets from observational data and tracking RWPs have attracted much attention since the time of discovery of the fact that Rossby waves play an important role in day-to-day weather variabilities in the midlatitude extratropics (Zimin et al. (2003)). The oldest technique to study the propagation of synoptic-scale waves was the Hovmöller diagram proposed by (Hovmöller (1949)) that considers time evolution of troughs and ridges. The Hovmöller diagram is a time-longitude diagram of an atmospheric variable (often geopotential height or meridional wind) which is averaged over a latitude band. In the Hovmöller diagram a series of positive and negative values in a diagonal direction are considered as a signature of a propagating wave packets. Though production of Hovmöller diagrams is straightforward, it fails at detecting the two-dimensional horizontal structure of the wave packets (Zimin et al. (2003)).
Zimin et al. (2003) proposed a powerful technique for extracting the envelope of atmospheric wave packets that is not affected by the Hovmöller diagram problem. The

technique is a well-known technique of digitial signal processing known as Hilbert transfrom technique which is used for extracting the envelope of atmospheric wave packets from meridional wind.
The Hilbert transform technique consists of three steps. First we calculate the Fourier tranform of the function $(v(x))$:

$$\hat{v}_k = \frac{1}{N}\sum_{l=1}^{N} v(\frac{2\pi l}{N}) e^{\frac{-2\pi i k l}{N}} \qquad and \qquad k = -\frac{N}{2}+1, ..., \frac{N}{2}. \tag{4.5}$$

where $(v(x))$ is a function that is considered on an equidistant grid in any given latitude circle and $0 < x \leq 2\pi$. for any even integer of N, the grid points are located at $x = \frac{2\pi l}{N}$ and $l = 1, 2, ..., N$. Afterward, we calculate the inverse Fourier transform of a selected band $(0 < \mathrm{k}_{min} \leq k \leq k_{max})$:

$$w(\frac{2\pi l}{N}) = 2\sum_{k=k_{min}}^{k_{max}} \hat{v}_k e^{\frac{2\pi i k l}{N}} \tag{4.6}$$

and finally envelopes of wave packets can be calculated by the following equation:

$$A(\frac{2\pi l}{N}) = |w(\frac{2\pi l}{N})| \tag{4.7}$$

The Hilbert transform technique is a filter that maintains only the desired wavenumber components.
Here we present two examples to demonstrate the application of Hilbert transform technique in extracting the envelopes of any given artificial signal. Figure. 4.6 shows two analytical examples of a given function represented by blue lines, $v(x)$, that consists of two wave packets with carrier wavenumbers 4 and 9. The red lines represent the envelopes of wave packets $(A(x))$.
Another example of extracting Wave Packet Amplitude (WPA) of RWPs from a real atmosphere is the major storm of January 2000 which hits the east coast of USA on 25-26 January 2000. The method for extracting WPA is based on a filtering of meridional wind at 300 hPa using a Hilbert transform technique and isolating synoptic waves (wavenumbers 4-11) along time mean stream lines (using zonal and meridional winds). Figure 4.7 shows a horizontal map of meridional wind (shaded in m/s) and 300 hPa geopotential height (every 40 dam starting at 840 dam). The time evolution of WPAs are shown in the right column. In this example the Interim European Center for Medium-Range Forecast Reanalysis (ERA-Interim) data are used to track the RWPs.
Rossby wave packets are very common in both Northern and Southern hemispheres. Souders et al. (2014b) reported that they have observed nearly 6000 RWPs globally from 1979-2010. Therefore the frequency of RWPs are about 200 yr^{-1}. They also reported that the probability of extreme RWPs occurrence (exceeding 45 $m.s^{-1}$) are

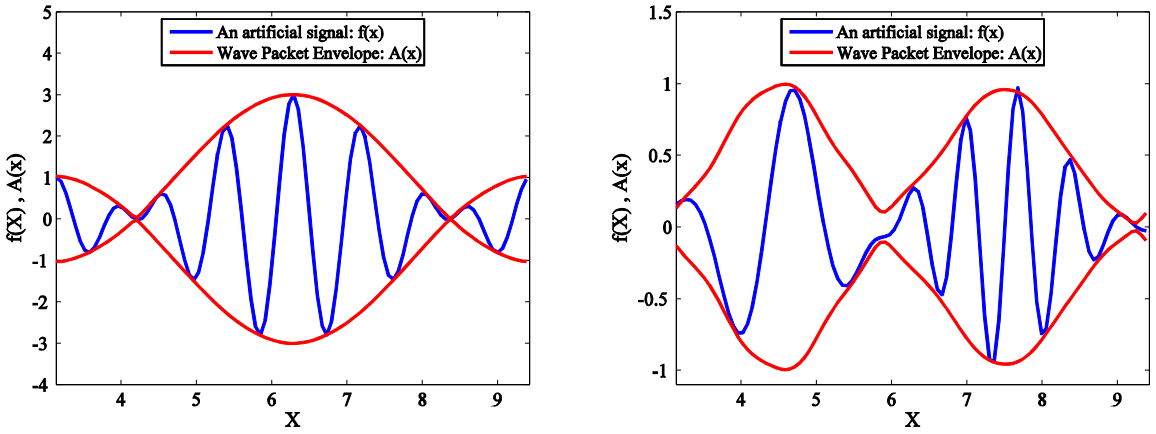

Figure 4.6: Two analytical examples of a given function represented by blue lines, $v(x)$, that consists of two wave packets with carrier wavenumbers 4 and 9. The red lines represent the envelopes of wave packets ($A(x)$). $v(x)$ are taken from (Zimin et al. (2003)).

higher in the Northern hemisphere compared to the Southern hemisphere (13 out of 19 extreme RWPs are in the Northern hemisphere).

4.3 Storm-Tracks

Eastward traveling, synoptic-scale ($\sim$ 1000 km) successive high and low pressure systems are responsible for much of the day-to-day weather variability in the mid-latitudes. Therefore their geographical locations, frequency of occurrences and magnitude were a topic of active research for a long time (Chang et al. (2002)). The preferred paths for the traveling cyclones are historically called storm tracks. The global distribution of storm activity as it was perceived in the ninteenth century is presented in Fig. 4.8. The regions of highest storm frequency are indicated by pink colors. The trajectories of the storms are indicated by arrows. Though, a primitive attempt for providing a global distribution of storms by (Hinman (1888)) failed to make a distinction between warm core tropical hurricanes and cold core extra-tropical baroclinic systems, however several features similar to the up-to-date synoptic map of the geographical distribution of storm occurrence frequency can be inferred from this primitive attempt (Chang et al. (2002)). For instance, a maximum in cyclone activity is found from east China across the Pacific ocean to the west of USA; a second maximum in occurrence extends from North America (eastern Rocky mountains) across the Atlantic toward northern Europe which gets weaker toward central Asia; a third relatively weak maxima in cyclone activity is extended over

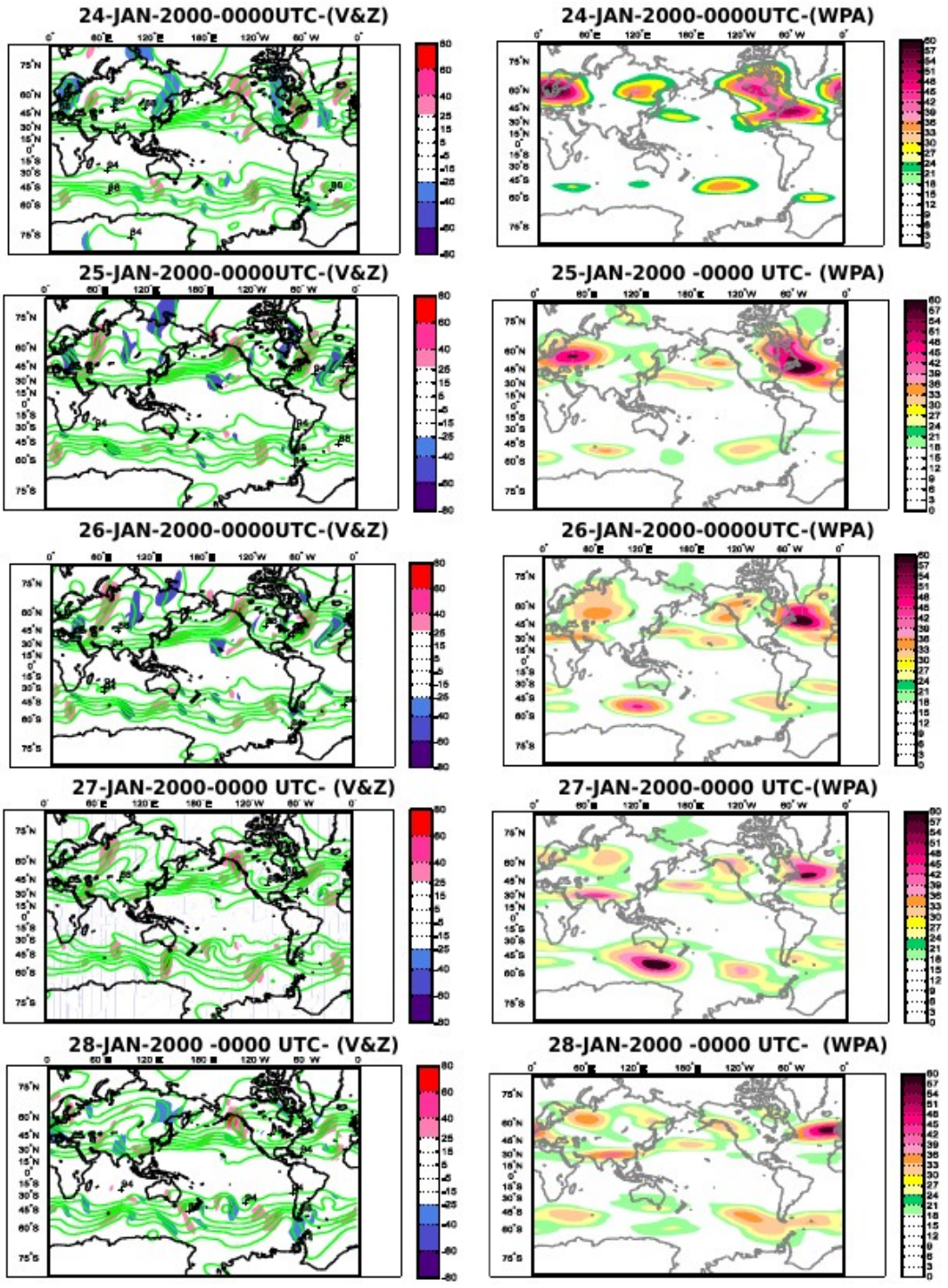

Figure 4.7: The major storm of January 2000 hits the east coast of USA on 25-26 January 2000. Left: A horizontal map of meridional wind (shaded in m/s) and 300 hPa geopotential height (every 40 dam starting at 840 dam). Right: Time evolution of WPAs (for wavenumbers 4-13). Since Rossby waves play a key role in shaping weather in the midlatitude extratropics, capability of tracking RWPs is crucial for understanding the regional climate variability. For this study ERA-Interim data are used. The meridional wind values are between $-80 < v < 80\ m.s^{-1}$ and the WPAs are between $0 - 60\ m$.

the Miditerranearn shading to a weaker activity in the middle east and central Asia. Since there is a strong connection between changes in the storm-tracks and day-to-day weather variability, any changes in either their location or the magnitude of the storm activity will lead to substantial anomalies in the precipitation. Storms are important elements of the atmospheric moisture transport in the Earth's atmosphere that give rise to different weather patterns (from deserts in the subtropics to wet stormy weather in the mid-latitudes). In response to any poleward or equatorward shift of the storm tracks, the Earth's major climatic zones will be dictated to shift in a concurrent manner with huge socio-economic consequences. In the next section a mathematical explanation for the generation of eddies (or alternatively waves or cyclones) in the mid-latitudes will be presented.

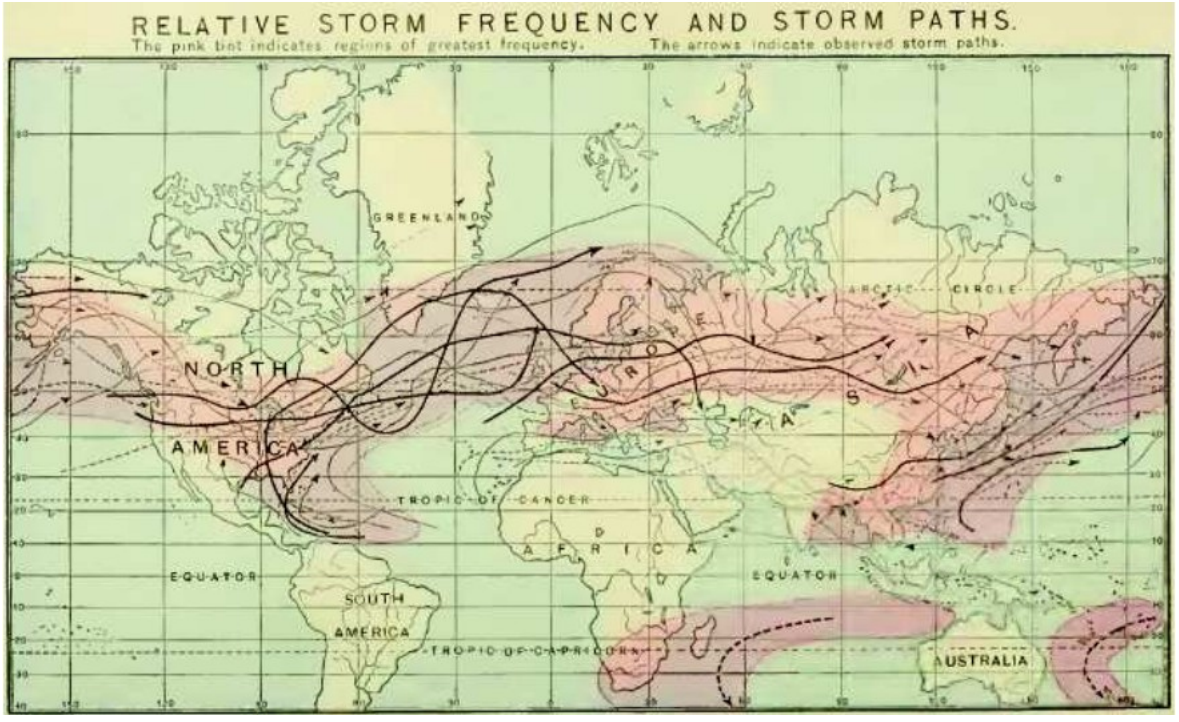

Figure 4.8: Relative Storm frequency and storm path as it was perceived in the nintheenth century from (Hinman (1888)). The regions of highest storm frequency are indicated by pink colors. The trajectories of the storms are indicated by arrows. The figure is taken from (Seland (2009)).

The Eady growth rate shown in the previous section show two distinct favorable regions for the development of the eddies in the mid-latitudes. These regions are called Pacific and Atlantic storm-tracks. The Pacific storm-track extends from the middle of Asia to the middle of the Pacific ocean and the Atlantic storm-track stretches from the east coast of the North America to the middle of the North Atlantic ocean.

These storm-tracks are formed near to the regions where the local sea-land temperature differences are the highest locally.

Hoskins and Valdes (1990) defines the exit regions of the storm-tracks as regions where the Eady growth rate is minimum. Therefore the eastern ends of the Pacific and Atlantic oceans are the exit regions of the storm-tracks. These regions are not favorable for the cyclogenesis.

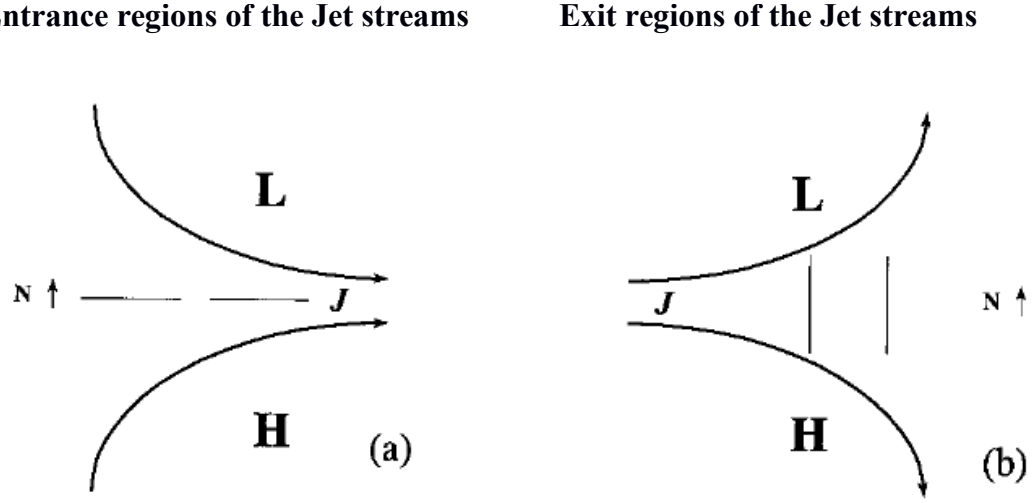

Figure 4.9: A schematic view of the typical stretching deformation in the mid-latitudes jet stream. (a): Entrance regions of the jet stream, (b): Exit regions of the jet stream. The figure is taken from Black and Dole (2000).

In addition to the baroclinicity which is crucial for the storm-tracks formation, there are other parameters that controls the structure of the storm-tracks. Black and Dole (2000) show that baroclinicity and barotropic deformation have nearly the same order of importance for the structure of the storm-tracks. The barotropic deformation is defined as follows:

$$D = D_1 + D_2 \qquad where \qquad D_1 = \frac{\partial u}{\partial x} - \frac{\partial v}{\partial y} \qquad , \qquad D_2 = \frac{\partial v}{\partial x} + \frac{\partial u}{\partial y} \tag{4.8}$$

where D is the total deformation and D_1 and D_2 are stretching and shearing deformations respectively (Martin (2006)). According to the equation (4.8) deformation is the change in the structure of the flow with regard to the local changes in the velocity fields. Figure. 4.9 illustrates the typical stretching deformations in the mid-latitudes jet streams. In both entrance and exit regions of the jet stream stretching deformation is important. In the core of jet stream shearing deformation is more important than the stretching deformation. In the entrance regions of the jet stream the stretching deformation acts to stretch the eddies in the zonal direction. In the exit regions of the jet stream the stretching deformation acts to stretch the eddies in

the meridional direction. The shearing deformation which is important in the core regions of the jet acts to tilt the eddies in northwest-southeast direction north of the jet and in the southwest-northeast direction south of the jet.
Maintenance of the storm-tracks are attributed to two different mechanisms namely orography and diabatic heating (Hoskins and Valdes (1990), Broccoli and Manabe (1992)). Accordign to (Hoskins and Valdes (1990)) the latent heat releases from the cyclones within the storm-tracks are responsible for the amplification of the baroclinicity in the storm-tracks region. Another mechanism that is responsible for the maintenance of the storm-tracks is the enhancement of the western Pacific and Atlantic current (Kuroshio currents and Gulf Stream respectively) due to the cyclones within the storm-tracks. From this viewpoint the storm-tracks are slef-maintained. The study of (Broccoli and Manabe (1992)) show that in the presense of mountains storm-tracks are more asymmetric. This is in contrast with the self-maintained view of the storm tracks because orography-induced variation in the storm-tracks are not necessarily a local forcing to the storm-tracks. For instance a remote mountain from the Pacific or Atlantic storm-tracks might induce a great difference in the structure of the storm-tracks.
The main source of the storm-tracks destruction is the surface friction. At the termination regions of the storm-tracks (east coast of Pacific and Atlantic oceans) the areas of enhanced surface friction act as a energy drain of baroclinic waves. Another important mechanism for the loss of energy of baroclinic waves within the storm-tracks is the deformed zonal flow due to the decelerated jet near the exit regions. Both mechanisms act as an hindrance for the baroclinic waves to gain energy from the mean flow (Chang and Orlanski (1993)).
Here we provide a climatology of the RWPs using WPA and their spatial and temporal distribution in the Northern and Southern hemispheres. Souders et al. (2014a), Souders et al. (2014b) based on method presented by (Zimin et al. (2003), Zimin et al. (2006)) suggest that the annual probabilities of WPA higher than a certain threshold (exceeding 30 $m.s^{-1}$) is closely tied to the midlatitude storm-tracks. I use the same criterion for identifying storm-tracks in midlatitudes during different seasons. The seasons in this chapter refer to seasons in the Northern hemisphere.

Figure. 4.10 shows the probability of significant WPA per grid cell during winter and spring seasons. During winter seasons three major storm-tracks can be observed globally. North Pacific, North Atlantic storm-tracks in the Northern hemisphere and Southern Indian ocean in the Southern hemisphere are major storm-tracks globally. It can be seen that a high level of interaction between Pacific and Atlantic storm-tracks exists during winter season. While the Pacific storm-tracks are relatively horizontal, the Atlantic storm-track has a tilt toward the southwest-northeast direction. It is important to mention that in both entrance and exit regions of the

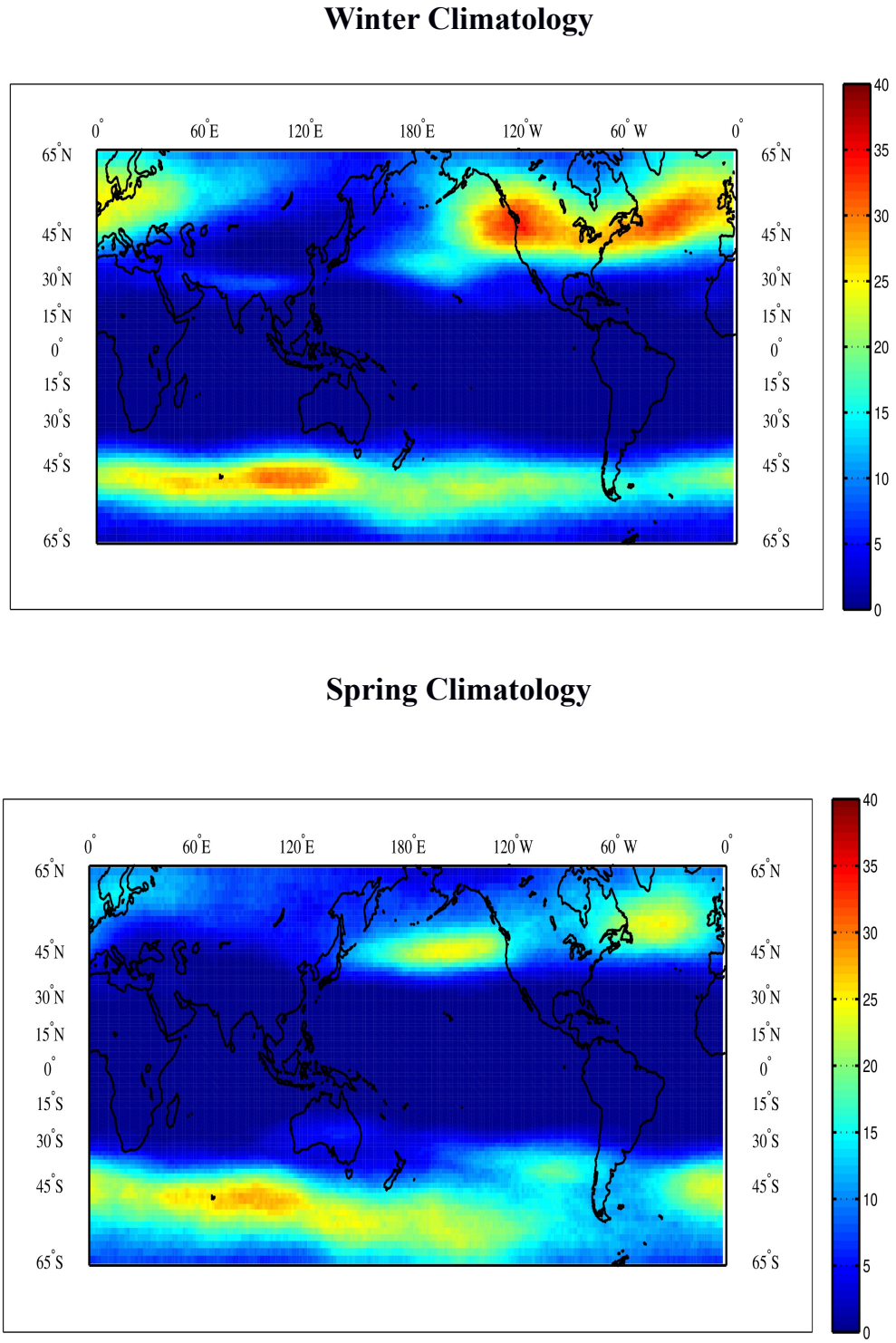

Figure 4.10: The probability of significant WPA per grid cell during winter and spring seasons. During winter seasons three major storm-tracks can be observed globally. North Pacific, North Atlantic storm-tracks in the Northern hemisphere and Southern Indian ocean in the Southern hemisphere are major storm-tracks globally.

storm-tracks stretching deformation is important. In the core of storm-tracks shearing deformation is more important than the stretching deformation. In the entrance regions of the storm-track the stretching deformation acts to stretch the eddies in the zonal direction. This effect is more pronounced in the Pacific storm-track than in the Atlantic storm-track. In the exit regions of the storm-track the stretching deformation acts to stretch the eddies in the meridional direction. The shearing deformation which is important in the core regions of the jet stream acts to tilt the eddies in northwest-southeast direction north of the jet and southwest-northeast direction south of the jet. This effect is more pronounced in the Atlantic storm-track than in the Pacific storm-track. During autumn the level of interaction between Pacific and Atlantic storm-tracks are higher than in the spring.
Figure. 4.11 show the probability of significant WPA per grid cell during summer and autumn seasons. The main difference between storm-tracks in the Southern hemisphere and Northern hemisphere is that the Southern Indian ocean storm-track is relatively active throughout the year. However the Northern hemisphere storm-tracks show a significant intraseasonal variability. The Southern Indian ocean storm-track is relatively continuous due to the less topographic barriers in the Southern hemisphere compared to the Northern hemisphere. A notable minimum of RWPs activity can be observed during summer season in the Northern hemisphere. The reduction in the RWP activity is less prounounced during summer season in the Southern hemisphere. A continued presence of strong baroclinicity close to the circumpolar jet near Antarctica, which favors a relatively active Southern Indian ocean storm track and RWPs even during the austral summer is the main reason for a year-round active RWPs activity in the Southern hemisphere (Souders et al. (2014b)).
The Pacific storm-track is more active during autumn compared to the spring. The southwest-northeast tilt of the Pacific storm-track is less pronounced during spring compared to the autumn. A so-called midwinter suppression of the North Pacific storm-track (Nakamura (1992)) can be observed. During winter season in the North Pacific region, the formation rate of baroclinic eddies remain nearly similar to the Atlantic region. However the amplitude of the wave packets decrease in this region (Souders et al. (2014b)).
A split in the storm-track near the Tibetan Plateau is observed during winter season. Some RWPs tend to propagate equatorward due to a waveguide in the southern Asia that allows the coherent propagation of RWPs across middle east. This particular feature is absent in other seasons.

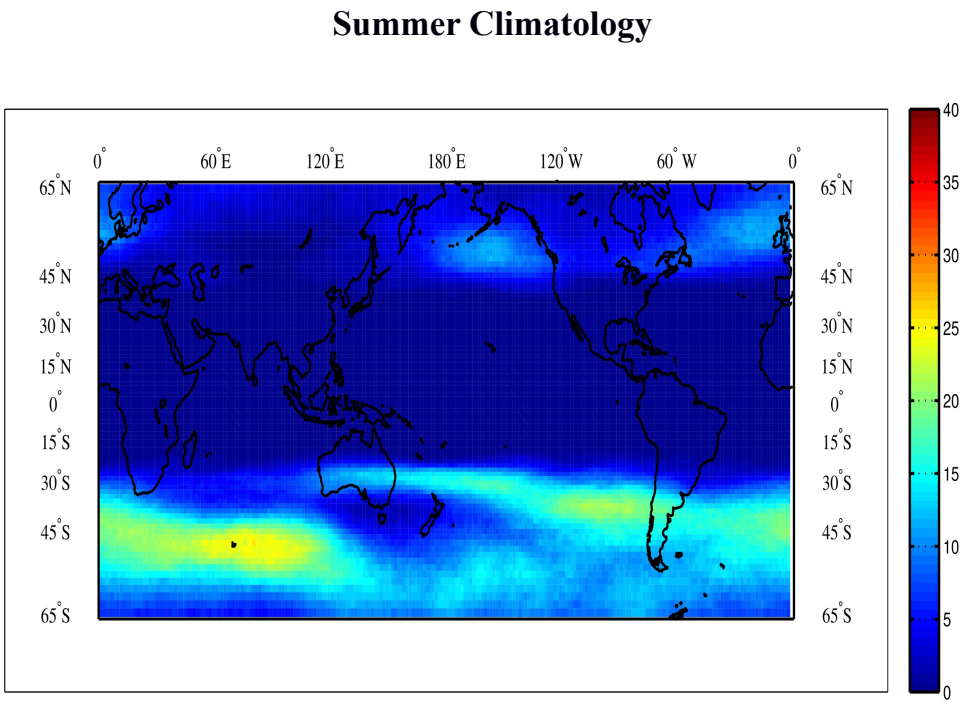

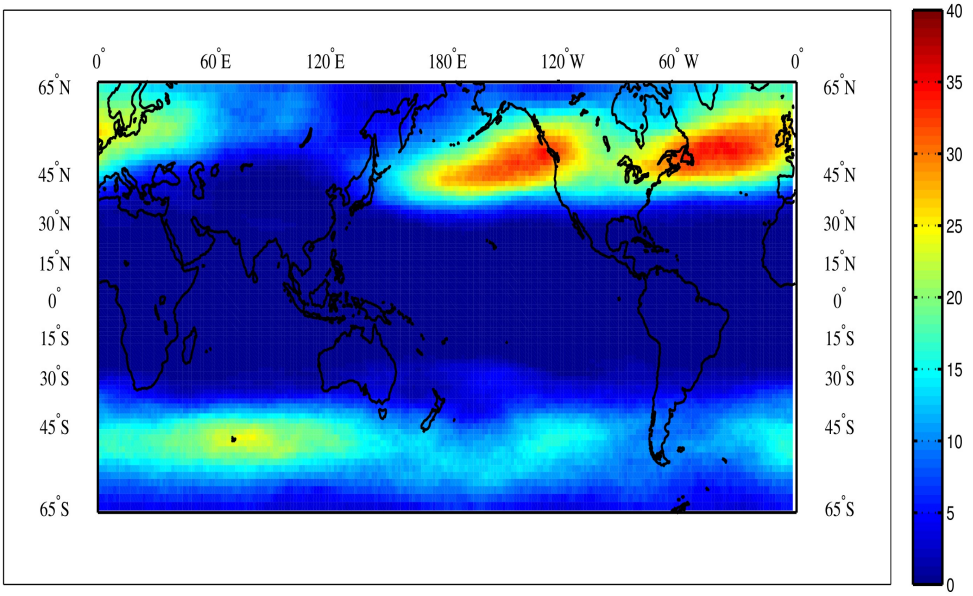

Figure 4.11: Same as Fig. 4.5 for summer and autumn seasons.

5 Thermal and Dynamical Responses of the Middle Atmosphere to the Solar and Geomagnetic Variabilities

In this chapter by using idealized model runs, we investigate the role of geomagnetic and solar forcing on the middle atmospheric temperature, wind and wave forcing. A specific research question that we investigate is whether the confined ozone changes in the middle atmosphere due to geomagnetic and solar activities can trigger large-scale dynamical anomalies.

5.1 Direct radiative impact of ozone depletion

The submodel FUBRAD is used to calculate the direct radiative impact of ozone depletion scenarios. The standard submodel for radiation in EMAC is RAD4ALL which is a reimplementation into the MESSy standard of the ECHAM5 radiation code. Nissen et al. (2007) developed the sub-submodel RAD4ALL-FUBRAD for the EMAC model. The main purpose of this work was a better representation of the solar cycle (which needs higher spectral resolution) in EMAC. FUBRAD has 49 bands for calculating short and long wave heating rates, ranging from 121.5-683 nm which takes into account the relevant radiative processes in the stratosphere and mesosphere (Table 5.1).

The absorption of short wave by ozone is weakly temperature dependent. However, long term (more than a few days) changes in the long wave radiation due to imposed ozone variation depends significantly on temperature variation. Here we try to separate the processes relevant for the thermal and dynamical changes in the model simulations. This approach is discussed in Langematz et al. (2003). I separate the direct radiative forcing from the dynamical forcing in the following way; we compare

Table 5.1: FUBRAD wavelength intervals in the shortwave radiation above 70 hPa.

Band	Gas	Wavelength (nm)	Number of intervals
Lyman-alpha	O_2	121.6	1
Schumann-Runge continum	O_2	125.0-175.0	3
Schumann-Runge bands	O_2	175.0-205.0	1
Herzberg cont./Hartley bands	$O_2/O3$	206.2-243.9	15
Hartley bands	O_3	243.9-277.8	10
Huggins bands	O_3	277.8-362.5	18
Chappuis band	O_3	407.5-682.5	1
			Total=49

the initial heating rates stored at the first output time step of the experiments after a day of integration. Since the radiative relaxation time (the time required for the adjustment of the atmosphere to any radiative forcing) is about 3-7 days in the upper stratosphere and about 20 days in the lower stratosphere, therefore a time interval of a day is reasonably too short for the atmosphere to adjust thermally to the imposed radiative forcing (due to ozone-depletion scenarios). Furthermore, within a day the dynamical heating rate's impact on the long wave heating rate is negligible Brasseur (2005). The characteristic time period of planetary wave at mesospheric and lower thermospheric altitudes are comparable to relaxation times in this altitude range (Karami et al. (2012)). Therefore for higher long wave integration over time especially more than 2 days, planetary wave periods and relaxation times are comparable in this region which implies a strong damping (depositing of heat and momentum) of Rossby waves. Therefore we interpret the changes in the long wave cooling rate as a direct result of radiative forcing due to the imposed ozone depletion.
Figure 5.1 shows the initial change to the short wave heating rate due to the imposed ozone depletion. As expected, only the sun-lit region is affected due to the prescribed ozone anomalies. It is also evident that the differences in short wave heating rates in both hemisphere have similar features. A potential source of different short wave heating rate responses in the Northern and Southern hemisphere might be different climatological ozone in hemispheres (we apply relative changes). Figure 5.1 shows that the strongest short wave heating rate changes occur in the

stratopause and upper stratosphere regions. At the terminator, however, the short wave heating rate differences vanish. In early NH spring (April) all latitudes in the lower stratosphere are affected by the ozone depletion, since all latitudes around this height are sunlit. The imposed ozone deficit in the lower stratosphere of the SH leads to short wave heating rate reduction of about $0.2K.day^{-1}$. An enhanced absorption of solar radiation in the upper stratosphere and mesosphere, which has not been absorbed above due to ozone deficit, leads to the local heating in these regions. This feature is most pronounced in June of the SH and December of the NH.

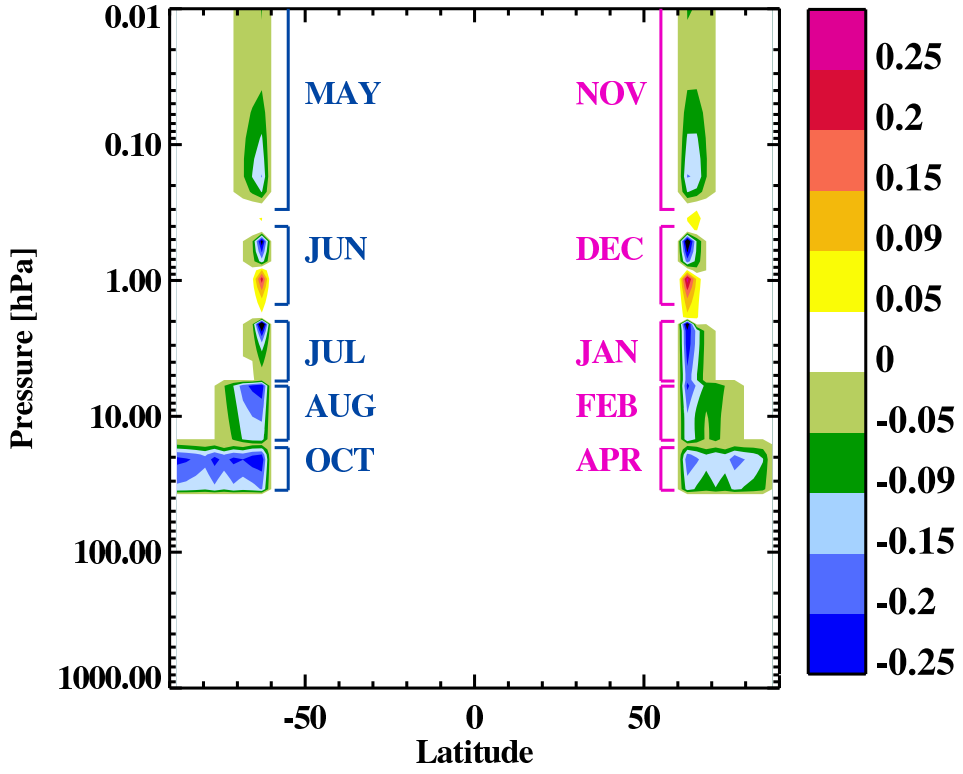

Figure 5.1: The initial change to the short wave heating rate due to the imposed ozone depletion scenarios. The units are in $Kday^{-1}$. The figure is taken from Karami et al. (2015b).

Figure 5.2 shows the initial change to the long wave heating rate due to the imposed ozone depletion. Since the distribution of radiative heating rate depends on both the distribution of ozone and outgoing long wave radiation, therefore the differences of the initial change to the long wave heating in the NH and SH are small. The long wave heating rate changes show an apposite behavior above and below the stratopause region. This behavior is contrary to the cooling effect of the imposed ozone depletion due to less short wave absorption. In the upper stratosphere and mesosphere a relative warming due to less ozone is found. This result is expected

because in these altitudes ozone locally emits long wave radiation and cools the atmosphere, therefore less cooling due to less ozone results in a relative warming. The lower stratosphere, however, cools weakly due to ozone depletion up to $0.1 K.day^{-1}$. The main reason for this cooling is because less ozone absorbs less outgoing long wave radiation and leads to a relative cooling. Therefore the net radiative heating rate at high latitudes is dominated by a warming effect due to the long wave component in the upper stratosphere and mesosphere, where the effect of short wave heating in the dark wintertime polar region is small. In the lower and middle stratosphere, both short wave and long wave heating rates contribute to a local cooling effect.

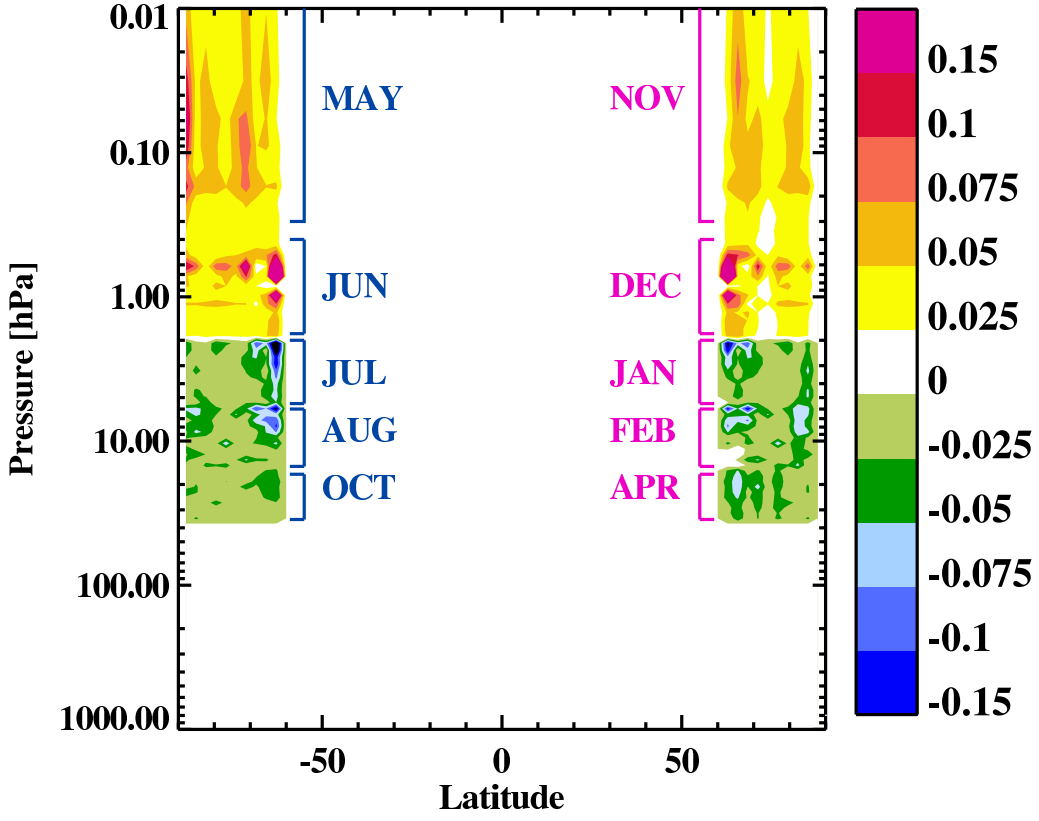

Figure 5.2: Same as Fig. 5.1 for the long wave heating rate. The figure is taken from Karami et al. (2015b).

5.2 Temperature and zonal wind response to imposed ozone anomalies

In order to show the impact of the imposed ozone anomalies on temperature and zonal wind, composite analyses are performed. In all of our analyses multi-year monthly means of zonally averaged temperature and zonal wind are calculated. The analyzed area is from tropics to poles of both hemispheres in the meridional-vertical

cross section. The differences between the control run and the ozone-perturbed simulations are compared with the inter-annual variability of the control simulation to investigate the significance of the temperature and zonal mean zonal wind responses to the imposed ozone anomalies.

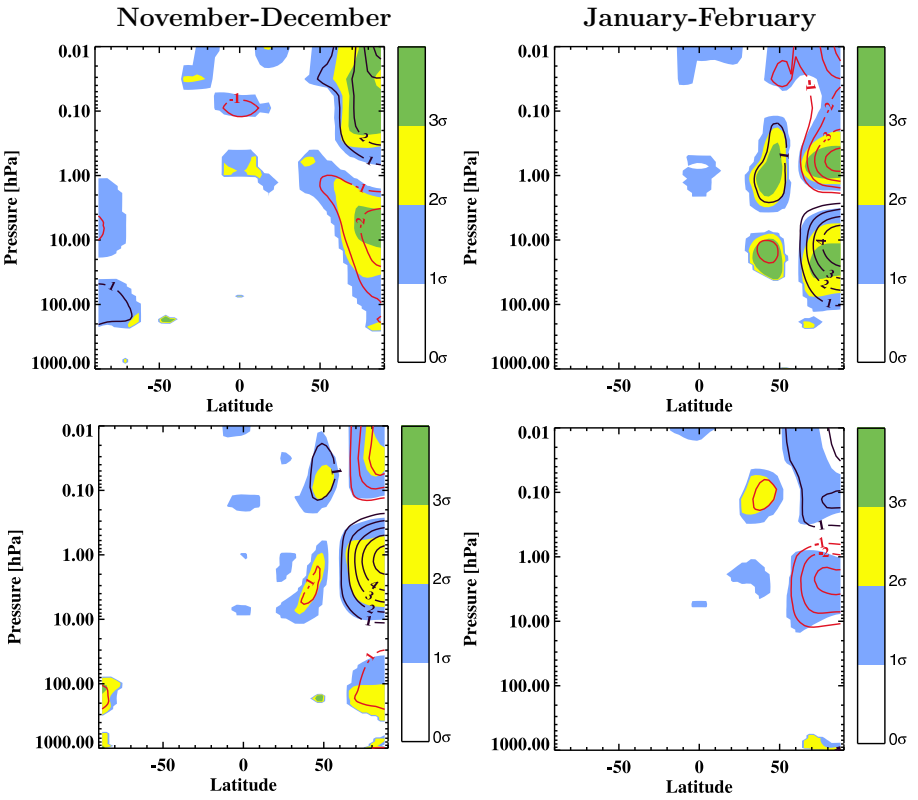

Figure 5.3: Monthly mean temperature changes between $(\Delta O_3 - NH)$ scenario and control run for November, December, January and February. Contour values represent the monthly mean zonal mean temperature differences and shaded areas denote the significance level. The contour interval is 1 K. Red contours show negative temperature anomaly while positive temperature anomalies are shown in black contours. The figure is taken from Karami et al. (2015b).

A meridional cross section of the monthly mean temperature changes between control run and $(\Delta O_3 - NH)$ scenario for NH winter months is shown in Fig. 5.3. The shaded regions denote the significance levels and the differences in monthly and zonal mean temperatures are denoted by contour values. The contour interval is ± 1 K.

At mesospheric altitudes of the NH polar region in November a statistically significant positive temperature anomaly is found. The magnitude of this positive temperature anomaly is about 4 K. In the same month, a statistically significant negative temperature can be seen in the stratosphere. This negative temperature anomaly

moves towards the stratosphere (downward) in December and reaches tropospheric altitudes; then the mesospheric positive temperature signal moves toward the lower altitudes (upper stratosphere) in December and a negative anomaly of temperature appears above it. As winter progresses both positive and negative temperature anomalies from mesospheric and upper stratospheric heights move downward and reach to lower stratospheric altitudes. The main difference between upper and lower stratospheric temperature signals is that the temperature anomalies in the lower stratosphere are not statistically significant in the late winter of the NH. In December a tropospheric temperature anomaly of about -1 K is evident.

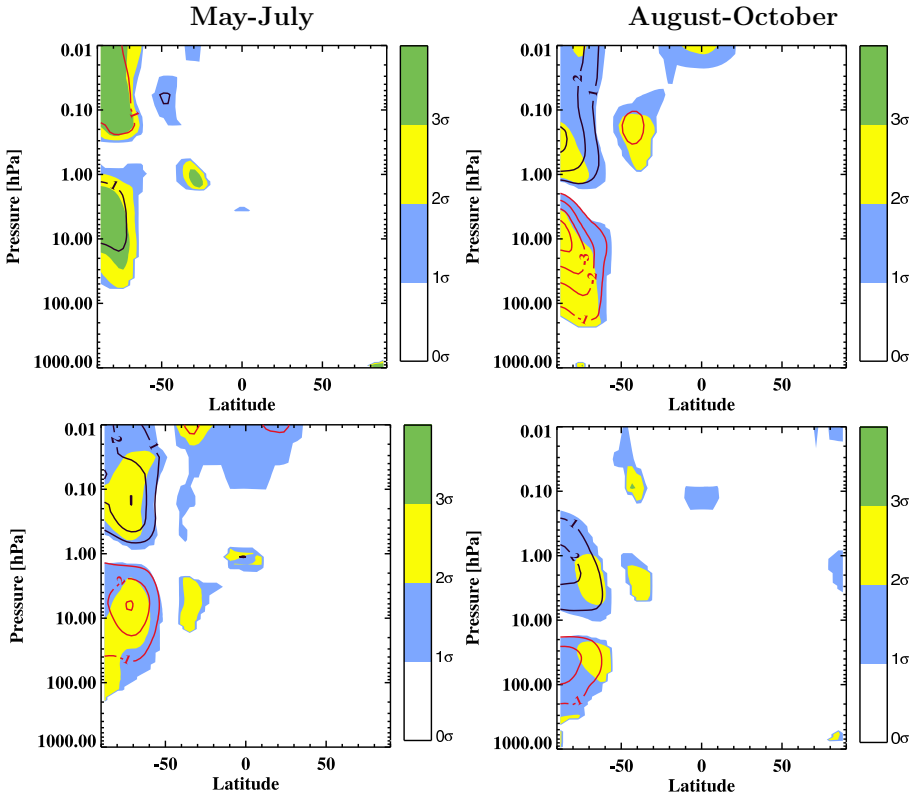

Figure 5.4: Monthly mean temperature changes in the model simulations for May, July, August and October for $(\Delta O_3 - SH)$ simulation. The figure is taken from Karami et al. (2015b).

A meridional cross section of the monthly mean temperature anomalies between $(\Delta O_3 - SH)$ simulation and the control simulation for the SH wintertime (May, July, August and October) is shown in Fig. 5.4. The SH polar mesosphere cools about 1 K in May and the negative signal of temperature exceeds the $\pm 3\sigma$ inter-annual variability of the control run. However a positive temperature anomaly which is statistically significant can be seen in the upper and middle stratosphere. The negative temperature anomalies (cooling effects) moves downward with time from July

to October. However, robustness and strength of the temperature signal are not constant over time. In August a cooling effect of about -4 K is evident. The negative temperature anomaly reaches to about -2 K in early SH spring (October). The downward movement of the temperature anomalies from the mesosphere and upper stratospheric height to the tropospheric altitudes has been previously reported by (Rozanov et al. (2005), Baumgaertner et al. (2011), Seppälä et al. (2013)). Baldwin and Dunkerton (2001)) showed that large anomalies in the stratospheric circulation that first appear in the stratosphere descent downward and reaches to the tropospheric altitudes and are followed by anomalous tropospheric weather regimes.
I will later show that how different dynamical forcings in the NH and SH hemispheres result in different temperature responses. Here we exclude the years with SSW from both control run and ozone-perturbed scenario to investigate how temperature respond to the ozone-perturbed scenario in the absence of a major dynamical forcing. A meridional cross section of the monthly mean temperature anomalies (SSW-excluded) between $(\Delta O_3 - NH)$ simulation and the control simulation for the NH wintertime is shown in Fig. 5.4. It is found that the temperature response in the SSW-excluded case is reversed compared to the original in early and mid-winter and is similar (qualitatively) to the $(\Delta O_3 - SH)$ simulation response. However the amplitude of the temperature response is larger than $(\Delta O_3 - SH)$ simulation which might be due to the smaller sampling size.

A meridional cross section of the monthly mean zonal mean zonal wind changes between control simulation and $(\Delta O_3 - NH)$ run for NH wintertime is shown in Fig. 5.6. A NH polar vortex acceleration of up to 5 ms^{-1} is evident in November. In December, however, the zonally averaged zonal wind decelerates strongly in mesospheric altitudes, while the polar night jet weakly accelerates below 10 hPa. A statistically insignificant changes in the zonal mean zonal wind can be seen from February to April. An oscillatory nature of the variability in the NH wintertime is found; when a positive or negative anomaly terminates in the lower stratosphere, another develops in the mesosphere.

A meridional cross section of the monthly mean zonal wind anomalies between $(\Delta O_3 - SH)$ simulation and control simulation for SH wintertime is presented in Fig. 5.7. From Fig. 5.4 and Fig. 5.7 it is evident that the positive anomaly of temperature in late fall of SH stratosphere is coincident with a decelerated zonal mean zonal wind. The zonal mean zonal winds shows a positive anomalies from July to October. In early winter in the polar upper stratosphere and mesosphere the ozone-perturbed zonal mean zonal wind anomalies have a positive anomaly of

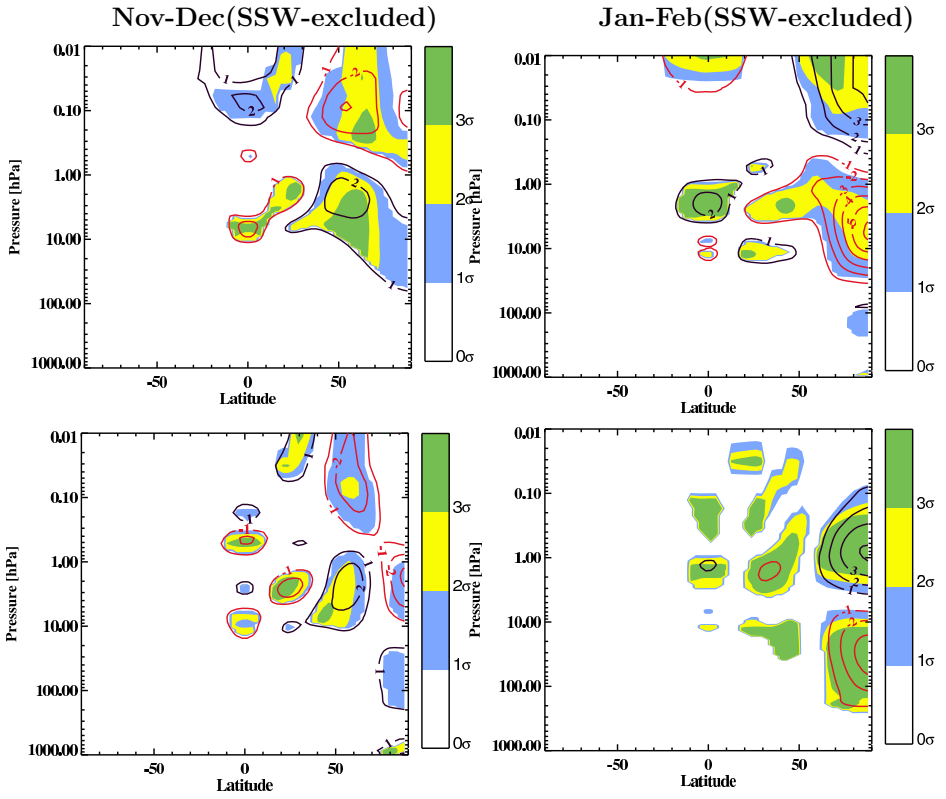

Figure 5.5: Monthly mean temperature changes (SSW-excluded) between ($\Delta O_3 - NH$) simulation and the control simulation for the NH wintertime.

up to 2 ms^{-1}. It is found that the maximum acceleration of the polar night jet in the SH occurs in July and August, when an increase in the zonal mean zonal wind of up to 6-7 ms^{-1} is present. Over time (from July to October), the center of the zonal wind anomaly moves poleward and downward. The positive zonal mean zonal wind anomaly extends from the middle troposphere to the upper stratosphere in October.

An enhancement of the westerlies and a cooling effect due to the lower ozone concentration in the ($\Delta O_3 - SH$) scenario are found. However this is not valid for the NH. This is expected because the NH winter is more disturbed by planetary wave activity than the SH winter. An interesting research question is to figure out the reason behind the temperature and zonal wind differences in July and January. Therefore there is a good motivation to study the wave-mean flow interactions in the different scenarios. Some of the simulated anomalies of temperature are very unlikely to be caused by in-situ ozone depletion and we suggest that an indirect dynamical feedback can be important. In other words the initial changes in the concentration of ozone in the middle atmosphere affect the radiative balance. The changed meridional temperature gradient due to the ozone depletion scenarios affect the vertical wind shear (through thermal wind balance) and hence the pattern of large-scale Rossby wave propagation. One of the parameters controlling the large-

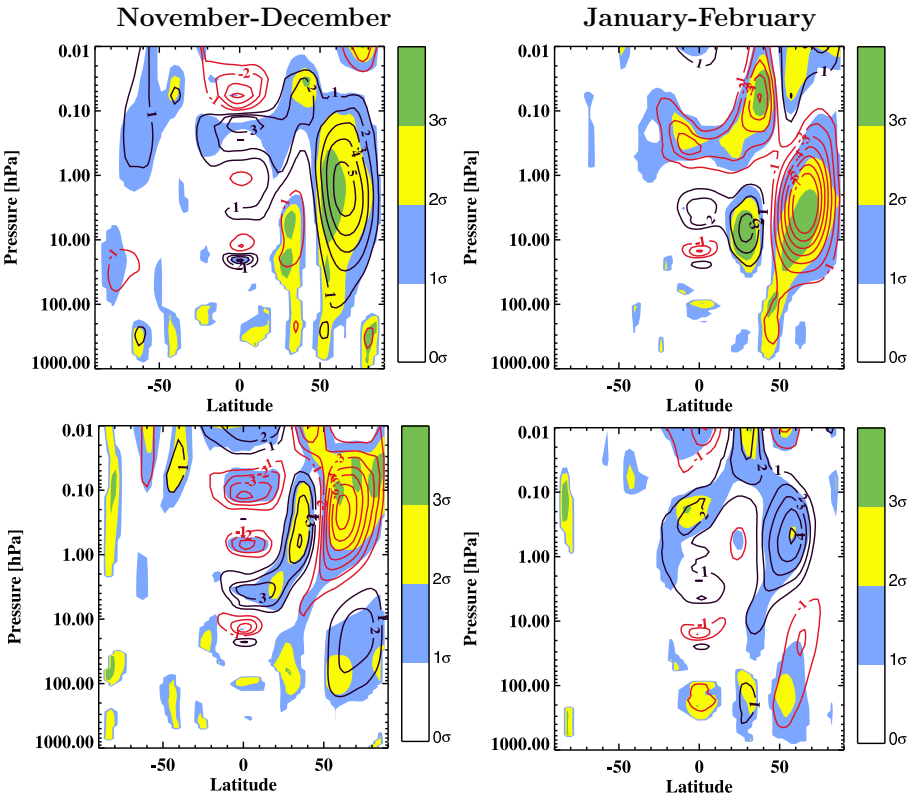

Figure 5.6: Monthly mean zonal mean zonal wind changes in the model simulations in November, December, January and February for $(\Delta O_3 - NH)$ simulation. Contour values represent the monthly mean zonal mean zonal wind differences and shaded areas denote the significance level. The contour interval is $1\,\mathrm{ms}^{-1}$. Red contours show negative zonal wind anomaly while positive zonal wind anomalies are shown in black contours. The figure is taken from Karami et al. (2015b).

scale wave propagation is the mean zonal wind condition which can be altered by in-situ temperature changed due to the imposed ozone loss scenarios. The background zonal wind, in turn, can be changed through the deposition of zonal heat and momentum by planetary waves. Therefore the next section is devoted to the study of wave-mean flow interactions in the presence of ozone-depletion scenarios.

5.3 Wave-mean flow interaction diagnostics (I): Changes in the wave activity

The anomalies of the EP flux (arrows) and its divergences for $(\Delta O_3 - NH)$ simulation are presented in Fig. 5.8. The red contours (positive differences) denote less convergence (or alternatively zonal mean zonal wind acceleration) in the ozone-perturbed simulation compared to the control run. The blue contours (negative differences)

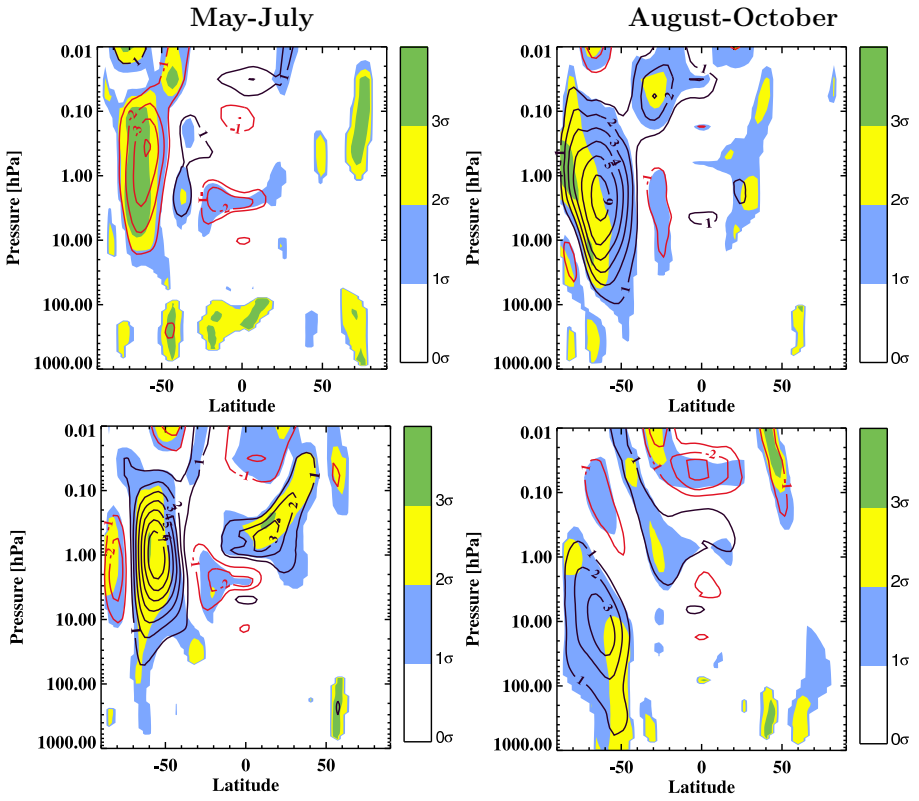

Figure 5.7: Monthly mean zonal wind changes in the model simulations for May, July, August and October for $(\Delta O_3 - SH)$ simulation. The figure is taken from Karami et al. (2015b).

denote more convergence of EP flux (decelaration of the zonal mean zonal wind) in the ozone-perturbed run.

Positive anomalies of the EP flux divergence lead to an acceleration of the NH stratospheric flow in November. The polar night jet decelerates due to the negative anomalies of the EP flux divergence in December and January. The wave-mean flow interaction acts to accelerate the polar vortex in February. In general the deceleration of zonal winds corresponds with negative anomalies of the EP flux divergence and the acceleration of zonal flow corresponds with positive anomalies of the EP flux divergence. The results suggest that in the NH winter the oscillatory nature of the downward propagating signal seen in temperature and zonal wind is a direct result of the interactions between the resolved waves in the model and the mean stratospheric flow. Therefore any change in the EP flux divergence results in the zonal mean zonal wind anomalies which in turn feeds back on the propagating of large-scale disturbances from the troposphere to the stratosphere. An interesting point is that the oscillation in the stratospheric anomaly are not necessarily linked to the oscillating tropospheric forcing. The oscillatory nature of the stratospheric large-scale waves are reported in (Holton and Dunkerton (1978), Holton and Mass

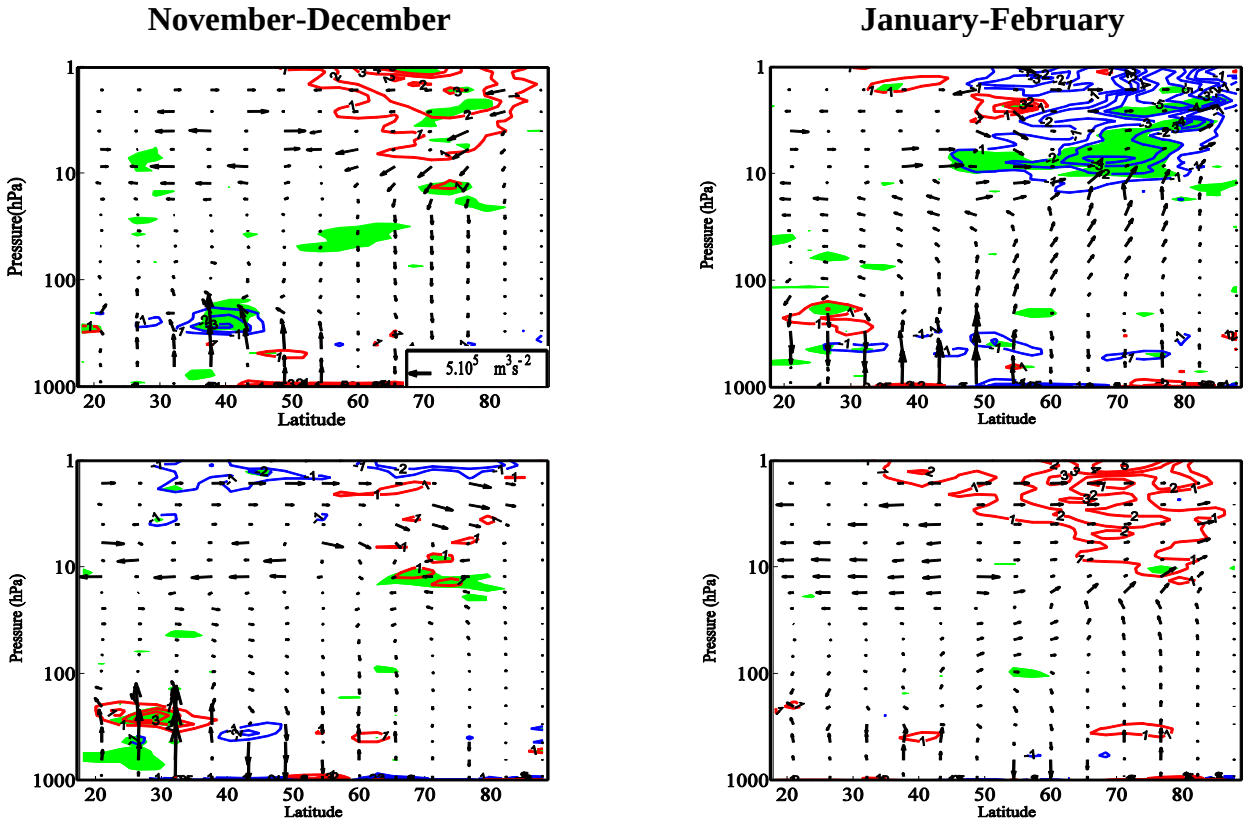

Figure 5.8: Anomalies of EP flux (arrows) and EP flux divergences for $(\Delta O_3 - NH)$ simulation. EP flux reference vector is shown in the right-below in November. Red lines (positive anomalies of EP flux divergences) denote acceleration of zonal flow by waves and blue lines (convergence of EP flux) denote deceleration of zonal flow. The contour interval is 1 $m.\mathrm{s}^{-1}\mathrm{day}^{-1}$. The regions shaded in green are significant, here the anomalies exceed the $\pm 3\sigma$ inter-annual variability of the EP flux divergence derived from the control simulation. The figure is taken from Karami et al. (2015b).

(1976), Yoden (1987)).

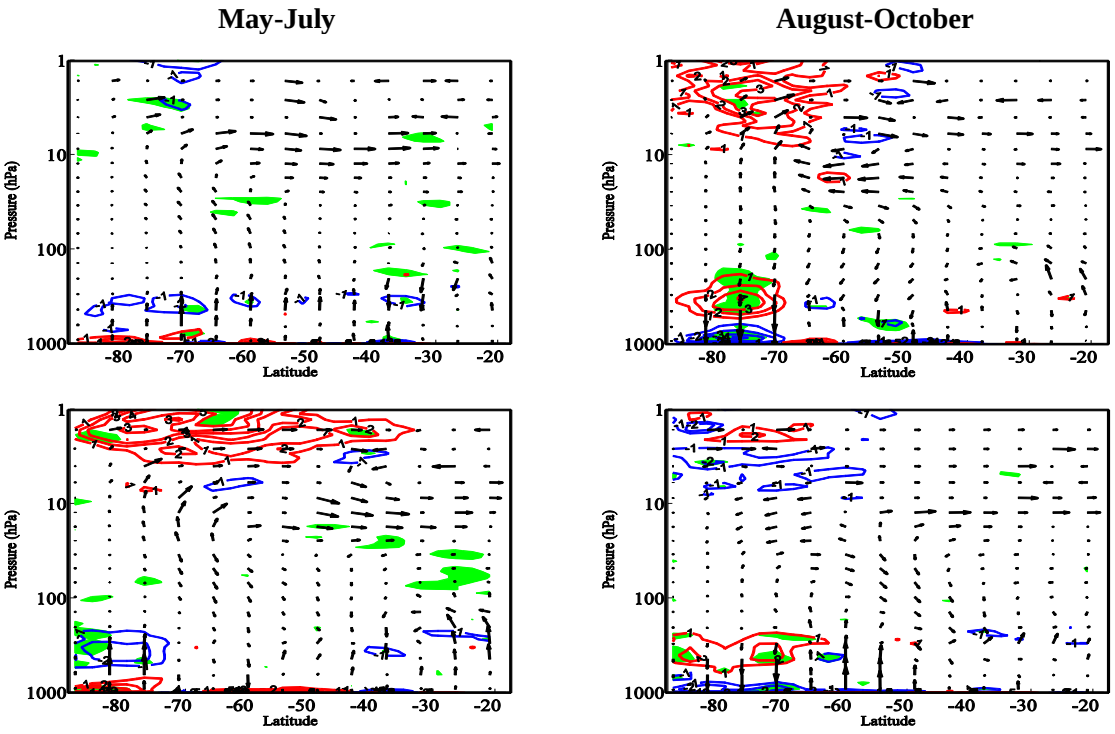

Figure 5.9: Anomalies of EP flux (arrows) and EP flux divergences for $(\Delta O_3 - SH)$ simulation. The figure is taken from Karami et al. (2015b).

Figure 5.9 shows the same analyses as Fig. 5.8 for the $(\Delta O_3 - SH)$ simulation. The negative anomalies of the EP flux divergence in the upper stratosphere act to decelerate the zonal mean zonal wind in early wintertime of the SH. However in mid and late winter of the SH, the strong positive anomalies of the EP flux divergence accelerate the polar night jet. The accelerated polar night jet of the SH reflect the vectors of EP flux toward the equator.

The anomalies of the probability of favourable condition for Rossby wave propagation for $(\Delta O_3 - NH)$ and $(\Delta O_3 - SH)$ simulations are presented in Fig. (5.10) and Fig. (5.11), respectively. In both NH and SH significant changes in the probability of favorable propagation condition of Rossby waves can be seen. Enhanced probability of Rossby wave propagation are shown by black contours and the red lines represents regions that have reduced probability of Rossby wave propagation.

An enhancement of the Rossby wave propagation poleward of 50°N can be seen in early winter (November-December) of the NH. At the same time, a reduction in the probability of Rossby wave propagation is found equatorward of 50°N. Changes in the propagation condition of Rossby waves in early winter is particularly important because it might affect the frequency of Sudden Stratospheric Warming (SSW) during January and February. A reduction of probability of Rossby wave propagation around the polar night jet region and an enhancement of this quantity equatorward

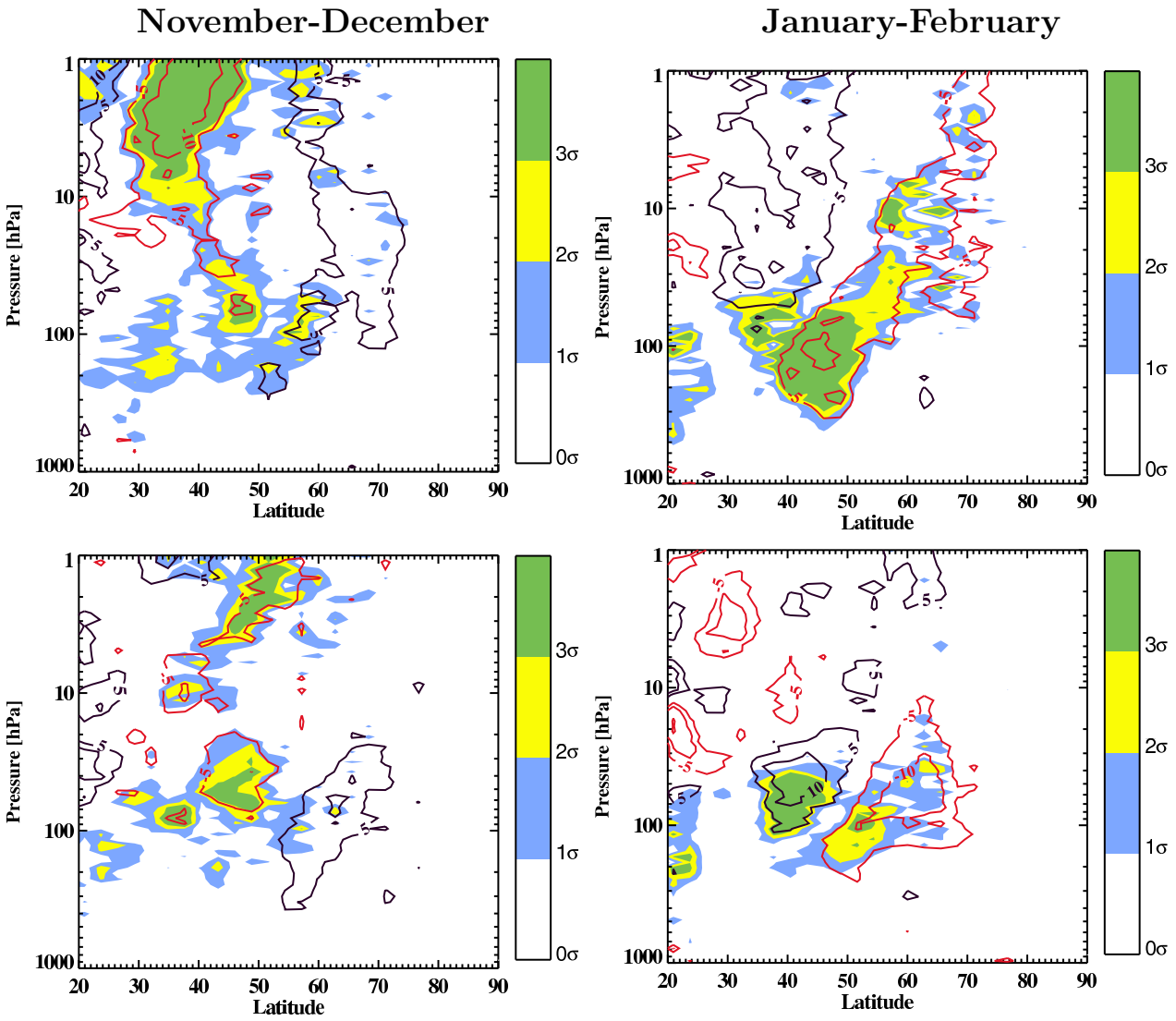

Figure 5.10: Changes in the propagation condition of Rossby waves for ZWN=1 for $(\Delta O_3 - NH)$ simulation. Black contours show regions that are more conducive to Rossby wave propagation and red lines show regions that are less favourable for Rossby wave propagation. The contour interval is [-20, -10, -5, 5, 10, 20]. The figure is taken from Karami et al. (2015b).

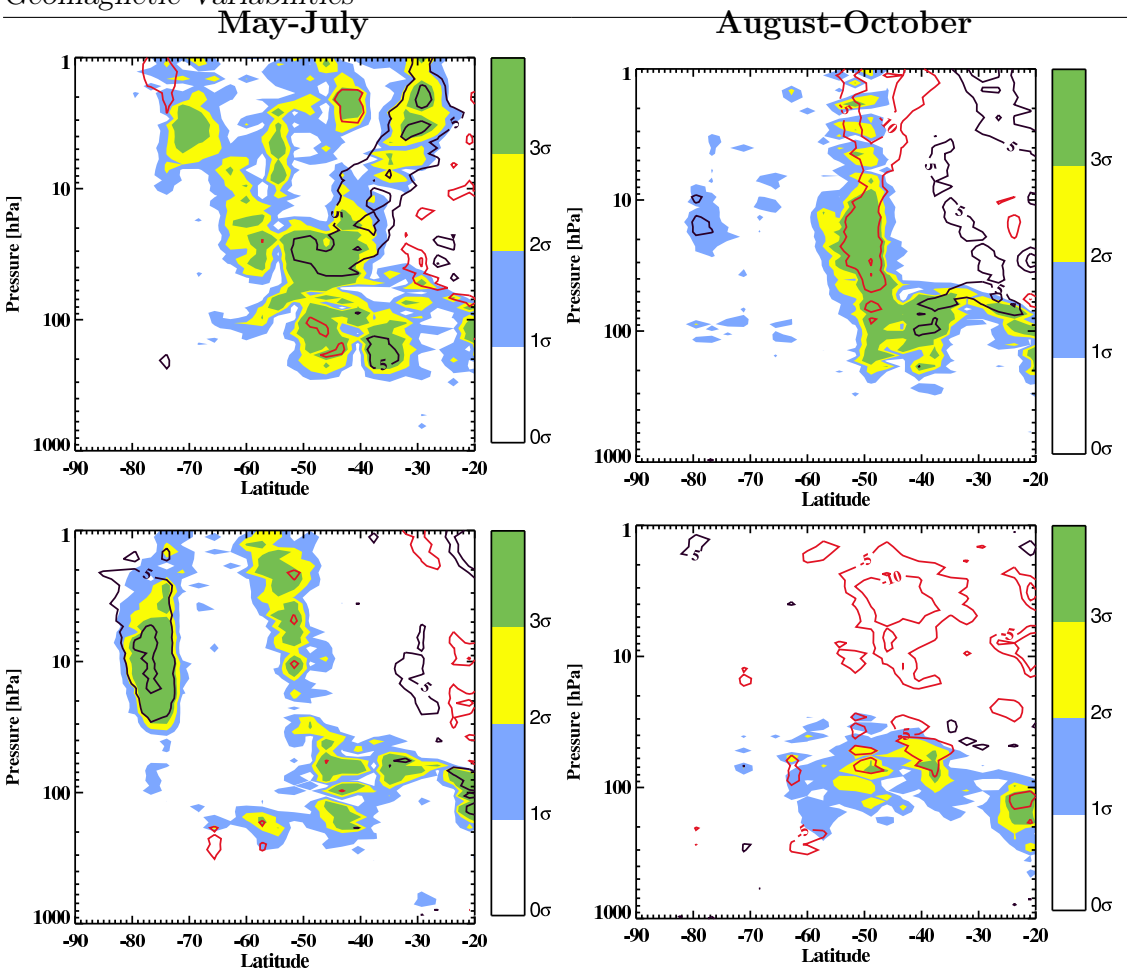

Figure 5.11: Changes in the propagation condition of Rossby waves for ZWN=1 for $(\Delta O_3 - SH)$ simulation. The figure is taken from Karami et al. (2015b).

of 40°N are found in midwinter of the NH (January and February).
In May, poleward of 50°S of stratospheric height, for Zonal Wave Number (ZWN=1) there is a reduction of wave propagation probability and equatorward of it, there is an enhancement of wave propagation possibility. For ZWN=1 around 100 hPa, we found an enhancement of wave propagation possibility during May. From July to October, there is a reduction of wave propagation chances equatorward of 60°S . During the SH wintertime, the ozone loss in the stratospheric heights leads to a relative cooling of the polar vortex region and increases the meridional temperature gradient between the equator and pole which in turn accelerates the polar night jet. The stronger polar night jet of the SH is more capable at blocking wave activity from high latitudes. These results are consistent with (Seppälä et al. (2013)) which suggests higher geomagnetic activities (compared to average geomagnetic activity period) result in an strengthened polar night jet by refracting planetary waves toward the equator.

Anomalies of zonal wind and temperature in late wintertime of both hemisphere reach to tropospheric heights (below 100 hPa), though this feature is more pronounced in the NH spring time. The refractive index of Rossby waves could be altered by atmospheric zonal flow ($\overline{u}$), vertical shear of zonal mean zonal wind ($\frac{\partial u}{\partial z}$), quadratic vertical shear of zonal mean zonal wind ($\frac{\partial^2 \overline{u}}{\partial z^2}$) and atmospheric stability ($N^2(y,z)$). The tropopause acts like a valve for the propagation of Rossby waves from the troposphere to the stratosphere (Chen and Robinson (1992)). Two key parameters that control the characteristics of the above-mentioned valve are the vertical gradient of buoyancy frequency and the vertical shear of the zonal winds at the tropopause region. They also suggested that the larger gradient of the buoyancy frequency reduces the propagation of Rossby waves from troposphere to the stratosphere. They suggest that the less the vertical wind shear, the more wave activity in the troposphere can penetrate into the stratosphere. Based on these analysis, we suggest that by changing the above mentioned parameters, the stratosphere plays an active role in the tropospheric variability and can determine, to a certain degree, its own budget of wave activity.

5.4 Wave-mean flow interaction diagnostics (II): Changes in the frequency of Sudden Stratospheric Warmings and Stratospheric Final Warming dates

Since SSW occurrence is important for stratospheric and tropospheric circulation, we investigate the modification of the frequency and timing of SSWs due to the imposed ozone perturbation. On the other hand, since the Stratospheric Final Warming Dates (SFWDs) are a key component of stratospheric and tropospheric variability in spring and summer of the SH (Wilcox and Charlton–Perez (2013)), therefore we investigate changes in the SFWDs due to the ozone-loss scenarios. A SFWD is defined as the final time when the zonal mean zonal wind at the central latitude of the westerly polar jet drops below zero and never recovers to a specified positive threshold value (with thresholds of 5 and 10 ms^{-1} of the NH and SH, respectively) until the subsequent autumn (Hu et al. (2014)).

The frequency of SSWs in early winter (E–W), midwinter (M–W) and late winter (L–W) is presented in Fig. (5.12). In the current thesis, 1$^{\mathrm{st}}$ November to 15$^{\mathrm{th}}$ of December is defined as early winter, 16$^{\mathrm{th}}$ of December to 15$^{\mathrm{th}}$ of February is

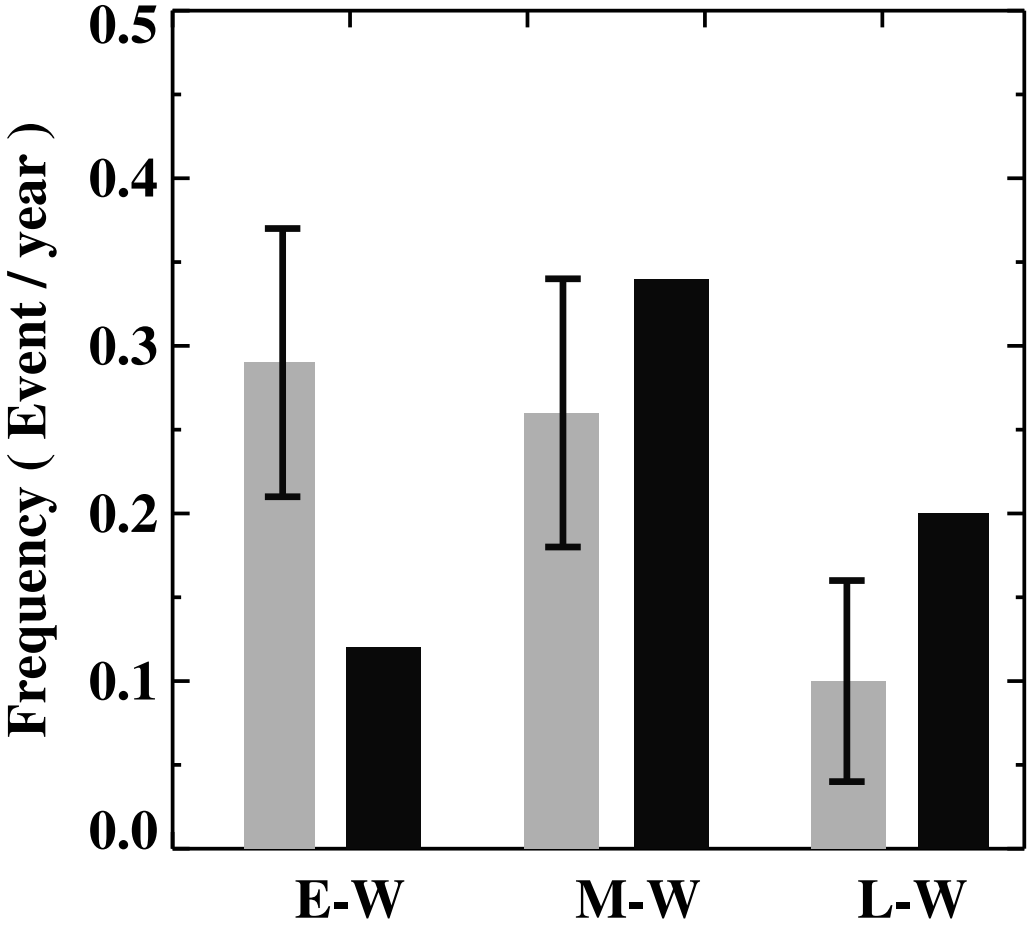

Figure 5.12: Frequency of sudden stratospheric warming in control simulation (gray) and ($\Delta O_3 - NH$) simulation (black). The error bars indicate the 2σ level. The figure is taken from Karami et al. (2015b).

considered as midwinter and 16$^{\text{th}}$ of February to the end of March is late winter-time. The frequency of events per year in a given period is shown in the vertical axis. The frequency of SSWs for control and perturbed simulations are shown by gray and black bars respectively. I found too many SSW events in early winter compared to the observations (Charlton and Polvani (2007)) for the control run. This bias has also been reported in other models that have deployed ECHAM5 as atmospheric base model and might be linked to an anomalous tropospheric forcing (Charlton et al. (2007), Ayarzagüena et al. (2013)). The distribution of SSW for the ozone–perturbed simulation is about 0.69, while the frequency of SSW occurrence for the control simulation is 0.65 events per year. This suggest that the frequency of SSW has not changed significantly. However, we found a shift in the timing of SSW in the ozone-loss scenario. A shift of SSW timing toward mid and late winter is detected. The changes in the occurrence of SSW is more than 3σ significant in early and late winter and about 2σ in midwinter.

The method introduced by (Black and McDaniel (2007), Black and McDaniel (2007)) is used to calculate the dates of stratospheric final warmings. First the zonal mean zonal wind at 60°S are smoothed using a 5-day low-pass filter (5-day running averages of daily zonal wind) and then warmings are identified when the smoothed winds first drop below $10\,\mathrm{ms}^{-1}$ at 50 hPa and remain below that threshold until the following winter. In our simulations about 5% of wintertime zonal mean zonal winds never become westward. Therefore we ignore these years from our analysis. The mean date of the stratospheric final warming in the SH for the control simulation is 13th November with a standard deviation of about 22.8 days (error of the mean equals to 2.28 days), while for ozone-perturbed simulation the mean date of SFWD is 26th November (two weeks difference in the occurrence of SFWDs).

5.5 Ozone–induced climate variation due to 11–year solar UV variability

The impact of an ozone anomaly of about 4% at the tropical stratopause due to the 11–year solar cycle on middle atmospheric dynamics and temperature is investigated in this section. Afterwards we compare the magnitude of the changes due to the 11-year solar cycle and ozone anomaly originated by ozone changes due to high energy particle precipitation's effect. Similar to the previous section, we perform composite analyses to detect the impact of imposed ozone loss on temperature and zonal wind. The multi–year monthly means of zonally averaged values for both zonal wind and temperature are used to compare the differences between the control simulation and ozone–perturbed simulation.

The meridional cross section of the monthly mean temperature changes between the $(\Delta O_3 - TS\ )$ scenario and the control run is presented in Fig. 5.13. The monthly mean zonal mean of temperature differences between the ozone–perturbed and the control simulation are shown by contour values. The shaded areas denote the level of significance. The contour interval is 1 K. As a result of ozone depletion in the tropical stratopause a local cooling is expected. This cooling is about -1 K in November. A non-local positive temperature signal which is about 3 K develops in the NH polar mesosphere. A statistically significant cooling effect is found in the upper and middle stratosphere in November. The mesospheric positive signal moves downward with time as NH winter progresses from December to March. However the magnitudes and the significances of this positive anomaly are not constant over time. For the negative temperature anomaly of polar latitudes, we found a similar downward movement. A negative temperature signal of about -2 K develops at polar region of

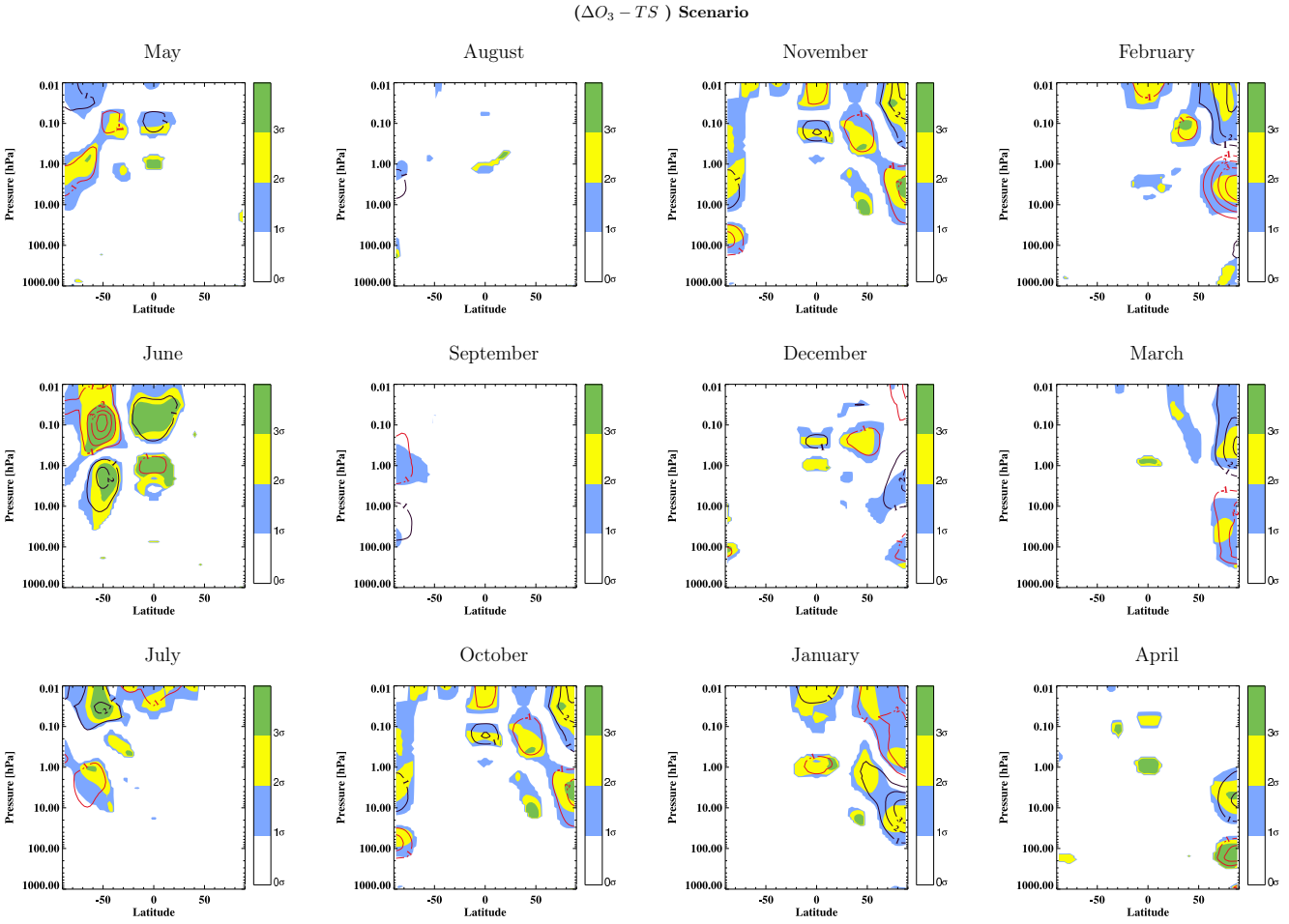

Figure 5.13: Monthly mean zonal mean temperature response of EMAC model to ($\Delta O_3 - TS$) scenario. The figure is taken from Karami et al. (2015b).

NH mesosphere in December. As winter progresses this negative signal moves downward, reaching to tropospheric altitudes in March. A local temperature cooling of about -1 K is evident over the tropical stratopause in January.

In the mesospheric polar region of the SH a positive temperature signal of about 1 K and a negative temperature anomaly with similar magnitude in stratospheric polar region develop in April. The mesospheric positive signal moves downward as time progresses and reach to stratospheric altitudes in May and a significant negative signal is substituted for positive temperature signal in mesospheric altitudes. This negative signal moves downward in June. However, after June (July-September) the magnitude of the temperature signal in polar regions of the SH is negligible.

A meridional cross section of the monthly mean zonal mean zonal wind changes between ($\Delta O_3 - TS$) scenario and control run is presented in Fig. 5.14. From December to April a positive zonal mean zonal wind signal that develops in tropical

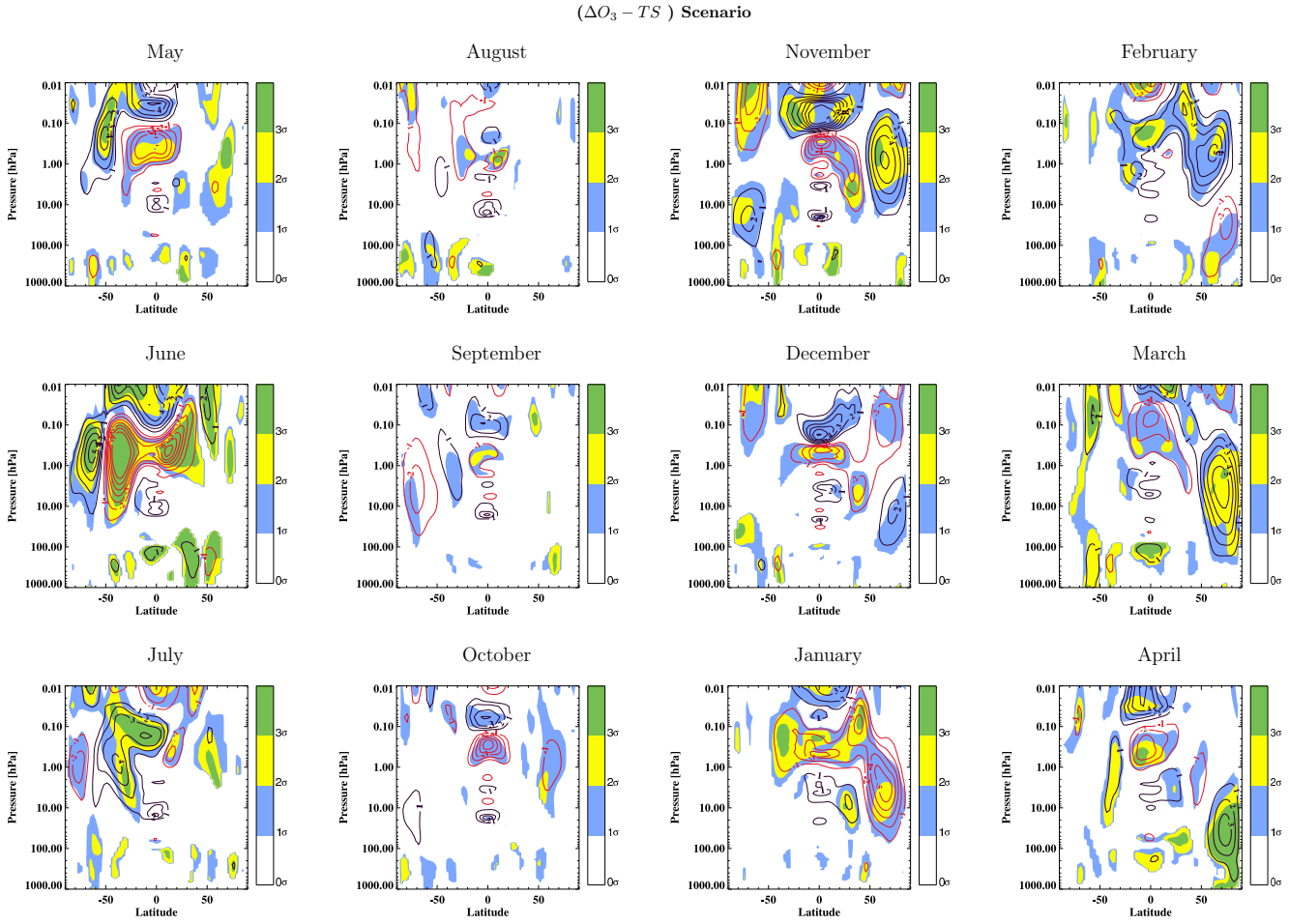

Figure 5.14: Monthly mean zonal mean zonal wind response of EMAC model to ($\Delta O_3 - TS$) scenario. The figure is taken from Karami et al. (2015b).

mesosphere of NH moves poleward and downward. Kodera and Kuroda (2002) reported a poleward and downward propagation of zonal mean zonal wind signal from early winter to late winter. There are small changes in the zonal wind in the SH between July-October. The unaffected winter of the SH suggests that in midwinter of the SH the polar vortex is too strong to be affected significantly by 4% ozone changes over the tropical stratopause. Moreover, the magnitudes of both zonal mean zonal wind and temperature differences between ozone-perturbed and control simulation suggest that in many cases the magnitudes of theses responses in the case of ozone perturbation due to high energy particle precipitation could exceed (or at least comparable) the responses of ozone changes due to the 11–year cycle UV variability. It is also interesting to mention that in our simulation, mesospheric-upper stratospheric temperature anomalies tend to move downward due to ($\Delta O_3 - TS$) scenario or ($\Delta O_3 - NH$)/($\Delta O_3 - SH$) scenarios.

6 The Influence of the Stratospheric Wind Regimes on the Atmospheric Waves and Tropospheric Baroclinicity

6.1 Large-Scale Rossby Waves as Influenced by the Stratospheric Wind Regimes

In this section I concentrate on demonstrating the potential benefits of the newly developed diagnostic tool for studying the influence of the mean flow on the Rossby wave propagation. To achieve this aim I investigate the sensitivity of both $n^2_{k,l}(y,z)$ and $Pr_{Ro}(y,z)$ to differnt zonal flow regimes in the stratosphere to figure out which one of these diagnostic tools is more capable of demonstrating the above-mentioned sensitivity. I start from identifying different stratospheric flow regimes following the method suggested by (Castanheira and Graf (2003)). I constructed two data sets based upon the strength of the westerly winds in the lower stratosphere (50 hPa) at 65°N. Since the upward wave propagation is prohibited when the background zonal flow is larger than a critical velocity, therfore a reasonable option for identifying different zonal flow regimes in the stratosphere is whether or not the background zonal flow is larger or small than the critical Rossby velocity. Castanheira and Graf (2003) reported that for a climatological Northern hemisphere zonal wind profile the critical Rossby velocity is about 20 ms^{-1} for zonal wavenumber=1. Then based upon this threshold the Strong Vortex Regime (SVR) is identified when $\overline{u}_{50}(65°N) > 20\,ms^{-1}$ and Weak Vortex Regime (WVR) is considered when $0 < \overline{u}_{50}(65°N) < 10\,ms^{-1}$, where $\overline{u}_{50}(65N)$ is the 50 hPa zonal mean zonal wind at $65°N$. These regimes should last at least 30 consecutive days in DJF to be considered in our results. Several examples of both SWR and WVR are presented in Fig. 6.1.

Table 3.2 shows the time intervals of different vortex regimes which last for at least 30 consecutive days in DJF in the Northern hemisphere. It is clear from Table 3.2 that the number of SVR events are greater than WVR events. Since in DJF the

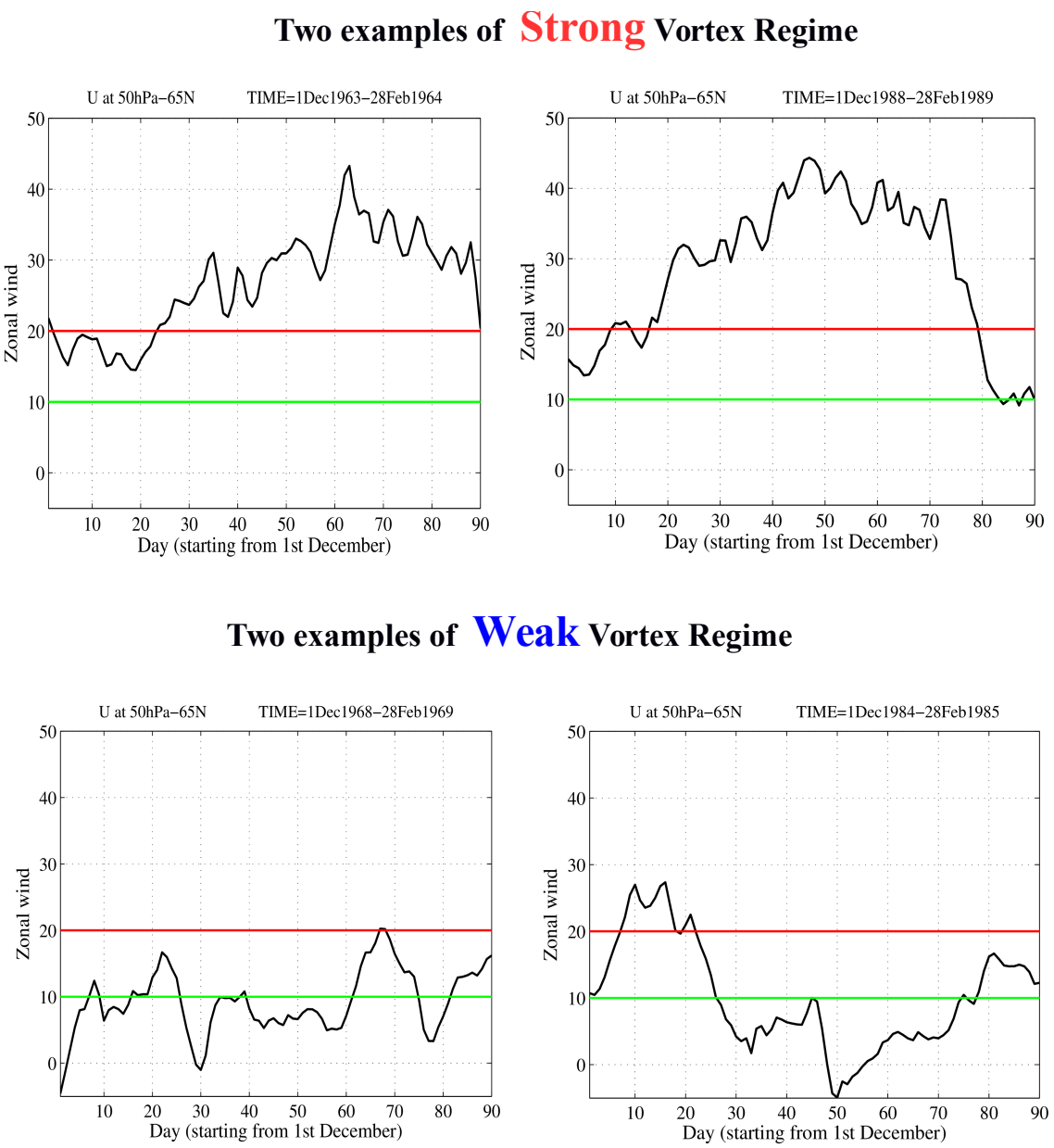

Figure 6.1: Top row: Two examples of strong vortex regime. The SVR is identified when $\overline{u}_{50}(65°N) > 20\,ms^{-1}$. Bottom row: Two examples of weak vortex regime. The WVR is considered when $0 < \overline{u}_{50}(65°N) < 10\,ms^{-1}$ and last at least 30 consecutive days in DJF.

strong polar night jet blocks upward wave propagation therefore the frequency of SVR is higher than WVR. Figure. 6.2 shows the results of $a^2 n^2_{k,l}(y,z)$ (first row) and $Pr_{Ro}(y,z)$(second row) during WVR and SVR for wave (1,1). I found nearly similar structure to the wintertime climatology of the $Pr_{Ro}(y,z)$ for both SVR and WVR. The mid-latitude waveguide is much wider in WVR than SVR. As expected the average values of $Pr_{Ro}(y,z)$ are greater in the stratosphere during WVR than SVR. These results confirm that planetary waves have more chance to penetrate and force the stratosphere in WVR than SVR.

Table 3.2: Periods of polar vortex regimes lasting for at least 30 consecutive days in DJF; left: Strong Vortex Regime. Right: Weak Vortex Regime.

Strong Vortex Regime (SVR)		Weak Vortex Regime (WVR)	
Starting date	Ending date	Starting date	Ending date
20 Dec 1961	20 Feb 1962	20 Dec 1968	27 Jan 1969
24 Dec 1963	28 Feb 1964	28 Dec 1984	13 Feb 1985
03 Jan 1967	28 Feb 1967	09 Dec 1998	11 Jan 1999
01 Dec 1975	28 Feb 1976	02 Jan 2004	28 Feb 2004
01 Dec 1987	14 Jan 1988		
16 Dec 1988	17 Feb 1989		
17 Dec 1989	28 Feb 1990		
01 Dec 1991	18 Jan 1992		
05 Dec 1992	11 Feb 1993		
01 Dec 1994	18 Jan 1995		
07 Dec 2004	21 Feb 2005		
30 Dec 2006	26 Feb 2007		
23 Dec 2007	13 Feb 2008		

Contrary to the noisy structure of the $a^2 n^2_{k,l}(y,z)$, values of $Pr_{Ro}(y,z)$ are sensitive to the stratospheric westerlies and are consistent with the general knowledge about planetary wave propagation from the troposphere to the stratosphere. While the noisy structure of the time mean refractive index make the analysis very difficult, the probability of the favorable propagation condition for Rossby waves show an enhancement of wave propagation northward of $70°N$ in the lower stratosphere and a slight reduction in the favorability of wave propagation between $50-70°N$ in the stratosphere for WVR.

Since the highest difference in the favorability of wave propagation between WVR and SVR occurs poleward of $50°N$ in the middle stratosphere, I now concentrate on the vertical component of EP fluxes for both SVR and WVR events. The difference in the vertical component of EP flux between WVR and SVR in this region is

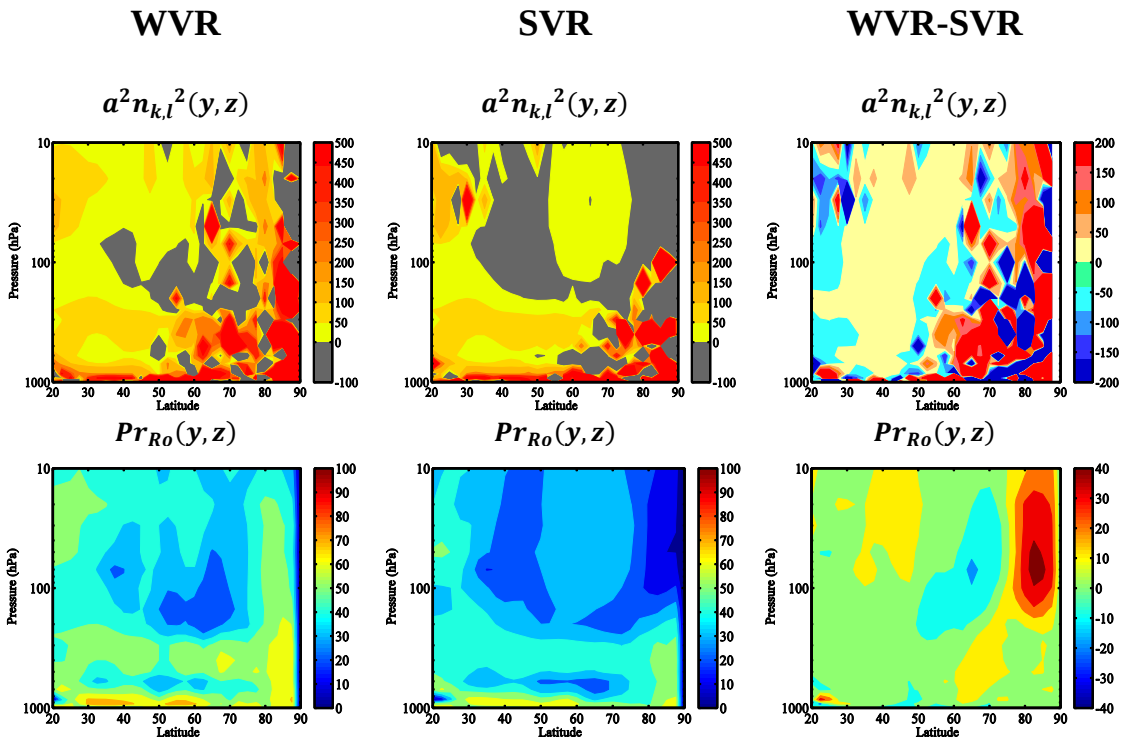

Figure 6.2: $a^2 n_{k,l}^2(y,z)$ (first row) and $Pr_{Ro}(y,z)$(second row) during WVR and SVR. While the noisy structure of the time mean refractive index make the analysis very difficult, the probability of the favorable propagation condition for Rossby waves show an enhancement of wave propagation northward of $70°N$ in the lower stratosphere and a slight reduction in the favorability of wave propagation between $50-70°N$ in the stratosphere for WVR. The figure is taken from (Karami et al. (2016)).

presented in Fig. 6.3. During WVR, an enhancement of vertical EP flux is obtained poleward of $65°N$ in the lower stratosphere. For WVR a reduction in the vertical component of EP flux is obtained southward of this region in the middle and upper stratosphere. Comparison between the differences of $a^2 n_{k,l}^2(y,z)$ and $Pr_{Ro}(y,z)$ and the vertical component of EP flux during WVR and SVR show that the pattern of differences between $Pr_{Ro}(y,z)$ and the vertical component of EP flux are similar. Therefore, based upon these analyses, I suggest that this diagnostic tool can be useful for studying the propagating properties of the planetary waves.

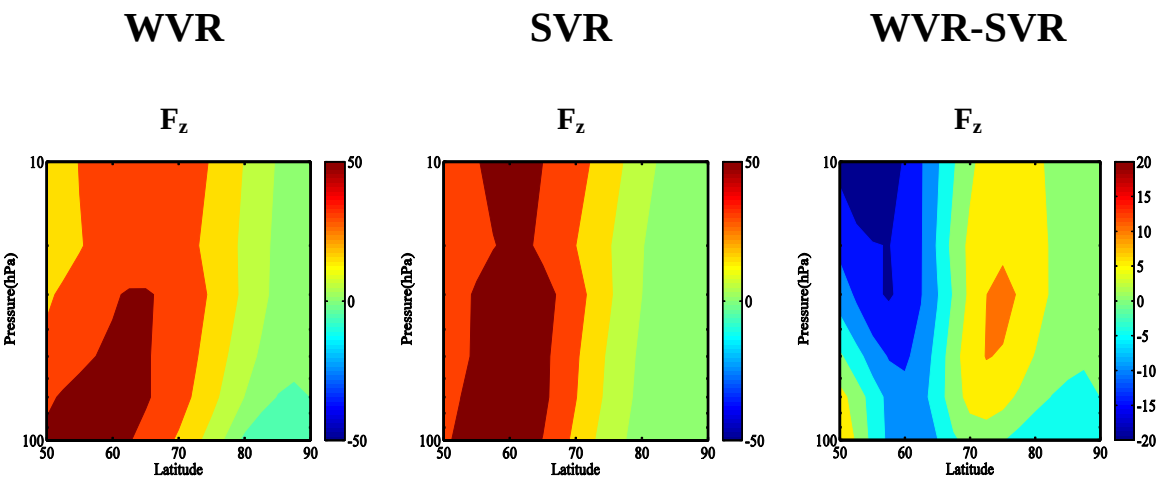

Figure 6.3: The vertical component of EP flux for WVR and SVR. The values are divided by 10^5. Since the highest differences in the $a^2 n_{k,l}^2(y,z)$ and $Pr_{Ro}(y,z)$ between WVR and SVR are in the high latitude stratosphere the vertical component of EP fluxes are shown in this region. Comparison between the differences of $a^2 n_{k,l}^2(y,z)$ and $Pr_{Ro}(y,z)$ and vertical component of EP flux during WVR and SVR show that the pattern of differences between $Pr_{Ro}(y,z)$ and vertical component of EP flux are similar. The figure is taken from (Karami et al. (2016)).

6.2 NAO-Like Sea Level Pressure Anomalies Induced by the Stratospheric Wind Regimes

Figure 6.4 shows the Sea Level Pressure (SLP) differences between SVR and WVR. A positive SLP anomaly in the subtropical region and a negative SLP anomaly over the Arctic indicates positive Northern Atlantic Oscillation (NAO) mode. An oscillation of atmospheric mass (or pressure) between the Arctic and the subtropical Atlantic is called NAO which determines climate variability from the eastern coast of the USA to Siberia and from the subtropical Atlantic to the Arctic, especially during winter time (Hurrell et al. (2001)). During positive phases of the NAO, the wintertime meridional pressure gradient over the North Atlantic enhances. Therefore during positive phases of the NAO, the Icelandic low-pressure center and the high-pressure center at the Azores are both strengthened. The opposite occurs during negative phase of NAO (both centers are weakened). Changes in the SLP from one phase to another induces large-scale changes in the weather patterns (e.g. storm tracks, heat and moisture transport and so forth) over the North Atlantic.
The SLP differences between SVR and WVR in both FUL-NUD and STR-NUD simulations are quite similar to ERA. The main difference between FUL-NUD and STR-NUD simulations is that the magnitude of the anomalies in the STR-NUD

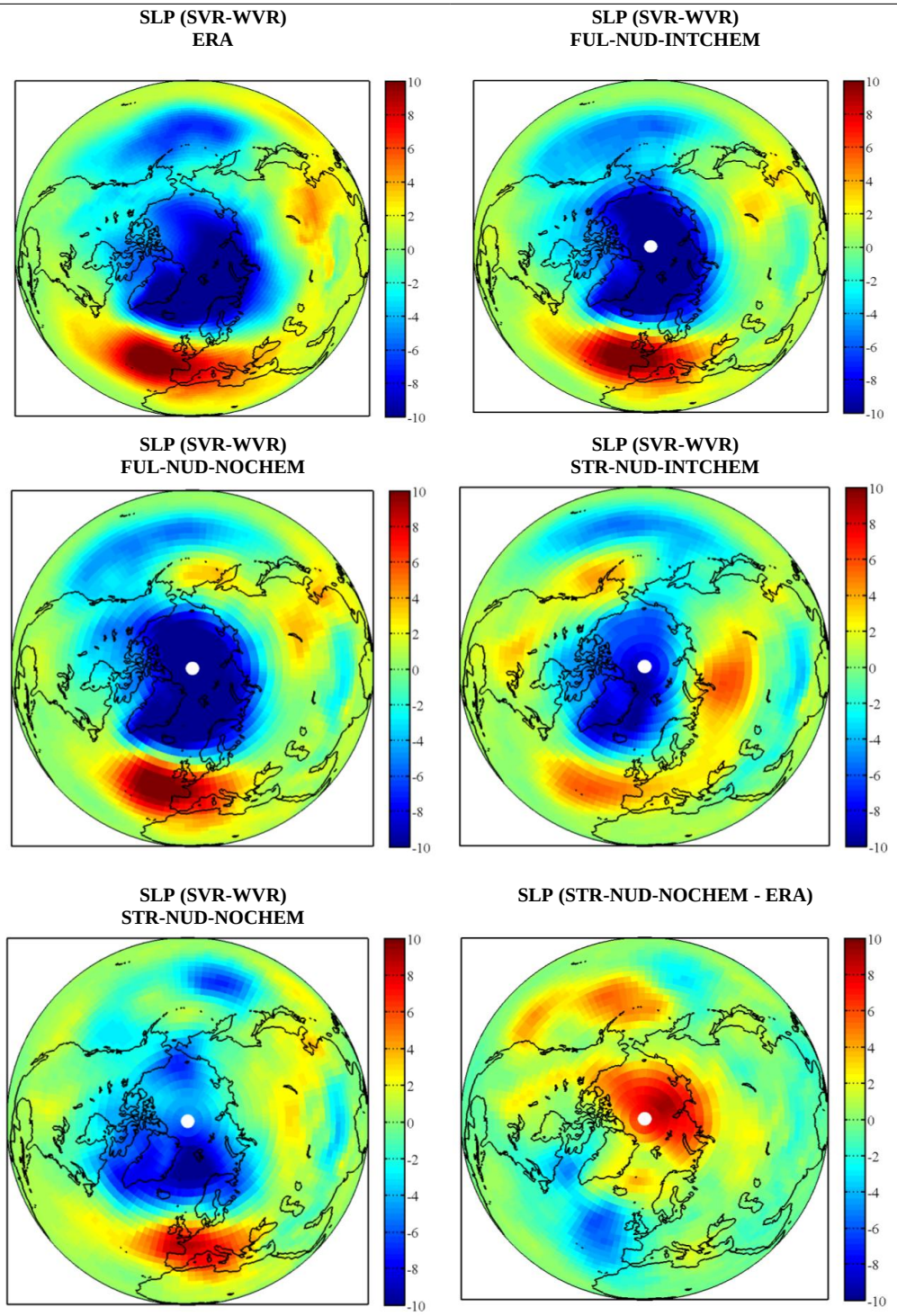

Figure 6.4: The surface pressure pattern associated with the variations in the strength of the stratospheric wind looks like NAO. The sea level pressure difference between STR-NUD-NOCHEM and ERA suggests that there should a mechanism in the troposphere to amplify the pressure signal at the surface. The pattern of the surface pressure differences in the STR-NUD-NOCHEM simulation (nudged in the stratosphere and free running mode in the troposphere) is similar to the ERA but the magnitudes of the differences are less than reanalysis dataset.

simulations are smaller than ERA and FUL-NUD simulations. A lower than average pressure anomaly over the pole and a higher than average pressure anomaly over the extra tropics during SVR indicate a positive NAO. It is interesting to mention that even though the surface pressure in the STR-NUD simulations is not nudged toward the reanalysis, however the model captures the main features (similar to the ERA) of pressure anomalies at the surface. In order to explain the stratospheric downward influence on sea level pressure anomalies, I use the so-called Transformed Eulerian Mean (TEM) momentum equation (Kidston et al. (2015)). The TEM momentum

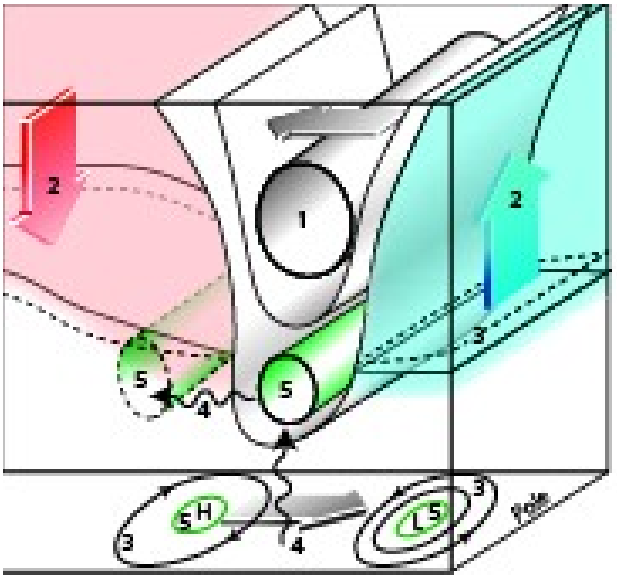

Figure 6.5: An schematic adapted from Kidston et al. (2015) illustrating the stratospheric downward influence.

equation can be defined as:

$$\overline{u}_t = \overline{v}^*(f - (a\cos\phi)^{-1}(\overline{u}\cos\phi)_\phi) - \overline{w}^*\overline{u}_z + (\rho_0 a\cos\phi)^{-1}\nabla\cdot\vec{F} + \overline{X} \qquad (6.1)$$
$$(i) \qquad (ii) \qquad (iii) \qquad (iv)$$

where $\overline{u}_t$ is the variability in the speed of the stratospheric circumpolar westerly flow and $(\overline{v}^*, \overline{w}^*)$ are meridional and vertical components of the residual mean circulation which essentially determines the transport of mass through the stratosphere. Wave flux denoted by $\vec{F}$ is important for the angular momentum transport by large-scale waves. Other forcings, such as small-scale gravity waves not resolved by models, are denoted by X. Subscripts denote the derivative with respect to that variable.
Upward propagation of both large and small scale waves $(iii), (iv)$ can force the stratospheric flow $(\overline{u}_t)$. Breaking waves in the stratosphere (iii) induce anomalies in the mean residual circulation $(i), (ii)$ such that the mean westerly momentum

transported across latitudes (i) and in the vertical (ii) acts to conserve angular momentum and maintain mass continuity. In the steady state ($\overline{u}_t = 0$) the two effects oppose each other and are in exact balance. If the wave forcing (iii) decreases then the stratospheric polar vortex becomes wider and stronger. The wider polar night jet induces an equatorward momentum transport (i). Mass continuity in the stratosphere suggests an upward mass transport over the Arctic, with sinking air at extra tropics (ii). If the wave breaking increases (iii), the opposite effects occur.
Figure 6.5 shows an schematic explaining the downward influence of the stratosphere on tropospheric surface pressure. The stratospheric polar night jet (1) is allowed to accelerate in the absence of wave forcing which is usually accompanied by an anomalous residual mean meridional circulation (2). In the case of stronger polar night jet, mass moves out of the polar cap and a compensating descent at mid latitudes is suggested. The rising air over the Arctic induces adiabatic cooling and sinking air over the extra tropic induces adiabatic warming in the stratosphere. During strong stratospheric vortex episode, the upwelling over the Arctic increases the tropopause height (3). A poleward shift of the tropospheric jet (5) during strong stratospheric vortex episode is linked to the tropospheric eddy feedbacks (4), although these details are not well understood.
A smaller pressure anomaly in the STR-NUD simulations in comparison to ERA or FUL-NUD simulations needs particular attention. It is suggested that there should be a mechanism in the troposphere that might amplify the pressure anomalies observed at the surface. The near-surface amplification of the sea level pressure originated from the stratospheric wind anomalies includes the eddy feedback within the troposphere. However the detail of this process is not fully understood. Motivated by the tropospheric amplification of sea level pressure originated from the stratospheric wind anomalies, I will provide insight (in the next sections) on the following questions: (1) In which way the stratospheric persistent westerlies affect the propagation characteristics of the RWPs in the upper troposphere? (2) Do the stratospheric persistent wind regimes have the capacity to generate new eddies (cyclogenesis) in the troposphere?

6.3 Rossby Wave Packets as Influenced by the Stratospheric Wind Regimes

As discussed in chapter 4, changes in the atmospheric wave packets are associated with changes in the storm-tracks. Figure 6.6 and Fig. 6.7 show the changes in the RWPs in response to variations in the stratospheric flow. It is suggested that the variations in the occurrence of upper-level Rossby wave-breaking events may lead

to the low-frequency variability of the North Atlantic Oscillation (NAO) (Woolings et al. (2008), Benedict et al. (2004)). Spatially long synoptic waves (wavenumbers 4-7) tend to break anticyclonically and Anticyclonic Wave Breaking (AWB) pushes the jet poleward leading to a positive NAO anomaly with falling pressure over the pole. Spatially small synoptic waves (wavenumbers 7-11), however, tend to break cyclonically and Cyclonic Wave Breaking (CWB) pushes the jet equatorward leading to a negative NAO anomaly. Wittman et al. (2007) suggest that Wavenumber 7 is the transition wavenumber from one type of breaking to another.

In ERA and FUL-NUD simulations, RWPs responses to the variations in the stratospheric wind resemble each other. Over the east coast of the USA and the Atlantic region which extends to the Eurasian region, I found an enhancement of significant RWPs, indicating a poleward shift of the storm track during SVR (both ERA and FUL-NUD simulations). I also found a decrease in the probability of significant RWPs in extra tropical regions. By comparing the results obtained from FUL-NUD-INTCHEM and FUL-NUD-NOCHEM simulations, I investigate the importance of the interactive chemistry in the stratospheric downward influence. The most noticeable difference is the enhanced reduction in the probability of significant WPAs in the Pacific region for FUL-NUD-INTCHEM simulation compared to the FUL-NUD-NOCHEM simulation. The behavior of spatially long synoptic waves (wavenumbers 4-7) can explain a large part of the significant RWPs responses to SVRs. The differences between smaller RWPs (wavenumbers 7-11) indicate a reduction of wave activity in mid latitudes, though the strength of the reduction is larger in ERA than FUL-NUD-NOCHEM simulation. However, the responses of RWPs for variations in the SWRs are quite similar in ERA and FUL-NUD simulations.
In the STR-NUD simulations (Fig. 6.7) the poleward shift of the significant RWPs over the east coast of USA and Atlantic region is not as strong as in ERA and FUL-NUD simulations. Over the eastern Pacific for the STR-NUD simulations, a significant enhancement in the wave packets is evident which is absent in ERA. This particular feature is produced by the response of both small and large synoptic eddies for variations in the SWRs in the STR-NUD simulations. The results obtained from the FRE-RUN simulation (compared to the ERA) show a relatively similar shift in the pattern of WPAs. However the magnitudes of the differences are much larger than the ERA. For the smaller wavenumbers (7-11), the pattern of the differences of WPAs are different from the ERA results. These results suggest that a realistic representation of the internal tropospheric processes in climate models are essential for obtaining the full details of stratospheric downward influence on tropospheric eddy activity, consistent with results of Garfinkel et al. (2013).

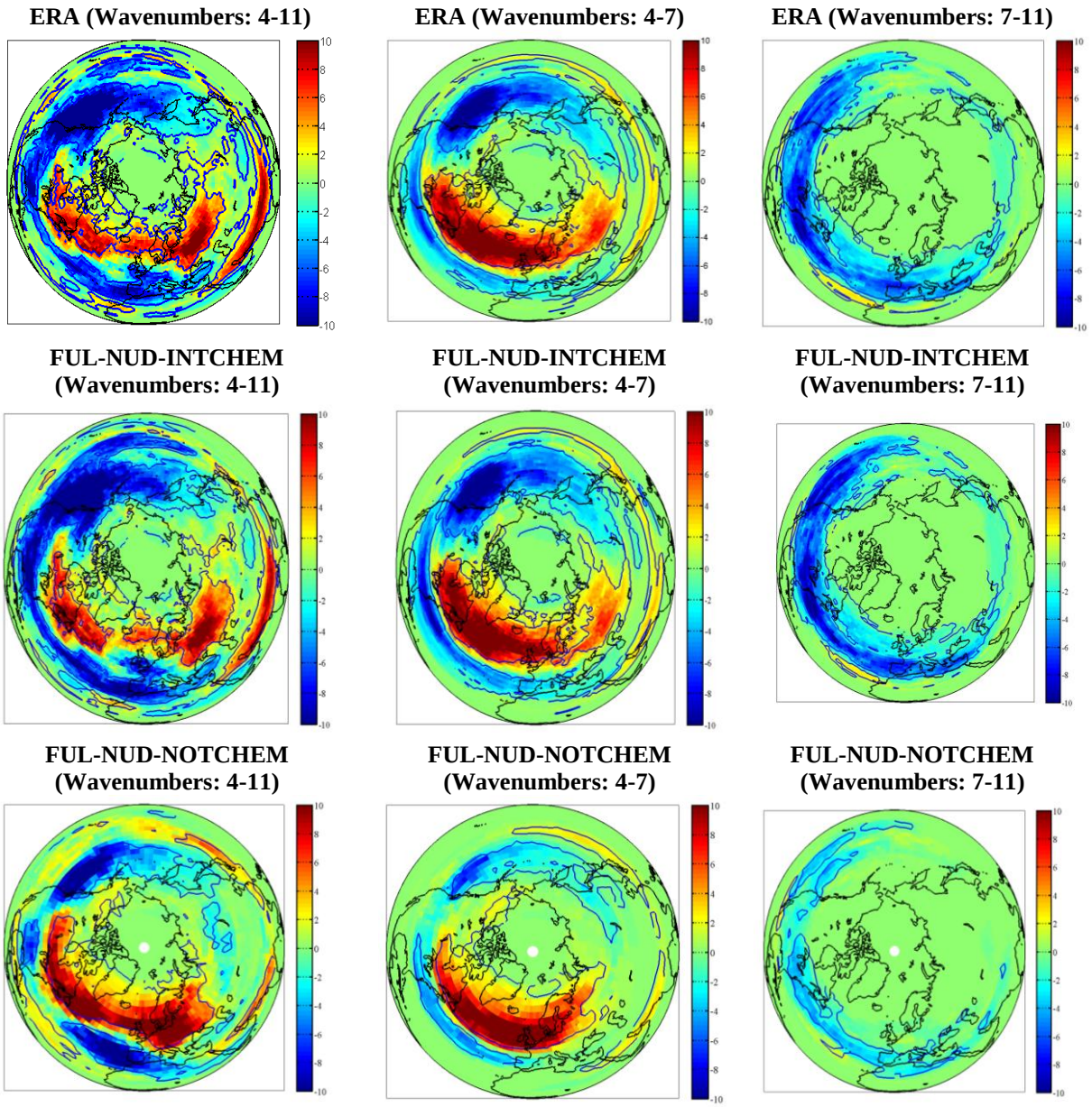

Figure 6.6: The difference in the probability of significant WPAs (exceeding 20 ms^{-1} per grid cell) at 250 hPa for spatially different wavenumbers during Northern Hemisphere extended winter. In all figures the difference in the probability of significant WPAs during SVR and WVR (SVR-WVR) are shown. During SVR an enhancement of WPAs in atlantic and east coast of USA indicate the poleward shift of the Atlantic storm track. The blue lines are the regions of the statistically significant changes according to student's t test with 99.5% significance level.

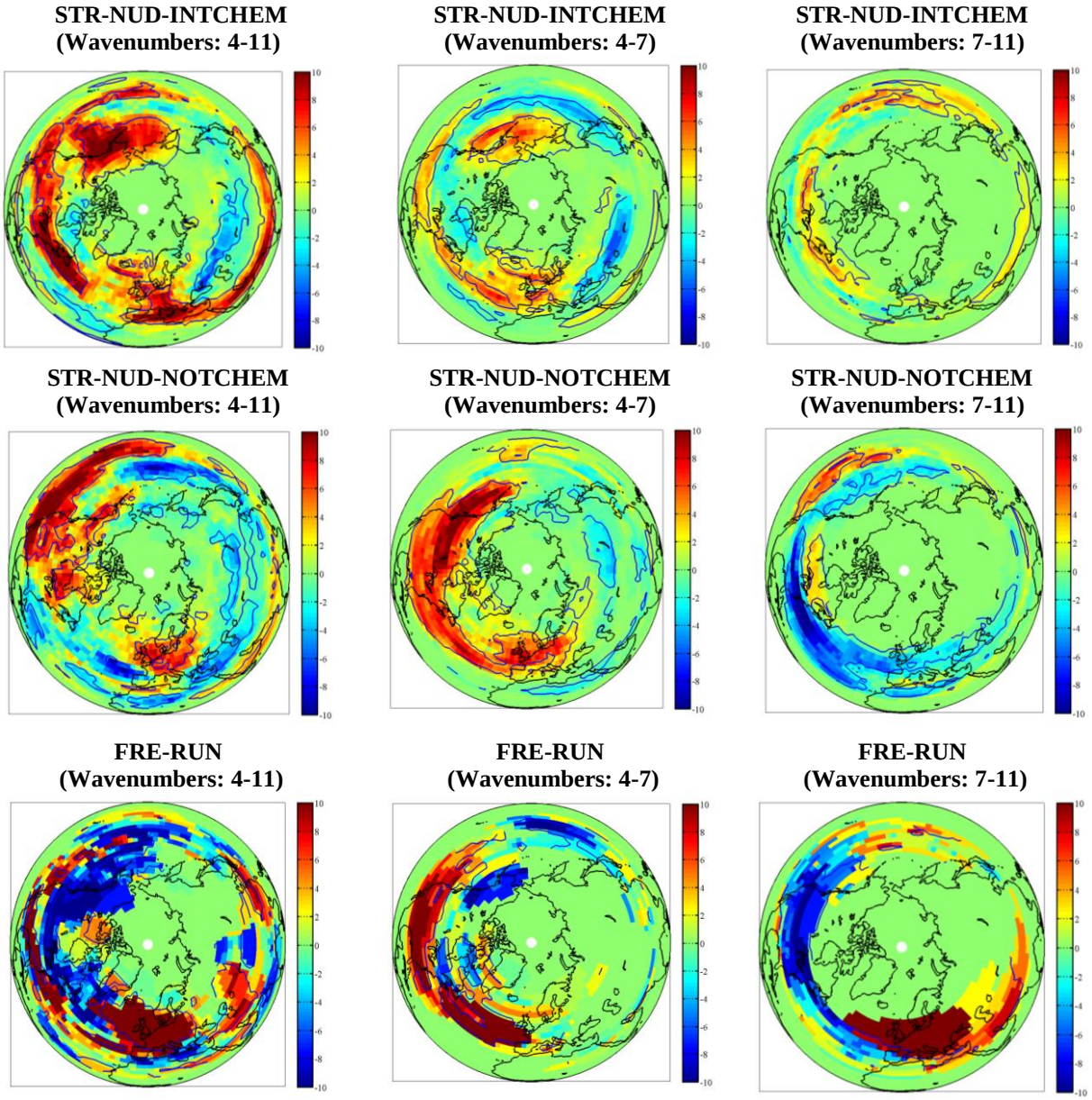

Figure 6.7: Same as Fig. 6.6 for the STR-NUD and FRE-RUN simulations.

6.4 Changes in the Tropospheric Baroclinicity and Tropopause Height as Influenced by the Stratospheric Wind Regimes

The difference in the Eady growth rate between the SVR and WVR at 250 hPa is presented in Fig. 6.8. Here changes in the Eady growth rate denote changes in the atmospheric baroclinicity. In ERA data northward of $50°N$ statistically significant changes in the atmospheric baroclinicity are found which indicate a strong potential for generation of new eddies in these regions. The differences in the FUL-NUD simulations resemble the changes in the reanalysis data, though the FUL-NUD-INTCHEM is more similar to the ERA than the FUL-NUD-NOCHEM simulation. However the regions of enhancement in the baroclinicity for STR-NUD-NOCHEM is larger than ERA and reach to midlatitudes. For the STR-NUD-INTCHEM simulation, the pattern of the differences are similar to the ERA, though the magnitude is smaller. The FRE-RUN show only a slight enhancement of the baroclinicity during SVR compared to the WVR period.
In the current study I used WMO (1957) criteria for the thermal tropopause determination. The lowest level (excluding surface inversions) at which the lapse-rate decreases to 2°C/km or less is defined as tropopause height. Figure 6.9 shows the height of the tropopause during SVR and WVR. The stratospheric mass redistribution acts in a way that during WVR adiabatic descent in the stratosphere pushes the tropopause height lower down making a shallower troposphere while the opposite take place during SVR (Ambaum and Hoskins (2002)). The deeper troposphere during the SVR provides a strong potential for the genesis of new eddies within the troposphere. I found approximately 2 km variations in the tropopause height near the Arctic in ERA data according to different states of the stratospheric flow. The FRE-RUN simulation shows a slight difference in the tropopause height northward of $75°N$. Therefore I conclude that a significant difference in the tropopause height in FRE-RUN is not found. In the STR-NUD simulations, I found the tropopause height approximately 0.5 km higher than ERA. Similar to ERA and FUL-NUD simulations, in the STR-NUD simulations the tropopause height during SVR and WVR are separated from each other from $60° - 90°N$. This behavior is not found in FRE-RUN simulation.

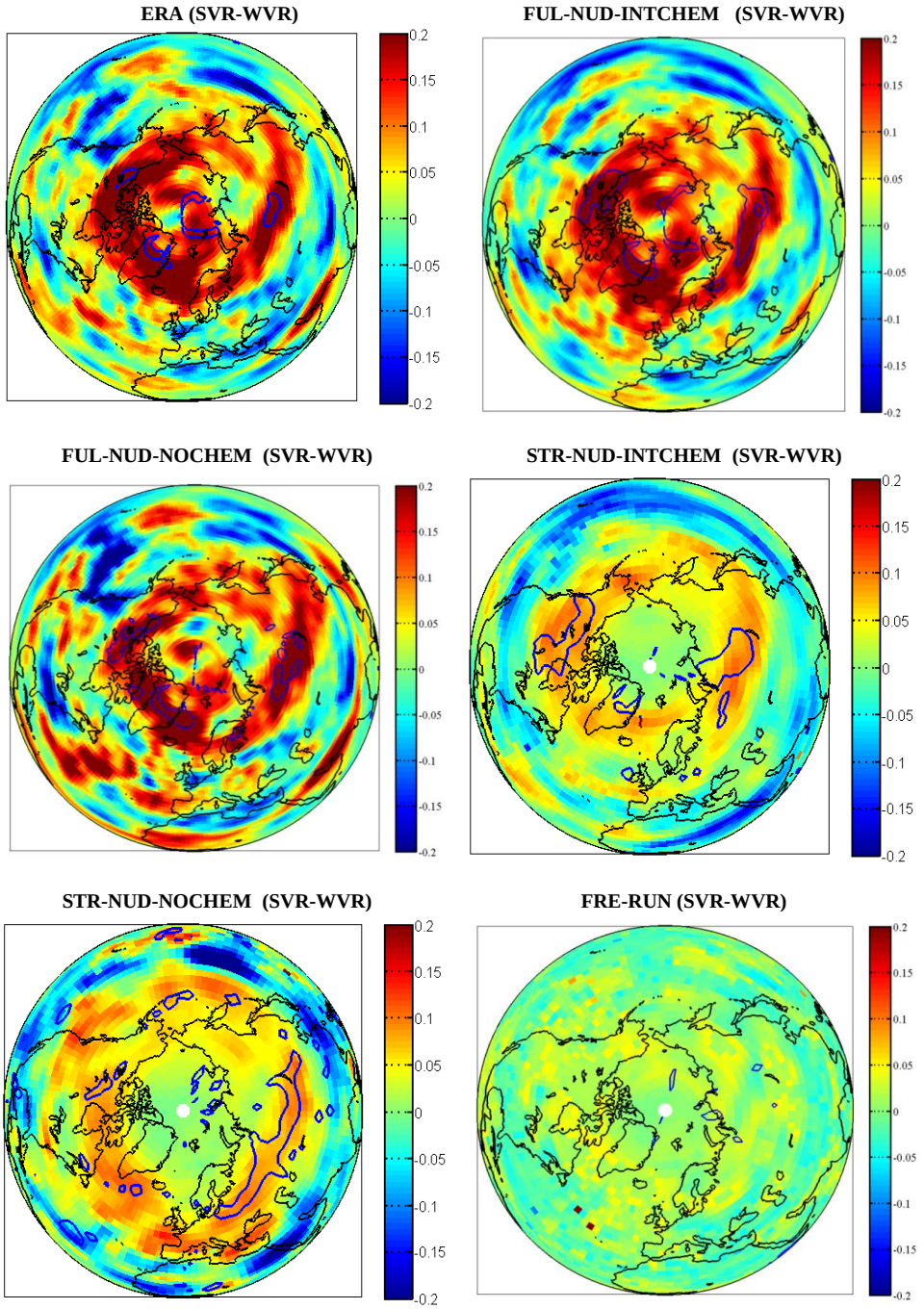

Figure 6.8: The difference in the measure of atmospheric baroclinicity at 250 hPa (day^{-1}). The upper-tropospheric enhancement in the Eady growth rate at polar regions show a source of the eddy feedback during SVR. The yellow/red colours represent the genesis locations. The blue lines are the regions of the statistically significant changes according to student's t test with 99.5% significance level.

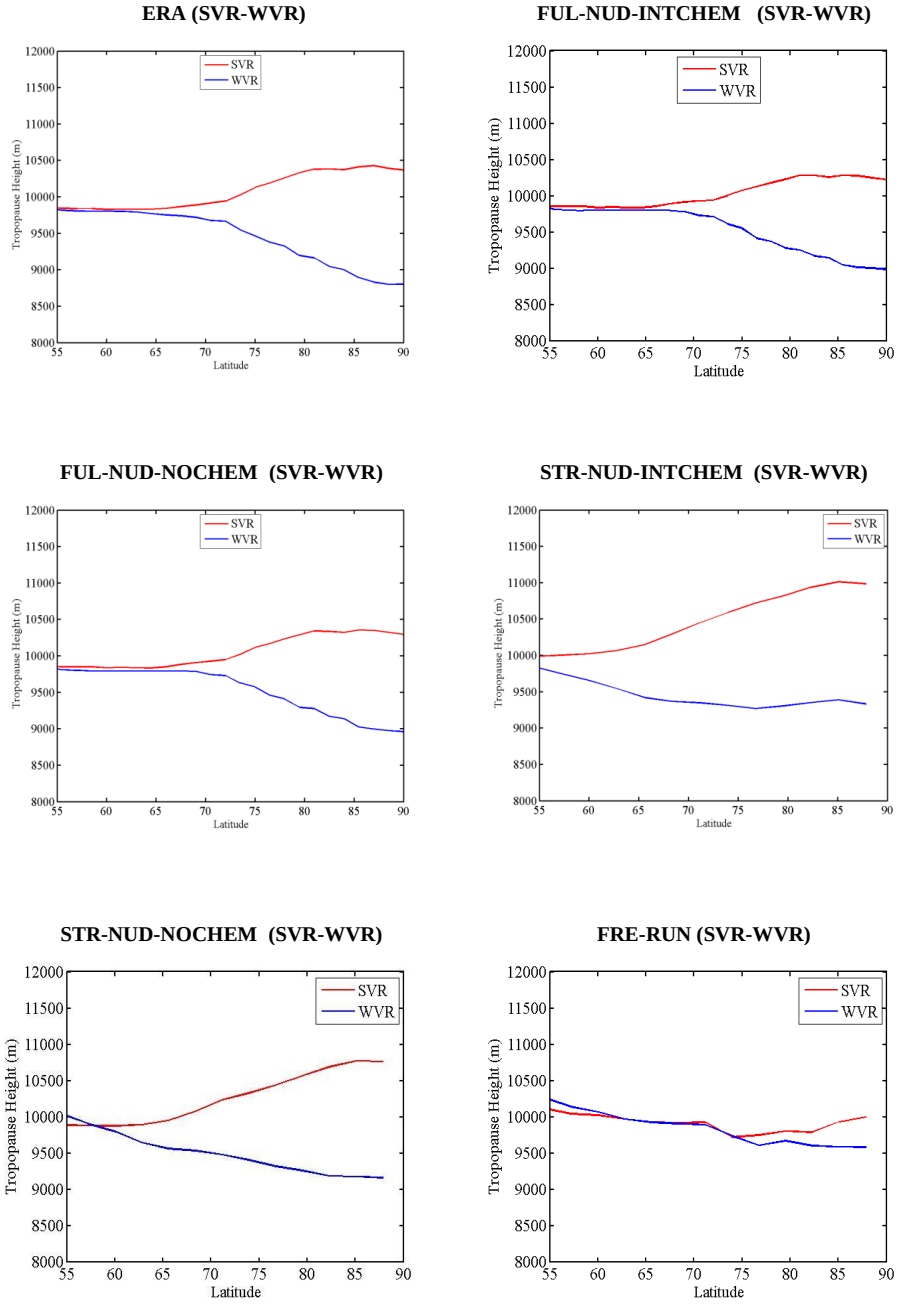

Figure 6.9: Changes in the tropopause height according to the different state of the stratospheric flow. Adiabatic descent of the stratospheric air pushes the tropopause lower down during WVR, causing a shallower troposphere. The deeper troposphere during the SVR provides a strong potential for the genesis of the new eddies within the troposphere.

6.5 Changes in the Stability and Wind Shear of the Atmosphere as Influenced by the Stratospheric Wind Regimes

In order to understand the dynamical mechanism of the above-mentioned localized enhancement in the baroclinicity, I further analyse the changes in the vertical shear of the zonal wind and the atmospheric stability in three different regions of the atmosphere namely North Atlantic, North Pacific and Eurasian regions (Fig. 6.10) for ERA data. A large positive difference in the vertical shear of zonal wind during SVR comparing to WVR indicates the impediment of the upward propagation of planetary waves from the troposphere to the stratosphere (Chen and Robinson (1992),Karami et al. (2016)). In all three regions the maximum of the differences in the vertical wind shear occurs in the lower-middle stratosphere (200 hPa- 20 hPa).

Northward of $50°N$ and above 20 hPa strong negative differences in the wind shear are found in all three regions. The positive changes in the atmospheric stability during SVR suggest that during these events the stratosphere is more stable than during the WVR. In contrast, the upper and middle troposphere become unstable during the SVR compared to WVR suggesting a stronger potential for the development of baroclinicity in these regions. Since the altitude of significant differences in the wind shear are already above 250 hPa, the enhancement of the Eady growth rate during SVR can be mainly explained by the reduction of the atmospheric stability during these events rather than changes in the propagation conditions of large-scale waves from the troposphere to the stratosphere. The regions of atmospheric instability during SVR is confined to poleward of $60°N$ in the upper troposphere and its maximum is near the north pole. The significant changes in the tropospheric stability in response to the different states of the stratospheric flow, suggest similar changes in the atmospheric lapse rate and the tropopause height.

The results obtained in this thesis suggest that the localized enhancement in the baroclinicity as well as changes in the tropopause height according to the different state of the stratospheric wind is mainly a dynamical process rather than a radiative or thermodynamical process. This dynamical relationship is weakly present in the free-running mode of the EMAC model (possibly due to the weak stratospheric westerlies in the free-running mode). However, through a realistic representation of the stratospheric flow, the EMAC model performs well compared to reanalysis data.

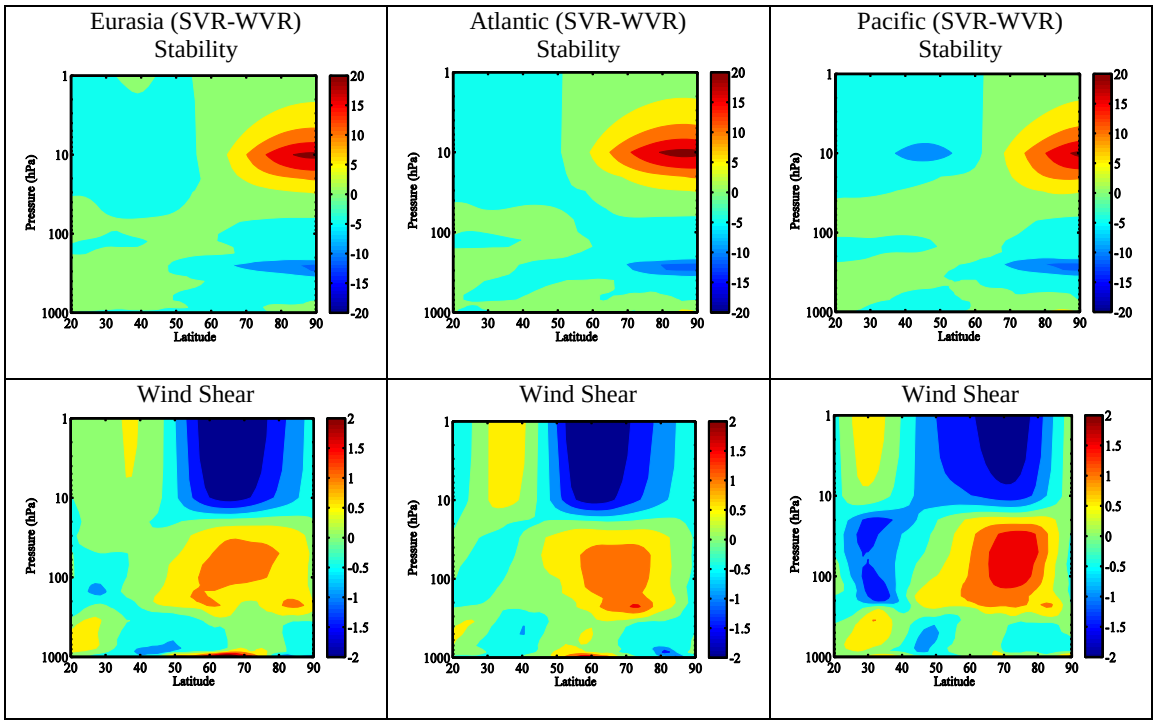

Figure 6.10: Changes in the determining factors for the atmospheric baroclinicity in response to different stratospheric wind regimes (for ERA data). The first row shows the changes in the stability of the atmosphere (normalized by 1e8). The positive values of this quantity indicates the regions with higher atmospheric stability while negative values shows the regions of lower atmospheric stability. Second row: changes in the vertical shear of zonal wind (SVR-WVR) which is normalized by 1000. The positive values imply the impediment of the planetary wave propagation from the troposphere to the stratosphere.

7 Summary and Outlook

In this thesis the downward influence of the middle atmosphere (from the solar and geomagnetic variabilities) on tropospheric weather and circulation has been investigated. To this end, two major topics are covered which are closely connected. The first topic is whether and how the confined ozone changes in the middle atmosphere due to geomagnetic and solar activities can trigger large-scale dynamical anomalies in the middle atmosphere. The second major topic which has been investigated in this thesis is how changes in the middle atmosphere can influence the weather (storm-tracks in particular) in the troposphere.

A chemistry-climate model (EMAC) is deployed to perform numerous perturbation runs to explore how persistent stratospheric wind regimes (during Northern hemispheric extended winter) influence the upper tropospheric synoptic-scale Rossby wave propagation and baroclinicity. A comparison of the results obtained with the EMAC model with ERA-Interim reanalysis data is performed. I also investigate the role of the near-pole persistent stratospheric wind regimes on the tropopause height variations and its potential influence on the upper-tropospheric baroclinicity. I find that the stratospheric persistent wind regimes can alter the stability, and hence the baroclinicity of the troposphere. The shallower troposphere during weak vortex regime restricts the upper tropospheric baroclinicity while the deeper troposphere during strong vortex regime provides a window of opportunity for the generation of new eddies within the troposphere (upper tropospheric enhancement of the baroclinicity during strong vortex regime). I also track the significant Rossby wave packets (wave packet amplitudes larger than $20\frac{m}{s}$) in different states of the stratospheric wind regimes for wavenumbers 4-11. An enhancement of the Rossby wave packet activity at high latitudes and a reduction at extra tropics indicate a poleward shift of the wave packets during strong vortex regime in ERA dataset.

I also investigate the role of the spatially long synoptic waves (wavenumbers 4-7) and smaller synoptic waves (wavenumbers 7-11) on the meridional shift of the eddy activities in the upper troposphere in response to variations in the strength of the stratospheric wind. The representation of the above-mentioned mechanisms in several types of simulations with the EMAC model and its comparison with the results

obtained by the ERA dataset suggests that a realistic representation of the internal tropospheric processes in EMAC model is essential for obtaining the full details of stratospheric downward influence on tropospheric eddy activity.

By using the EMAC model I have determined the downward influence of the changed ozone concentrations (due to the solar and geomagnetic variabilities) on the middle atmospheric temperature and circulation. The direct radiative impact of wintertime ozone depletion inside the polar night jet suggests that the strongest short wave heating rate changes occur in the stratopause and upper stratosphere regions. The net effect of ozone depletion is local cooling. However, in the mesospheric altitudes, a local heating is found possibly due to the enhanced absorption of solar radiation, which has not been absorbed above due to ozone loss. Contrary to the net cooling effect of imposed ozone depletion due to less short wave absorption, the long wave heating rate changes show opposite behavior above and below of approximately the stratopause. A relative warming effect is found in the upper stratosphere and mesosphere possibly due to the fact the in these altitudes ozone locally emits long wave radiation and cools the atmosphere, less cooling due to less ozone will result in a relative warming effect. The Southern and Northern hemispheric polar night jet accelerates and decelerated respectively due to the imposed ozone changes. The accelerated polar night jet of Southern hemisphere is interpreted as the direct radiative impact of ozone depletion inside of the Southern hemisphere polar vortex. However, the weakened polar night jet of Northern hemisphere is very unlikely to be caused in situ by ozone depletion and indirect dynamical conditions play a great role in the Northern hemisphere. Analysis of the frequency and timing of the sudden stratospheric warmings in the Northern hemisphere show that the frequency of warmings has not changed significantly. However, a shift of their timing toward mid and late winter is detected. Analysis of the Rossby wave propagation condition suggest that changes in the ozone concentration in stratospheric and mesospheric heights have the capability to alter the propagation condition of Rossby waves. The signal of changes in this quantity can reach to tropospheric height in late winter and early spring of both hemispheres. I also found that the magnitude of the temperature and zonal wind responses in the case of ozone perturbation due to high energy particle precipitation could exceed (or at least be comparable) to the responses of ozone changes due to the solar UV variability.

The results obtained in this thesis as well as their theoretical explanation of the downward influence of the stratosphere on tropospheric weather and circulation will help to explain how the solar as well as geomagnetic variabilities can affect the troposphere. During this study several additional research questions were raised which answering might provide further insight to further characterize the relationship be-

tween the middle atmosphere and troposphere.

The first question is the time scale in which the middle atmosphere troposphere coupling occurs. Whether the influence of the middle atmosphere on the troposphere is instantaneous or there exists time lag for the coupling is an interesting research question to explore in the future. Answering to this question is particularly important because it might help answering another very interesting research question which is how the middle atmosphere can improve the skill of the tropospheric weather forecasts.

Bibliography

Ambaum M., Hoskins B. J. (2002). The NAO troposphere-stratosphere connection. *J. Clim. 15*, 1969–1978.

Andersson M. E., Verronen P. T., Rodger C. J., Clilverd M. A., Seppälä A. (2014). Missing driver in the Sun-Earth connection from energetic electron precipitation impacts mesospheric ozone. *Nature communications* , doi:10.1038/ncomms6197.

Andrews G.G., Leovy C.B., Holton J.R. (1987). Middle Atmosphere Dynamics. *Academic Press, San Diego* , isbn:978-0120585762.

Austin J., Hood L.L., Soukharev B.E. (2007). Solar cycle variations of stratospheric ozone and temperature in simulations of a coupled chemistry-climate model. *Atmos. Chem. Phys. 7*, 1693–1706.

Ayarzagüena B., Langematz U., Meul S., Oberländer S., Abalichin J., Kubin A.(2013). The role of climate change and ozone recovery for the future timing of Major Stratospheric Warmings. *Geophysical Research Letters 40*, 2460–2465.

Bailey S. M., Thurairajah B., Randall C.E., Holt L., Siskind D.E., Harvey V.L., Venkataramani K., Hervig M.E., Rong P., Russell J.M.(2014). A multi tracer analysis of thermosphere to stratosphere descent triggered by the 2013 Stratospheric Sudden Warming. *Geophys. Res. Lett.* , doi:10.1002/2014GL059860.

Baldwin M. P., and Dunkerton, T. J. (2001). Stratospheric harbingers of anomalous weather regimes. *SCIENCE. 294*, 581–584.

Baldwin M. P., and Dunkerton, T. J. (1999). Propagation of the Arctic Oscillation from the stratosphere to the troposphere. *J. Geophys. Res. 104*, 30,937-30,946.

Baumgaertner A.J.G., Jöckel P., Brühl C. (2009). Energetic particle precipitation in ECHAM5/MeSSy1 - Part 1: Downward transport of upper atmospheric NOx produced by low energy electrons. *Atmos. Chem. Phys. 9*, 2729–2740.

Baumgaertner A. J. G., Seppälä A., Jöckel P., Clilverd M.A. (2011). Geomagnetic activity related NOx enhancements and polar surface air temperature variability in a chemistry climate model: modulation of the NAM index. *Atmos. Chem. Phys. 11*, 4521–4531.

Benedict J.J., Lee S., Feldstein S.B. (2004). Synoptic view of the North Atlantic Oscillation. *J. Atmos. Sci. 61*, 121–144.

Black R.X., Dole R. (2000). Storm Tracks and Barotropic Deformation in Climate Models. *Journal of Climate 13*, 2712-2728.

Black R.X., McDaniel B. (2007). Interannual variability in the Southern Hemisphere circulation organized by stratospheric final warming events. *Atmospheric Sciences 64*, 2968–2975.

Black R.X., McDaniel B. (2007). The dynamics of Northern Hemisphere stratospheric final warming events. *Atmospheric Sciences 64*, 2932–2946.

Blackmon M.L., Lee Y.H., Wallace J.M. (1984). Horizontal structure of 500 mb height fluctuations with long, intermediate and short time scales. *J. Atmos. Sci. 41*, 961-980.

Boville B. A. (1984). The Influence of the Polar Night Jet on the Tropospheric Circulation in a GCM. *Journal of the Atmospheric Sciences. 41(7)*, 1132–1142.

Brasseur G. (2005). Aeronomy of the middle atmosphere, chemistry and physics of the stratosphere and mesosphere. *Kluwer Academic Publishers, Springer US.* , isbn: 978-1-4020-3824.

Braesicke P., Pyle J.A. (2003). Changing ozone and changing circulation in northern mid-latitudes: Possible feedbacks? *Geophysical Research Letters 30*, doi:10.1029/2002GL015973.

Bracegirdle T.(2011). The seasonal cycle of stratosphere-troposphere coupling at southern high latitudes associated with the semi-annual oscillation in sea-level pressure. *Climate Dynamics 37*, doi:10.1007/s00382-011-1014-4.

Broccoli A.J., Manabe S.(1992). The Effects of Orography on Midlatitude Northern Hemisphere Dry Climates. *Journal of climate 5*, 1181-1201.

Brönnimann S., Bhend J., Franke J., Fückiger S., Fischer A.M., Bleisch R., Bodeker G., Hassler B., Rozanov E., Schraner M.(2013). A global historical ozone data set and prominent features of stratospheric variability prior to 1979. *Atmos. Chem. Phys. 13*, 9623–9639.

Castanheira J.M., Graf H.(2003) North Pacific-North Atlantic relationships under stratospheric control?. *J. Geophys. Res.* , doi=10.1029/2002JD002754.

Chang E., Orlanski I.(1993). On the Dynamics of a Storm Track. *Journal of the Atmospheric Sciences 50(7)*, 999-1015.

Chang E.(2001). The Structure of Baroclinic Wave Packets. *Journal of the Atmospheric Sciences. 58*, 1694-1713.

Chang E., Lee S., Swanson K.(2002). Storm Tracks Dynamics. *Journal of climate 15*, 2163-2183.

Chang E.(2005). The role of wave packets in wave/mean flow interactions during Southern Hemisphere summer. *J. Atmos. Sci. 62*, 2467-2483.

Charlton A. J., ONeill A., Lahoz W. A., Massacand A. C., and Berrisford P. (2005). The impact of the stratosphere on the troposphere during the southern hemisphere stratospheric sudden warming, September 2002. *Q. J. R. Meteorol. Soc. 8*, doi:10.1256/qj.04.43.

Charlton A. J., Polvani L. M. (2007). A new look at stratospheric sudden

warmings. Part I : Climatology and modeling benchmarks. *Journal of climate 20*,449–469.

Charlton A.J., Polvani L.M., Perlwitz J., Sassi F., Manzini E., Shibata K., Pawson S., Nielsen J.E., Rind D.(2007). A new look at stratospheric sudden warmings. Part II: Evaluation of numerical model simulations. *Journal of climate 20*,470–488.

Charney J.G., Drazin P.G. (1961). Propagation of planetary scale disturbances from the lower into the upper atmosphere. *Journal of Geophysical Research 66*,83–109.

Chen P. C., Held G. (2007). Phase speed spectra and the recent poleward shift of Southern Hemisphere surface westerlies *Geophys. Res. Lett. 34*, doi=10.1029/2007GL031200.

Chen P. C., and Robinson W. A. (1992). propagation of planetary waves between the troposphere and stratosphere *J. Atmos. Sci. 49*, 2533–2545.

Christiansen B., Guldberg A., Hansen A.W., Riishojgaard L.P.(1997). On the response of a three–dimensional general circulation model to imposed changes in the ozone distribution. *Journal of Geophysical Research 102*, 13051–13077.

Dhomse S.S., Chipperfield M.P. Feng W., Ball W.T. Unruh Y.T. Haigh J.D., Krivova N.A., Solanki S.K., Smith A.K. (2013). Stratospheric O3 changes during 2001-2010: the small role of solar flux variations in a chemical transport model. *Atmospheric Chemistry and Physics 13*, doi:10.5194/acp-13-10113-2013.

Dickinson R.E.(1969a). Theory of planetary wave–zonal flow interaction. *Journal of Atmospheric Science 26*, 73–81.

Dickinson R.E.(1969b). Vertical propagation of planetary Rossby waves through and atmosphere with Newtonian cooling. *Journal of Geophysical Research 74*, 929–938.

Dunkerton T. J., Hsu C. P. F., McIntyre M. E.(1981). Some Eulerian and Lagrangian diagnostics for a model stratospheric warming. *Journal of Atmospheric Science 38*, 819–843.

Edmon H. J., Hoskins J. B. J., McIntyre M. E.(1980). Eliassen–Palm cross sections for the troposphere. *Journal of Geophysical Research 37*, 2600–2616.

Eliassen A., Palm E. (1960). On the transfer of energy in stationary mountain waves. *J. Atmos. Sci. 22*, 1–23.

Fortuin J.P.F., Langematz U. (1994). An update on the global ozone climatology and on concurrent ozone and temperature trends. *SPIE Atmos. Sens. Model. 2311*, 207–216.

Fröhlich C., and Lean J. (2004). Solar radiative output and its variability: evidence and mechanisms *Astron. Astrophys. Rev. 12(4)*, 273–320.

Funke B., López-Puertas M., Gil-Lopez S., Von Clarmann T., Stiller G., Fis-

cher H., Kellmann S.(2005). Downward transport of upper atmospheric NOx into the polar stratosphere and lower mesosphere during the Antarctic 2003 and Arctic 2002/2003 winters. *Journal of Geophysical Research 110*, doi:10.1029/2005JD006463.

Funke B., López-Puertas M., Stiller G. P., Von Clarmann T. (2014). Mesospheric and stratospheric NOy produced by energetic particle precipitation during 2002-2012. *Journal of Geophysical Research 119*, 4429-4446.

Fytterer T., Mlynczak M.G., Nieder H., Perot K., Sinnhuber M., Stiller G., Urban J. (2015a). Energetic particle induced intra-seasonal variability of ozone inside the Antarctic polar vortex observed in satellite data. *Atmos. Chem. Phys.* , doi:10.5194/acpd-14-1-2014.

Fytterer T., Santee M.L., Sinnhuber M., Wang S. (2015b). The 27day solar rotational effect on mesospheric nighttime OH and O3 observations induced by geomagnetic activity. *J. Geophys. Res. 49*, doi:10.1002/2015JA021183.

Garfinkel C., Waugh D., Gerber E. (2013). The effect of tropospheric jet latitude on coupling between the stratospheric polar vortex and the troposphere. *J. Clim. 26*, doi:10.1175/JCLI-D-12-00301.1.

Gray L. J., Beer J., Geller M., Haigh J. D., Lockwood M., Matthes K., Cubasch U., Fleitmann D. Harrison G., Hood L., Luterbacher J., Meehl G. A., Shindell D., van Geel B., White W. (2010). Solar influences on climate. *Reviews of Geophysics 48*, doi:10.1029/2009RG000282.

Grise K., Thompson D., Forster P.(2009). On the Role of Radiative Processes in Stratosphere-Troposphere Coupling. *JOURNAL OF CLIMATE 22*, 4154–4161.

Gruzdev A.N.(2014). Estimate of the Effect of the 11-Year Solar Activity Cycle on the Ozone Content in the Stratosphere. *Geomag. Aeronom. 54*, 633–639.

Haigh J.D.(1994). The role of stratospheric ozone in modulating the solar radiative forcing of climate. *Nature 370*, 544–546.

Haigh J.D., Winning A.R., Toumi R., Harder J.W.(2010). An influence of solar spectral variations on radiative forcing of climate. *Nature 467*, 696–699.

Hakim G.J.(2005). Vertical structure of midlatitude analysis and forecast errors. *Mon. Wea. Rev. 133*, 567-578.

Hauchecorne A., Bertaux J.L., Dalaudier F., Russell J.M., Mlynczak M.G., Kyrölä E., Fussen D.(2007). Large increase of NO2 in the north polar mesosphere in January-February 2004: Evidence of a dynamical origin from GOMOS/ENVISAT and SABER/TIMED data. *Geophys. Res. Lett. 34*, doi:10.1029/2006GL027628.

Haynes P.H., Marks C.J., McIntyre M.E., Shepherd T.G., Shine K.P.(1991). On the Downward Control of Extratropical Diabatic Circulations by Eddy-Induced Mean Zonal Forces. *Journal of the Atmospheric Sciences 48(4)*, 651–

679.

Hinman R.(1888). Eclectic Physical Geography. *The Eclectic Geographies (American Book Company) 1. edition.*

Hirota I., Sato Y. (1969). Periodic variation of the winter stratospheric circulation and intermittent vertical propagation of planetary waves. *Journal of the Meteorological Society of Japan 47*, 390–402.

Holton J.R., Tan H.C.(1980). The influence of the equatorial quasi-biennial oscillation on the global circulation at 50 mb. *J. Atmos. Sci. 37*, 2200–2208.

Holton J.R., Tan H.C.(1982). The quasi-biennial oscillation in the Northern Hemisphere lower stratosphere. *J. Meteor. Soc. Japan. 60*, 140–148.

Holton J. R. (2004). An Introduction to Dynamic Meteorology. *isbn=978-0123540157 47*, Elsevier.

Holton J.R., Mass C. (1976). Stratospheric vacillation cycles. *Journal of Atmospheric Science 33*, 2218–2225.

Holton J.R., Dunkerton T. (1978). On the Role of Wave Transience and Dissipation in Stratospheric Mean Flow Vacillations. *Journal of Atmospheric Science 35*, 740–744.

Hood L.L., Soukharev B.E. (2012). The Lower-Stratospheric Response to 11-Ye Solar Forcing: Coupling to the Troposphere-Ocean Response. *Journal of Atmospheric Science 34*, doi:10.1175/JAS-D-11-086.1.

Hood L.L., Misios S., Mitchell D.M., Rozanov E., Gray L.J., Tourpali K., Matthes K., Schmidt H., Chiodo G., Thieblemont R., Shindell D., Krivolutsky A.(2015). Solar signals in CMIP-5 simulations: the ozone response. *Q. J. R. Meteorol. Soc.* , doi:10.1002/qj.2553.

Hoskins B. J., McIntyre M. E., Robertson A. W. (1985). On the use and significance of isentropic potential vorticity maps. *Q. J. R. Meteorol. Soc. 111*, 877–946.

Hoskins B. J., Valdes P.J. (1990). On the Existence of Storm-Tracks. *Journal of the Atmospheric Sciences 47(15)*, 1854–1864.

Hovmöller E. (1949). The trough-and-ridge diagram. *Tellus 1*, 62–66.

Hu J.G., Ren R.C., Yu Y.Y., Xu H. (2014). The boreal spring stratospheric final warming and its interannual and interdecadal variability. *Science China Earth Sciences 14*, 710–718.

Hu Y., Tung K.K. (2002). Interannual and decadal variations of planetary wave activity, stratospheric cooling, and northern hemisphere annular mode. *Journal of Climate 15*, 1659–1673.

Huang R., Gambo K.(2002). The response of a Hemispheric Multi-Level Model Atmosphere to Forcing by Topography and Stationary Heat Sources (I) Foring by Topography. *J. Meteorol. Soc. Japan 60*, 78–92.

Hurrell J., Kushnir Y., Visbeck M. (2001). The North Atlantic Oscillation. *SCI-*

ENCE 291, 603–605.

Ineson S., and Scaife A. A. (2009). The role of the stratosphere in the European climate response to El Nino. *Nat. Geosci. 2*, 32–36.

Ineson S., Scaife A. A., Knight J. R., Dunstone J. C., Gray L. J., and Haigh J. D. (2011). Solar forcing of winter climate variability in the Northern Hemisphere *Nat. Geosci. 4*, 753–757.

Jackman C.H., Fleming E.L., Vitt F.M. (2000). Influence of extremely large solar proton events in a changing stratosphere. *Journal of Geophysical Research 11*, 659-670.

Jackman C. H., Roble R. G., Fleming E. L. (2007). Mesospheric dynamical changes induced by the solar proton events in October–November 2003. *Geophiysical Research Letters 34*, doi:10.1029/2006GL028328.

Jöckel P., Sander R., Kerkweg A., Tost H., Lelieveld J. (2005). Technical Note: The Modular Earth Submodel System (MESSy) - a new approach towards Earth System Modeling. *Atmospheric Chemistry and Physics 5*, 433–444.

Jöckel P. Tost H. Pozzer A. Brühl C. Buchholz J. Ganzveld L. Hoor P. Kerkweg A. Lawrence M. G. Sander R. Steil B. Stiller G. Tanarhte M. Taraborrelli D. van Aardenne J. Leliveld J. (2006). The atmospheric chemistry general circulation model ECHAM5/MESSy1: consistent simulation of ozone from the surface to the mesosphere. *Atmospheric Chemistry and Physics 6*, 5067–5104.

Jöckel P. Kerkweg A. Pozzer A. Sander R. Tost H. Riede H. Baumgaertner A. Gromov S. Kern B. (2010). Development cycle 2 of the Modular Earth Submodel System (MESSy2). *Geosci. Model Dev. 3*, 717–752.

Kalnay E. Kanamitsu M. Kistler R. Collins W. Deaven D. Gandin L. Iredell M. Saha S. White G. Woollen J. Zhu Y. Leetmaa A. Reynolds R. Chelliah M. Ebiasuzaki W. Higgins W. janowiak J. Mo K. C. Ropelewski C. Wang J. Jenne. R. Joseph D. (1996). The NCEP/NCAR 40-Year Reanalysis Project. *Bull. Amer. Meteor. Soc. 77*, 437–471.

Karami K., Ghader S., Bidokhti A. A., Joghataei M., Neyestani A., Mohammadabadi A. (2012). Planetary and tidal wave–type oscillations in the ionospheric sporadic E layers over Tehran region. *Journal of Geophysical Research 117*, doi=10.1029/2011JA017466.

Karami K., Braesicke P., Sinnhuber M., and Versick S. (2016). On the climatological probability of the vertical propagation of stationary planetary waves *Atmos. Chem. Phys. 16*, doi=10.5194/acp-16-8447-2016.

Karami K., Braesicke P., Kunze M., Langematz U., Sinnhuber M., and Versick S. (2015b). Modelled thermal and dynamical responses of the middle atmosphere to EPP-induced ozone changes. *Atmos. Chem. Phys. Discuss. 15*, doi=10.5194/acpd-15-33283-2015.

karoly D.J., Hoskins B.J(1982). Three dimensional propagation of planetary

waves. *J. Meteorol. Soc. Jpn. 60*, 109–122.

Kidston, J., Scaife, A. A., Hardiman S.,Mitchell D., Butchart N., Baldwin M., and Gray L. (2015). Stratospheric influence on tropospheric jet streams, storm tracks and surface weather. *Nat. Geosci. 8*, 433–440.

Kiehl J.T., Boville B.A. (1988). The radiative–dynamical response of a stratospheric-tropospheric general circulation model to changes in ozone. *Journal of Atmospheric Science 45*, 1798–1817.

Kodera K., Kuroda Y.(2002). Dynamical response to the solar cycle: Winter stratopause and lower stratosphere. *Journal of Geophysical Research 107(D24), 4749*, doi=10.1029/2002JD002224.

Kunz T., Fraedrich K., Lunkeit F. (2015). Synoptic scale wave breaking and its potential to drive NAO-like circulation dipoles: A simplified GCM approach. *Q. J. R. Meteorol. Soc. 135*, 1–19.

Labitzke K. (1987). Sunspots, the QBO and the stratospheric temperature in the north polar region. *Geophys. Res. Lett. 14*, 535-537.

Labitzke K., van Loon H. (1995). Connections between the troposphere and stratosphere on a decadal scale. *Tellus, Ser. A. 47*, 275-286.

Langematz U., Kunze M., Krüger K., Labitzke K., Roff G.L.(2003). Thermal and dynamical changes of the stratosphere since 1979 and their link to ozone and $CO2$ changes *Journal of Geophysical Research 108(D1)*, doi:10.1029/2002JD002069.

Langematz U., Grenfell J.L., Matthes K., Mieth P., Kunze M., Steil B., Brühl C. (2005). Chemical effects in 11-year solar cycle simulations with the Freie Universitat Berlin Climate Middle Atmosphere Model with online chemistry (FUB-CMAM-CHEM). *Geophys. Res. Lett. 32*, doi:10.1029/ 2005GL022686.

Lary D.J. (1997). Catalytic destruction of stratospheric ozone. *J. Geophys. Res. 102*, 21515-21526.

Lean J., Rottman G., Kyle H., Woods T., Hickey J., Puga L.(1997). Detection and parameterisation of variations in solar midand near-ultraviolet radiation (200-400 nm). *J. Geophys. Res. 102(D25)*, 939-956.

Li Q. Garf H.F., Giorgetta M.A.(2007). Stationary planetary wave propagation in Northern Hemisphere winte - climatological analysis of the refractive index. *Atmospheric Chemistry and Physics 7*, 183–200.

Limpasuvan V., Hartmann D. L.(2000). Wave-maintained annular modes of climate variability. *J. Climate. 13*, 4414–4429.

Li Y., Lau N.C.(2012). Contributions of downstream eddy development to the teleconnection between ENSO and the atmospheric circulation over the North Atlantic. *J. Climate. 25*, 4993-5010.

Lopez-Puertas M., Funke B., von Clarmann T., Fischer H., Stiller G.P. (2006). The stratospheric and mesospheric NOy in the 2002-2004 polar winters as

measured by MIPAS/ENVISAT. *Space Sci. Rev. 125*, doi=10.1007/s11214-006-9073-2.

Lu H., Clilverd M.A., Seppälä A., Hood L.L.(2008). Geomagnetic perturbations on stratospheric circulation in late winter and spring. *Journal of Geophysical Research 113*, doi=10.1029/2007JD008915.

Maritus O., Schwierz C., Davies H.C.(2007). Breaking waves at the tropopause in the wintertime Northern Hemisphere: Climatological analyses of the orientation and the theoretical LC1/2 classification. *J. Atmos. Sci. 64*, 2576-2592.

Maritus O., Schwierz C., Davies H.C.(2008). Far-upstream precursors of heavy precipitation events on the Alpine south-side. *Quart. J. Roy. Meteor. Soc. 134*, 417-428.

Maritus O., Schwierz C., Davies H.C.(2010). Tropopause level waveguides. *J. Atmos. Sci. 67*, 866-879.

Marsh D.R., Garcia R.R., Kinnison D.E., Boville B.A., Sassi F., Solomon S.C., Matthes K.(2007). Modeling the whole atmosphere response to solar cycle changes in radiative and geomagnetic forcing. *Journal of Geophysical Research 112*, doi:10.1029/2006JD008306.

Martin J. (2006). Mid-Latitude Atmospheric dynamics. *Wiley* .

Matsuno. T (1970). Vertical propagation of stationary planetary waves in the winter Northern Hemisphere. *J. Atmos. Sci. 27*, 871–883.

McInturff R.M. (1978). Stratospheric warmings: Synoptic, dynamic and general–circulation aspects *Tech. Rep. NASA–RP–1017, NASA Reference Publ., Washington, DC* .

Merkel A.W., Harder J.W., Marsh D.R., Smith A.K., Fontenla J.M., Woods T.(2011). The impact of solar spectral irradiance variability on middle atmospheric ozone. *Geophys. Res., Lett. 38*, doi:10.1029/2011GL047561.

Monier E., Weare B. C.(2011). Climatology and trends in the forcing of the stratospheric zonal–mean flow. *Atmospheric Chemistry and Physics 11*, 12751–12771.

Mukougawa H. Hirooka T.(2004). Predictability of stratospheric sudden warming: A case study for 1998/99 winter. *Mon. Wea. Rev. 132*, 1764–1776.

Nakamura H. (1992). Midwinter suppression of baroclinic wave activity in the North Pacific. *J. Atmos. Sci. 49*, doi:10.1175/1520-0469(1992)049,1629:MSOBWA.2.0.CO;2.

Natarajan M., Remsberg E.E. Deaver L.E. Russell J.M. (2004). Anomalously high levels of NOx in the polar upper stratosphere during April, 2004: Photochemical consistency of HALOE observations. *Geophys. Res., Lett.* , doi:10.1029/2004GL020566.

Nissen K. M., Matthes K., Langematz U., Mayer B. (2007). Towards a better representation of the solar cycle in general circulation models. *Atmospheric*

Chemistry and Physics 7, 5391–5400.

Novak V., Perfilieva I., Mocker J. (1999). Mathematical principles of fuzzy logic. *Kluwer Academic Publishers, Springer US* , isbn: 0-7923-8595-0.

Ogurtsov M. G., Nagovitsyn Y. A., Kocharov G., Jungner E. (2002). Long-period cycles of the SunâĂŹs activity recorded in direct solar data and proxies *Solar Physics 211(1-2)*, 371–394.

Päivärinta S.M., Seppälä A., Andersson M.E., Verronen P.T. Thölix L., Kyrölä E.(2013). Observed effects of solar proton events and sudden stratospheric warmings on odd nitrogen and ozone in the polar middle atmosphere. *Journal of Geophysical Research 118*, 6837–6848.

Palmer T.N. Diagnostic study of a wavenumber, 2, Stratospheric sudden warming in a transformed Eulerian–mean formalism. *Journal of Atmospheric Science 38*, 844–855.

Perlwitz L., and Harnik N. (2003). Observational evidence of a stratospheric influence on the troposphere by planetary wave reflection. *J. Clim. 16*, 3011-3026.

Perlwitz L., and Harnik N. (2004). Downward coupling between the stratosphere and troposphere: The relative roles of wave and zonal mean processes. *J. Clim. 17(24)*, 4902-4909.

Perot K., Urban J., Murtagh D.P.(2014). Unusually strong nitric oxide descent oin the Arctic middle atmosphere in early 2013 as observed by ODIN/SMR. *Atmos. Chem. Phys. 14*, 8009-8015.

Pierrehumbert R.T., Swanson K.L.(1995). Baroclinic instability. *Annu. Rev. Fluid Mech. 27*, 419-467.

Plumb A.(2003). On the seasonal cycle of stratospheric planetary waves. *Pure and Applied Geophysics 130 (2/3)*, 233-242.

Randall C.E., Rusch D.W., Bevilacqua R.M, Hoppel W., Lumpe J.D.(1998). Polar ozone and aerosol meausurement (POAM) II stratospheric NO_2, 1993–1996. *Journal of Geophysical Research 28*, 361–371.

Randall C.E., Harvey V.L., Manney G.L., Orsolini Y., Codrescu M., Sioris C., Brohede S., Haley C.S., Gordley L.L., Zawodny J.M., Russell J.M.(2005). Stratospheric effects of energetic particle precipitation in 2003–2004. *Geophys. Res., Lett. 32*, doi:10.1029/2004GL022003.

Randall C.E., Harvey V.L., Singleton C.S., Bernath P.F., Boone C.D., Zozyra J.U. (2006). Enhanced NOx in 2006 linked to strong upper stratospheric Arctic vortex. *Geophys. Res., Lett. 33*, doi:10.1029/2006GL027160.

Randall C.E., Harvey V.L., Singleton C.S., Bailey S.M., Bernath P.F., Codrescu M., Nakajima H., Russell J.M.(2007). Energetic particle precipitation effects on the Southern Hemisphere stratosphere in 1992-2005. *J. Geophys. Res. 112*, doi:10.1029/2006JD007696.

Randall C.E., Harvey V.L., Siskind D.E., France J., Bernath P.F., Boone C.D.,

Walker K.A. (2009). NO_x descent in the Arctic middle atmosphere in early 2009. *Geophysical Research Letters 36*, doi:10.1029/ 2009GL039706.

Randel W.J.(1988). The seasonal evolution of planetary waves in the southern hemisphere stratosphere and troposphere. *Q. J. R. Meteorol. Soc. 114*, 1385-1409.

Randall C. E., Harvey V. L., Siskind D. E., France J., Bernath P. F., Boone C. D., Walker K. A. (2009). NO_x descent in the Arctic middle atmosphere in early 2009. *Geophysical Research Letters 36*, doi=10.1029/ 2009GL039706.

Reddmann T., Ruhnke R., Versick S., Kouker W. (2010). Modeling disturbed stratospheric chemistry during solar-induced NOx enhancements observed with MIPAS/ENVISAT. *J. Geophys. Res. 115*, doi:10.1029/2009JD012569.

Remsberg E.E.(2008). On the response of Halogen Occultation Experiment (HALOE) stratospheric ozone and temperature to the 11-year solar cycle forcing. *J. Geophys. Res. 113*, doi=10.1029/2208JD010189.

Riviere G. (2011). A dynamical interpretation of the poleward shift of the jet streams in global warming scenarios *J. Atmos. Sci. 68*, 1253–1272.

Roeckner E., Bauml G., Bonaventura L., Brokopf R., Esch M., Giorgetta M., Hagemann S., Kirchner I., Kornblueh L., Manzini E., Rhodin A., Schlese U., Schulzweida U., and Tompkins, A. (2003). The atmospheric general circulation model ECHAM5. PART I: Model description. *Tech. rep., Max Planck Institute for Meteorology,MPI-Report 349* .

Roeckner E., Brokopf R., Esch M. Giorgetta M. Hagemann S. Kornblueh L. Manzini E. Schlese U. Schulzweida U.(2004). The atmospheric general circulation model ECHAM5. PART II: Sensitivity of Simulated Climate to Horizontal and Vertical Resolution. *Tech. rep., Max Planck Institute for Meteorology,MPI-Report 354* .

Rozanov E., Callis L., Schlesinger M., Yang F., Andronova N., Zubov V.(2005). Atmospheric response to NO_y source due to energetic electron precipitation. *Geophysical Research Letters 32*, doi:10.1029/ 2005GL023041.

Rozanov E., Calisto M., Egorova T., Peter T., Schmutz W.(2012). Influence of the Precipitating Energetic Particles on Atmospheric Chemistry and Climate. *Sur. Geo. 33*, doi:10.1007/s10712-012-9192-0.

Russel J.M., Solomon S., Gordley L.L., Remsberg E.E., Callis L.B.(1984). The Variability of Stratospheric and Mesospheric NO2 in the Polar Winter Night Observed by LIMS. *J. Geophys. Res. 89*, 7267–7275.

Salmi S.-M., Verronen P.T., Thölix L., Kyrölä E., Backman L., Karpechko A.Y., Seppälä A.(2011). Mesosphere-to-stratosphere descent of odd nitrogen in February-March 2009 after suden stratospheric warming. *Atmos. Chem. Phys. 89*, doi:10.5194/acp-11-4645-2011.

Scaife A. A., Knight J. K., Vallis G. K., Folland C. K. (2005). A stratospheric

influence on the winter NAO and North Atlantic surface climate. *Geophys. Res. Lett. 32*, 1–5.

Seland L (2009). Investigating the shift in the North-Atlantic storm track. *Thesis for the degree of Master of Science, Oslo University* , 1-156.

Semeniuk K., Fomichev V.I., McConnell J.C. Fu C., Melo S.M.K. Usoskin I.,(2011). Middle atmosphere response to the solar cycle in irradiance and ionizing particle precipitation. *Atmos. Chem. Phys. 11*, doi:10.5194/acp-11-5045-2011.

Seppälä A., Verronen P.T., Kyrölä E., Hassinen S., Backman L., Hauchecorne A., Bertaux J.L., Fussen D. (2004). Solar proton events of October–November 2003: Ozone depletion in the Northern Hemisphere polar winter as seen by GOMOS/Envisat. *Geophysical Research Letters 31*, doi:10.1029/2004GL021042.

Seppälä A., Verronen P.T., Clilverd M.A., Randall C.E., Tamminen J., Sofieva V., Backman L., Kyrölä E. (2007a). Arctic and Antarctic polar winter NOx and energetic particle precipitation in 2002-2006. *Geophysical Research Letters 34*, doi:10.1029/2007Gl029733.

Seppälä A., Clilverd M.A., Rodger C.J. (2007b). NOx enhancements in the middle atmosphere during 2003-2004 polar winter: Relative significance of solar proton events and the aurora as a source. *J. Geophys. Res. 112*, doi:10.1029/2006JD008326.

Seppälä A., Randall C.E. Clilverd M.A., Rozanov E., Rodger C.(2009). Geomagnetic activity and polar surface air temperature variability. *J. Geophys. Res. 114*, doi:10.1029/2008JA014029.

Seppälä A., Lu H., Clilverd M.A., Rodger C.(2013). Geomagnetic activity signatures in wintertime stratosphere wind, temperature, and wave response. *J. Geophys. Res. 118*, doi:10.1002/jgrd.50236.

Sigmond M., Siegmund P. C., and Kelder H. (2003). Analysis of the coupling between the stratospheric meridional wind and the surface level zonal wind during 1979-93 Northern Hemisphere extratropical winters. *Climate Dynamics 22(2)*, 211–219.

Simpson I., Blackburn M., Haigh J. D. (2009). The Role of Eddies in Driving the Tropospheric Response to Stratospheric Heating Perturbations. *J. Atmos. Sci. 66*, 1374–1365.

Simpson I.(2009). Solar influence on stratosphere-troposphere dynamical coupling. *PhD thesis at Space and Atmospheric Physics Group, IMPERIAL COLLEGE,* ,1–229.

Sinnhuber M., Nieder H., Wieters N. (2012). Energetic particle precipitation and the chemistry of the mesosphere/lower thermosphere. *Surveys in Geophysics 33*, doi:10.1007/s10712-012-9201-3.

Sinnhuber B.-M., Kiesewetter G., Burrows J.P., Langematz U., Lubken F.J.

(2012b). Data assimilation and model calculations to study chemistry climate interactions in the stratosphere. *Climate and Weather of the Sun-Earth System (CAWSES)* , publisher: Springer, Dordrecht, The Netherlands.

Sinnhuber M., Funke B., von Clarmann T., Lopez-Puertas M., Stiller G.P., Seppälä A.(2014). Variability of NOx in the polar middle atmosphere from October 2003 to March 2004: vertical transport versus local production by energetic particles. *Atmos. Chem. Phys. 14*, doi:10.5194/acp-14-7681-2014.

Siskind D.E., Russell J.M. (1996). Coupling between middle and upper atmospheric NO: Contraints from HALOE observations. *Geophys. Res. Lett. 23*, 137-140.

Siskind D.E., Nedoluha G.E., Randall C.E., Fromm M., Russell J.M.(2000). An assessment of Southern Hemisphere stratospheric NO_x enhancements due to transport from the upper atmosphere. *Geophys. Res. Lett. 27*, doi=10.1029/1999GL010940.

Smith D., Scaife A. A., Kirtman B. (2005). What is the current state of scientific knowledge with regard to seasonal and decadal forecasting?. *Environ. Res. Lett. 7*, 1–12.

Smith D., Scaife A. A., Eade R., Knight J. K. (2014). Seasonal to decadal prediction of the winter North Atlantic Oscillation: emerging capability and future prospects. *Q. J. R. Meteorol. Soc.* , doi:10.1002/qj.2479.

Smith A. R. (1983). Stationary waves in the winter stratosphere: Seasonal and interannual variability. *Journal of Atmospheric Science 40*, 245–261.

Solomon S., Crutzen P.J. Roble R.G. (1982). Photochemical Coupling Between the Thermosphere and the Lower Atmosphere 1. Odd Nitrogen From 50 to 120 km. *J. Geophys. Res. 87*, 7206–7220.

Souders M. B., Colle B.A., Chang E.K.M.(2014a). A description and evaluation of an automated approach for feature-based tracking of Rossby wave packets. *Mon. Wea. Rev. 142*, 3505-3527.

Souders M. B., Colle B.A., Chang E.K.M.(2014b). The climatology and characteristics of Rossby wave packets using a feature-based tracking technique. *Mon. Wea. Rev. 142*, 3528-3548.

Soukharev B. E. and Hood L. L. (2006). The solar cycle variation of stratospheric ozone: Multiple regression analysis of long–term satellite data sets and comparisons with models. *Journal of Geophysical Research 111* , doi: 10.1029/2006JD007107.

Sun C. Li J. Jin F. Xie F. (2014). Contrasting meridional structures of stratospheric and tropospheric planetary wave variability in the Northern Hemisphere. *Tellus 66*, 25303.

Sun C. Li J. Jin (2012). Space-Time Spectral Analysis of the Southern Hemisphere Daily 500-hPa Geopotential Height. *Mon. Wea. Rev. 140*, 3844–3856.

Swartz W.H., Stolarski R.S., Oman L.D., Fleming E.L., Jackman C.H.(2012). Middle atmosphere response to different descriptsions of the 11-year solar cycle in spectral irradiance in a chemistry-climate model. *Atmos. Chem. Phys. 12*, doi:10.5194/acp-12-5937-2012.

Tripathi O. P., Baldwin M., Charlton A., Charron M., Eckermann S. D., Gerber E., Harrison G., Jackson D. R., Kim B-M., Kuroda Y., Lang A., Mahmood S., Mizuta R., Roff G., Sigmondk M., Son S-W. (2014). The predictability of the extratropical stratosphere on monthly time-scales and its impact on the skill of tropospheric forecasts. *Q. J. R. Meteorol. Soc. 141*, 987-1003.

Van Loon H., and Jenne R.L.(1972). The zonal harmonic standing waves in the Southern Hemisphere. *Journal of Geophysical Research 77*, 992–1003.

Verronen P.T., Lehmann R. (2015). Enhancement of odd nitrogen modifies mesospheric ozone chemistry during polar winter. *Geophys. Res. Lett. 42*, 10445–10452.

Wilcox L.J., Charlton–Perez (2013). Final warming of the southern hemisphere polar vortex in high–and low–top CMIP5 models. *Journal of Geophysical Research 118 (6)*, 2535–2546.

Wittman M., Charlton A., Polvani L. (2007). The effect of lower stratospheric shear on baroclinic instability. *J. Atmos. Sci. 64*, 479–496.

WMO (1957). Meteorology A Three-Dimensional Science: Second Session of the Commission for Aerology. *WMO, Geneva Bulletin IV(4)*, 134–138.

Woods T., Rottman G.(2002). Solar ultraviolet variability over time periods of aeronomic interest, in Atmospheres in the Solar System: Comparative Aeronomy, Geophys. Monogr. Ser., vol. 130, edited by M. Mendillo, A. Nagy, and J. H. Waite, AGU, Washington, D. C. *42*, 221–234.

Woolings T., Hoskins B., Blackburn M., Berrisford P. (2008). A New Rossby Wave-Breaking Interpretation of the North Atlantic Oscillation. *J. Atmos. Sci. 65*, 609–626.

Yamashita Y., Sakamoto K., Akiyoshi H., Takahashi M., Nagashima T., Zhou L.B. (2010). Ozone and temperature response of a chemistry climate model to the solar cycle and sea surface temperature. *J. Geophys. Res. 115*, doi:10.1029/2009JD013436.

Yin J.(2005). A Consistent Poleward Shift of the Storm Tracks in Simulations of the 21st Century Climate. *Geophysical Research Letters 32*.

Yoden S. (1987). Bifurcation properties of a stratospheric vacillation model. *Journal of Atmospheric Science 44*, 1723–1733.

Zadeh L.A. (1965). Fuzzy sets. *Inform, Control. 8*, 338–353.

Zimin A.V., Szunyogh I., Patil D.J., Hunt B.R., Ott E. (2003). Extracting envelopes of Rossby wave packets. *Mon. Wea. Rev. 131*, 1011-1017.

Zimin A.V., Szunyogh I., Patil D.J., Hunt B.R., Ott E. (2006). Extracting en-

velopes of nonzonally propagationing Rossby wave packets. *Mon. Wea. Rev. 134*, 1329-1333.

Acknowledgment:

First and foremost I like to thank my supervisor Dr. Miriam Sinnhuber for giving me the opportunity to do this PhD work. I like to thank her for all the helps, supports and advices that she offered me throughout my PhD. She always managed to find whatever time was needed to discuss about my PhD work. The freedom in research that she offered me as well as her patience were important sources of encouragement and enthusiasm through many of the difficult moments in my PhD.

I also wish to thank my committee members (Prof. Johannes Orphal and Prof. Peter Braesicke) for reading this thesis and guiding me through this work. My special thanks go to Prof. Peter Braesicke who inspired me in many ways and for his scientific advice and knowledge and many insightful suggestions and discussions. I also like to thank him for providing me the opportunity to visit and stay at the Department of Applied Mathematics and Theoretical Physics in Cambridge University and work with Prof. Peter Haynes (a pioneering researcher in middle atmospheric dynamics) and Dr. Peter Hitchcock. The financial help provided by GRAduate school for Climate and Environment (GRACE) for visiting Cambridge University is also appreciated. I also like to thank Dr. Tilo Fytterer for writing a german abstract for my thesis. I thank Dr. Stefan Versick for providing advice during my PhD (especially running the EMAC model).

Finally, I would like to thank my family for all their love and encouragement. Words can not express how grateful I am to my wife (Mahdieh Fathi Barnaji) for her love and patience. She sacrificed her career to stay with me during my PhD. I hope to repay her sacrifice one day. I also like to thank my parents who raised me with a love of science. They supported me in all of my pursuits.